TESIS DE LA UNIVERSIDAD
DE ZARAGOZA

2013

72

Laura Seguí Iglesia

Pattern Recognition in a High Pressure Time Projection Chamber prototype with a Micromegas readout for the 136Xe double beta decay

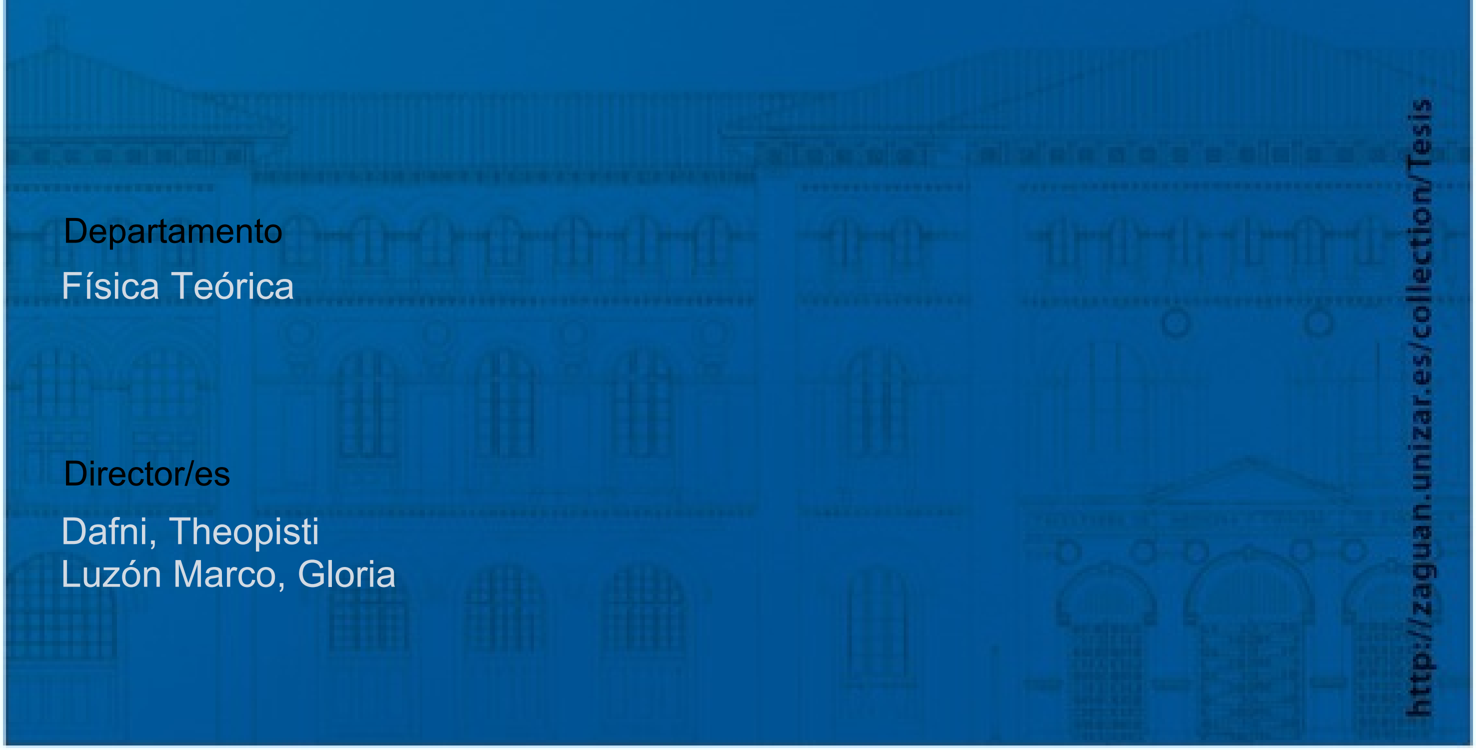

Departamento

Física Teórica

Director/es

Dafni, Theopisti
Luzón Marco, Gloria

ISSN 2254-7606

Prensas de la Universidad
Universidad Zaragoza

Tesis Doctoral

PATTERN RECOGNITION IN A HIGH PRESSURE TIME PROJECTION CHAMBER PROTOTYPE WITH A MICROMEGAS READOUT FOR THE 136XE DOUBLE BETA DECAY

Autor

Laura Seguí Iglesia

Director/es

Dafni, Theopisti
Luzón Marco, Gloria

UNIVERSIDAD DE ZARAGOZA
Física Teórica

2013

Pattern Recognition in a High Pressure Time Projection Chamber prototype with a Micromegas readout for the ^{136}Xe double beta decay

Memoria presentada por

Laura Seguí Iglesia

para optar al grado de
Doctora en Física

en el
Laboratorio de Física Nuclear y Astropartículas
Área de Física Atómica, Molecular y Nuclear
Departamento de Física Teórica
UNIVERSIDAD DE ZARAGOZA

Abril 2013

Agradecimientos

En primer lugar me gustaría dedicar esta tesis a la memoria de Julio Morales, que me permitió comenzar mi etapa investigadora en el grupo de Física Nuclear y Astropartículas de la Universidad de Zaragoza.

Este trabajo no hubiera sido posible sin el contínuo apoyo y guía de mis directoras Gloria Luzón y Theopisti Dafní (*ευχαριστώ*). Quiero agradecerles su tiempo y dedicación, así como su consejo en las múltiples discusiones que hemos mantenido. A ambas les quiero agradecer el haberme enseñado a ser crítica con mi trabajo, a no dejar de buscar cabos sueltos y el haberme transmitido su valentía y entusiasmo ayudándome a formarme como física.

Me gustaría también agradecer a Igor G. Irastorza la confianza que siempre ha demostrado en mi trabajo, así como el transmitirme su entusiamo por la Física y estar siempre dispuesto a ayudarme.

También mi agradecimineto a José Ángel Villar por su constante intéres a lo largo de estos años.

Mi reconocimineto se hace extensivo a todos mis compañeros del departamento en especial a Héctor Gómez, por su disposición continua ante las numerosas dudas y problemas que han surgido durante la realización de esta tesis. Igualmente agradezco a Francisco Iguaz y Alfredo Tomás su continua ayuda, en especial, con el software. Gracias también a Juan Castel y Ángel Lagraba porque sin ellos no hubiese sido posible la construcción del prototipo usado en esta investigación. Quiero nombrar también especialmente a mi compañera de despacho, Clara Cuesta, porque sin su apoyo y nuestras conversaciones arreglando el mundo este camino hubiera sido más largo. A ella y a Asun Rodríguez quiero agradecerles los ratos de diván. Al resto de compañeros mis sinceras gracias porque siempre habéis estado dispuestos a ayudarme.

Me gustaría agradecer a todo el experimento NEXT el haberme permitido realizar mi tesis dentro de la colaboración.

Tambien me gustaría nombrar a los compañeros que he tenido durante mis estancias en otros centros. Especialmente mi agradecimineto a Esther Ferrer Ribas, por permitirme desarrollar mi investigación en un gran centro como CEA de Saclay donde he mejorado mis conocimientos con los detectores Micromegas. Gracias también a Thomas Papaevangelou y a Iannis Giomataris por su amabilidad y consejo así como al resto de mis compaeros en mis estancias en Saclay y en CAST.

Por último gracias a toda mi familia, en especial a Antonio José, Anne-Marie, Álvaro e Inés, y a todos mis amigos por su apoyo y comprensión durante estos años.

Contents

Agradecimientos iii

Preface 1

I Neutrino Physics and Motivation 3

1 Neutrino physics and double beta decay: theory and experiments 7
- 1.1 Neutrino Physics 8
  - 1.1.1 Neutrino mass and oscillations 9
  - 1.1.2 The seesaw mass mechanism and neutrino masses 12
- 1.2 Double beta decay 13
- 1.3 The search of neutrinoless double beta decay 19
  - 1.3.1 Techniques of detection 19
  - 1.3.2 Experimental challenge 20
  - 1.3.3 Sensitivity of an experiment 22
- 1.4 Experimental situation: Past, present and future experiments 23
  - 1.4.1 Past Experiments 24
  - 1.4.2 Present situation 26
  - 1.4.3 Micromegas for rare event searches 30

II Operation of Micromegas detectors focus on a $\beta\beta0\nu$ experiment. 33

2 Phenomenology of particles in gases and gaseous detectors. Micromegas Detectors. 37
- 2.1 Ionization in gases 38
- 2.2 Transport of electrons in gases 39
  - 2.2.1 Diffusion 41
  - 2.2.2 Intrinsic uncertainties in gaseous detectors 42
- 2.3 Operation of a gas detector and the avalanche multiplication region. Townsend coefficients 45
- 2.4 Signal creation 49
- 2.5 Energy resolution 50
  - 2.5.1 Statistical contributions 50
  - 2.5.2 Other factors 52
- 2.6 Gaseous detectors 52
  - 2.6.1 Time Projection Chamber 53
  - 2.6.2 Micromegas detectors 54
  - 2.6.3 Micromegas Technology 57
    - 2.6.3.1 Bulk technology 57
    - 2.6.3.2 Microbulk Technology 58

3 NEXT-MM prototype: design and commissioning 61
3.1 The NEXT experiment 62
3.2 NEXT-MM 64
    3.2.1 Experimental setup 64
        3.2.1.1 Vessel and internal components 64
        3.2.1.2 Gas system 66
        3.2.1.3 Acquisition system 68
    3.2.2 The Micromegas Detectors used 71
3.3 Operational tests with NEXT-MM prototype 73
    3.3.1 High pressure test 73
    3.3.2 Vacuum and outgassing 73
    3.3.3 High voltage tests 75
3.4 Main features of the detectors in Ar-isobutane: gain curves and first energy resolution estimations. 76
    3.4.1 Electron transparency 78
    3.4.2 Absolute Gain 78
    3.4.3 Energy resolution 79
    3.4.4 Cosmic Rays 80
3.5 Commissioning of the detectors and the electronics in NEXT-MM 80
    3.5.1 Bulk detector: First Results 81
    3.5.2 Microbulk detector: First Results 82

4 NEXT-MM: First data with Xe-TMA 87
4.1 Analysis code 88
4.2 First tracks 89
    4.2.1 Energy resolution results 95
4.3 Tracking with more than one detector 96
4.4 Trigger from an external source. 102
    4.4.1 Energy resolution 105
    4.4.2 Drift velocity 117
    4.4.3 Preliminary attachment results 117
4.5 Summary 119

III Physics potential of a $\beta\beta0\nu$ experiment with Micromegas in a HP Xe TPC. 121

5 Background studies and discrimination algorithms 125
5.1 Simulation codes 126
    5.1.1 Decay0 127
    5.1.2 Geant4 127
    5.1.3 Simulation of the Physical system and anylisis: RESTSoft 128
5.2 Simulated Events 131
    5.2.1 Signal 131
    5.2.2 Background 133
5.3 Simulated geometry 137
5.4 The topology of the events 138
    5.4.1 Signal Events 138
    5.4.2 Background 139
    5.4.3 Deterioration of pattern recognition 142
5.5 Discrimination Algorithms 149
    5.5.1 A figure of merit for background reduction 149
    5.5.2 Energy 150

5.5.3 Track selection 150
5.5.4 Topology Selection 153
5.5.5 Fiducial rejection 160
5.5.6 Summary 160
5.6 Background Rejection 160
5.6.1 High diffusion gas: Pure Xenon 161
5.6.2 Low diffusion gas: Xenon-TMA. 162
5.6.3 Comparison between the two diffusions 163
5.6.4 Surviving events 165
5.7 Energy Resolution studies 168
5.8 Background level 173
5.9 Sensitivity for the neutrino effective mass 178

6 Perspectives for a 1 ton HPXeTPC **183**
6.1 Signal 184
6.2 Rejection Factor 185
6.3 Expected sensitivity 186

7 Conclusions **191**

Resumen de la memoria y conclusiones **197**

Bibliography **209**

Preface

The main objective of the work presented here is the study of the pattern recognition impact in the background rejection in a high pressure gaseous time projection chamber with Micromegas for the ^{136}Xe neutrinoless double beta decay.

Since in 1930 Wolfgang Pauli, in his famous letter starting with "Dear radioactive ladies and gentlemen", postulated the existence of the neutrino, it was a mysterious and evasive particle. In the Standard Model of electroweak interactions it has no mass and can appear only as a left-handed particle (a right-handed for the antineutrino). Moreover, in the 60's appeared the so-called "solar neutrino problem" with the detection of less than the expected neutrinos coming from the sun. It is not until the discovery of neutrino oscillations that this effect is explained. With this observation, the massive nature of the neutrino was demonstrated. This fact leaves the door open for physics beyond the Standard Model. However, from the oscillation measurements, only information about square differences of masses between the different neutrino types can be obtained, but not the absolute scale. In addition the nature of the neutrino, Dirac or Majorana, is still unknown. The neutrinoless double beta decay can shed light on both questions at the same time and has become a hot topic both, theoretically and experimentally.

The neutrinoless double beta decay search implies an experimental challenge because it is a very rare process with a long half-life and only few counts per year are expected using 100 kg of beta emitter. As in all the experiments looking for rare events, to reduce the background that can hide or mimic the signal is one of the essential requirements. An experiment with a gaseous time projection chamber (TPC) equipped with high granularity detectors has the advantage to reconstruct the topology of the event that deposits energy interacting with the gas, and, therefore, can develop discrimination algorithms based on the topological signature differences expected between the signal and the background. This is the approach of the NEXT experiment, in which also the energy resolution expected is very good (another key parameter for this search), of the order of 1% FWHM at $Q_{\beta\beta}$. NEXT is based on the detection of the electroluminescent signal, where the energy is registered with a PMT plane and the topology information is provided by a SiPM array. The option to use Micromegas detectors for a TPC for a further phase has motivated the construction of a prototype equipped with these detectors in the University of Zaragoza.

In order to evaluate the option to construct a high pressure TPC for the neutrinoless double beta decay search different studies are performed. The work presented here is structured in three parts: the first one is an introduction to the neutrino and double beta decay physics and experimental status. In the second one, the operation of Micromegas detectors in gas focused on a neutrinoless double beta decay with a medium size prototype is presented, and in the third part is studied the expected physical potential of this option for a 100 kg scale experiment. In particular:

- Chapter 1 highlights briefly the main points in neutrino physics and neutrinoless double beta decay. Specially the mass mechanism and the implication of new physics in the detection of this signal are discussed. Moreover, an experimental review of the past, present and future experimental situation is given.
- In the second chapter the main processes occurring in a gaseous detector while a radiative particle interacts are explained, in particular, factors crucial for a neutrinoless double beta decay as the intrinsic energy resolution. In the second part of the chapter the Micromegas detectors are presented as well as their main features and manufacturing technologies.
- The description of the experimental TPC equipped with Micromegas that has been constructed and commissioned is done in chapter 3. In particular, the operational tests and the commissioning of the detectors and the electronics, are summarized.
- In chapter 4 are presented the first results obtained in Xe-TMA at 1 bar with the prototype. The track that different particles produced in the pixelized anode plane of the Micromegas, are shown, as well as first energy resolution results.
- In chapter 5 is presented the full simulation chain used to study the topology of signal and backgrounds in a possible future neutrinoless double beta decay with a high pressure Xenon TPC equipped with Micromegas. Also, a discussion about the differences between both populations (signal and background) is done. These differences led to the definition of different algorithms to maximize the signal efficiency while rejecting background. The effect of these algorithms is studied in two different gases having a high and low diffusion coefficient respectively, which has a high influence in the topological recognition of the events. In addition, it is studied the effect of the energy resolution in the discrimination power. Also the expected background is obtained. In the last section it is discussed the expected sensitivity for the effective electronic neutrino mass with these results.
- In chapter 6 is evaluated the possibility to go to a 1 ton experiment with this technique.
- Finally, in the last chapter are summarized the main conclusions of the different results presented along the work.

Part I

Neutrino Physics and Motivation

The main goal of the work presented here is to evaluate the physics potential of a neutrinoless double beta decay ($\beta\beta0\nu$) experiment based on a gaseous Xenon time projection chamber equipped with Micromegas. The $\beta\beta0\nu$ search is one of the hottest topics in particle and astroparticle physics nowadays because its measure could give basic information about neutrino nature, and intrinsic properties like its mass, and about the Universe.

Oscillation experiments have proved that neutrinos are massive particles, opening the door to new physics. In this landscape, determination of the absolute mass of this particle has become a crucial point. Different experimental approaches are valid to obtain information about the neutrino mass: cosmological observations, direct measurements and $\beta\beta0\nu$ experiment, but the latest is of special interest because its detection would lead to conclude that neutrino and antineutrino are the same particles, revealing its Majorana nature.

Before summarizing the experimental studies performed, a general summary of the neutrino physics and properties which have motivated this work, is presented. In addition, past experiments and the results obtained are reviewed. Since only upper limits for the neutrino mass were reached, several experiments of the so-called new generation have been proposed claiming to be sensitive enough to explore lower mass regions thanks to the appearance of new technologies. A global view of these new experiments and techniques is also presented.

Chapter 1

Neutrino physics and double beta decay: theory and experiments

Contents

1.1 Neutrino Physics 8
- 1.1.1 Neutrino mass and oscillations 9
- 1.1.2 The seesaw mass mechanism and neutrino masses 12

1.2 Double beta decay 13

1.3 The search of neutrinoless double beta decay 19
- 1.3.1 Techniques of detection 19
- 1.3.2 Experimental challenge 20
- 1.3.3 Sensitivity of an experiment 22

1.4 Experimental situation: Past, present and future experiments . . 23
- 1.4.1 Past Experiments 24
- 1.4.2 Present situation 26
- 1.4.3 Micromegas for rare event searches 30

The neutrino was first proposed theoretically in 1930 by W. Pauli [1] to explain the continuous beta spectrum observed by J. Chadwick in 1914 and like this, preserve the energy, momentum and angular momentum. In 1933 E. Fermi proposed the name neutrino and one year later published the first theory of beta decay based on this particle [2], but it was not experimentally observed until 1956 in the Reines-Cowan experiment [3]. Reines was rewarded with the Nobel Prize in 1995.

In 1962 L. M. Lederman, M. Schwartz and J. Steinberger showed the existence of more than one type of neutrinos by first detecting interactions of the muon neutrino at the Brookhaven National Laboratory [4] and they earned Nobel Prize in Physics in 1988. The third type of neutrino was discovered in 2000 by the DONUT collaboration at Fermilab [5]. Its existence had already been inferred by, both, theoretical consistency and experimental data from the Large Electron Positron Collider in CERN.

From the mid-60's to 2002 remained unsolved the so-called solar neutrino problem. In the late 1960s, R. Davis and J. N. Bahcall were the first physicists to measure the flux of neutrinos from the Sun and detect a deficit in the Homestake Experiment.This deficit was confirmed twenty years later by the experiment Kamiokande II (in the Mozumi mine in Japan) [6]. In 2001 the SNO Experiment (Sudbury Neutrino Observatory, in Canada) gave the first evidence of neutrino oscillation that could solve this problem [7]. The neutrino oscillation concept was first proposed by B. Pontecorvo in 1957 [8] in a similar way as K meson oscillations. In 2005 Z. Maki, M. Nakagawa and S. Sakata developed this idea in the theory of neutrino flavour mixing and flavour oscillations [9]. The oscillations of neutrino can only be possible if neutrinos have mass. In 2002 Ray Davis and Masatoshi Koshiba won part of the Nobel Prize in Physics for experimental work that found the flux of solar neutrinos to be around a third of the number predicted by the standard solar model.

The neutrino flavour oscillation has also been observed in neutrinos produced in the atmosphere or in reactors. As in the solar case, it causes a deficit in the number of detected neutrinos as proved by IMB [10] and in Kamiokande [6] in 1985 and was explained with neutrino oscillation theories in 1988 in the Super-Kamiokande [11, 12] for atmosphere neutrinos. The deficit in reactor neutrinos was observed by KamLAND in 2002 [13]. The confirmation of neutrino oscillation entails that neutrino has mass, giving a rebirth of experiments looking for the neutrinoless double beta decay between nuclei and neutrino physics beyond the Standard Model.

1.1 Neutrino Physics

The neutrino is an elementary particle with spin 1/2 and does not carry electric charge. Moreover, from the Standard Model (SM) it has zero mass. This is constrained by three independent reasons: there are only left-handed (LH) neutrinos, ν_L; there are only Higss doublets of $SU(2)_L$ and there are only renormalizable terms.

In the SM these conditions apply and the three neutrino flavours, ν_e, ν_μ and ν_τ can be distinguished by separate lepton numbers. In addition, as only LH neutrinos exist (and right-handed antineutrinos, RH), the chirality is not conserved, violating parity. However, from the experiment of oscillations it is known that neutrinos have mass $\neq 0$. To generate a Lorentz invariant neutrino mass term some of the previous conditions must be relaxed. A Dirac mass term may be generated if neutrino, ν_i, and anti-neutrino, $\bar{\nu_i}$, have the same mass and different lepton number in the usual way as for fermions

$$M_D[\bar{\nu}_R \nu_L + \bar{\nu}^c_L \nu^c_R]. \tag{1.1}$$

The quantum states form a four-component object of mass m that can be described by the Dirac equations

$$i(\hat{\sigma}^{\mu}\partial_{\mu})\psi_R - m_D\epsilon\psi_L = 0 \tag{1.2}$$

$$i(\sigma^{\mu}\partial_{\mu})\psi_L - m_D\epsilon\psi_R, \tag{1.3}$$

where $\bar{\sigma}^{\mu} = \sigma^0\vec{\sigma}$, $\sigma^{\mu} = \sigma^0 - \vec{\sigma}$ and $(\sigma^0\vec{\sigma})$ are the Pauli matrices. The chirality states ψ_R and ψ_L are two-component spinors that couple to form a four-component bi-spinor quantum state.

On the other hand, if there is no conservation of lepton number, as in a $\beta\beta0\nu$ decay, Majorana [14] suggested an alternative description of massive fermions. A Majorana particle denotes a particle that is identical to its antiparticle, therefore, for neutrinos $\nu_i \equiv \bar{\nu_i}$, while Dirac particles distinguish between the two. This characteristic implies that, mathematically, Majorana particles are two-component objects, ψ_R (mass m_R) and ψ_L (mass m_L) which obey independent equations

$$i(\hat{\sigma}^{\mu}\partial_{\mu})\psi_R - m_R\epsilon\psi_R^* = 0 \tag{1.4}$$

$$i(\sigma^{\mu}\partial_{\mu})\psi_L - m_L\epsilon\psi_L^* = 0, \tag{1.5}$$

$$\tag{1.6}$$

where $\epsilon = i\sigma_y$. The Majorana fields can be expressed in four-component notation:

$$\psi_L(x) = \begin{pmatrix} -\epsilon\psi_L^*(x) \\ \psi_L(x) \end{pmatrix}, \psi_R(x) = \begin{pmatrix} \psi_R(x) \\ \epsilon\psi_L^*(x) \end{pmatrix}. \tag{1.7}$$

These spinors are autoconjugate states, $\psi^c_{L(R)}(x) = \psi_{L(R)}(x)$. The change in the chirality requires for the antiparticle to be equal to the particle and a massive one. The Lorentz invariant mass terms for a Majorana neutrino are

$$M_L[(\bar{\nu_L})^c\nu_L + \bar{\nu_L}\nu_L^c] \tag{1.8}$$

$$M_R[(\bar{\nu_R})^c\nu_R + \bar{\nu_R}\nu_R^c]. \tag{1.9}$$

Notice that these terms are only allowed for neutral particles.

1.1.1 Neutrino mass and oscillations

Oscillations of neutrinos are a consequence of the presence of neutrino flavour mixing in vacuum. Therefore, neutrinos of a defined flavour (ν_l) have not to be necessary states of a definite mass (ν_i). The Lagrangian term of charged current used to describe the interactions of flavour neutrinos is given in the SM by

$$L^{CC}(x) = \frac{-g}{2\sqrt{2}} \sum_{l=e,\mu,\tau} \bar{\nu_{lL}}(x)\, \gamma_\alpha l_L(x)\, W^\alpha(x) \,+\, h.c., \tag{1.10}$$

where W is the gauge boson mediating the weak interactions, l denotes the lepton particles, $\nu_{lL}(x)$ are the LH component of the field of the neutrino ν_l and γ_α the Gamma matrices. The flavour neutrino field $\nu_{lL}(x)$ are linear combinations of the fields of three (or more) neutrinos ν_i with masses $m_i \neq 0$

$$\nu_{lL}(x) = \sum_i U_{li}\, \nu_{iL}(x), \tag{1.11}$$

U being a unitary 3×3 ($N \times N$ if there exist N neutrinos families) mixing matrix called the Pontecorvo-Maki-Nakagawa-Sakata (PMNS) mixing matrix [8, 9]

$$U = \begin{pmatrix} U_{e1} & U_{e2} & U_{e3} \\ U_{\mu1} & U_{\mu2} & U_{\mu3} \\ U_{\tau1} & U_{\tau2} & U_{\tau3} \end{pmatrix} =$$

$$= \begin{pmatrix} c_{12}\, c_{13} & s_{12}\, c_{13} & s_{13}\, e^{i\delta} \\ -s_{12}c_{23} - c_{12}s_{23}s_{13}\, e^{i\delta} & c_{12}c_{23} - s_{13}s_{23}s_{13}\, e^{i\delta} & s_{23}c_{13} \\ s_{12}s_{23} - c_{12}c_{23}s_{13}\, e^{i\delta} & -c_{12}c_{23} - s_{12}c_{23}s_{13}\, e^{i\delta} & c_{23}c_{13} \end{pmatrix} \begin{pmatrix} e^{i\alpha_1/2} & 0 & 0 \\ 0 & e^{i\alpha_2/2} & 0 \\ 0 & 0 & 1 \end{pmatrix}. \tag{1.12}$$

where $c_{ij} = \cos\theta_{ij}$ and $s_{ij} = \sin\theta_{ij}$, being θ_{ij} the mixing angles $[0 - \pi/2]$ that takes into account the different origins of the oscillations (θ_{12} solar, θ_{23} atmospheric and θ_{13} from reactors). $\delta = [0-2\pi]$ is the Dirac CP phase that would be $\neq 0$ only if neutrino oscillation violates CP (this is expected but has not yet been observed). α_1 and α_2 are two Majorana CP violating phases only relevant if neutrinos are Majorana particles (can result in CP violation if their values differs from a multiple of π) and they do not affect oscillation experiments [15]. If experiment shows that the PMNS matrix is not unitary, a sterile neutrino or some other new physics is required.

Equation 1.11 can be rewritten as

$$|\nu_i\rangle = \sum_l U_{li}\ |\nu_l\rangle \tag{1.13}$$

$$|\nu_l\rangle = \sum_i U^*_{li}\ |\nu_i\rangle \tag{1.14}$$

The probability of the transition between an state ν_l to $\nu_{l'}$ in vacuum is given by

$$P\left(\nu_l \to \nu_{l'}\right) = \left| \sum_{i=1}^{3} U_{l'i}\, e^{-i \frac{\Delta m^2_{ij}\, L}{2\, E}}\, U^*_{li} \right|^2, \tag{1.15}$$

where j is an arbitrary index 1,2 or 3, $\Delta m^2_{ij} = |m^2_i - m^2_j|$, L is the propagation length and E is the neutrino energy. This expression is obtained taking into account the ultra-relativistic nature of the neutrinos in the Schrödinger equation of the eigenstates [16]. In addition, to obtain this expression it has been assumed that the momentum of the initial and ending neutrino state is the same $p_i = p_j$ [17]. The probability 1.15 depends on six parameters: two mass-squared differences, three mixing angles and a CP phase, δ. The oscillation probability of an antineutrino is the same as the one of the neutrino except for the mixing matrix U that is transformed to its complex conjugated U^*, implying that if U is not real the oscillation probabilities are different. If CPT is conserved, the difference in the probability of oscillation between neutrinos and antineutrinos is an indication of CP violation.

The first evidence of the oscillation process was observed by SNO [7] in solar neutrinos, and SuperKamiokande [11, 12, 18] in atmospheric neutrinos. Since these first measurements, some of the unknowns in previous equations have been measured or limited by different experiments dedicated to neutrino oscillations like SNO [7, 19–22], KamLand [13], CHOOZ [23], K2K [24–26], MINOS [27], BOREXINO [28]. Recent results from Daya-Bay [29] give a non-zero value for θ_{13}, the last of the angles to be determined. Combined with results from RENO [30], DoubleCHOOZ [31], T2K [32] and MINOS [33] $\theta_{13} = 0$ is now excluded at more than 10σ.

Two different neutrino mass spectra are compatible with existing data in the case of three massive neutrinos because there are only two independent neutrino mass squared differences. $|\Delta m^2_{21}|$ is usually identified with the smaller of the two neutrino mass squared differences. From the data it is known that $|\Delta m^2_{21}|$ is positive, so ν_2 is heavier than ν_1 (called like this for convenience), but nothing can be said about ν_3. Therefore, the two scenarios are:

1. Normal spectrum or hierarchy (NH): $m_1 < m_2 < m_3$, $\Delta m^2_{21} \ll \Delta m^2_{23}$
2. Inverted spectrum or hierarchy (IH): $m_3 < m_1 < m_2$, $\Delta m^2_{21} \ll |\Delta m^2_{13}|$

When all three masses are significantly larger than Δm^2_{32}, the hierarchy is referred to as quasidegenerate (QD, $m_1 \cong m_2 \cong m_3$), no matter which eigenstate is the lightest. In all the cases, one of the neutrinos have to have a neutrino mass of the order of 50 meV. In Figure1.1 the different scenarios are schematically shown.

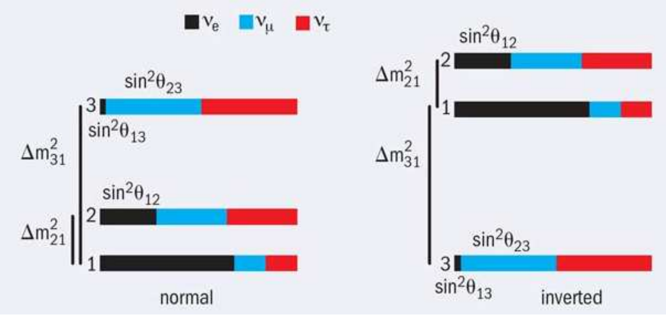

FIGURE 1.1: *Sketch of the possible neutrino mass hierarchies: normal hierarchy (left) and inverted hierarchy (right) (image extracted from [34]).*

1.1.2 The seesaw mass mechanism and neutrino masses

There are several ways to extend the Standard Model to introduce a mass mechanism that generates neutrino masses and also accommodates its small values naturally. If right-handed neutrinos exist, a Dirac mass can be generated as usual. However, this mass term would not explain easily the small values of the neutrino mass, because it requires fine-tuning of the Yukawa coupling (some extra-dimensions theory can accommodate this small Yukawa couplings).

The most popular scenario is the see-saw mechanism [35], that goes beyond the Standard Model postulating the existence of a right-handed neutrino field inert under the electroweak interaction, and also requires a very large mass scale. This mass scale can be identified with the theoretically predicted scale of grand unification ($\sim 10^{15}$ GeV).

In the SM there is no need of right-handed neutrinos. Without them, neutrinos can acquire a mass by the existence of so-called irrelevant operators. These are operators of dimensions larger than four that require the existence of a cut-off. Otherwise, for an infinite cut-off, the mass of the neutrino would be zero. The cut-off cannot be the Planck scale, 10^{19} GeV, because it predicts a mass for the neutrino of the order of 10^{-5} eV, not compatible with the observation from neutrino oscillation experiments. But, it is believed that the SM accommodates in a larger gauge group in the Grand Unified Theories (GUT) with a smaller cut-off. Very schematically, the consistency (absence of anomalies) of the GUT requires the existence of right-handed sterile neutrinos that, as are sterile under the SM gauge group ($SU(3) \times SU(2) \times U(1)$) acquire a mass of the order of the cut-off.

If a sterile RH neutrino is introduced in the theory, the Lorentz invariant mass terms can appear in three different forms, one for the Dirac type 1.1 and two for the Majorana one 1.9. The most general Lagrangian can be written as

$$L = -\frac{1}{2}\begin{pmatrix} \bar{\nu_L}^c & \nu_R^c \end{pmatrix}\begin{pmatrix} M_L & M_D^T \\ M_D & M_R \end{pmatrix}\begin{pmatrix} \nu_L \\ \nu_R^c \end{pmatrix} + h.c. \tag{1.16}$$

For three neutrino families, the neutrino fields, ν, are three component vectors, and the elements of the mass matrix, M, are 3×3 matrices. In order to obtain the mass eigenstates we need to diagonalize the mass matrix, resulting in two generally non-degenerate eigenvalues for each flavour. In the see-saw mechanism we have $M_R \gg M_D \gg M_L \sim 0$ ($M_L = 0$ corresponds to the type I see-saw mechanism)

$$\begin{pmatrix} 0 & M_D^T \\ M_D & M_R \end{pmatrix} \tag{1.17}$$

The light neutrino, after diagonalization, acquires a mass

$$m_\nu \sim \frac{M_D^2}{M_R} \tag{1.18}$$

M_D is of the order of the electroweak scale 10^2 GeV, the observed neutrino mass is of the order of $\sqrt{\delta m^2} \sim 0.01$ eV. This implies that the scale of the cut-off is $M_R \sim 10^{15}$ GeV, the GUT scale energy. In an effective way, the small value of the mass of the neutrino opens a window to the high energy physics and this can also address the baryonic observed asymmetry in the Universe [36].

Neutrino mass measurements

They exist different ways that try to determine the exact value of the neutrino mass.

Direct searches via Tritium β decay

Direct investigations do not rely on further assumptions on the neutrino mass type. The direct or kinematical approach to the search of the neutrino rest mass is based on the study of the relativistic energy momentum relation $E^2 = p^2c^2 + m^2c^4$ and in the energy and momentum conservation in weak semileptonic decays. The most sensitive direct searches for the electron neutrino mass up to now are based on the investigation of the electron spectrum of tritium β decay $^3\mathrm{H} \rightarrow {}^3\mathrm{He}^+ + e^- + \bar{\nu_e}$. The Mainz Experiment [37] reached a sensitivity of 2.3 eV at 95% C.L and the Troitsk [38] re-analysis put a limit for electronic neutrino mass of 2.05 eV at 95% C.L. The future experiment KATRIN [39], under construction, expects to have a sensitivity of 0.2 eV.

A different approach to directly measure the electron neutrino mass is the use of cryogenic bolometers. In this case, the β source can be identical to the β electron spectrometer. Two isotopes are mainly under study: ^{187}Re and ^{163}Ho and the experiments, as MARE [40], are still in the early stage of development.

Cosmological bounds

Cosmology provides bounds on the sum of the neutrino masses. From the Cosmic Microwave Background (CMB) data of the WMAP experiment, combined with supernovae data and data on galaxy clustering it is obtained a limit $\sum_i m_1 \leq 0.3 - 1.3$ eV at 95% C.L [41]. This limit is also marked in Figure 1.1

It follows from these measurements that neutrino masses are much smaller than the masses of charged leptons by at least 6 orders of magnitude. It is natural to suppose that this difference hides new physical mechanisms or processes beyond those predicted by the SM.

Double beta decay

This process will be explained in detail in the next section because it is the objective of this work. The detection of this nuclear process is proportional to effective neutrino electronic mass.

1.2 Double beta decay

A double beta decay ($\beta\beta$) is a weak second order nuclear transition between two even-even isobars. An initial nucleus (A, Z) decays to an isobar $(A, Z + 2)$ through the emission of two electrons. This transition is only possible in nuclei in which the β decay is energetically forbidden or highly suppressed by a high angular momentum difference. A generic level diagram can be seen in Figure 1.2 (a). This process has been largely studied. The decay can exist in two modes

$$(A, Z) \rightarrow (A, Z+2) \;+\; 2e^{-} \;+\; 2\nu_e, \tag{1.19}$$

$$(A, Z) \rightarrow (A, Z+2) \;+\; 2e^{-}. \tag{1.20}$$

The mode with the emission of neutrinos ($\beta\beta2\nu$) is a process allowed by the SM model and has been observed in different isotopes (summarized in Table 1.1). The neutrinoless mode ($\beta\beta0\nu$) has only been theoretically predicted and implies physics beyond the Standard Model (BSM) because the violation of the leptonic number is required. Moreover, it is only possible if the neutrino and antineutrino are the same particles, that is, if neutrino nature is Majorana. The Feynman diagrams of both decays are shown in Figure 1.3.

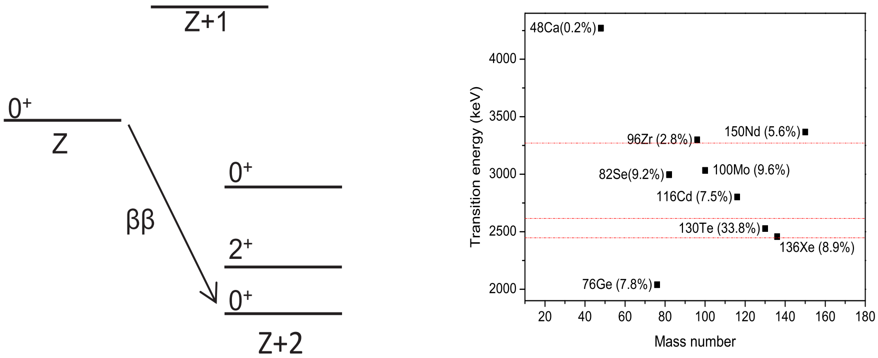

(a) (b)

Figure 1.2: *(a) An scheme with a generic level diagram of a $\beta\beta$ decay (modified from [42]. (b) Plot of the mass and transition energy ($Q_{\beta\beta}$ in keV) for different isotopes in which the $\beta\beta0\nu$ decay is more favourable experimentally due to its high $Q_{\beta\beta}$ value. Energies of the main background sources are also indicated in red ($^{214}Bi(\beta) = 3270\,keV$, $^{214}Bi(\gamma) = 2447\,keV$, $^{208}Tl(\gamma) = 2615\,keV$) (modified from [43]).*

Isotope	$T^{2\nu}_{1/2}$ y
^{48}Ca	$(4.4\pm^{0.6}_{0.5})\times^{19}$
^{76}Ge	$(1.5 \pm 0.1) \times 10^{21}$
^{82}Se	$(0.92 \pm 0.07) \times 10^{20}$
^{96}Zr	$(2.3 \pm 0.2) \times 10^{19}$
^{100}Mo	$(7.1 \pm 0.4) \times 10^{18}$
^{116}Cd	$(2.8 \pm 0.2) \times 10^{19}$
^{128}Te	$(1.9 \pm 0.4) \times 10^{24}$
^{130}Te	$(6.8\pm^{1.2}_{1.1}) \times 10^{20}$
^{136}Xe	$(2.1 \pm 0.14(stat) \pm 0.2(syst)) \times 10^{21}$
^{150}Nd	$(8.2 \pm 0.9) \times 10^{18}$
^{288}U	$(2.0 \pm 0.6) \times 10^{21}$

Table 1.1: *List of $\beta\beta2\nu$ decay half-lifes measured in different isotopes, extracted from [44, 45].*

The mode with neutrinos was firstly proposed in 1935 by Maria Goeppert-Mayer [46], after Pauli's hypothesis of the existence of the neutrino in 1930 and the β theory in 1933. Two years later Majorana [14] formulated his theory where neutrino and antineutrino are the same particle and that the β theory can be rewritten with this assumption. In the same year, Racah, proposed the possibility to study the nature of the neutrino with inverse β decay. Finally, in 1938, Furry [47] postulated for the first time the mode without neutrinos. One year later, Furry calculated approximate rates. The first experimental observation of the mode with neutrinos was in 1987 [48] measuring the half-life of the ^{82}Se. Since then a lot of experimental and theoretical work has been done and a lot of reviews can be found as [15, 43, 49–51].

Experimentally, the two decay modes are distinguished because in the $\beta\beta0\nu$ mode all the transition energy, $Q_{\beta\beta}$, is shared between the electrons, because the nuclear recoil can be neglected, and the final event has always the same energy. In the case of the $\beta\beta2\nu$ mode, the energy spectrum is a continuous of energy, because the energy is shared with the neutrinos too (with a maximum at around $1/3\,Q_{\beta\beta}$). The shape of these spectra is shown in Figure 1.4. In practice, the signal of the $\beta\beta0\nu$ mode has a width related with the energy resolution of the detector and, the tail of the $\beta\beta2\nu$ mode can enter in this region acting as a background. Different isotopes with a better scenario for the $\beta\beta0\nu$ searches are plotted in Figure 1.2 (b) in function of their mass and transition energy, $Q_{\beta\beta}$.

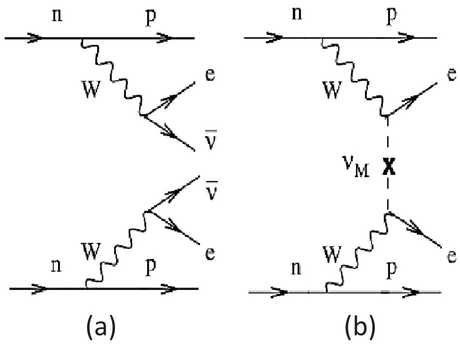

FIGURE 1.3: *Feynman diagrams of the two $\beta\beta$ decay modes: (a) with the emission of neutrinos and (b) without the emission of neutrinos. (b) can only be produced if neutrino and antineutrino are the same particle.*

The $\beta\beta2\nu$ mode has life times between $10^{18} - 10^{21}$ y, while in the $\beta\beta0\nu$ they are expected to be larger than 10^{25} y. The half-life for the $\beta\beta2\nu$ is

$$|T^{2\nu}_{1/2}(0^+ \to 0^+)|^{-1} = G_{2\nu}(Q_{\beta\beta}, Z)\ \left|M^{2\nu}_{GT}\right|^2, \tag{1.21}$$

where $G^{2\nu}$ is the exactly calculated phase space integral and $M^{2\nu}_{GT}$ is Gamow-Teller nuclear matrix element. This decay rate doe not depend on the neutrino mass and there is no distinction between the nature its nature (Dirac or Majorana).

The main proposal for the neutrinoless mode is that it occurs via the exchange of a light Majorana neutrino; in this case the half-life of the $\beta\beta0\nu$ mode, considering the transition from the ground state to the ground state, is

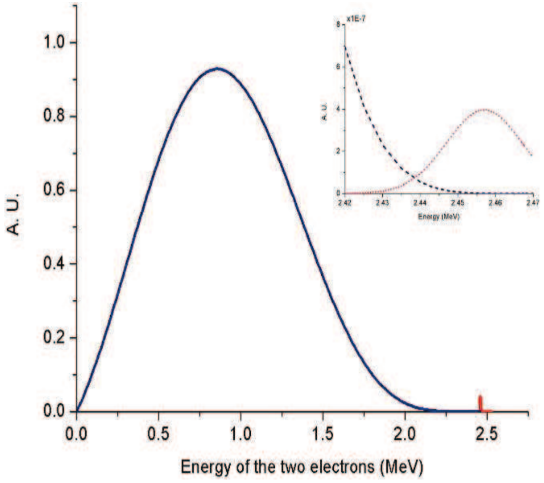

FIGURE 1.4: *Energy spectra of the two $\beta\beta2\nu$ mode discussed. Also it is marked the expected spectrum for the $\beta\beta0\nu$ mode. In detail it is shown the possible interference between both modes if the energy resolution of the measure is not good enough.*

$$|T^{0\nu}_{1/2}(0^+ \to 0^+)|^{-1} = G_{0\nu}(Q_{\beta\beta}, Z) \left| M^{0\nu}_{GT} - \frac{g_v^2}{g_A^2} M^{0\nu}_F \right|^2 \frac{\langle m_\nu \rangle^2}{m_e^2}, \tag{1.22}$$

where $G^{0\nu}$ is the exactly calculated phase space integral, $M^{0\nu}_{GT}$ and $M^{0\nu}_F$ represent the nuclear part of the amplitude, being the first term the Gamow-Teller nuclear matrix and the second the Fermi nuclear matrix. g_v and g_A are the vector and axial-vector coupling constants. The nuclear part is usually defined as $M^{0\nu} = M^{0\nu}_{GT} - \frac{g_v^2}{g_A^2} M^{0\nu}_F$ and the product $G_{0\nu}\, M_{0\nu} = F_N$ as a nuclear factor of merit, as in [42]. $\langle m_\nu \rangle$ is the effective electronic neutrino mass

$$|\langle m_\nu \rangle| = |c_{12}^2 c_{13}^2 e^{i\alpha_1} m_1 + s_{12}^2 c_{13}^2 e^{i\alpha_2} m_2 + s_{13}^2 e^{i2\delta} m_3, \tag{1.23}$$

obtained from 1.14. The relation of the effective neutrino mass with the absolute mass of the lightest eigenstate, that varies from one mas hierarchy scenario to another, is shown in Figure 1.5.

Equation 1.23 can be rewritten as

$$\langle m_\nu \rangle = \sum_i U_{ei}^2 m_i. \tag{1.24}$$

If $\beta\beta0\nu$ were observed, an appropriate value for the effective neutrino mass, $\langle m_\nu \rangle$ could be deduced. If only an upper limit for the rate is established from experiments, then an upper limit on $\langle m_\nu \rangle$ can be deduced. Therefore, from the information that can be obtained for the neutrino

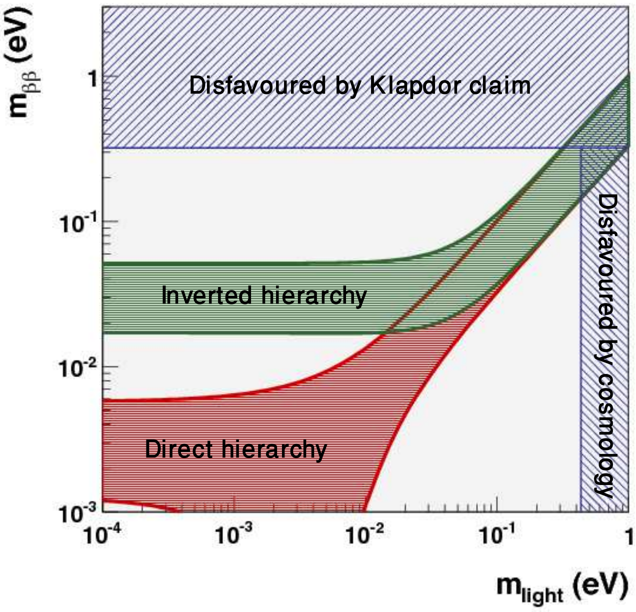

FIGURE 1.5: *Mass of the effective neutrino obtained from the $\beta\beta0\nu$ decay as a function of the lightest neutrino mass and in the context of the normal and inverted hierarchy (image extracted from [52]).*

mass scale and its nature in a $\beta\beta0\nu$ experiment, this phenomena and its experimental search have been and are one of the hottest topics in particle physics.

However, in both cases, the value on the $\langle m_\nu \rangle$ would be determined through the knowledge of the nuclear matrix elements, the main uncertainties in a $\beta\beta0\nu$ experiment nowadays and that represent a field with a high theoretical activity along these years. In a double beta decay two neutrons bound in the ground state are simultaneously transformed in the ground or excited state of the final nucleus (0^+,2^+). It is necessary to evaluate the wave functions of the two nuclei and the matrix elements of the $\beta\beta0\nu$ operator connecting them. The calculation of the nuclear matrix elements is a complicated many-body problem. Exact models exist only up to $A = 4$, computationally exact methods exist for A up to 16. For higher A, it is needed some approximation or truncation. There exist two main approaches: the *Quasiparticle Random Phase Approximation* (QRPA) [53–55] and the *Nuclear Shell Model* (NSM). The NSM is attractive because different spectroscopic data led to think on a shell nuclear structure. It assumes the existence of a nucleon field (usually a spherically symmetric oscillator potential). The description of the valence nucleons is made through one-particle states of this field, introducing an effective interaction in the Hamiltonian. All the details of the modern NSM can be found in [56]. Further, additional distance dependence is introduced by the so-called short-range correlations [57, 58]. A recent approach takes these correlations into account into an Unitary Correlation Operator Method (UCOM) [59]. The QRPA method includes pairing correlations in nuclear wave functions through the introduction of quasiparticles (particle-hole pairs). In this method there exist more basic one-particle states that can be used than in the NSM model. Also in this last model the short-range correlations have to be taken into account. Other methods exist, that take also into account the short-range correlations. Other models that treat the short-range correlations and the finite size effects are the Interacting Boson Model [60] and the Generator Coordinate

Method with the Gogny force [61]. In the IBM model bosons can interact through 1 and 2-body interactions which give rise to bosonic wave functions. Today the different approaches start to converge for each individual nuclei and the discrepancy is of the order of 4, as can be seen in Figure 1.6 extracted from [43]. In this

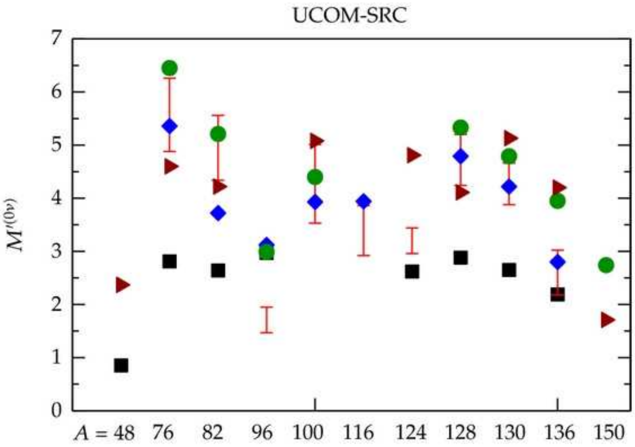

Figure 1.6: *Nuclear matrix elements for the neutrinoless double beta decay predicted by different models: QRPA (red bars) [55] and diamonds [53, 54], ISM (squres), IBM (circles) [60] and GCM (triangles)[61], (extracted from [43]).*

Neutrinoless double beta decay and new physics

The mechanism previously described to explain the mode without neutrinos is only one of the possible processes. The main feature of a $\beta\beta0\nu$ decay is the violation of the leptonic number. If it is really established that there is a neutrinoless double beta peak, the question will be to disentangle the physical process. Different mechanisms BSM would allow $\Delta L = 2$ and generate a Majorana neutrino mass term. However, the Schechter-Valle Theorem [62] guarantees that if $\beta\beta0\nu$ process is detected, neutrinos are Majorana particles. Hence, all realizations of the $\beta\beta0\nu$ decay are connected to a Majorana neutrino mass via the black-box diagram shown in Figure 1.7. There are different processes BSM. For instance, if there are right-handed weak-current interactions (V+A interactions), the right-handed neutrino emitted will be absorbed via the V+A current by the second W boson without the requirement of flip helicity. In this case the expected angular distribution of the electrons will be different, and could be determined in experiments with tracking capabilities. Another option are R-parity violating SUSY processes that occur by the exchange of a supersymetric particle χ, instead of a Majorana particle. Another alternative mechanism is the emission of a Majoron, the goldstone boson related to the L-B symmetry breaking. In this case, it is the energy spectrum what is distorted. Finally it can occur via double charged Higgs-bosons and Kaluza-Klein excitations. A complete review of the possible mechanisms can be found in [63].

However, after the discovery of neutrino flavour oscillations, the mass mechanism occupies a special place. It constrains the experimental parameter landscape fixing clearly the targets and allowing to compare different experiments.

In conclusion, from all the above uncertainties (including nuclear matrix elements), a signal in at least 3-4 different isotopes would be needed to extract information reliable about neutrino mass to delimit the neutrino mass scale.

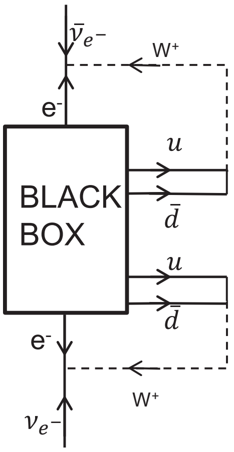

Figure 1.7: Diagram showing the Schechter-Valle Theorem, from which any $\beta\beta0\nu$ decay process induces a transition that is a Majorana mass term.

1.3 The search of neutrinoless double beta decay

A positive signal from a neutrinoless double beta decay experiment would help in the determination of the neutrino mass scale and it will prove that neutrinos are Majorana particles. The nature and rarity of the process makes its detection a high experimental challenge. Also, since it can occur in different isotopes, different techniques of detection exist. Moreover, in order to evaluate these techniques, it is important not only the nucleus under study but also the intrinsic characteristics of the detector, like its energy resolution, its efficiency, and the power to reject the background.

In this section the different techniques of detection are reviewed, putting emphasis on direct counting experiments. In the second point, the different aspects to take into account for a neutrinoless double beta experiment proposal are listed. After that, a figure of merit to evaluate the sensitivity of the different experiments is shown. In the next section an overview of the experimental situation will be given.

1.3.1 Techniques of detection

Three different techniques exist to look for a $\beta\beta0\nu$ signal. First of all the geochemical experiments. They are based on the search of an excess of daughter nuclei, $(A, Z \pm 2)$, accumulated in materials with a high concentration of $\beta\beta$ emitter isotope during long geological time periods ($T_{1/2} \approx 10^{6-7}$ years). As examples, the measurement of the double beta mode in ^{82}Se [48], also in ^{128}Te and in ^{130}Te [64, 65].

The radiochemical experiment is another approach that is based on the detection of the daughter nuclei of a double beta emitter after its accumulation in a material. The main limitation of this technique is that the daughter nuclei have to be also radioactive. This method has been used to study the ^{238}U [66].

Finally, the currently most used technique is the direct counting measurement. The idea is to measure the energy spectrum. Theoretically, if the energy resolution of the detector were good enough, it could distinguish between the two modes, as shown in Figure 1.4. Some of these experiments also track the electrons topology and might even be able to measure the angular distribution at the vertex between both electrons of the $\beta\beta0\nu$ emission. Depending on the isotope and detector different techniques can be used in this approach. The main classification of this kind of experiments is based on whether the emitter source is embedded in the detector media or if they are different [43].

In the calorimetric approach, where the source of $\beta\beta$ emitter is equal to the detector, very large masses are possible to scale to a 1 ton experiment. It can be obtained a very good energy resolution by electing semiconductor detectors (Ge or Te whose ^{130}Te and ^{76}Ge isotopes are $\beta\beta$ emitters) as in the case of GERDA [67], or bolometers. Also, in approaches with gas the topology of the events can be detected and used to discriminate the background, as in NEXT [68]. The main limitation is that there exist constraints on the detector materials.

In the external-source approach, where the beta emitter source is different to the detection media, the main advantages are the net reconstruction of the event topology and that several candidates can be studied at the same time, as it is proposed by SuperNEMO [69]. The main drawbacks are the difficulty to go to high source masses because of self-absorption in the source and the low energy resolution normally achieved.

Apart from this classification the direct counting experiments can also be classified in function of the kind of detector: semiconductors, scintillators, time projection chambers (TPCs) and cryogenics.

1.3.2 Experimental challenge

The experimental challenge of a neutrinoless double beta experiment implies different factors that are here mentioned. These criteria are also discussed in [15, 42, 43, 51]. The objective is to detect the two emitted electrons and to obtain their sum energy spectrum. We focus on the requirements for the so-called next generation of experiments, that aim to be sensitive to neutrino effective mass of 50-100 meV, and future ones that intend to scrutinize the inverted hierarchy region, down to 20 meV. Principal characteristics are listed:

1. The type of isotope. The most favourable isotopes are marked in Figure 1.2 that correspond to those with a high $Q_{\beta\beta}$ (higher than 2 MeV). A high $Q_{\beta\beta}$ increases the rate of the process (as this scales with $Q_{\beta\beta}^5$) and reduces most of the potential backgrounds. In addition, its selection is determined by its natural abundance and the enrichment process in the desired isotope. Through this enrichment it is usually obtained a good level of

purification, another requirement for a $\beta\beta$ experiment. The nuclear parameters for the isotope are also important. A nucleus with a higher phase-space and higher predicted nuclear matrix elements is more favourable to reach lower neutrino mass sensitivity as Equation 1.22 shows. In addition, an improvement of the nuclear theory may help to reduce uncertainties. Xenon gas fulfill most of these requirements.

2. A large amount of isotope. In order to develop the experiment in a real time, due to the low expected rate of $\beta\beta0\nu$ events, a large amount of mass is required. To cover completely the degenerate hierarchy region of masses, an isotope mass scale between 10-100 kg is needed. In order to enter in the inverted hierarchy region the 1 ton scale is required.

3. High energy resolution. To discriminate the $\beta\beta0\nu$ peak from the tail of the $\beta\beta2\nu$ mode and to reduce the background in the region of interest. It can be shown [49] that the expected number of counts of the $\beta\beta0\nu$ decay over those due to $\beta\beta2\nu$ is

   $$R_{0\nu/2\nu} = \frac{m_e}{7\,Q_{\beta\beta}\delta^6}\frac{T^{0\nu}_{1/2}}{T^{2\nu}_{1/2}}, \tag{1.25}$$

   where $\delta = \frac{\Delta E}{Q_{\beta\beta}}$. From Equation 1.25 it is clear that candidates with a short $\beta\beta2\nu$ half-life (as Xenon) are favourable. Also, the better the energy resolution is, the better the discrimination between signal and background will be. For the next generation of experiments, an energy resolution of the order of 1% FWHM at $Q_{\beta\beta}$ is required.

4. Low background. It is a crucial point in a direct counting experiment because background can distort and even hide the awaited $\beta\beta$ signal and it is the only parameter that can be improved through the analysis of the detected events. The main components of the background are the cosmic radiation (muons, protons, gammas...) and the environmental radiation, mainly composed by the isotopes from the natural radioactivity chains of ^{232}Th, ^{235}U and ^{238}U as well as some isotopes as ^{40}K or ^{60}Co. Of special interest is the Radon present in the air or that can be emanated from the materials. It is necessary to differentiate between external and internal backgrounds. To address the reduction of the background different mechanisms exist.

   (a) Underground placement of the detector to reduce the external cosmic contribution. The surface muons flux is $4 \times 10^9\,\mathrm{m}^2\mathrm{y}^{-1}$ for an energy range between 0.01 MeV to 500 GeV [70]. This flux can be drastically reduced in an underground experiment, by the rock that acts as a shielding.

   (b) Passive shielding. The stopping power of the different materials for the different particles and energies can be used to design a passive shielding. Usually, lead, copper or water is employed to stop the high energetic gammas. For a more detailed discussion of the different materials see [17, 71].

   (c) Active shielding. It is used to reduce the background level by detecting the background events. Some of the most used techniques are:

      - Anti-muons veto. Even working in an underground facility sometimes the level of muons must be reduced to a lower value. The detection of the muons signal in two detectors (at different time) can allow for it.

- Anti-coincidence techniques. It is based on the fact that the background, mainly, will produce separated deposits of energy or will travel a longer distances than the electrons emitted in the $\beta\beta 2\nu$ decay. Therefore, if the detector is segmented, or if different detectors are used, anti-coincidence techniques can be useful to reject those events that interact in different parts of the setup.

(d) Materials selection. For the inner components of the detectors it is very difficult or even impossible to develop passive shielding. Hence, a careful selection of the materials according to their radioactivity is required. A screening campaign has to be done by the experiments to control all the elements installed inside the detector. Special care has to be taken with those elements very close to the fiducial volume.

(e) Discrimination Techniques. The differences between the signal and background events allow the development of analysis techniques to discriminate background. Once the materials are selected this is the only way to reduce background from the internal components to lower levels. An advantage in a gaseous time projection chamber is the possibility to reconstruct the track of the event and, based on pattern recognition, to carry out different analysis. The reduction of the background in a neutrinoless double beta decay of ^{136}Xe in a gaseous TPC equipped with pixelized detectors is one of the objectives of this work and is covered in the third part of the thesis. Also it can be very useful the identification of the daughter nuclei, as in the proposition made by EXO [72] to tag the ^{136}Ba daughter ion in the ^{136}Xe decay, to eliminate all the backgrounds. In experiments without tracking capabilities, as GERDA, pulse-shape analysis is developed [73].

1.3.3 Sensitivity of an experiment

In order to compare different experiments and also to design a future one, a figure of merit can be defined to obtain a value of the expected sensitivity for the effective neutrino mass in a $\beta\beta 0\nu$ experiment. The half-life of the decay is the signal measured in a $\beta\beta 0\nu$ experiment that can be related to the effective electronic neutrino mass with expression 1.22. The half-life of a radioactive decay can be written as

$$T^{0\nu}_{1/2} = \frac{\ln 2}{\lambda} \tag{1.26}$$

where λ is the decay constant that can be expressed as the activity, A, divided by the number of nucleus, N. The number of nucleus is

$$N = N_{Av}\frac{M \cdot f}{W}. \tag{1.27}$$

In this expression N_{Av} is the Avogadro's number, W is the molecular weight of the $\beta\beta$ decaying isotope atoms, f is the isotopic abundance and M the mass of beta emitter. The activity can be expressed in terms of the detected signal, s, in a time t as

$$A = \frac{s}{\epsilon t} \tag{1.28}$$

being ϵ the efficiency of the detector. Combining expression 1.27 and 1.28, Equation 1.26 can be rewritten as

$$T_{1/2}^{0\nu} = \ln 2 \cdot N_{Av} \frac{M \cdot f}{W} \frac{\epsilon t}{s}. \tag{1.29}$$

It is clear that, to obtain the best sensitivity, a detector that maximizes the signal counting rate over the background has to be built. The signal sensitivity is proportional to the statistical precision of the background determination. Since the number of background counts is a linear function of time, the sensitivity increases with the square root of time. In absence of a positive signal an upper limit to the expected signal can be given as, at 1σ of confidence level,

$$s < \sqrt{b \cdot \Delta E \cdot M \cdot t} \tag{1.30}$$

where b is the background level in $\mathrm{c\,keV^{-1}\,kg^{-1}\,y^{-1}}$, ΔE is the energy window (the energy resolution of the detector) in keV, M in this case has to be expressed in kg. With this expression a lower limit for the half-life of the decay can be obtained from 1.29 as

$$T_{1/2}^{0\nu} > \ln 2 \cdot N_{Av} \frac{\epsilon \cdot f}{W} \sqrt{\frac{\epsilon t}{s}}. \tag{1.31}$$

From this expression the factors determinant are the mass of the beta emitter, the background level expressed in $\mathrm{c\,keV^{-1}\,kg^{-1}\,y^{-1}}$ and the energy resolution of the detector. $M \times T$ is usually defined as the exposure of the experiment, the sensitivity increases as the exposure increases until some point that the behaviour is asymptotic. Finally, to obtain a limit for the neutrino mass expression 1.22 is used on which variables related to the nucleus and its structure play an important role.

1.4 Experimental situation: Past, present and future experiments

At the present, we are entering in a very exciting era for neutrinoless double beta decay experiments. Those proposed and others already taking data will cover the sensitivity of the Heidelberg-Moscow claim [74] and will also enter into the inverted hierarchy region of masses. Before explaining the present experiments, a review of the past ones and their main results has to be done. A more complete description of the different experiments is done in [42], [75] and in the recent [43].

1.4.1 Past Experiments

Among the past experiments there were two based on germanium detectors: IGEX (International Germanium Experiment) [76], placed in the Canfranc Underground Laboratory (LSC) with around 6 kg of ^{76}Ge enriched at 86% and the Heidelberg-Moscow (HM) experiment [77], placed in Gran Sasso (LNGS) with around 10 kg of isotope. Part of the HM collaboration claimed in 2001 an evidence of a $\beta\beta 0\nu$ signal [74]. This result was not accepted by some members of the community as well as from part of the collaboration [78], [79], [80] and for this reason one of the main goals for the future experiments is to cover the pointed region of masses. The result claimed in the last paper [81], with higher statistics and a different pulse-shape analysis, is a $T^0_\nu = 2.3 \times 10^{25}$ y that corresponds to a neutrino effective mass of $\langle m_\nu \rangle = 0.44$ eV. Apart from this result, the two experiments (IGEX and HM) are compatible and they put an upper limit on the half-life of the decay of the order of $T^0_\nu = 1.5 \times 10^{25}$ y ($\langle m_\nu \rangle \leq 0.33 - 1.35$ eV) [76, 82].

The bolometric technique is, also, a suitable one for $\beta\beta 0\nu$ searches, and rare events in general, due to its high energy resolution [83, 84]. From 2003 to 2008 the Cuoriccino experiment, proposed in 1994 (an extension of MIBETA, and a previous step for CUORE), operated with TeO_2 crystal bolometers with an isotopic abundance of 33.8% and a mass of the order of 40 kg in the LNGS. They improved the results obtained previously with the MIBETA experiment [85] and put an upper limit for the half-life of the ^{130}Te isotope of $T^0_\nu > 2.8 \times 10^{24}$ y that corresponds (with a 90% C.L) to a neutrino effective mass of $\langle m_\nu \rangle \leq 0.30 - 0.71$ eV, [86, 87].

Up to now the mentioned experiments operated in the calorimetric approach. The best experiment of the external-source technique was NEMO3 (Neutrino Ettore Majorana Observatory) [88] operating in the Laboratoire Souterrain de Modane (LSM), in France. The detection technique is based on the reconstruction of the track of the particle bent in the presence of a magnetic field in Geiger wire cells. Also a calorimeter surrounding the tracking wires was installed with scintillator blocks connected to photomultipliers (PMT) to read the energy signal. It could measure different beta emitters at the same run installing foils of different isotopes in the middle of the detector that is divided into 20 sectors. The $\beta\beta 2\nu$ mode was measured for the seven installed isotopes while for the $\beta\beta 0\nu$ mode only upper limits were obtained being the most stringent one for the ^{100}Mo with a half-life of $T^0_\nu > 5.8 \times 10^{23}$ y ($\langle m_\nu \rangle \leq 0.61 - 1.26$ eV).

Finally, it is important to mention the Gothard Xenon TPC Experiment [89] that ran in the 90s. It was the first double beta experiment using a gaseous TPC filled with the emitter gas, in this case ^{136}Xe mixed with CF_4 at 5 bar. They only put limits for both $\beta\beta$ modes but proved that the tracking capabilities could reduce the background even with a modest energy resolution [90]. The idea of using a gaseous TPC was abandoned for few years due to drawbacks of the technique as the poor energy resolution ot its difficulty to scale to higher masses. Currently, it is a promising technique exploited by the EXO and NEXT experiments. The details of the previously mentioned experiments are listed in Table 1.2.

Experiment and Laboratory	Isotope	$Q_{\beta\beta}$ (keV)	Mass (kg)	Technique	Efficiency	Background in the RoI ($\mathrm{c\,keV^{-1}\,kg^{-1}\,y^{-1}}$)	ERes at $Q_{\beta\beta}$	$\langle m_\nu \rangle$ (eV)	ref.
IGEX (LSC)	^{76}Ge	2039	6	Ge diodes	90%	0.1	4 keV	0.33-1.35	[76]
HM (LNGS)	^{76}Ge	2039	10.9	Ge diodes	95%	0.17	4 keV	0.35-0.60	[77]*
CUORICCINO (LNGS)	^{130}Te	2528	40.7	TeO_2 bolometers	84%	0.1	8 keV	0.30-0.71	[86],[87]
NEMO3 (LSM)	^{100}Mo/^{82}Se		7/1	Tracking +calorimeter	18%	0.1	11-14% FWHM	0.61-1.26	[88]
Gothard Xe TPC	^{136}Xe	2457	3.3	Tracking +calorimeter	70%	0.01	164 keV	$>4.4\times10^{23}$ y	[89][90]

Table 1.2: *Summary of the main parameters relevant in a neutrinoless double beta decay. Here are mentioned the main past experiments that have been discussed in the text. In all cases a limit to the effective neutrino mass was obtained (excepting the claim by the HM collaboration mentioned in the text). In the last column are given the references for a complete description of the experiments and results.*

1.4.2 Present situation

The main experiments currently taking data or proposed for the near future are briefly described. A full review of them can be found in [42, 43] and references therein. In the present situation the main goals are to cover the sensitivity of the HM claim in the degenerate region of masses and to enter in the inverted hierarchy one ($\langle m_\nu \leq 50\rangle$ meV). To fully investigate this region (from $\langle m_\nu\rangle = 50\,\text{meV}$ to $20\,\text{meV}$) the required background must be of the order of 1 c/y/ton and an excellent energy resolution is also mandatory, of the order of 1% FWHM. Moreover, the different tracking or analysis capabilities can decrease the background level and improve the expected sensitivity in those experiments with a limited energy resolution. At the end, one has to choose one characteristic over the others when designing a $\beta\beta0\nu$ experiment. Along this section the different experiments will be briefly explained and in Table 1.3 are summarized the main features of the current experiments. Some of them as GERDA, EXO or KamLand-Zen are already taking data.

Most of the proposed experiments are based on the search of the double beta decay in the same isotope as in the past but with a higher mass and new techniques. This is the case for GERDA and MAJORANA looking for the nuclear transition in ^{76}Ge.

GERDA (GERmanium Detector Array): It is a ^{76}Ge experiment with Ge diodes arrays immersed in liquid Argon [91], [67] installed in LNGS. The experiment is divided in different phases. The first one started in November 2011 using 8 refurbished enriched diodes from HM and IGEX [92] (14.6 kg) with an energy resolution of 4.5 keV at 2039 keV. The background level was $0.1\,\text{c}\,\text{keV}^{-1}\,\text{kg}^{-1}\,\text{y}^{-1}$. With the application of pulse-shape analysis (PSA) they expect to decrease it by one order of magnitude. In this first run they obtained the half-life for the $\beta\beta2\nu$ mode [93] being of $T^{2\nu}_{1/2} = 1.84^{+0.14}_{-0.10} \times 10^{21}$ y. In the second phase they will operate 20 kg of broad-energy Germanium with a higher energy resolution and better PSA and also in this phase will take place the installation of a liquid Argon (LAr) scintillation veto. It will start the present year.

MAJORANA: The Majorana project [94], [95] will be composed by Ge diodes operated in conventional copper cryostat having a mass of 1 ton of ^{76}Ge. They will be located at Stanford Underground Facility (SURF) in the USA. The first phase, called *MAJORANA Demonstrator* [96], will consist of 40 kg of Ge and its main purpose is to prove that a background level of $0.001\,\text{c}\,\text{keV}^{-1}\,\text{kg}^{-1}\,\text{y}^{-1}$ can be obtained in the 1 ton extension. The proven energy resolution is 0.16% FWHM at $Q_{\beta\beta}$. The MAJORANA and GERDA experiments will merge for the future 1 ton experiment combining the best results in both cases [97]; this corresponds to the third phase of GERDA.

As extensions of past experiments there are the CUORE and the SuperNEMO experiments.

CUORE (Cryogenic Underground Observatory for Rare Event): [98] is an extension of CUORICCINO with 988 TeO$_2$ bolometers to be installed in the LNGS. They will be arrange in 19 towers operating at 10 mK. They look for the $\beta\beta0\nu$ decay of ^{130}Te with a total mass of 200 kg. The expected energy resolution is 0.25% FWHM and the expected background is of the order of 0.02-0.01 $\text{c}\,\text{keV}^{-1}\,\text{kg}^{-1}\,\text{y}^{-1}$, one order of magnitude better than in CUORICCINO. With these background levels a sensitivity of $T^{0\nu}_{1/2} \approx 9.7 \times 10^{25}$ y is expected (50-130 meV). The first tower that will operate in LNGS along this year is known as CUORE-0.

SuperNEMO [69, 99]: As in NEMO3 it will follow a modular concept of 20 units with 5 kg of isotope each one and will be installed in LSM. The electrons emitted from the foil source placed in the middle of the detector will traverse the tracking module composed by Geiger cells and enter the calorimeter made with 600 channels of organic scintillator blocks coupled to PMTs. It improves the NEMO3 features having an efficiency of 30%, an energy resolution of 7.5% FWHM and could reduce the background to 0.01 c/kg/y. It will investigate mainly the ^{82}Se double beta emission because is a good $\beta\beta0\nu$ emitter and part with the advantage of previous knowledge of backgrounds and analysis from NEMO previous phase. Other isotopes can be studied as ^{150}Nd, ^{96}Zr and ^{48}Ca. The predicted 5y sensitivity for the ^{82}Se is 10^{26} y, which corresponds to a neutrino effective mass between 40-110 meV. At the moment, a dedicated radiopurity detector, BIPO [100], has been installed in Canfranc (LSC) to measure, with enough sensitivity, the contamination of the $\beta\beta$ source foils that will be installed in SuperNEMO.

Another approach is the SNO+ experiment investigating the ^{150}Nd isotope detecting the Cerenkov light in a scintillating media.

SNO+: [101], [102] is an upgrade of the SNO (Sudbury Neutrino Observatory) solar neutrino experiment located at the SNOLAB in Canada. The idea is to fill the detector with Nd loaded liquid scintillator to investigate the ^{150}Nd $\beta\beta$ decay. It is expected to be filled along this year with a mass of 43.7 kg and an energy resolution of 6.4% FWHM. After 3y the expected sensitivity is 1.3×10^{25} y (an effective neutrino mass between 120-410 meV). Finally 500 kg of enriched isotope will be used. The main drawback is the difficulty to enrich this quantity of ^{150}Nd, while one of the advantages of this experiment is the low background. The expected sensitivity for the 500 kg run is $T^{0\nu}_{1/2} = 1 \times 10^{25}$, that will allow to investigate the region for the effective neutrino mass from 55 to 180 meV.

The next group of experiments are those looking for the emission in ^{136}Xe.

KamLand-Zen (Kamioka Large Anti Neutrino Detector Zenon): [103] is a modification of the KamLand detector located in the Kamioka mine in Japan. Xe gas is dissolved in an organic liquid scintillator contained in a nylon balloon. This balloon is suspended at the centre of the KamLand detector and it is surrounded by 1 kton of liquid scintillator contained in an outer balloon that acts as active veto. The enriched Xe is 300 kg, being 125 kg in the sensitive volume. It has an energy resolution of 10% FWHM. After a total live time of 112.3 days a value for the half-life of the $\beta\beta2\nu$ mode was obtained [104] of $T^{2\nu}_{1/2} = 2.38 \pm 0.02(stat) \pm 0.14(syst) \times 10^{21}$ y, completely compatible with the previous result by EXO. An extra background was observed in both regions $\beta\beta2\nu$ and $\beta\beta0\nu$. Studies point out that this contributions are due to the emission of unexpected isotopes when the Fukushima fallout [105] or to spallation of ^{136}Xe on surface. The main issue now is to reduce this background, for example, recirculating the Xenon to reach the expected value that allows to explore sensitivities of the order of 10^{24} y for the $\beta\beta0\nu$ mode. Also they plan to increase the amount of Xenon up to 1 ton.

Another proposal with Xe is BOREXINO with few tons of ^{136}Xe [28] dissolved in a scintillator.

After Gothard, the option to use a Xe filled TPC is considered in the EXO and NEXT experiments.

EXO (Enriched Xe Observatory) [72]: is a liquid Xe TPC that can measure both the scintillation light and the ionization in a plane of 250 large-area avalanche photo-diodes (LAAPDs). The first phase, called EXO-200, is already taking data in the Waste Isolation Pilot Plant (WIPP). It has 175 kg of Xe enriched to 80% ^{136}Xe. It has an energy resolution of 3.9% FWHM in the region of interest and a background of $0.0015\,\mathrm{c\,keV^{-1}\,kg^{-1}\,y^{-1}}$. They were the first to obtain the half-life of the $\beta\beta 2\nu$ mode [45] with a value of $T^{2\nu}_{1/2} = 2.11 \pm 0.14(stat) \pm 0.21(syst) \times 10^{21}$ y in complete agreement with the posterior result obtained by the KamLand-ZEN collaboration [104]. They also put a lower limit for the half-life of the $\beta\beta 0\nu$ mode [106] of $T^{0\nu}_{1/2} > 1.6 \times 10^{25}$ y. In future phases it will have a mass between 1 and 4 ton with a sensitivity of 10^{27} y; this extension is called nEXO [107].

NEXT (Neutrino Experiment with a Xe TPC): [68] will be installed in the LSC. It will operate with 100 kg gas Xenon at 10 bar and will measure the electroluminescent signal. More details are given in Chapter 3.

This idea is implemented in the present work with the development of a high pressure TPC fill with gaseous Xe to look for its beta decays and the use of pixelized detectors as Micromegas to discriminate, based on topology, between signal and background. With these detectors an energy resolution of at least 1% is expected [108], [109].

Other proposals not mentioned here are summarized in Table 1.3 and are mainly in an R&D phase. These experiments are MOON [110, 111], CANDLES [112], LUCIFER [113], COBRA [114], and AMORE [115, 116] (that will look for Dark Matter also). See also [42] for other projects.

In the future, in order to investigate the normal hierarchy region of neutrino masses ($\langle m_\nu \rangle$ between 2-4 meV) it is needed to go to masses of beta emitter of 10 ton and background levels of 0.1-0.01 c/ton/y.

Experiment and Laboratory	Isotope	Mass (kg)	Technique	Background ($\mathrm{c\,keV^{-1}\,kg^{-1}\,y^{-1}}$)	ERes %FWHM at $Q_{\beta\beta}$	$T^{0\nu}_{1/2}$ (y)	$\langle m_\nu \rangle$ (meV)	Status .
GERDA (LNGS)	^{76}Ge	35	Ge diodes	0.02	0.25	2×10^{26}	$60 - 200^a$	In progress
MAJORANA (SURF)	^{76}Ge	30	Ge diodes	4 c/t/y	0.16	10^{26}	$90 - 300^a$	In progress
MAJORANA-GERDA	^{76}Ge	1000	Ge diodes	0.001	0.16	6×10^{27}	$10 - 40^b$	R&D
CUORE (LNGS)	^{130}Te	200	$\mathrm{TeO_2}$*bolometers*	0.01	0.25	10^{26}	$50 - 130^a$	In progress
SuperNEMO (LSM)	^{76}Se	100-200	Tracking + calorimeter	0.01	7.5	2×10^{26}	$40 - 110^a$	Installation first module, R&D
EXO (WIPP)	^{136}Xe	140	TPC ionization+ scintillation	0.0015	3.9	$> 1.6 \times 10^{25}$	$< 140 - 380^c$	Current
	^{136}Xe	1000	Id. (+Ba tagging)	≥ 0.0015	1.6	8×10^{26}	$20 - 55^a$	R&D
NEXT (LSC)	^{136}Xe	100-150	Tracking + calorimeter	0.0008	< 1	5.9×10^{25}	$102 - 129^b$	In progress
KamLand-Zen (Kamioka)	^{136}Xe	130	Liquid scintillation		6.8	2×10^{26}	$40 - 110^a$	Current
	^{136}Xe	1000				10^{27}	$18 - 50^a$	R&D
SNO+ (Sudbury)	^{150}Nd	43.7	Liquid scintillation	5×10^{-7}	6.4	1.3×10^{25}	$120 - 410^b$	In progress
		500	idem				40	R&D
COBRA (LNGS)	^{116}Cd	117	CdZnTe semiconductor + tracker	0.001	1.9	$> 10^{26}$	50	R&D
LUCIFER (LNGS)	^{82}Se	10	ZnSe bolometers	0.0001	< 1	2×10^{26}	$\approx 100^b$	R&D
AMORE (Y2L)	^{100}Mo	50	$\mathrm{CaMoO_4}$ bolometers	—	0.5	3×10^{26}	20-60^e	R&D
MOON	^{100}Mo	480	Tracking+scintillator	20 c/ton/y	2.2	3×10^{26}	45^d	R&D
CANDLESS (Kamioka)	^{48}Ca	3200	Scintillation	1 c/ton/y	0.2	—	30^d	R&D

Table 1.3: *Summary of the main neutrinoless double beta decay experiments at present with its main features and its status. References to each experiment can be found along the text. The effective neutrino mass range depends on the nuclear matrix element used. For this reason it is mentioned the reference from where these values were taken: (a) is [50], (b)[43], (c) is [106], (d) [51], (e)[115]*

1.4.3 Micromegas for rare event searches

The forthcoming generation of neutrinoless double beta decay experiments will need to go to the few tons scale to reach sensitivities down to 10-20 meV and to fully investigate the inverted hierarchy region of masses. However, larger masses do not assure such sensitivity and it has to come with continuous improvements in energy resolution and in background reduction techniques [15]. Specially, the background has to be of the order of $10^{-5}\,\mathrm{c\,keV^{-1}\,kg^{-1}\,y^{-1}}$. The background level is up to a certain point related to the energy resolution that marks off the region of interest (RoI). Nonetheless, the required minimum energy resolution is limited by the intensity of the $\beta\beta2\nu$ mode, because it is needed to separate the signal peak from the tail of the $\beta\beta2\nu$ distribution. In ^{136}Xe a minimum 4.5% FWHM at 2458 keV is required at the 100 kg scale, while in the landscape of a 1 ton experiment it is needed to be at least 2.5% FWHM [15].

Within the TREX project [117] (TPCs for rare event searches), the use of Micromegas readouts in a gaseous TPC together with ultra-low background techniques to develop ideas for rare event searches is studied. TPCs were normally used for tracking rather than calorimetry. This was due mainly to the large volumes and times of exposure needed in those experiments making these detectors complex in terms of mechanics (wire tension), electrostatically (field under control over large volumes) and operation. In addition, the use of wire planes implied a poor energy resolution. The Gothard Xenon TPC Experiment was a pioneer experiment that showed the background rejection potential of a gaseous TPC, based on the characteristic topology of the $\beta\beta0\nu$ signal (a long track with two high energy depositions at both ends) [118]. Though promising, the idea stopped for few years due to drawbacks of the technique as the low energy resolution and spatial resolution obtained. These perspective changed with the use of the previously invention of the Micropattern Gas Detectors (MPGD) in 1988 by A. Oed [119], when he demonstrated the first functional Microstrip Gas Chambers (MSGCs). From this moment different detectors arose replacing the traditional wires with readouts that use metallic strips or pads precisely printed with photolitograpic techniques. In general the MPGD can achieve higher spatial resolution, are simpler and more robust and also had an impact on the electronics. One of the most attractive MPGD to use in double beta decay searches (and rare event searches in general) is the MICRO MEsh GAseous Structure detector (Micromegas) [120]. The Micromegas detector also have a very good energy resolution and have shown a high stability, granularity and homogeneity in experiments as CAST [121], [122], [123], the first application of this detector in rare event searches (dark matter). The idea to use a TPC has already given very good results, as discussed previously, in the EXO experiment and it has been proposed for the NEXT experiment. In general, two approaches are promising: the detection of the electroluminescent signal (NEXT, EXO) or the use of a novel charge readout detector as Micromegas, option also considered by the mentioned experiments.

The use of a Micromegas detector for the neutrinoless double beta decay searches was evaluated in [108]. One of the main drawbacks could be the stability and features of these detectors at high pressure. It has been proven that Micromegas have an energy resolution of around 3% FWHM with an alpha source up to 5 bar in pure Xenon [108], with the best result being 2.5% FWHM at 4 bar. With a detailed analysis removing edge effect this value is improved obtaining a 1.8% FWHM at 4 bar. Recent studies with a gamma source in Xe gas mixtures with thrimetilamine

[109], show that the energy resolution obtained extrapolates to be of the order of 1% FWHM at the $Q_{\beta\beta}(^{136}Xe)$ up to 10 bar. With these results it is experimentally demonstrated the feasibility and competitiveness of the Micromegas readouts for a Xe TPC double beta decay experiment.

To fully explore this option in a larger TPC, a prototype was designed and built inside the NEXT collaboration, NEXT-MM, to study the performance of Micromegas at high pressure in a prototype with the dimensions to fully contain electron tracks in its fiducial volume and that can hold 1 kg of Xe at 10 bar. Although, the baseline of NEXT is to detect the electroluminescent signal with photomultipliers, NEXT-MM explores the tracking capabilities and studies different gas mixtures. In addition, a complete simulation has been done to study the expected background in a future possible $\beta\beta0\nu$ high pressure TPC (HPTPC) with 100 kg of Xe at 10 bar equipped with Micromegas and to develop discrimination algorithms that can reduce the background to the require limits. In the next part of the thesis the phenomenology in a gaseous detector and the principle of operation of a TPC equipped with Micromegas detectors is explained in detail. It is also described the TPC prototype, and the first results on tracking and calorimetry obtained with it are presented. In the third part of the work the physical potential of this proposal is studied, evaluating the different backgrounds and the rejection potential obtained with the application of pattern recognition criteria developed.

Part II

Operation of Micromegas detectors focus on a $\beta\beta0\nu$ experiment.

The present neutrinoless double beta experimental situation is very exciting with the new generation experiments, running or proposed, having a sensitivity higher than the past experiments. The use of a gaseous TPC is one of the promising approaches thanks to the tracking capabilities in these kind of detectors, allowing the application of powerful background discrimination techniques. These set-ups are also motivated by the appearance of new and improved multi pattern gaseous detectors. The MICRO MEsh GASeous structure (Micromegas), is one of the new detectors more suitable for the $\beta\beta0\nu$ decay searches because of its very promising features in terms of energy resolution and radiopurity, two of the stringiest requirements in a $\beta\beta$ experiment. In this line, the Nuclear and Astroparticle Physics group of the University of Zaragoza has constructed a TPC prototype equipped with Micromegas detectors inside the NEXT Collaboration to test the viability of this option.

In this part of the dissertation it is explained the different processes occurring in a gas with the passage of an incident radiative particle. The Micromegas detector operation principle and properties are also described. In the third and fourth chapter it is explained in detail the NEXT Experiment and the NEXT-MM prototype, and there are shown the first results obtained for tracking and energy resolution.

Chapter 2

Phenomenology of particles in gases and gaseous detectors. Micromegas Detectors.

Contents

2.1 Ionization in gases 38

2.2 Transport of electrons in gases 39

2.2.1 Diffusion 41

2.2.2 Intrinsic uncertainties in gaseous detectors 42

2.3 Operation of a gas detector and the avalanche multiplication region. Townsend coefficients 45

2.4 Signal creation 49

2.5 Energy resolution 50

2.5.1 Statistical contributions 50

2.5.2 Other factors 52

2.6 Gaseous detectors 52

2.6.1 Time Projection Chamber 53

2.6.2 Micromegas detectors 54

2.6.3 Micromegas Technology 57

Radiation and particle detection is the main goal in particle physics experiments. It can be detected in a gas by the effect that they produce on it. The primary modes of interaction are ionization and excitation of gas molecules along their path. In the following we will focus on the ionization process. The electron cloud produced can be detected on detectors based on electron collection, as the Micromegas, which will be used in this work.

The charged particles ionize the medium when interacting with the gas molecules releasing part of their kinetic energy to produce an e^--ion pair. The required energy depends on the medium but is of the order of few eV. The produced electrons can then be drifted by the application of an electric field and amplified in avalanches until reaching the readout plane where they are read as electrical pulses. These electrical signals could provide information about the original location and ionization density of every track segment.

The choice of the medium is very important and depends on the purpose of the experiment. Here the processes will be described in general but we give more details for the case of Xenon gas. A major advantage of the use of gas instead of liquid is that the topological information reconstructed by a pixelized detector can be used to distinguish between signal and background. However, if a big amount of isotope is needed, as in a neutrinoless double beta experiment, it implies a big volume or working at high pressure. Regarding the gas, in the case of very penetrating radiation, heavy noble gases, as Ar or Xe [124], are advantageous because of their high stopping power. As a consequence the interest in these gases is increasing. The advantages that Xe presents for a $\beta\beta0\nu$ experiment have been already pointed out in Section 1.3.2 and are its high $Q_{\beta\beta}$ (2458 keV), its slow half-life of the order of $T^{2\nu}_{\frac{1}{2}} \approx 2 \times 10^{21}$ y and that it easy to enrich. Xenon can also emit secondary scintillation light that could create additional ionization that, if it is detected, can produce a loss in proportionality. This effect can be reduced adding a small amount of a polyatomic gas that suppress the photon-induced effects. This is usually called a *quencher*. The basic properties of the gas change by adding a small concentration of some additive, specially interesting is the case when the secondary gas has an ionization potential smaller than the one of the base gas. If there exist long-lived or metastable excited states in the principal gas, then a *Penning* mixture is obtained. In those cases an improvement in the gain and energy resolution arises because an extra ionization appears through a collision with the metastable state that produces more ion-electron pairs. The increment in the electrons increases the gain and that fact reduces the statistical fluctuations in the total number of particles per energy that corresponds to an improvement in the energy resolution [71]. In particular, some studies have been carried out with Trimetylamine (TMA) showing this performance [109]. An extra advantage from this gas is that the diffusion coefficient is smaller. We will discuss in Chapter 5 how this improves the topological reconstruction of the track compared with pure Xenon, where the diffusion is higher. In the first sections of this chapter the different processes that take place in a gaseous detector are described. As general references [71, 124–127] have been used.

Another important selection is the detector to be used which depends on the requirements for the expected signal. As emphasized previously in a neutrinoless double beta decay experiment it is required a very good energy and spatial resolution and a low background budget. All these characteristics are fulfilled in a Time Projection Chamber detector equipped with Micromegas [108, 109]. In the second part of the chapter a general view of the different gaseous detectors is briefly presented to move on to explain in detail the Micromegas detectors and their different technologies.

2.1 Ionization in gases

A charged particle passing through a gas creates both excited and ionized molecules along its path. The encounters with the gas molecules are purely random and they are characterized by the mean free path, $\lambda = 1/(n\sigma_I)$ where n is the density of electrons, and σ is the effective cross-section area for the encounters with the gas, that in general will depend on the energy of the scattering. The number of encounters along a length L follows a Poisson distribution.

Different ionization mechanisms exist. They can be distinguished between primary and secondary ionization. When an incident electron gives enough energy to the atom, a bound electron can be ejected, resulting in the ionization of the atom and in the formation of an electron-ion pair (e^--ion pair). The energy of the ejected electron depends on the incident electron energy and on its binding energy. If the energy carried away by the ejected electron is enough to produce secondary ionization, in the same manner as the primary, the process can continue. An avalanche of electrons is produced until the energy is less than the ionization potential of the atom. This process is sketched in figure 2.1 (a). As it is a probabilistic process, not all the electrons that have energy higher than the ionization potential of the atom produce subsequent ionization.

The practical parameter is the number of e^--ion pairs produced along the trajectory of the particle. This quantity depends on the so-called *W-value*, the energy required to produce an e^--ion pair. It is determined experimentally and it is higher than the ionization potential because some energy is also usually lost due to excitation. W depends on the cross section, i.e. it depends on the gas (its composition and density) and on the nature and energy of the incident particle. However, experimentally, it has been found that it is independent of the incident energy above a few keV for electrons and a few MeV for alphas. In the case of Xenon, W has been found to be 22 eV/(e^--ion pair). For more values in different gases reader is referred to [71] or [127], for example.

Therefore, the number of e^--ion pairs can be obtained experimentally as the energy of the incident particle over the energy needed to create an ion pair, W, as shown in Equation 2.1. In the case of partial energy loss of the incident particle it can be computed using the stopping power $\frac{dE}{dx}$ as in Equation 2.2.

$$N = \frac{E}{W} \tag{2.1}$$

$$N = \frac{1}{W}\frac{dE}{dx}\Delta x \tag{2.2}$$

2.2 Transport of electrons in gases

The electrons and ions produced in a gas move randomly and are scattered by collisions with the gas molecules. They rapidly thermalize adopting a Maxwellian distribution in absence of an external electric field. At room temperature this thermalization occurs at 0.04 eV. The diffusion of the charge is isotropic because there is not a preferred direction of motion. Therefore, the diffusion in any direction can be described using a Gaussian distribution.

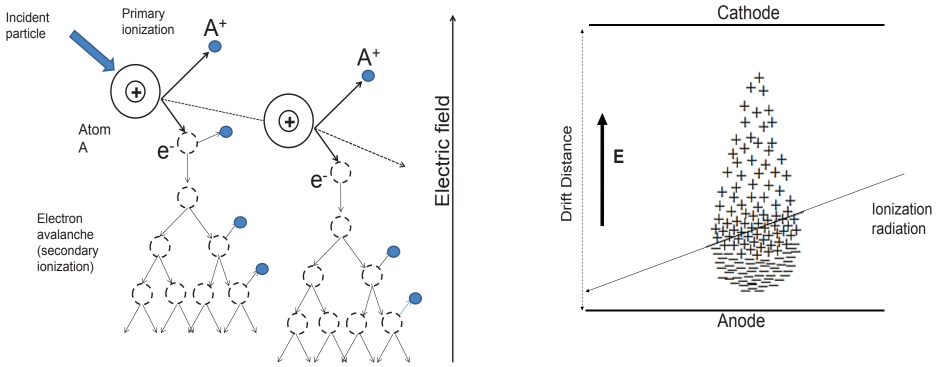

(a) (b)

FIGURE 2.1: *(a) Effect of the passing of radiation through a gas. Primary* e^-*-ion pairs are formed when interacting with the gas molecules. In the presence of an electric field a secondary ionization is produced leading to an avalanche of charge pairs. (b) Liquid-drop profile of the avalanche multiplication due to the fact that the electrons have smaller mass than the ions and then drift faster to the anode. Images modified from [127].*

In the presence of an external electric field, E, the electrons gain an extra velocity between collisions due to the acceleration produced by the electric force. This extra velocity appears macroscopically and it is called *drift velocity*, v_d,

$$v_d = \frac{eE}{m}\left\langle \frac{\lambda}{v} \right\rangle = \frac{eE}{m}\tau, \tag{2.3}$$

where v is the velocity of the electron and λ its mean free path, so τ is the average time between collisions. e is the electron charge. The drift velocity depends on the pressure of the gas. Because the density of molecules in space changes with the pressure, the probability of collisions is modified. Then, the mean free path of the electron is inversely proportional to the pressure (P) and the electron energy is a function of the reduced field E/P. Therefore, the drift velocity is also a function of the E/P ratio and it is called *reduced drift velocity*.

Expression 2.3 is deduced in [126] and is based on the classical kinetic theory of gases. A more rigorous statistical theory, it is the **transport theory** that is based on the solution of transport and energy conservation equations for free electrons under the influence of external fields [128].In the transport theory, an electron distribution function is introduced for the six dimensions space (positions and velocities) and appropriate differential equations are describing density and energy conservation.

In the last decades, the drift properties and the diffusion in a large variety of gases and gas mixtures have been studied (experimentally and theoretically). In particular, a computer programme Magboltz [129] exists (and it is continuously updated with new data) to simulate electrons in gases giving drift velocity and diffusion coefficients with an accuracy better than 2%. In Table 2.1 values of the drift velocity and diffusion at 1 kV/cm for the drift field are summarized for the gases under study in this work. A drift field of 1 kV/cm is required to obtain the optimum gain of the detectors at 10 bar. The values have been obtained using Magboltz. In Figure 2.2

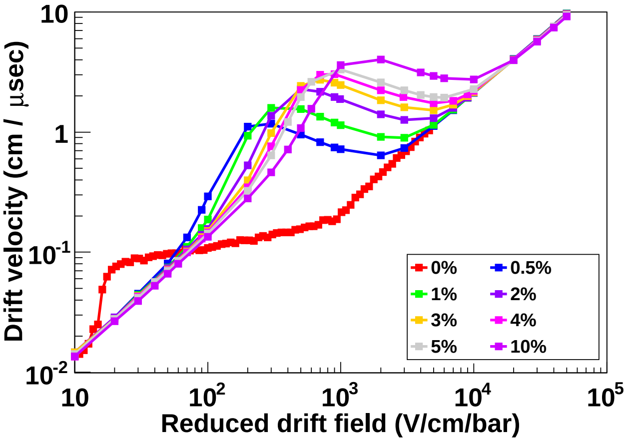

Figure 2.2: Dependence of the drift velocity with the reduced drift field for pure Xe and Xe-TMA mixtures at different concentrations. The addition of a quencher increases the velocity of the gas.

is shown the drift velocity in pure Xe and Xe-TMA at different concentrations obtained with Magboltz in function of the reduced drift voltage[1].

Gas	P (bar)	Drift velocity (cm/μs)	σ_L ($\mu cm/\sqrt{cm}$)	σ_T ($\mu cm/\sqrt{cm}$)
Xe	1	0.11	960	2487
Xe	10	0.11	355	850
XeTMA (3.5%)	1	0.24	218	312
XeTMA (3.5%)	10	0.24	218	312
Ar	1	0.3	1050	800
Ar	10	0.25	312	1000
Ar-C_4H_{10}(2%)	1	3.2	35	370
Ar-C_4H_{10}(2%)	10	3.0	400	700

Table 2.1: *Drift velocities and diffusion coefficients obtained using Magboltz for the gas mixtures used in this work. Results where obtain at* $V_d = 1\,\mathrm{kV\,cm^{-1}}$ *at 10 bar and 150* $\mathrm{kV\,cm^{-1}}$ *at 1 bar.*

2.2.1 Diffusion

Diffusion is one of several transport phenomena that occur in nature. In a gas the atoms and molecules are in constant thermal motion. The flux of particles per unit area and per unit time, $\vec{J}$, can be written as

$$\vec{J} = n\vec{v_d} - D\vec{\nabla}n, \tag{2.4}$$

where D is the diffusion coefficient and n the number density of carriers.

The electrons and ions produced when a particle interacts with the gas molecules also take part in the random thermal motion and therefore have some tendency to diffuse away. Because of

---

[1] Simulations done by F. Iguaz

their lower mass the electrons have in average a higher thermal velocity than the ions (of the order of $cm/\mu s$ for electrons and $10^{-2}\, cm/\mu s$ for ions, at room temperature) and their diffusion is much more pronounced. In absence of an external electric field the diffusion is isotropic and a point-like collection of free electrons will spread around the original point (we take here the origin) following a Gaussian spatial distribution whose width will increase with time. In any direction and integrating the relation 2.4 with $v_d = 0$, it can be described by

$$dN = \frac{N}{\sqrt{4\pi Dt}} e^{\left(\frac{-x^2}{4Dt}\right)} dx. \tag{2.5}$$

This distribution represents the number of charges dN that can be found in a differential element dx at a distance x from the centrer of the initial charge distribution after a time t. D can be used to determine the standard deviation through the relation

$$\sigma = \sqrt{2Dt}. \tag{2.6}$$

In the presence of an electric field the diffusion is no longer isotropic and in this case it is a tensor with two non-zero components: a longitudinal, D_L, in the direction of the drift field and a transversal component, D_T, orthogonal to the drift field. Integrating again the relation 2.4, now with the drift field term present, it is obtained

$$n(x, y, z, t) = \frac{N}{4\pi D_T t \sqrt{(4\pi D_L t)}} exp\left(\frac{-(x^2 + y^2)}{4D_T t}\right) exp\left(\frac{-(z + v_d t)^2}{4D_L t}\right), \tag{2.7}$$

where the initial condition at $t = 0$ is $n(x, y, z, 0) = N\delta(x)\delta(y)\delta(z)$ (with δ representing the Dirac-δ distribution). A detailed study can be found, for example in [130].

In general, the longitudinal component is smaller than the transversal one as can be seen in Table 2.1. In Figure 2.3 is plotted the obtained transversal and longitudinal diffusion coefficient in Xe and Xe-TMA mixtures using Magboltz[2]. It can be seen that the diffusion is less important when the drift field increases. Also, the addition of a quencher to the main gas reduces the diffusion coefficients.

2.2.2 Intrinsic uncertainties in gaseous detectors

Ideally the measured current in any readout would be all the electrons coming from the generated e$^-$-ion pairs. However, due to different processes, not all of them are collected and some losses of charges occur along the drift distance. These losses can be important in the gain and energy resolution of a detector and must be taken into account for precise measurements. In this section some of the main effects that lead to the uncertainties are discussed.

Recombination of ions and electrons in gases

---

[2] Simulations done by F. Iguaz

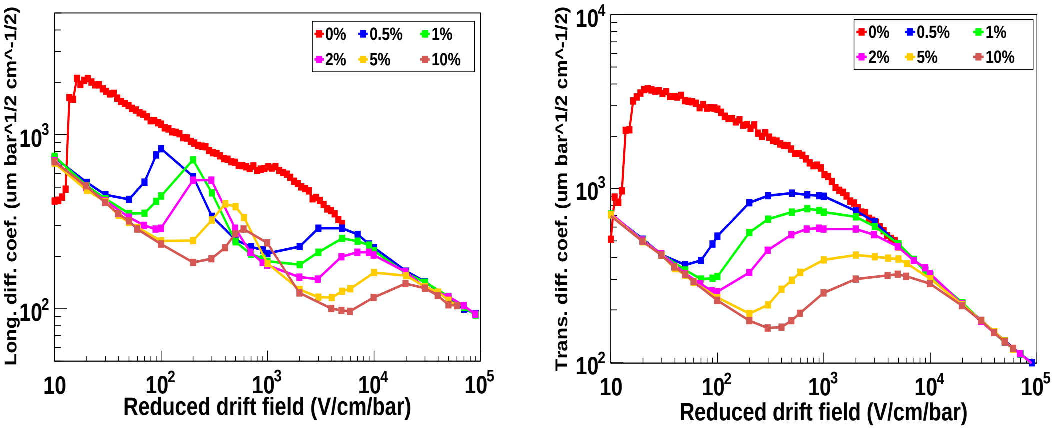

(a) (b)

FIGURE 2.3: *Longitudinal and transversal diffusion coefficients versus the reduced drift field for pure Xenon and Xe-TMA mixtures. It can be seen how the diffusion decreases with the addition of a quencher.*

The recombination process depends on the number of charge carriers and on the recombination coefficient. This process implies a decrease in the number density of e$^-$-ion pairs , n, along the drift distance (along the time) that follows the equation

$$\frac{dn}{dt} = p_r n^+ n^-, \tag{2.8}$$

where p_r is the recombination coefficient, usually of the order of $10^{-7}\,\mathrm{cm}^{-3}\,\mathrm{s}^{-1}$ and n^- (n^+) are the number density of electrons (ions). Though this process is not usually very important, there is a general tendency to increase with the e$^-$-ion pair concentration, and therefore, in the case of noble gas detectors the recombination rates are usually higher [124] than in other gases. This effect is reduced when applying an electric field between the cathode and anode plane. Experiments with Xe-TMA [131] show that recombination is reduced doping the Xe with TMA.

In pure Xe the recombination coefficient was measured by [132] with densities between 0.05 and 1.7 g/cm^3. It was found that it is practically independent of gamma ray energy until the low energy range (below 400 keV).

Effect of contaminants or attachment

The effect of impurities in the gas can produce the loss of some charge carriers, and consequently, a degradation in the detected signal. These contaminants are electronegative molecules that usually have several vibrational energy levels and, therefore, they are able to absorb electrons in a wide range of energies. When absorbing electrons they can form stable or metastable ions. Noble gases and most organic molecules can only form stable negative ions at collision energies of several eV, which are higher than energies reached during any electron drift. However, there are some molecules that are capable of absorbing electrons at much lower collision energies, these molecules are called impurities and are mainly oxygen, air and water. In Table 2.2 are shown some of the main impurities with its electron affinity.

Molecule	Electron affinity (eV)	Negative Ion	Electron affinity (eV)
O_2	0.44	O^-	1.47
C_2	3.54	C^-	1.27
Cl_2	2.38	Cl^-	3.61
OH	1.83	H^-	0.75

Table 2.2: *Electron affinities of different molecules and ions from [127]*

Three different mechanisms to produce the capture of electrons by the contaminants are usually considered:

1. Radiative Attachment: the capture of an electron leaves the atom in an excited state. It occurs only in molecules with positive electron affinity.

$$e^- + X \to X^{-*}, \tag{2.9}$$

$$X^{-*} \to X^- + \gamma. \tag{2.10}$$

   It has usually a small cross-section.

2. Dissociative Attachment: the molecule that captures the electron dissociate into simpler molecules emitting an electron with an energy smaller than the original one.

$$e^- + AB \to AB^* + e^- \to A^+ + B^- + e^-. \tag{2.11}$$

   Not all the polyatomic molecules emit secondary electrons, they can also dissociate into stable molecules.

$$e^- + AB \to AB^- \to A^* + B^-. \tag{2.12}$$

3. Three-body attachment: in this process the polyatomic molecule captures an electron and it transfers its excess energy to another molecule.

$$e^- + AB \leftrightarrow AB^{-*}, \tag{2.13}$$

$$AB^{-*} + X \to AB^- + X. \tag{2.14}$$

   The energy released in this process is known as *electron affinity*.

In order to compare the attachment in different gases, a probability of electron attachment can be defined

$$p = \frac{1}{\tau_e \nu_e}, \tag{2.15}$$

where τ_e is the mean lifetime of the electrons and ν_e their collision frequency, both magnitudes can be determined experimentally. Then, expression 2.15 represents the probability of capture in a single collision. The values for the same gases are shown in Table 2.3. The extremely small capture lifetimes make that this probability increases and could be a serious problem for precise measurements.

Gas	τ_e (s)	ν_e (s^{-1})	p
O_2	7.1×10^{-4}	2.2×10^{11}	6.4×10^{-9}
CO_2	1.9×10^{-7}	2.1×10^{11}	2.5×10^{-5}
H_20	1.4×10^{-7}	2.8×10^{11}	2.5×10^{-5}
Cl_2	4.7×10^{-9}	4.5×10^{11}	4.7×10^{-4}

Table 2.3: *Probability of electron capture in a single collision, p, for different gases. p is defined in 2.15. τ_e is the capture lifetime of the electrons and ν_e their collision frequency.*

The electron lifetime, τ_e, is the average time for an electron to be drifted before it is captured by an electronegative molecule and therefore, lost to generate the signal. It follows an exponential law

$$N(t) = N_0 e^{\frac{-t}{\tau_e}}, \tag{2.16}$$

where N_0 is the number of original electrons.

Attachment Origins

Attachment, as mentioned, is produced when the gas contains electronegative impurities. These molecules may be there because a low enough vacuum level had not been achieved before injecting the gas or they may appear once the gas is inside the chamber due to **outgassing** processes:

- Real leaks: air and oxygen can reach the gas.
- Internal or virtual leaks: volumes of air separated from the main one, by little tubes like screws or by additives. They are difficult to extract pumping. Therefore, the design of the different elements have to be made taking this effect into account and also, a possible solution is to make little holes in the conflictive elements that allows the gas flux.
- Vaporization: release of impurities molecules that were trapped in the surface materials.
- Permeation: through the detector walls. This effect is important in TPCs if they have many plastic O-rings.

Apart from the real leaks, the other processes can be controlled. For example, selecting low outgassing materials. Also pumping and making bake-out cycles. Results of bake-out cycles and outgassing measurements are presented in Chapter 3 for the designed prototype.

2.3 Operation of a gas detector and the avalanche multiplication region. Townsend coefficients

A gas filled detector shows different regions of operation depending on the applied bias drift voltage. The main differences between these modes are the amount of charges produced in the ionization, their movement inside the detector and whether the output signal is proportional to the original energy of the particle or not. In Figure 2.4 the different regions are shown. In the following a brief explanation of each region is given focusing in the avalanche process. For more information the reader is referred to [127], for example.

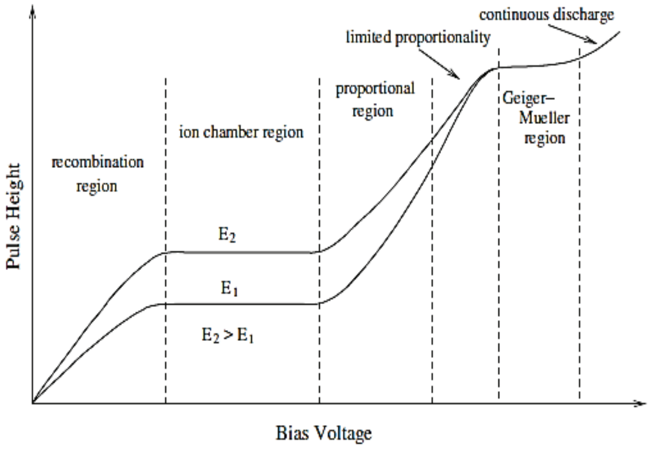

FIGURE 2.4: *Regions of operation of gas filled detectors based on the applied bias voltage. The two curves correspond to two different energies of incident radiation. Figure extracted from [127].*

In the absence of an external electric field, as it has been mentioned the electrons and ions produced by an external radiation interacting with the gas molecules are quickly recombined, as the voltage increases some of the ions can reach the detector. The **recombination region** refers to this region up to a voltage high enough to consider recombination negligible. The output signal at these voltages of operation is not proportional to the incident energy.

As the voltage increases the detector enters in the **ion chamber region** where all the charges produced are recollected. The current measured is proportional to the energy deposited by the incident particle and it is called saturation current. The detectors designed to operate in this mode are called ionization chambers.

Then, as the voltage is kept increasing the detector enters the so-called **proportional region**. In this region the produced e^--ion pairs have enough energy to produce additional pairs, process called secondary ionization, as can be seen in Figure 2.1 (a). The electrons, owing to their small mass, are the ones that cause most of the subsequent ionizations. This multiplication of charges is exploited in the proportional detectors to increase the height of the output signal being still proportional to the initial energy of the incident particle. The final number of pairs produced is proportional to the initial number of charges. In the next section the charge multiplication process is explained in detail.

Avalanche multiplication

An avalanche multiplication is a process that consists in a rapid multiplication of charges by the primary charges produced from the incident radiation. This multiplication occurs at higher voltages, of the order of few kV/cm, that also decreases the charge collection time of the detector.

This charge multiplication results in the increase of the output pulse amplitude but keeping its proportionality with the energy of the incident particle.

Due to the high electric field between the electrodes, the charges quickly gain energy between collisions. If the total energy of an electron or an ion becomes higher than the ionization potential of the gas atoms, it can ionize another atom, thus creating a new e^--ion pair.

Under constant conditions of electric field, temperature, or pressure and if the electric field is uniform, the change in the number of electron-ion pairs per unit path length is proportional to the total number of charge pairs, as reflected in

$$\frac{dN}{dx} = \alpha N, \tag{2.17}$$

N being the total number of e^--ion pairs and α is known as the **first Townsend coefficient**. It represents the number of collisions that create an e^--ion pair per unit length. Therefore, it is simply the inverse of the mean free path of ionization:

$$\alpha = \frac{1}{\lambda} \tag{2.18}$$

where α depends on the energy that the electron gains in a mean free path and the ionization potential of the gas. The solution of Equation 2.17 is an exponential in which, if $\alpha > 0$, the number of charges grows exponentially with the distance. If the field is uniform (α constant), integrating 2.17, a multiplication factor, M (or gas gain, G) is obtained

$$M = \frac{N}{N_0} = e^{\alpha x}. \tag{2.19}$$

If the field is not uniform, then the Townsend coefficient becomes a function of x and, for an electron moving from x_1 to x_2, the gain can be written as the integral

$$M = exp\left[\int_{x_2}^{x_1} \alpha(x)dx\right]. \tag{2.20}$$

The gas gain is of fundamental importance in gas detectors. To determine analytically the spatial profile of the Townsend coefficient is very challenging and a lot of effort has been put both, experimentally and theoretically. A commonly used expression is the one originally proposed by Korff [133]

$$\frac{\alpha}{P} = A\,exp\left(-\frac{BP}{E}\right), \tag{2.21}$$

P being the pressure. In expression 2.21 the dependence of the α parameter with the reduced electric field is taken into account and the parameters A and B depend on the gas and on the electric field intensity. These parameters have been experimentally determined. Based on the publication [134] the parameters A and B can be interpreted as $\frac{1}{\lambda}$ and the ionization threshold, I_e, (normalized to P), respectively if the secondary ionization is neglected.

An interesting property of the avalanche is its geometric progression. Due to the different masses of electrons and ions, they move at different drift velocities. The electrons reach quickly the anode and leave behind them a tail of ions drifting slower. Finally the profile of the avalanche takes the shape of a liquid drop, as shown schematically in Figure 2.1 (b).

Region of limited proportionality

As the voltage is increased more e^--ion pairs are created. As it has been mentioned, the ions move much slower and can produce a kind of cloud of positive charges between the electrodes and then shield the effect of the electric field on the charges. It could produce a loss in the proportionality of the produced charges with respect to the initial ones and the collected energy could not be proportional to the energy of the incident radiation.

Geiger-Muller region

Increasing the bias voltage the detector enters the Geiger-Muller (GM) region. Here the avalanche is so severe that produces a pulse of several Volts and it is possible to count individually the incident particles but not to obtain their energy because the output pulse is not proportional to the deposited energy.

Breakdown

As mentioned before, ions produced in an avalanche move slowly and take longer to reach the anode. When these heavy ions strike the cathode wall more ions can been released from the cathode material into the gas. The efficiency of this process is what is called the **second Townsend coefficient**, γ, and is usually less than the 10%. At moderate voltages, γ is not enough to produce extra charges but starts to be relevant as the voltage is increased because it may start discharge in the gas. At this point the current measured by the electronics goes to higher values and the height of the pulse becomes independent of the e^--ion pairs.

Quantitatively, from [135] it can be shown that if the discharge becomes independent of the ionization of the gas, expression 2.17 should be replaced by

$$M = \frac{e^{\alpha x}}{1 - \gamma(e^{\alpha x} - 1)}. \tag{2.22}$$

The singularity in Equation 2.22 represents the breakdown (infinite current, theoretically). Therefore we can deduce an expression for the second Townsend coefficient, γ, as

$$\gamma = \frac{1}{e^{\alpha x} - 1}, \tag{2.23}$$

γ being the critical value at which the breakdown starts. It depends not only on the first Townsend coefficient, α, but also on the position x. Since α depends on the electric field and on the pressure we can try to obtain a value for the breakdown voltage. Rewriting expression 2.23 as

$$\alpha x = ln\left(1 + \frac{1}{\gamma}\right), \tag{2.24}$$

and substituting in 2.21 we obtain for the electric amplification field E the following expression

$$E = \frac{BP}{ln\left[\frac{APx}{ln(1+1/\gamma)}\right]}. \tag{2.25}$$

If the geometry is a pair of parallel electrodes separated a distance d, as occurs in a TPC, the electric field can be written as $E = V/d$. Therefore, an expression for the breakdown voltage, V_{break}, is given by

$$V_{break} = \frac{BPd}{ln\left[\frac{APd}{ln(1+1/\gamma)}\right]}. \tag{2.26}$$

Relation 2.26 tells us that for a given gas the breakdown voltage depends on the pressure times the electrode separation (Pd). It is generally known as **Paschen's law** and the curve of Pd vs V_{break} is the *Paschen's curve.* The minimum represents the voltage below which the breakdown is not possible.

Continuous Discharge

The breakdown process can further advance to the continuous discharge if the voltage is raised to higher values. In this region electric arcs can be produced between the electrodes and eventually can damage the detector. Therefore, these voltages have to be avoided.

2.4 Signal creation

The signal detected is produced by the moving charges between two electrodes, read with some amplifier device connected to them. An avalanche of electrons is needed in order to produce a signal above the electric noise. The determination of the signal is a complicated electrostatical problem which is commonly addressed by means of the Ramo's Theorem [136] that allows to determine the amplitude of the signal. It states that the instantaneous current I induced on a given electrode, i due to a charge's motion is

$$I_i(t) = Q \cdot E_{w_i} \cdot v_d(t), \tag{2.27}$$

where Q is the charge of the particle and E_{w_i} is the component of the electric field in the direction of v_d at the charge's instantaneous position, calculated with the condition that the electrode is at 1 V and the other are grounded, this is usually called "weighted fiel". We can see the dependence with the drift velocity, implying that as faster the charge moves, more pronounced will be the change in I.

2.5 Energy resolution

The ability of a detector to determine an energy is given by its energy resolution. It is measured as the energy peak width in a pulse height signal acquired from the detector. This peak is generated by a monoenergetic ionizing particle. There exist different methods to determine this width, the most common way is to measure the so-called *Full Width at Half Maximum (FWHM)* of the peak. This FWHM is related with the standard deviation, σ, of a Gaussian fit of the peak by

$$FWHM = 2\sqrt{2ln2}\sigma \approx 2.3548\sigma. \tag{2.28}$$

2.5.1 Statistical contributions

Following the discussion in [71], two factors affect intrinsically the energy resolution: the fluctuations in the ion-electron pairs production and in the single-electron avalanches. The charge, Q, collected in a proportional detector as a Micromegas can be assumed to be the sum of the charges created in each avalanche. It can be written as

$$Q = N_0 e M, \tag{2.29}$$

where N_0 is the number of e$^-$-ion pairs, e the electron charge and M represents the average multiplication factor and is defined as

$$M = \frac{1}{N_0}\sum_{i=1}^{N_0} A_i \equiv \bar{A}, \tag{2.30}$$

where A_i is the electron multiplication factor for each avalanche triggered by an electron "i". If the factors N_0 and M of 2.29 are independent variables, the variance in the charge can be written as

$$\left(\frac{\sigma_Q}{Q}\right)^2 = \left(\frac{\sigma_{N_0}}{N_0}\right)^2 + \left(\frac{\sigma_M}{M}\right)^2. \tag{2.31}$$

Using 2.19, Equation 2.31 can be rewritten as

$$\left(\frac{\sigma_Q}{Q}\right)^2 = \left(\frac{\sigma_{N_0}}{N_0}\right)^2 + \frac{1}{N_0}\left(\frac{\sigma_A}{\bar{A}}\right)^2. \tag{2.32}$$

Expression 2.32 represents the dependence of the variance in the pulse amplitude separated in two terms, the first one corresponds to the contribution from ion pair fluctuations and the second from single-electron multiplication variations.

Gas	F	Energy (keV)	Particle
He	0.17		β
Ne	0.17		
Ar	0.23 ± 0.05	5.9	γ
	0.23 ± 0.05	5305	α
Xe	0.170 ± 0.007	1.49	γ
	0.13 ± 0.01	5.9	γ
C_4H_{10}	0.26	1.49	γ
CO_2	0.33	1.49	γ

TABLE 2.4: *Measured Fano Factor for different gases and with different particles and energies. Extracted from [138]*

The first assumption is that the formation of e^--ion pairs follows a Poisson statistics. Therefore, if N_0 electrons are produced, the variance would be, N_0. However, this is not the case and Fano in 1947 [137] demonstrated that the standard deviation in the fluctuation of the number of pairs produced, when all the energy is absorbed in the detector, is different from Poisson distribution by a factor F, the *Fano Factor.* This factor represents the deviation of the ionization process from independent, identically distributed ionization events. If the entire incident energy were always converted into e^--ion pairs, the number of pairs would be always the same and there would not be any fluctuation, so F would be equal to zero. In the case the process will follow a Poissonian distribution then $F = 1$. In general, the deviation in the generation of e^--ion pairs is given by

$$(\sigma_{N_0})^2 = FN_0. \tag{2.33}$$

The *Fano factor* depends on the gas and on the electron energy. Values lie between 0.15-0.2 for noble gases and 0.2-0.4 for molecular gases. The lowest values are achieved for binary gas mixtures in which the Penning effect is important. In Table 2.4 values for different gases are summarized. The Fano factor gives a limit to the energy resolution of a particle with energy E. It is an intrinsic limitation from the gas called the **Fano limit**. Remembering that it is the first term in expression 2.32 and using equations 2.33 and 2.1, the energy resolution can be expressed as

$$FWHM = 2.35\sqrt{\frac{FW}{E}}. \tag{2.34}$$

The second term in expression 2.32 represents the random nature of the electron multiplication process that leads to fluctuations in the avalanche size. Together with the fluctuations in the ionization process, avalanche fluctuations set a fundamental limit to detector resolution. Several models have been used to describe the amplification phenomena. If the probability of ionization by an electron is considered to be dependent only on the electric field, the Furry distribution can be used and in this case the factor $\left(\frac{\sigma_A}{A}\right)^2 = 1$. This is valid at lower electric fields, but once the field is higher the process is more complicated. In the model proposed by Byrne [139] the probability distribution is adjusted to a Polya distribution. In this case, if the multiplication, A, is large, the variance in the avalanche can be written as $\left(\frac{\sigma_A}{A}\right)^2 \approx b$, where b is the parameter from the Polya fit that, as W and F depends on the gas. However, there exists some indications that b can also be electrical field dependent [140] and it is not exactly a constant. Therefore, from expression 2.32 and using 2.1 the relative standard deviation of the pulse amplitude is

$$\left(\frac{\sigma_Q}{Q}\right) = \left(\frac{F+b}{N_0}\right)^{1/2} = \left(\frac{W(F+b)}{E}\right)^{1/2} . \tag{2.35}$$

From this expression the statistical limit of the energy resolution of a proportional counter varies inversely with the square root of the energy of the incident particle and depends only on the gas used.

2.5.2 Other factors

There exist other factors that can contribute to the energy resolution limit. In order to approach as much as possible to the statistical limit, special care has to be taken with some parameters, as the electronic and capacitive noise (with dependence $\propto C^{1/2}$), the geometrical defects and the operation parameters. Moreover, the purity of the gas, must be considered because, as mentioned previously, traces of electronegative impurities can reduce the multiplication factor by absorbing electrons.

Another important effect appears when electrons have to be drifted long distances. During the path to the detector the electrons may gain or lose extra energy from the drift field. In the case of an electric field of the order of $0.1\,\mathrm{kV\,cm^{-1}\,bar^{-1}}$ the degradation to the energy resolution is of the order of 0.5% FWHM in Xenon (with a linear dependence with the electric field) (see [141]).

2.6 Gaseous detectors

The first gaseous detectors appeared in the twentieth century with the invention of the single wire proportional counter [142] and the Geiger-Muller counter [143]. With these detectors it is possible to count only the number of particles but it is not possible to obtain the electron trajectory. With the Multi Wire Proportional Chamber (MWPC) invention by G. Chapark [144] in 1968, the reconstruction of the trajectories was attained. With the possibility to reconstruct the two dimensional trajectory left by the particle, a new generation of detectors appeared in order to obtain the third dimension: the drift chamber [145] and the time projection chamber (TPC) [146]. However, as has been mentioned previously, the MWPC had a low spatial resolution and low rate capabilities and were not suitable for rare event searches.

With the invention of the Micro-Strip Gas Chamber (MSGC) in 1988 [119] a new time arises for the gaseous detectors and different readouts start to be developed known as micropattern gaseous detectors (MPGD). With this new technology detectors more robust, stable and with higher gains are possible. Among them the MICRO MEsh GAseous Structure (Micromegas) [120] stands out in terms of gain and energy resolution.

In this section it is explained in detail the principle of operation of a TPC and of a Micromegas detector. In addition the main features and technologies of manufacturing these readouts are also explained.

2.6.1 Time Projection Chamber

A revolution in charged particle tracking happened in 1974, with the Time-Projection Chamber (TPC) invention by David Nygren [146]. The main idea is to define a long drift distance volume where a constant electric field is applied. The electrons produced by ionising particles in this volume follow the electrical field lines towards the MWPC detectors, located at the end of the volume. Once the electrons are close to the anode they suffer a multiplication process and the avalanches are detected in the pads plane. The two coordinates of the track of the particle are obtained in the MWPC detector while the third one is obtained from the drift time measurement of the electrons to the anode plane. For a given constant gas mixture and a drift electric field, the electron drift velocity is also constant. Typical values are of the order of few $cm/\mu s$.

In its first design, a cylindrical TPC with a central cathode and two anode planes at the end-caps was constructed. It was used for collider physics, specially it was designed for the e^+-e^- PEP-4 collider experiment at Stanford. Furthermore, a magnetic field was applied along the length of the cylinder, parallel to the electric field, to measure momentum from the curvature of the track produced by the magnetic field over charged particles. The actual designs can vary from this one while keeping the same philosophy. In the case of rare event searches a very large and dense volume is required in order to increase the interaction probability and no magnetic field is needed.

In Figure 2.5 are shown the different process that take place in a TPC and that have been already mentioned in the previous sections: 1) the ionization of the medium by an incident particle, 2) the drift of the secondary electrons to the readout plane, 3) the amplification of the signal in the device, and finally 4) the creation of the signal.

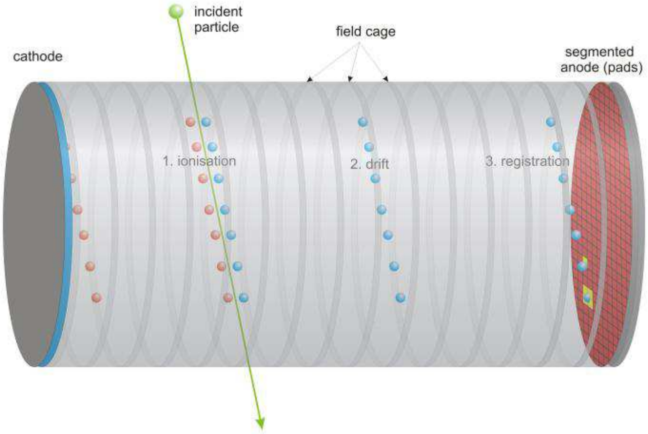

Figure 2.5: *Sketch of the different process that a charge suffer while traversing a TPC.*

While the principle of operation looks simple, there are many constraints on its realisation, especially for the gas choice. The drift over a long distance can produce a loss in the spatial resolution due to attachment or diffusion in the gas. Therefore, the gas has to be carefully selected in function of its attachment, drift velocity and diffusion, as well as for their ionisation and multiplication capabilities. Finally, the applied electric field must be uniform and constant, for this reason field cages are constructed to assure its uniformity.

2.6.2 Micromegas detectors

The Micromegas detector is a two-stage parallel-plate avalanche chamber invented by I. Giomataris in 1995 [120]. It consists of two parallel plates: a metallic micromesh suspended over an anode plane by insulator pillars. The gap is usually 50-100 μm. It is combined with a conversion-drift space; inside a TPC, the mesh and the cathode define this drift region. The mesh and the anode define the amplification region.

The operating principle of a Micromegas is shown in Figure 2.6. Voltages are applied in the three electrodes of the detector. The electrons freed in the gas are drifted to the detector by an electric field of the order of $10^2 - 10^3\,\mathrm{V\,cm^{-1}}$. Then they cross the mesh holes entering in the amplification region where an avalanche takes place producing detectable signals. The generated ions are collected in the grid and the electrons in the anode. Usually amplification fields of $10^4 - 10^5\,\mathrm{V\,cm^{-1}}$ are applied.

In this configuration of fields the field lines from the drift region will enter through the holes of the mesh as is shown in Figure 2.7 assuring the transmission of the produced electrons into the gap. Also the fields are homogeneous inside both regions except a very little deviation in the openings of the mesh.

The accumulation of positive ions on the insulator can also modify locally the field and therefore lower the gain. This was one of the main drawbacks in the previous MPGD and is surpassed in the Micromegas because the high field in the gap also assure the fast collection of the ion cloud in the mesh. Moreover, only a small part of the ions, inversely proportional to the electric field ratio [147], escape to the drift region, effect known as *ion backflow.* Also the fast evacuation of the ions, together with the high granularity of the detector give them high rate capabilities [148].

The detector **gain** depends directly on the size of the gap. The gain is defined in Equation 2.19. Substituting α from Equation 2.21 it is obtained

$$M = exp(A\,P\,d\,e^{-B\,P\,d/V}), \tag{2.36}$$

where A, B are gas parameters, P is the operating pressure and V the voltage. From this equation different aspects can be extrapolated. The gain increases as d increases, until it reaches a maximum as is shown in [148]. The maximum multiplication value can be obtained differentiating the equation and it is $d = V/B$ at 1 bar. In general the gain variations due to flatness defects between the mesh and the anode are minimized for $d \approx V/Bp$. The variation of the gain with the gap size also follows the same relation. For higher pressures, smaller gap sizes will produce higher gains.

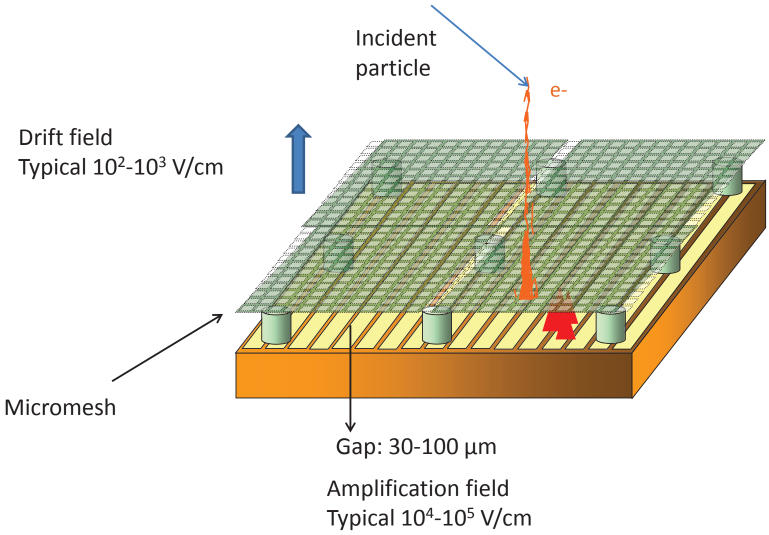

FIGURE 2.6: *Sketch of the different process that occurs in a Micromegas. In the conversion region, delimited by the cathode and mesh, the particles ionize the gas and the electrons are drifted to the Micromegas. Electric field of* $10^2 - 10^3$ *V/cm are usually applied. In the gap of the Micromegas an avalanche of electrons produces the amplification of the charge. In this region electric field of* $10^4 - 10^5$ *V/cm are usually applied. The ions are detected in the mesh and the electrons in the anode, that can be pixelized.*

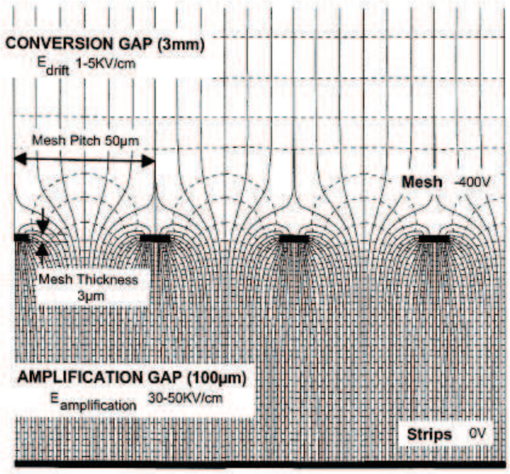

FIGURE 2.7: *Electric field lines in the Micromegas, image from [148].*

The gap dimension also plays an important role in the performance of the Micromegas. The gap reduction from 100 μm to 50 μm reduces the signal rise time by a factor of 3. Therefore the signal in the mesh is decreased from 100 ns to ~30 ns. This allows to work at moderate gains preventing sparks and also decrease the time the ions are collected. The drift velocity of the electrons is 100 times bigger, therefore the typical signals are of the order of 1 ns. These fast signals allow to reach time resolution of the order of 1 ns, in particular, in the KABES experiment [149] they obtained a time resolution of 0.60 ns.

The **electron transmission**, T, is defined as the proportion of primary electrons (n_D) that reach the amplification region and are therefore detected (n_A)

$$T = \frac{n_A}{n_D}. \tag{2.37}$$

The absolute transmission is difficult to measure experimentally and as an approximation, signals are normalized to the maximum. For a given amplification field, the transparency is low at high drift fields because most of the field lines end up in the mesh. As the drift field decreases the transparency is close or equal to one along several values of the field ratio (known as the *plateau* of operation). In this configuration, most of the field lines go through the mesh holes. For very low drift fields, the transparency sharply decreases because the drift velocity of the electrons is very low and attachment starts to be more relevant. The transmission depends mainly on the geometry of the detector (size holes and pitch) and the ratio of fields, as mentioned.

The Micromegas is the MPGD with the best **energy resolution**. The reasons are inherent to the avalanche process and some of them have been already mentioned as the spatial homogeneity of the gain or the minimal loss of charge before the avalanche. Also the gain is less dependent on environmental factors as temperature or pressure than in MWPC. Moreover, the ions are evacuated fast and efficiently. The relation with the avalanche can be seen from expression 2.35,where the energy resolution can be written in terms of the Fano factor and the fluctuation in the number of charges produced in the avalanche.

$$FWHM = 2.35\sqrt{\frac{W}{E}(F+b)}. \tag{2.38}$$

In this expression E is the energy of the incident particle, W is the mean energy per e^--ion pair, F the Fano Factor and b is avalanche contribution. The energy resolution depends on the amplification field (the gain) and on the ratio of fields (transmission). It is stable when the electron transmission is maximum. With respect to the gain, the energy resolution deteriorates at lower gains and also at very high ones, because it is close to the spark limit and the field could not be very stable.

Other factors considered non-fundamental can worsen the resolution but in principle they can be overcome (although with experimental difficulties). Some of them are the non-uniformity of the readout plane, problems of equalization of multiple channels or the attachment.

In general, energy resolutions of 11% FWHM with a 5.9 keV ^{55}Fe are routinely achieved in Argon-isobutane mixtures for the new Microbulk Micromegas. Tests in different gases or pressures are not standardized but studies with different mixtures were obtained showing similar results [150]. In addition, values with an ^{241}Am alpha source were obtained, showing an energy resolution of 1.8% FWHM at 5.5 MeV (with evidence of less than 1%) in Ar-isobutane [151]. Data with the same source have been obtained in pure Xe [108] with results of around 3% FWHM up to 5 bar. Recently, studies in Xe-TMA mixtures showed energy resolution of 7.6% (9.6%) FWHM at 1(10) bar for the 22.1 keV ^{109}Cd peak [109]. With respect to the **spatial resolution**, in most of the cases is only limited by diffusion, and values down to 11 μm were achieved [152].

2.6.3 Micromegas Technology

The construction of Micromegas detectors is in continuous innovation and development in close collaboration of the experimentalists with the manufacturer experts from CERN and CEA/Saclay. The original Micromegas [120] micromesh was a metallic grid made of thin electroformed Nickel (as the Frisch grid). The mesh was stretched and glued on a removable glass-fibre frame. The anode strips of gold-coated copper were printed by metal deposition techniques in a Kapton substrate. The first strips were 5 μm thick while thinner ones could be obtained by vacuum deposition. The pillars between the anode and the mesh were small cylindrical insulating spacers made of photo-imaginable resin, 100 μm thick and 150 μm diameter, and they were printed on top of the anode by a standard printed circuit technique. The two frames were screwed together. By applying a voltage between them, the mesh was pulled down by the intense electric field obtaining the flatness and parallelism of both surfaces and the gap size was defined by the pillars height with an accuracy better than 10 μm.

Subsequently, another type of mesh was developed [153]. It was based on etching techniques. The raw material was a double-sided Kapton foil of 50 μm stretched on a frame. The holes and pillars pattern was done applying two lithographic masks at both sides of the Kapton. Kapton was partially removed defining the pillars spacers. The high accuracy of the process allows to print on a 5 μm copper grid with 25 μm opening holes and a pitch of 50 μm.

Since then, efforts have been focused on producing the amplification region from a single piece to avoid the delicate operation of screw the anode to the mesh.Reducing, at the same time, the mass amount of materials. Two different detectors were developed with this “all-in-one”fabrication techniques: the **bulk** and **microbulk** Micromegas.

2.6.3.1 Bulk technology

In the bulk technology [154] a woven wire mesh is used instead of the usual electroformed micromesh. Different materials are available (Fe, Cu, Ti, Ni, Au) in rolls 40 × 40 m that are commonly produced making this option inexpensive and that can cover large surfaces. They are also robust for stretching and handling.

In a bulk Micromegas the anode plane carrying the copper strips, the mesh and a photoresitive film with the thickness of the gap are laminated together at high temperature to form a single object. The pillars are produced by photolitograpic methods etching the photoresistive film. The fabrication process is sketched in Figure 2.8.

The main advantages of this technique are the uniformity and robustness, lower capacity (that implies a low noise) and easy fabrication (they do not need a support frame). It allows the construction of large area detectors, also curved ones.They have shown acceptable energy resolution (18% FWHM at 5.9 keV) and good maximal gains (of the order of 10^4 in Ar-isobutane). The mesh thickness could be a disadvantage in some applications, while the ideal gap size depends on the application, for example bigger gaps are an advantage at low pressure.

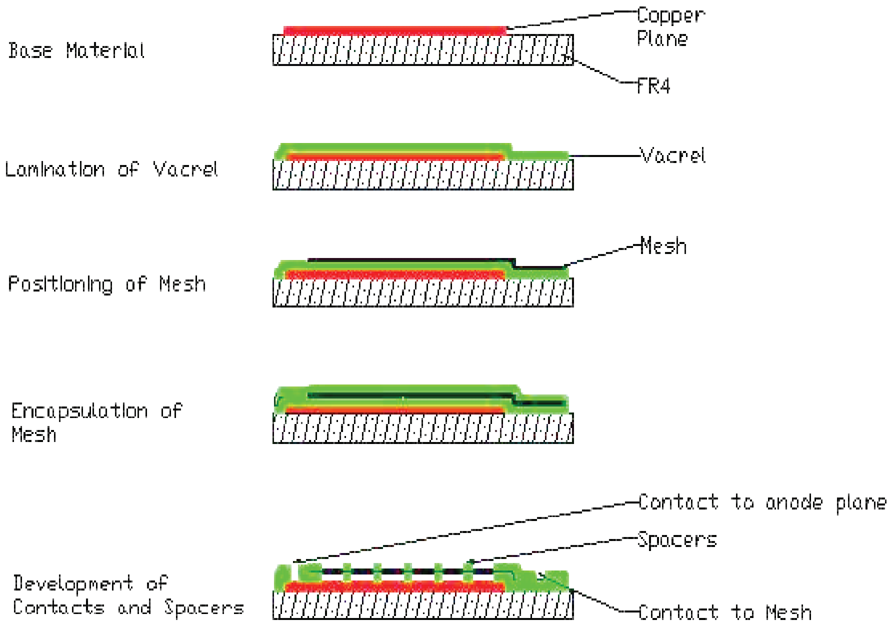

Figure 2.8: *Fabrication process of the bulk Micromegas detector [154].*

2.6.3.2 Microbulk Technology

In the microbulk fabrication [151] the raw material is a thin flexible poliamide foil with a thin copper layer on both sides. It is usually glued on top of a rigid substrate that provides the support and usually is were the strips or pixels are made by photolitography. Then a thin photoresistive film is laminated on top of the Kapton and it is isolated by UV light to produce the mask. The copper is removed by standard lithographic obtaining the holes of the mesh.

Two approaches were made to obtain the gap space. In one the polyamide is etched and partially removed in order to create thin pillars below the copper mesh. In the other approach, the polyamide is completely removed except the points where small pillars are created. In order to achieve this an additional spot is formed during the insulation process producing a Copper spot of 200 μm after the litographic process. By controlling the etching duration the polyamide can be completely removed except under these Copper spots. A sketch of the process is shown in Figure 2.9.

With this process there are no space connections under the mesh and each avalanche takes place under the mesh holes decreasing the fluctuations in the process. This property, together with the fact that the homogeneity of the gap is higher than in previous methods, allows to achieve the best energy resolution among the MPGD detectors. The pillars are under the shadow of the copper pads, avoiding any dead space.

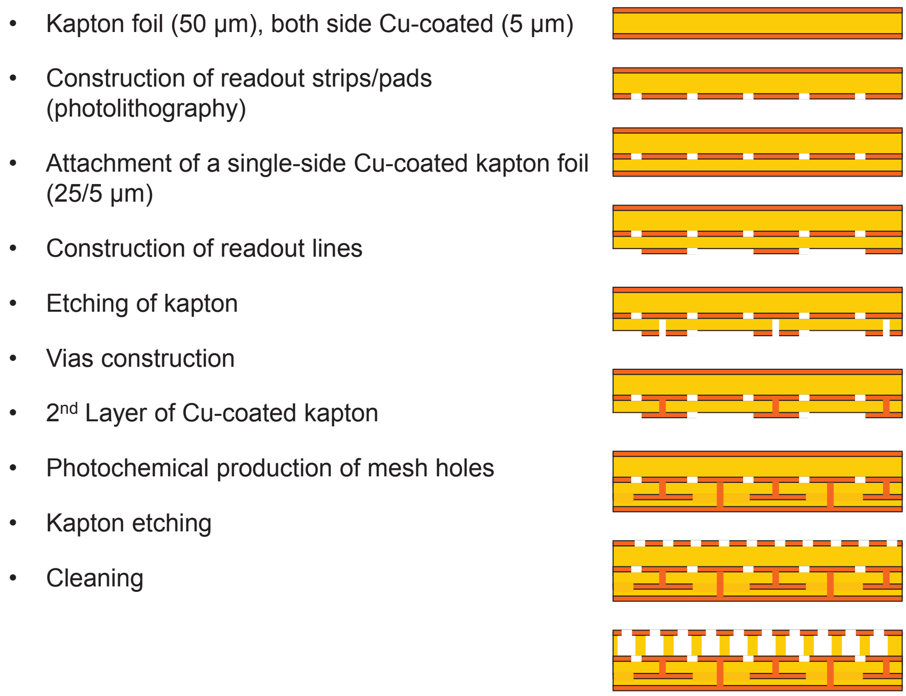

- Kapton foil (50 μm), both side Cu-coated (5 μm)
- Construction of readout strips/pads (photolithography)
- Attachment of a single-side Cu-coated kapton foil (25/5 μm)
- Construction of readout lines
- Etching of kapton
- Vias construction
- 2^{nd} Layer of Cu-coated kapton
- Photochemical production of mesh holes
- Kapton etching
- Cleaning

Figure 2.9: *Fabrication process of the bulk Micromegas detector.*

Another important advantage of a microbulk Micromegas is that it can be extremely light and most of the raw material is Kapton and Copper, two materials that can achieve the best levels of radiopurity [155]. Indeed, the first radiopurity study of Micromegas [156] shows that current microbulk detectors contain levels at least as low as $57 \pm 25\,\mu\mathrm{Bq/cm^2}$ for ^{40}K, $26 \pm 14\,\mu\mathrm{Bq/cm^2}$ for ^{238}U and $< 9.3\,\mu\mathrm{Bq/cm^2}$ for ^{232}Th (the big values of the errors make them compatible with a lower limit due to the Minimum Detectable Activity of the germanium detectors used).

Moreover, the contamination probably comes from the treatment of the materials used and can be then reduced with a careful selection of them. Next steps are focused on the identification of the contaminating steps in the fabrication and find alternatives, as well as to make a more precise measurement.

In this chapter a brief study of the phenomenology of particles in gaseous detectors, emphasizing the Micromegas detectors which are the ones with the better features for a neutrinoless double beta decay experiment. In the next chapter the description of the TPC constructed and the first results with different Micromegas are presented.

Chapter 3

NEXT-MM prototype: design and commissioning

Contents

3.1 The NEXT experiment 62

3.2 NEXT-MM 64

3.2.1 Experimental setup 64

3.2.2 The Micromegas Detectors used 71

3.3 Operational tests with NEXT-MM prototype 73

3.3.1 High pressure test 73

3.3.2 Vacuum and outgassing 73

3.3.3 High voltage tests 75

3.4 Main features of the detectors in Ar-isobutane: gain curves and first energy resolution estimations. 76

3.4.1 Electron transparency 78

3.4.2 Absolute Gain 78

3.4.3 Energy resolution 79

3.4.4 Cosmic Rays 80

3.5 Commissioning of the detectors and the electronics in NEXT-MM 80

3.5.1 Bulk detector: First Results 81

3.5.2 Microbulk detector: First Results 82

In the NEXT collaboration, a detector prototype with Micromegas readouts has been constructed and commissioned in the group of the University of Zaragoza. In this chapter, first, the NEXT experiment and the operation of the different prototypes are presented. A separate section is dedicated to describe the NEXT-MM prototype, based on Micromegas readouts. Its setup is explained summarizing all the work done for the commissioning. Finally, the first operational results are presented as well as the first data taken to commission the Micromegas detectors. The analysis program for the data acquisition and the first results regarding energy resolution and tracking obtained in Xe-TMA will be deeply described in the next chapter.

3.1 The NEXT experiment

The NEXT experiment (Neutrino Experiment with a Xenon TPC) [68] aims at measuring the neutrinoless double beta decay of ^{136}Xe using a high pressure (HP) gaseous electroluminescent time projection chamber (TPC). It will operate with 100 kg of Xe (90% enriched to ^{136}Xe) at 10 bar with the possibility to go up to 15 bar, that means a mass of Xe of around 150 kg.

The NEXT experiment is a broad collaboration with Spanish groups together with international groups from Europe and America. It will be installed in the Canfranc Underground Laboratory (LSC [157]) under the Spanish Pyrinees, more specifically under the Tobazo mountain that provides an overburden of 2450 m.w.e.

The use of Xe has several advantages for the double beta decay searches. The first advantage is its high $Q_{\beta\beta}$ value of 2458 keV [158]. Therefore, the $\beta\beta0\nu$ signal is separated from most of the emissions presented in the natural radioactive chains. Recently, the $\beta\beta2\nu$ has been measured by [45], [104] and it has a slow half-life of the order of $T^{2\nu}_{\frac{1}{2}} \approx 2 \times 10^{21}$y. As we can see in Equation 1.25, if the $\beta\beta2\nu$ mode is considered as background for the $\beta\beta0\nu$ mode, it is better if its half-life is short. Another advantage is its high abundance, of 9% in ^{136}Xe; also, as it is a gas, is easy to enrich to higher levels. In terms of its nuclear structure it has a high phase-space factor and favourable nuclear matrix elements.

NEXT combines two of the technological advantages in the $\beta\beta0\nu$ decay searches. One is its promising good energy resolution, of around 1% FWHM at $Q_{\beta\beta}$ [159, 160]. On the other hand, a gaseous TPC can provide topological information of the track of the event using a pixelized detector. This allows to develop very efficient discrimination algorithms to separate between signal and background events. In order to evaluate the power of rejection in a pixelized TPC based on pattern recognition, Montecarlo simulations can be performed. This is one of the main points of this work and results are presented in Chapter 5.

The NEXT detection principle is based on the *SOFT* concept: Separated Optimized Energy Function from Tracking: it measures separately the energy and performs the reconstruction of the path of the event. In the experimental setup there will be two planes of detectors, as sketched in Figure 3.1. At one side of the field cage is placed a photomultiplier plane (PMTs) with which the energy will be measured, and on the other side a Silicon photomultiplier's plane (SiPMs) having enough pixelization to reconstruct the path followed by the event. In the PMTs plane is also determined the start-of-event time, to obtain the third dimension of the track.

The physical process and detection concept in NEXT is the following. Any particle interacting in the gas (signal or background) will produce a first scintillation light that will be detected in the PMTs plane and will give the start-of-event, t_0. As explained in Chapter 2, then an ionization process starts. The electrons produced are drifted by an electric field to an electroluminescence region. It consists of a gap of the order of few mm delimited by the SiPMs plane and two meshes, where a high voltage is applied to obtain an electric field of the order of few kV/cm in the gap. With these electric fields the atoms of the gas when excited by the electrons produce secondary scintillation light. This secondary light is measured both, in the PMTs plane and in the SiPMs plane. In the first plane to obtain the energy of the event and in the second one to reconstruct the track of the particle.

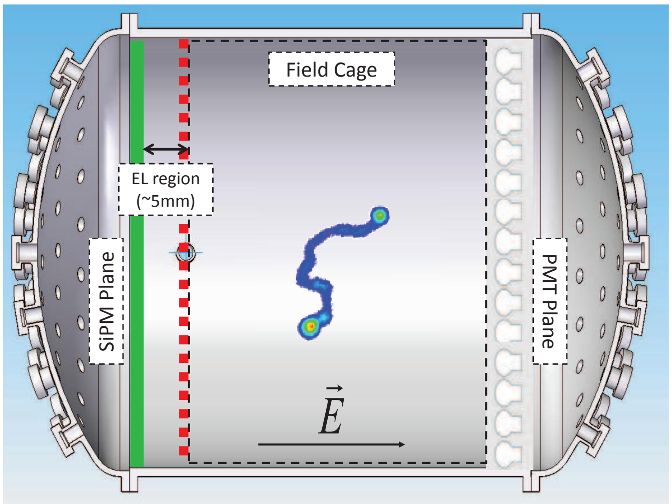

Figure 3.1: *Sketch of the different elements and the detection principle in the NEXT Experiment.*

Up today a Conceptual Design Report (CDR) [161] and a Technical Design Report (TDR) [162] have been developed as well as some technical papers related to prototype detectors that will be used [163, 164]. Moreover, a paper [165] summarizing all the work carried out by the collaboration to perform a radiopurity database with the radioactive contamination of materials to be used; some data comes from the literature but most of them by measurements performed with Germanium spectroscopy in the LSC or with other techniques like GDMS (Glow Discharge Mass Spectroscopy). In addition different works studying the expected energy resolution limit [166, 167] and studies about the electroluminescent process and yields in Xe gas were carried out [168, 169]. The collaboration has started to install the platform and the gas system in the main hall of the laboratory and it is currently taking data with several prototypes operating in different institutions.

One of them is NEXT-DEMO at IFIC (Instituto de Fisica Corpuscular de Valencia). This prototype is a cylindrical vessel made of stainless steel, with a fiducial volume of 30 cm drift and a diameter of 16 cm that can handle 0.34 kg of Xe at 10 bar. It has a PMT plane with 19 detectors and a SiPM plane. Its main purpose is to demonstrate the performance of the technological choice. First results with this prototype have appeared recently in [159]

Another prototype has been constructed at Berkeley, in LBNL, called NEXT-DBDM. NEXT-DBDM is an electroluminescent stainless steel vessel which main goal is to perform detailed energy resolution studies [160]. It is equipped with a plane with 19 PMTs.

Finally, an alternative method of signal multiplication, is the R&D project to use the TPC in a charge mode and readout the signal with a Micromegas detector. Although the decided baseline for the NEXT detector is an electroluminescent photosensor readout, the development of Micromegas is still motivated as a backup option or for eventual future extension to larger masses, due to the promising prospects for large areas offered by MPGDs. To investigate this option a third prototype has been constructed. It is NEXT-MM, and it is the detector used in this work. For this reason its characteristics and the detectors used will be explained in more detail in the next sections.

3.2 NEXT-MM

The experimental work was mainly done in the NEXT-MM prototype. In this section the experimental setup and the first operational tests performed to commission the detector before starting the data taking phase are presented.

3.2.1 Experimental setup

The setup can be divided into three parts: the vessel and its different internal elements, the acquisition system and the gas system. For the detector description a separate section (3.2.2) is presented.

The main objective of the prototype is to test Micromegas readouts under HP conditions in a chamber with a long drift distance (tests with MMs up to 10 bar were first done using a smaller chamber and results are presented in [170] and in [109]). For this reason the vessel, as well as the different elements, were designed to hold up to 15 bar. Also, they have been chosen to have a low outgassing rate to keep the purity of the gas as high as possible. Porous materials, as plastics, tend to have higher outgassing rates and have been avoided.

Another important characteristic for a neutrinoless double beta decay is the radiopurity of the detector. For the future phase of the experiment this requirement has been taken into account trying to test radiopurity solutions in NET1-MM, though it was not intended to be radiopure (mainly because the vessel is made by normal stainless steel), more of the technical options could be used in the final setup.

3.2.1.1 Vessel and internal components

The body of the vessel and the end caps are made out of 316-L stainless steel. The central body has a length of 53 cm and an inner diameter of 40 cm. The thickness is 1 cm and it was welded using conventional TIG welding (Tungsten Inert Gas). The end caps are flat and, as well as the body of the vessel, have several feedthroughs of different sizes to install the different equipment as the gas inlets or the readout wires. In picture 3.2 different views of the vessel can be observed. The assembling of the end caps and the different feedthroughs with the vessel body have been done using standard copper CF-F flanges to preserve the required conditions of HP and ultra high vacuum.

One of the main elements installed inside the vessel is the field cage to produce a constant electric field along the z coordinate that drifts the electrons until they reach the detector, as explained in Section 2.6.1.

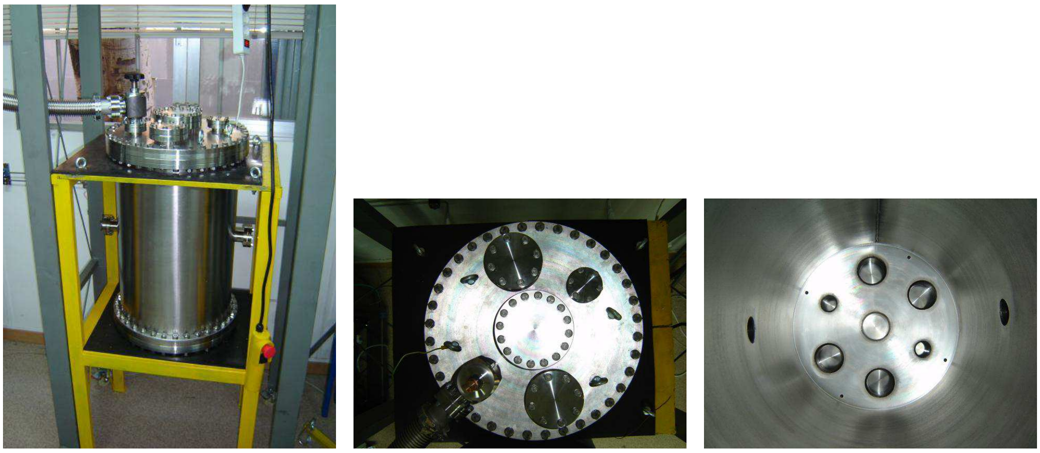

(a) (b) (c)

Figure 3.2: *(a)General view of the pressure vessel. The valves for the gas, as well as the super valve to insulate the system from a turbomolecular pump, and the structure, are shown. (b) External view of the upper end cap and (c) internal view of the lower end cap.*

The field cage consists of 34 rings connected between them by ceramic resistors (with a resistance of 10 MΩ each one). The rings are made of copper, they have an inner diameter of 30 cm and a thickness of 1 mm being the distance between them 1 cm. There is also a cathode made by copper; it is a disk with the same diameter as the rings and with a hole in the middle to position a calibration source. All these elements are joined together using 4 PEEK bars, defining a resistive volume with a diameter of 30 cm and a length which is 35 cm when operating with bulk detectors or 38 cm with microbulk detectors. With these dimensions it can handle 1 kg of Xenon at 10 bar. High voltage (HV) is applied to the cathode and the resistances along the drift produce a constant electric field along its direction. The last ring is connected to an external variable resistor to tune the field in the last cm (between the last ring and the detector) and homogenize it also there. After first tests, sparks were produced between the rings and the inner wall of the body vessel. Therefore a Cirlex screen has been placed along the higher two thirds of the field cage to insulate the system. Images of the field cage, the rings and the Cirlex protection can be seen in Figure 3.3. The other main component is the detector explained in detail in Section 3.2.2.

Different small elements have also been installed, mainly for the electronic connections and the HV supply:

- HV cables: the selected cable is made by copper as conductor and kapton as insulator. They fulfil two conditions: radiopurity and low outgassing rate. This wire is used to connect the mesh, the cathode, the last ring of the filed cage and other connections needed, to their corresponding feedthroughs. In order to avoid any soldering (usually with high contamination and producing air bubbles that translate into outgassing) different clamps and grips are used.
- Pixel readout cables: To read the pixel signal, flat cables are used. These cables are capable to read independently 300 lines without any soldering, because the connection between the cable and the detector is made through commercial solderless connectors. In our experiment connectors made basically by LCP (Liquid Crystal Polymer) and copper from Samtec are


(a) (b)

FIGURE 3.3: *A picture of the field cage in (a) and with the cirlex protection (b).*

used. The flat cables, or *limandes*, to readout the Micromegas are made by copper, Kapton and PCB, so in principle they can also be radiopure if selecting the appropriate batch of materials. A picture of the limande and the Samtec connector are shown in 3.8 (a) and (b) respectively. Different limandes were used, being the main differences between them the length and also the way the lines that do not connect to any pixel are grounded.

- HV feedthrough: To apply the HV to the cathode of the field cage, a feedthrough made of copper and Teflon has been developed that supply the required voltages. In order to work at 10 bar, 35 kV are required to have a field of the order of $1\,\mathrm{kV\,cm^{-1}}$ (Figure 3.4 (a)).
- Mesh signal feedthrough: Commercial 4-SHV connector feedthroughs have been installed in order to apply the operational voltage and extract the signal from the detector meshes, as well as to make any other necessary connections, for example, from the lowest ring of the field cage (Figure 3.4 (b)). Two of them have been installed. When operating the four microbulk detectors, 4 connections are needed to feed the mesh with voltage. Another one is used to connect to the last ring in the field cage.
- Pixels signal feedthrough: These feedthroughs are specially designed to fit the pixel readout cables connectors to them. They have been produced machining a commercial CF-63 port to hold a PCB board with the same profile as the connector (Figure 3.4 (c)). There are four of these CF flanges.

There are also some other small pieces that have been installed to fix the detector, the field cage and the other components. Although it is not essential to describe them in detail, it is important to mention that all of them have been fabricated using low outgassing materials like PEEK, cirlex or kapton, and that can also be radiopure [155, 165].

3.2.1.2 Gas system

The gas system of the experimental setup has to be able to recirculate and to purify the gas that is used and it has to work up to 10 bar. It can be divided into four subsystems: vacuum,

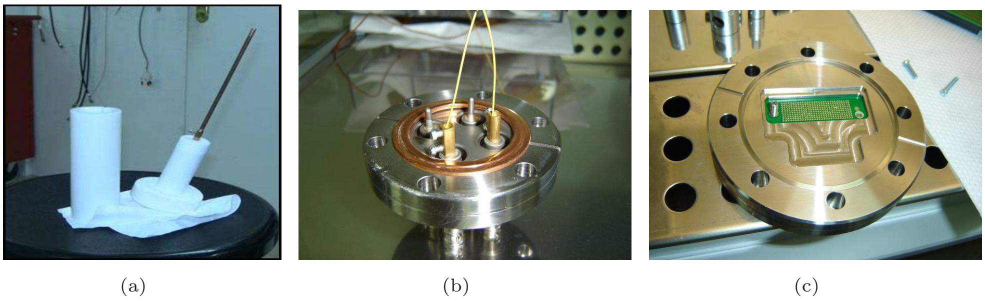
(a)

(b)

(c)

Figure 3.4: *Pictures of the different inner elements. (a) HV feedthrough to feed the cathode. It has been designed to hold up to 35 kV. It is made by Teflon and copper. (b) Commercial 4-SHV feedthrough for the needed low-voltage connections as the mesh signal or last ring signal. Two of these feedthrough was installed. (c) feedthrough for the pixel signal cables, specially designed to connect the flat cables using connectors instead of soldering.*

recirculation, purification and recovery. A sketch of the system and the different elements is showed in Figure 3.5 and in Figure 3.6 (c).

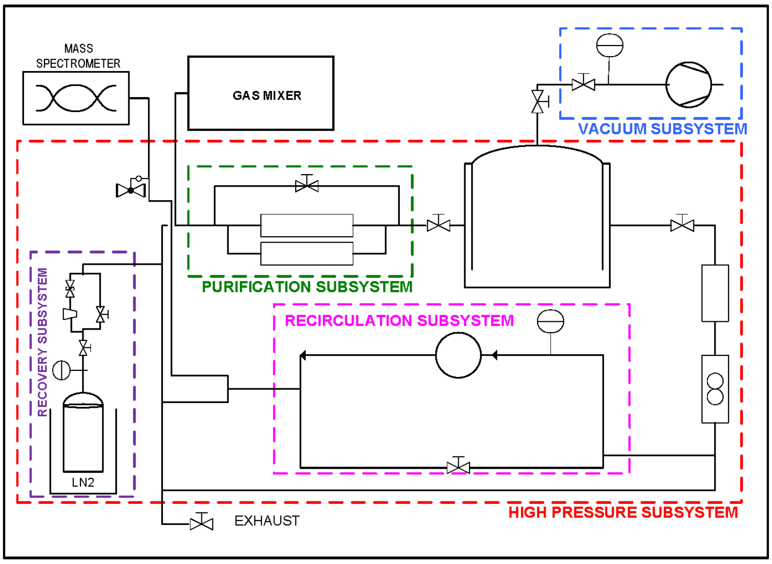

Figure 3.5: *Sketch of the gas system. Explanation of each subsystem can be found in the text.*

The vacuum subsystem consists of a turbomolecular pump that allows the system to reach pressure values down to 10^{-7} mbar. It is isolated from the HP subsystem by two consecutive valves: a vacuum valve and an all-metal one valve. The different elements are shown in Figure 3.6.

The filling of the TPC is done through the gas inlet. It can be done providing one gas (or a premixed gas) or a mixture of a gas with a maximum of three components. The mixer has three independent gas lines with Bronkhorst mass flow controllers. Usually it would be a base gas (a noble gas like Xe or Ar) and one or two quenchers. The base gas line is filtered by an Oxisorb before it enters the mixer. All the lines can be purged with N_2. In general, the quenchers used are in small percentage with respect to the main gas.

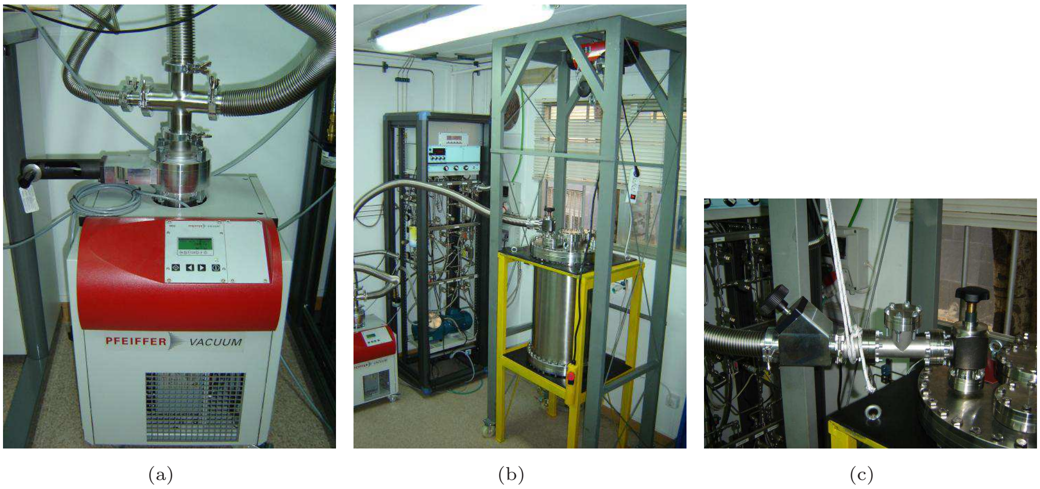

(a) (b) (c)

FIGURE 3.6: *Pictures of the different elements of the vacuum system: (a) the turbomolecular pump that allows to reach pressures values down to* 10^{-7}*. (b) Image of the vessel and the gas system. (c) Vacuum valve to isolate from the high pressure subsystem.*

The recirculation is done through a closed loop by means of a KNF membrane pump and it is pumped at maximum flow of $12\,\mathrm{l\,h^{-1}}$ in Ar. The recirculation flow is measured by a high precision flowmeter and the pressure in the vessel is controlled by a back-pressure controller. From the recirculation pump the gas can be forced to pass through a filter. Actually in the system a SAES 702 filter is installed, which removes water, vapour, and electronegative impurities (H_2O, O_2, CO_2) and it is compatible with trimethylamine (TMA). To control the purity of the gas a Pfeiffer OmniStar mass spectrometer has been added to the gas system via a low pressure gas line. The mass spectrometer is used to quantify not only the impurities but also the concentration of the quencher if a gas mixture is used, as for example, Xe-TMA.

The gas recovery subsystem for the Xe consists in a stainless steel cylinder of 2.2 litres that is immersed in a Dewar vessel filled with liquid nitrogen (LN_2) during the recovery process. The operational basis is the liquefaction of the Xenon that occurs at 165 K, higher than the LN_2 temperature of 77 K. With this procedure two things are possible: first of all the recovery of the Xe, and also, as only the Xe would be in liquid phase all the impurities can be pumped out because they would be in gas state. However, this is not the case with the TMA of which the liquefaction temperature is 156 K and therefore, would be in liquid phase also. In Table 3.1 are summarized the different temperatures of some important gases.

	LN_2	Xe	O_2	H_2	TMA	CH_4
Temp. (K)	77	165	54	33	156	113

TABLE 3.1: *Liquation temperatures for different gases.*

3.2.1.3 Acquisition system

The DAQ system of the prototype can be divided into two parts: one for the treatment of the mesh signal and the other chain for the pixels signal.

For the mesh, the signal is read by a pre-amplifier (PA), in this work, a Canberra 2004 PA, which also allows to supply the operational voltage to the Micromegas through the bias line. The PA output is sent through an RC low-pass filter to reduce the electronic noise. The preamplified signal is a measurement of the total energy of the event registered in the mesh, so it could be used as input in an amplifier module or used as trigger signal for the pixels acquisition. The amplified signal can be recorded by a multi-channel analyser (MCA) to obtain the spectrum of the mesh.

For the pixelized anode, the signals of each pixel are independently read using a reduced version of the T2K experiment electronics [171], that is based on the chip AFTER [172]. The imprint of the pads in the Micromegas is connected through a limande to the inner side of the feedthrough. Outside, another limande cable connects to an interface card designed on purpose to connect flexibly to a FEC card. The connection between the limandes, Micromegas and feedthrough is done using special high density contact Samtec connectors. In the case of a bulk detector there exist four points to do the connection to the pixels in the Micromegas and in the case in which the surface is covered with 4 microbulk detectors each one is read independently. Therefore, in both cases, the connection of the full surface of pixels is done through 4 of the following chains: (inner limande + outer limande + interface) to the FEC card. These FEC cards are connected to a FEM (Front-End Mezzanine) that concentrates the different signals and, through a Full Duplex Gbit optical, linked to a DCC (Data Concentrator Card) card RS232. The DCC is connected by Ethernet to the PC where the DAQ interface is installed. The FEM card has a capacity to read 1728 channels divided in connection to 6 cards through 4 ERNI connectors each one with 72 channels per ERNI ($6 \times (72 \times 4)$ channels can be read independently). A schematic view of the chain is shown in Figure 3.7 and a picture of each element is presented in Figure 3.8.

The acquisition trigger for the pixels is given through the DCC card. It is a positive TTL signal. Several possibilities have been used for the trigger of the pixels. Most of the data are taken in self-trigger with the mesh signal. In this case the mesh signal is sent to a Low Level Discriminator (LLD), either from the PA or from the amplifier. The signals that go beyond a given voltage threshold are sent to a NIM-TTL converter and then to the DCC (the trigger must be a positive signal, if it is necessary, it is switched in the NIM-TTL module). Other options are possible, as for example, to send an external trigger signal, if we want to measure in coincidence with another setup. This option is explained in more detail in Section 4.4.

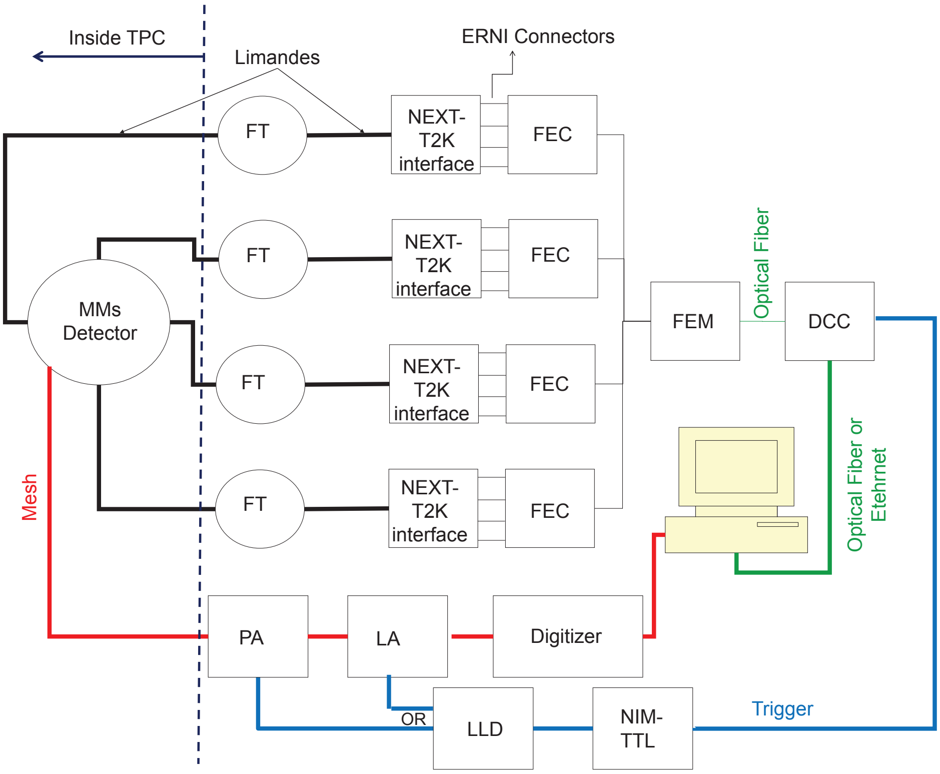

Figure 3.7: *Conceptual sketch of the acquisition system of the prototype. In black the chain for the pixels signal to the T2K electronics. In red the mesh signal is shown, that can also be used as trigger for the pixels (blue line).*

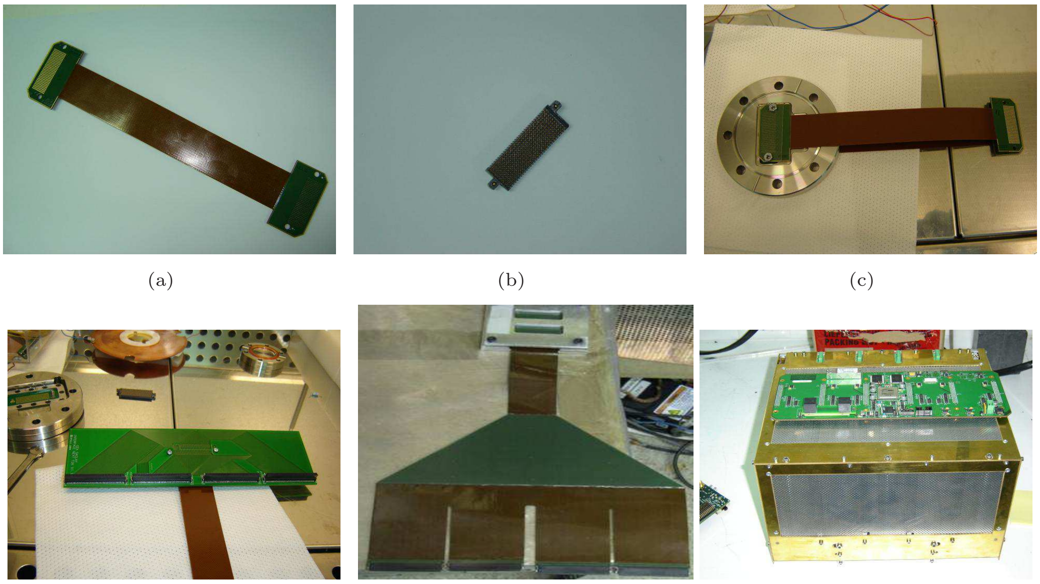

(a) (b) (c)

(d) (e) (f)

Figure 3.8: *Pictures of the different elements of the electronic chain to read the pixels. (a) Flat cable, or limande, to transport the pixels signals. (b) Samtec connector that is used between the Micromegas and the limande and between the different limandes. (c) feedthrough that transport the signal from inside to outside the vessel with the two limandes connected. (d)(e) Interface cards used that connects to the FEC card. (f) FEM card connected with the FEC cards in a Faraday cage.*

3.2.2 The Micromegas Detectors used

The detectors used in NEXT-MM are Micromegas detectors. As it was explained in detail in Section 2.6.2, they have an amplification gap between a mesh and an anode plane of the order of few μm where a high electric field produces an avalanche of electrons that can be detected in both sides. Two different technologies were used in NEXT-MM, the bulk and the microbulk.

Bulk detector

The first detector installed inside NEXT-MM was a bulk Micromegas. It had a diameter of 30 cm, with a gap of 50 μm, mesh holes diameter of 35 μm and a pitch of 100 μm. It covered all the sensitive surface of the prototype as shown in picture 3.9 (a). The anode was pixelized in 1152 independent pixels, as it could be seen in the design presented in Figure 3.11, of 0.8×0.8 cm^2 each one.

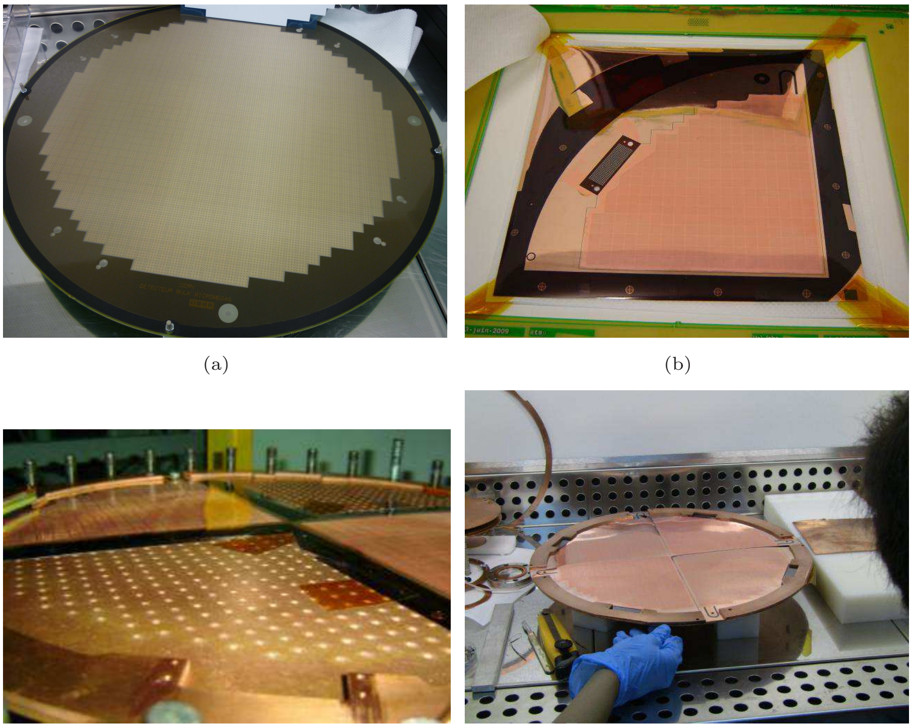
(a) (b)

(c) (d)

FIGURE 3.9: *Micromegas used (a) Bulk detector (b) Microbulk detector. Four equal detectors have been designed in order to cover all the NEXT-MM surface. (c) Installation of two of the microbulk detectors. They are placed over a copper plate, the external ring not only fixes the detector but also connect the rim lines to a voltage a bit higher of the mesh to avoid dead space (see text for more details). (d) Installation of the four microbulk detectors.*

Microbulk detector

Up to today limitations exist in the fabrication procedure for a Microbulk, and only detectors with a diameter up to 20 cm can be done. For this reason, to cover all the active surface of the detector, four identical sectoral detectors, with the shape of a quarter of a circle, were manufactured (Figure 3.9 (b)). They are made with the microbulk technology with a radius of 15 cm, and a gap of 50 μm, mesh holes diameter of 35 μm and a pitch of 100 μm. The tolerances achievable in the assembly of the neighbouring modules can be well below the mm. However, no dead zone is allowed in the readout if we want to keep high energy resolution. This is achievable by means of the *rim* concept. In each detector, around the mesh, an independent strip of about 100 μm is engraved in the same process of the mesh manufacturing. This strip "surrounds"the mesh and if powered independently with a voltage a bit higher than that of the mesh, the field lines of the drift region (and therefore, the drifted electrons) in the border of the surfaces of each detector are pushed towards the sensitive surface. In addition, the deformation of the drift lines is much less than the pixel size, so there is no consequences on the topology information. We can see a simulation done with COMSOL of this effect in Figure 3.10. Then border effects in the field lines and dead space between the detectors are avoided.

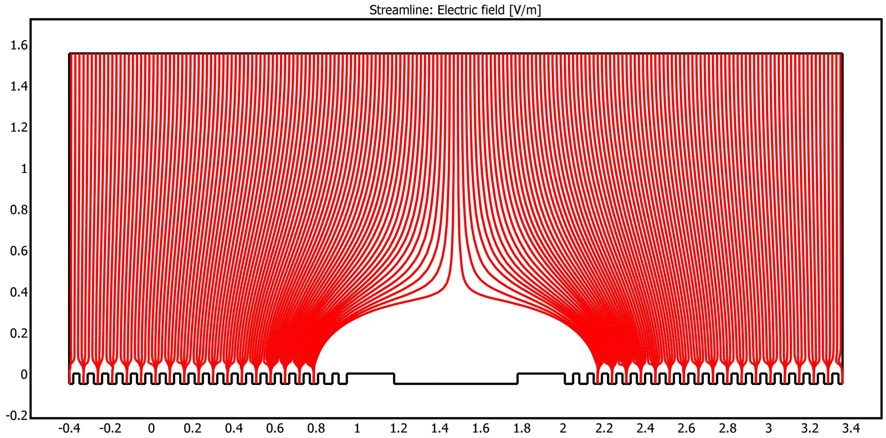

FIGURE 3.10: *Comsol simulation (2D-approximation) of the rim effect described in the text for the drift lines around the boundary between two microbulk detectors. In this simulation the rim (a 200 μm metallic strip placed at 200 μm from the active region of the Micromegas) was placed at -255 V while the mesh was with a voltage slightly lower (-250 V). The Micromegas anode is grounded and the drift field was of 100 V cm^{-1}. It can be seen how the drift lines are gently pushed into the active area of the detectors, while if the rim is at 0 V would have fallen on the dead area between Micromegas. Dimensions are expressed in mm being the overall distortion below this scale.*

The four detectors in NEXT-MM are placed on top of a copper plate grounded. Four copper pieces, as 4 quarter rings, are used to screw the Micromegas to the plate using PEEK screws. It is done in the insulator part of the detector. In this way movements when placing inside the prototype or when pumping the detector are avoided. Moreover they help to unify the surface of the detectors. These copper pieces are electrically connected between them and connected to the *rim* line described before. Therefore, applying a voltage to the ring the field in the boundary of the detectors is unified. A picture of the plate with two microbulk detectors installed and one with the four is shown in Figure 3.9 (c) and (d)).

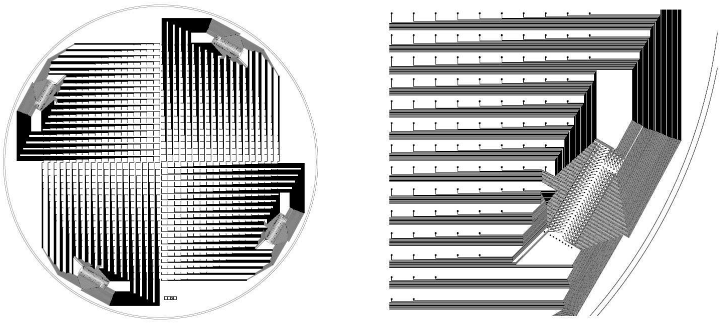

Figure 3.11: *Design of the pixels distribution and routing for the pixelized anode of the Bulk Micromegas (a). In (b) detail of the routing at the level of one of the four connectors prepared for the signal readout. The routing of the microbulk Micromegas used and described in the text, is equivalent to one quarter of the bulk design.*

3.3 Operational tests with NEXT-MM prototype

Different operational tests were done before starting the acquisition phase in order to check the performance of the setup and the capability of it to reach the values of HP, vacuum and HV needed to operate with the detector in Xenon. The results are presented in the next subsections.

3.3.1 High pressure test

The vessel is constructed to be able to hold up to 15 bar. A pressure test in pure Argon was done in order, not only to verify the specifications assured by the manufacturer, but also to test the sealing, the capability of the different feedthroughs and valves installed and the capability of the gas system described in Section 3.2.1.2 to hold up to more than 10 bar. The pressure of the system as well as the temperature were monitored for 11 days after placing 11 bar of pure Ar in the chamber. In Figure 3.12 the evolution of the pressure and the temperature during these days is shown; the small oscillations of the pressure are correlated with variations in the temperature so if the ratio $P/T{\times}T_{mean}$ is plotted (Figure 3.12 (b)) the pressure is constant during all the tests, taking into account the uncertainties in the measurement of P and T. Moreover, the best linear fit of the recorded data limits the possible leak of the system to be $< 5.9 \times 10^{-4}\,\mathrm{mbar{\times}l{\times}s^{-1}}$, value that is limited by the accuracy of the high pressure nanometer.

3.3.2 Vacuum and outgassing

Another important parameter is the vacuum that the system can be pumped down before filling it with gas. A good vacuum assures the system has no leaks and allows to keep the purity of the gas as high as possible, even if a recirculation through filters is done. In addition, the outgassing of some of the impurities trapped in the inner materials can also degrade the purity of the gas, as mentioned in (2.2.2). Therefore, the vacuum reached could change after the installation of new elements inside the vessel.

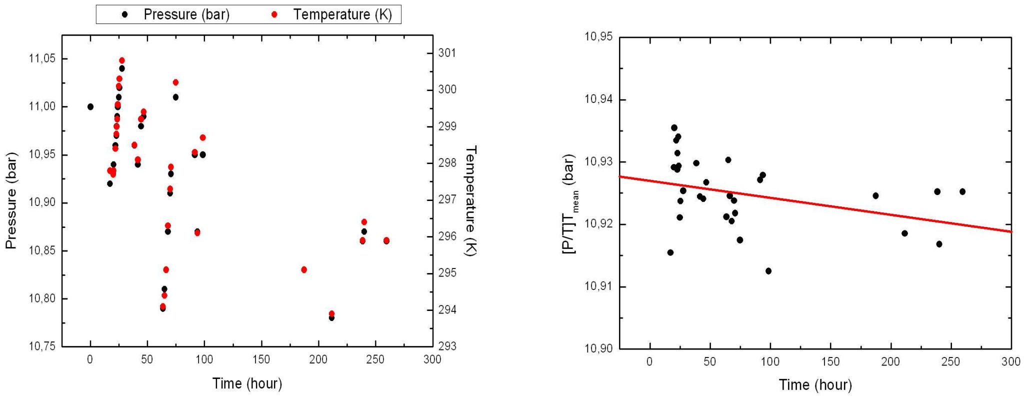

(a) (b)

Figure 3.12: *(a) Evolution of the pressure (P) and temperature (T) during a HP test done with the vessel fill with Ar at 11 bar. The variations of the pressure are related with environmental changes in the temperature. (b) Evolution of the ratio P/T normalized by the mean temperature along time. A variation of less than 1% is observed. However, the tendence to decrease shows a possible leak rate below* 5.9×10^{-4} *mbar×l×s^{-1} and is conditioned by the accuracy of the high pressure manometer.*

A way to accelerate this outgassing and reduce it before injecting gas inside the vessel is to do a heating process. This process is called *bake-out* and consists in heating up the system in vacuum and keep pumping it at a high temperature. During the heating the emanation process is increased and the impurities are released from the materials more quickly. After several hours the heaters are switched off but not the pumping. Usually the pumping continues at least until the temperature goes back to ambient temperature. The outgassing is calculated as the difference in pressure over time and volume ($\Delta P \times Volume/\Delta t$) and is expressed in mbar l s^{-1}.

In order to heat the vessel, several resistors are attached to the outer wall of the vessel. They are surrounded by an insulator coat to keep the heat, we can see a picture of the device in Figure 3.13. The heater operation is centralized in a programmable control unit that allows to go up to 200 °C. This temperature is enough for our system but, at the end, is limited by the thermal resistance of the inner components, specially the Micromegas detector which is not convenient to heat up to more than 150 °C

This process was first done with the vessel empty and was repeated after the installation of any new element in the vessel. The first elements to be placed were those with higher heating capacitance allowing to make the first bake-out cycle at higher temperatures. Before the first bake-out cycle, the empty vessel was pumped with all the metallic seals installed in order to obtain a reference value for the vacuum that could be reached. After 95 hours of pumping a pressure of 7.8×10^{-7} mbar was obtained, which is in good agreement with the vacuum certification from the manufacturer.

Results for the different outgassing rates after the installation of different elements are summarized in Table 3.2. The main parameters are: the time the system is heated and pumped simultaneously (heating time) and the temperature and the time the system is pumped after the heating system is switched off (pumping time). Even if the cycles are not comparable (since the


(a) (b)

FIGURE 3.13: *(a) Bake-out system: different resistors are connected to the vessel to warm it up. It is surrounded by an insulator coat. The temperature can be controlled with a programable unit that fix it (b).*

temperature and times are not equivalent) the obtained results show that the longer the bake-out time is for the common components (like the vessel or the field cage), the better outgassing rates are obtained, even if more new components have been installed. This phenomenon leads to think that regular bake-out cycles could be necessary to keep or even improve the outgassing rates reached in the prototype.

The last bake-out cycle was done with the full setup installed that corresponds to the detector, the field cage with the resistors and the cirlex protection and all the necessary internal cables and the required feedthroughs described in 3.2.1.1. For the full system the outgassing rate obtained is 4.5×10^{-7} mbar×l×s^{-1}, a value that seems enough to assure the purity conditions of the gas, specially if the recirculation of the gas is done.

Components	Heating time(h)	Heating T(°C)	Pumping time(h)	P_0 (mbar)	Outgassing (mbar×l×s^{-1})
Empty Vessel	140	180	26	7.4×10^{-7}	4.7×10^{-7}
Field Cage(F.C.)	100	155	17	3.8×10^{-7}	3.4×10^{-7}
F.C. + Resistors	113	150	6	9.8×10^{-8}	5.9×10^{-8}
F.C. + Resistors+ Bulk MMs	94	160	144	6.1×10^{-8}	3.2×10^{-8}
Full Setup	112	150	11	7.6×10^{-7}	4.5×10^{-7}

TABLE 3.2: *Summary of the bake-out cycles carried out in NEXT-MM prototype. In the table are indicated the components in the vessel (see text for explanation of full setup), and the main variables as well as the obtained outgassing rate measured for each case.*

3.3.3 High voltage tests

Another important point is to check the application of HV in the drift region. The optimal drift field for the electrons at 10 bar is of the order of $\sim 1\,\mathrm{kV\,cm^{-1}}$, therefore, in order to reach this electric field, the voltage that should be applied to the cathode at 10 bar is 35 kV, taking into account the drift distance. A HV source is connected to the cathode through the HV cable and feedthrough described in Section 3.2.1.1. The possible problem is that discharges could appear in any point between the cathode, field cage, resistors and the vessel, if a good insulation is not performed. Some protections were already installed like the cirlex screen between the field cage and vessel (see Figure 3.3) or Kapton scotch to cover any sharp point and avoid such discharges. A break point is defined as the voltage when the current begins to be higher than expected (based on the total impedance of the field cage), which indicates that some derivation to mass, mainly to the vessel, is happening. To study the breakpoint in the system, the electric current passing through the field cage has been monitored while the voltage was increasing. This test has been carried out for different pressures, up to 8 bar, using pure Argon. Results are shown in Figure 3.14. In Figure 3.14 (left) the evolution of the current with respect to the applied voltage is plotted for each pressure and, in Figure 3.14 (right), the curve for the different break points obtained in pure Ar for different pressures is shown. The trend of the points show that at 12 bar, 35 kV can be reached in pure Ar. In the case of Xenon the break point is approximately 2 times better [173] than for Ar, which allow to think that these voltages could be reached at pressures higher that $4 - 5$ bar.

Other elements where a voltage has to be supplied is in the Micromegas detector. For the Micromegas a standard SHV feedthrough is used that allows to supply up to 3.5 kV, being much more that the operational voltage for the MMs (usually between $100 - 500$ V, depending on the pressure and gas). Hence, the ramping up of the voltaje in the Micromegas does not present a problem.

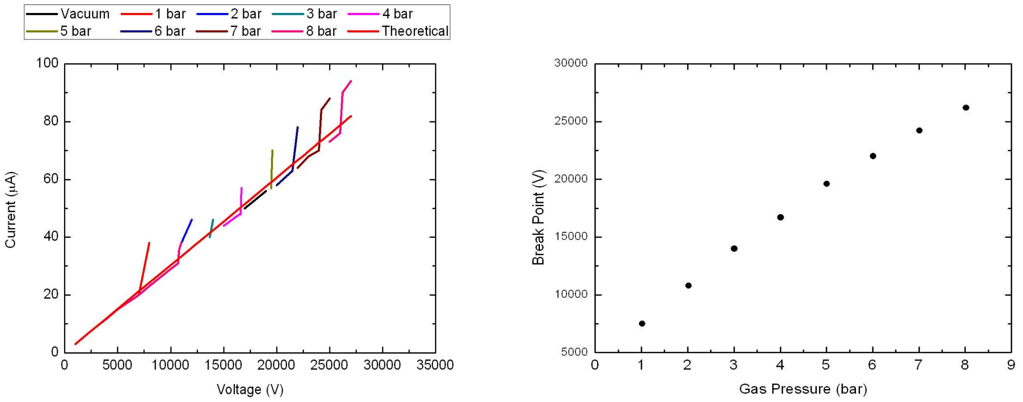

FIGURE 3.14: *High voltage tests. In the left it is shown the current evolution for each voltage and each pressure and in the right it is shown the break point evolution for each pressure. It can be seen how a higher pressure the break point occurs at higher voltages. Also it fits with the theoretical line. All data were taken in pure Argon.*

3.4 Main features of the detectors in Ar-isobutane: gain curves and first energy resolution estimations.

Before installing the detectors in NEXT-MM, a full characterization is done in a smaller chamber specifically designed to develop fast tests of the Micromegas detectors. It has a lateral length of 18 cm and is made of stainless steel of 1 cm thickness. Inside the field cage, it is installed a field cage in the same way as in NEXT-MM but smaller (16 cm) and without the cirlex protection because smaller voltages are applied to the cathode. A picture of the detector and its field cage is shown in Figure 3.15 (a) and (b). There are two possible calibration positions for the sources centred in two of the detectors as it can be observed in Figure 3.15 (b). This chamber is not expected to work at HP because it is not leak tight; for this reason Xe is not used.

The performance of the Micromegas detectors was studied in Ar-isobutane (Ar-iCH$_4$) at 2%. This gas is a good point to start checking the detectors because the Micromegas are usually tested on it, and a lot of data exists to compare the behaviour of the detectors with the standard ones before installing in NEXT-MM. The gas was in a continuous flow of 5 l/h and at 1 bar; data taking starts after few hours of circulation to assure the purity of the gas inside the chamber.

Particle	Energy (keV)	Intensity (%)
X-Ray	3.15	2.64
X-Ray	21.99	29.5
X-Ray	22.16	55.7
X-Ray	24.91	4.76
X-Ray	24.94	9.2
X-Ray	25.45	2.30
γ	88.04	3.61

TABLE 3.3: *Summary of the emissions from the ^{109}Cd. It is shown the nature of the emission, its energy and intensity.*

All the tests were done with a ^{109}Cd calibration source placed in one of the designed positions. In Table 3.3 are summarized the main emissions from this source. The four microbulk to be installed in NEXT-MM were characterized two by two. They are labelled as MM1, MM2, MM3 and MM4. Unfortunately, MM3 behaved strange and no peaks were recorded. However, when installed in NEXT-MM it recovered. The main problem in this small chamber was the noise level for the detectors. An extra problem comes from the limitation in the drift voltage, sparks start at around 3000 V.

The drift voltage was applied using a Spellman HV power supply and the mesh voltages using a CAEN N471A module. The signal amplified in the Micromegas is read from the mesh using a CANBERRA 2005 PA. The PA output is fed to a CANBERRA 2022 amplifier module with a shaping time of 8 μs. Subsequently it is fed to a multichannel analyser AMPTEK MCA-8000A that produces the pulse height distribution proportional to the signal amplitude.

In this part of the work the data used are the signals from the mesh. The recorded spectrum with the MCA (in ASCII) is converted into a ROOT file. It is then analysed using a C++ macro. In this analysis, the 22.1 keV gamma peak is used to obtain the gain and energy resolution. The procedure is as follows. First, a Gaussian fit is done in the peak. Then a background is estimated fitting to a line. The final fit is done convoluting two Gaussian, one at 22.1 keV and another at 25 keV, with the linear background. In the second fit the parameters from the first Gaussian are used. To fit the 25 keV the amplitude is calculated in function of the amplitude at 22 keV by the relative intensity of the two gammas. The errors obtained with the analysis in the peak determination are less than 2% and in the FWHM of the peak less than 0.1%.

During the characterization, the pixels are grounded connecting them to the acquisition explained in 3.2.1.3 and the pixels signals are not used for the characterization of the detectors but the data registered were used to obtain the 2D information of the events.

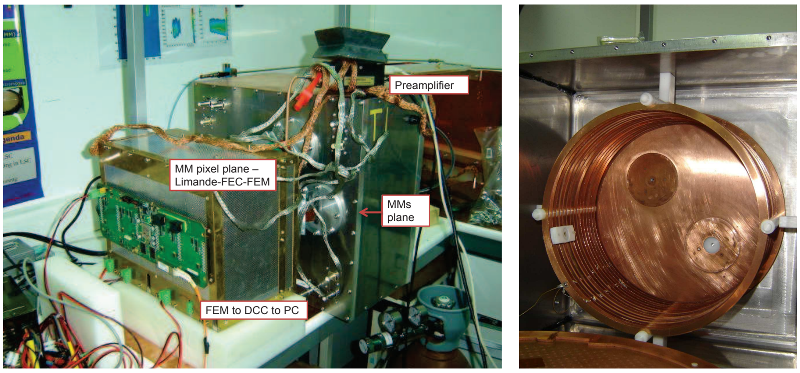

(a) (b)

FIGURE 3.15: *Chamber specifically designed to test microbulk Micromegas at 1 bar before installing them in NEXT-MM. (a) Setup. The Micromegas detectors are placed perpendicular to the floor. They are fed with a CANBERRA pre-amplifier and the signal from the mesh is obtained from the bias output.(b) Field cage made by copper rings. The two designed calibration position in the cathode at 16 cm from the detectors can be seen.*

3.4.1 Electron transparency

First of all, the electron transmission curves were obtained. The procedure is to vary the drift voltage at a fixed mesh voltage to obtain the transparency of the mesh to primary ionization. In Figure 3.16 is shown the relative electron transmission as a function of the drift to amplification field ratio. Data were obtained in the plateau where the transmission is maximum. At higher drift voltages the electron transmission is expected to decrease because the drift field lines start to end in the mesh instead of passing through the holes. However, this region could not be reached because sparks started appearing at the drift early. The results are in concordance with previous results with a microbulk in Ar-isobutane at 2% [150].

3.4.2 Absolute Gain

The evolution of the peak position with the mesh voltage gives the gain curve. For each voltage in the mesh, the drift voltage was selected to be operating in the plateau and always with the same ratio of drift-to-amplification fields. In order to calculate the absolute gain from the position of the peak in the spectrum, it is necessary to take into account different factors from the electronic chain.

Firstly, the amplification gain introduced by the pre-amplifier (F_{PA}). It depends on the model used, in this case the CANBERRA 2005 PA was in the position where a factor of 9 mV/e$^-$ was applied (F_{PA}). It can be interpreted as the conversion factor convert charge (e$^-$) to mV. Then, the amplifier factor (F_A) has also to be taken into account. The peak in the MCA is given in mV/channel. The number of charges created by the incident particle is calculated using the

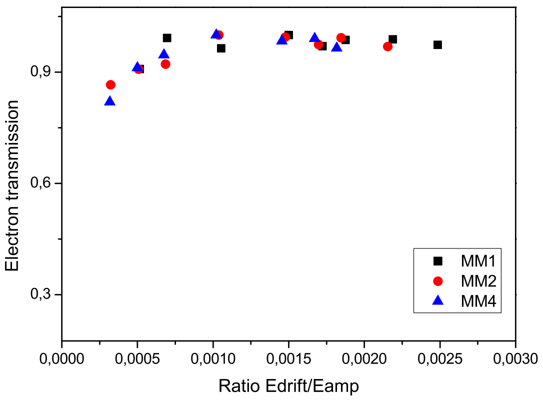

FIGURE 3.16: *Electron transmission of the detectors as a function of the ratio of drift-to-amplification fields in Ar-isobutane at 2%. The different set of points correspond to the different detectors studied: black square points for MM1, red circles for MM2 and blue triangles for MM4.*

W-value of Argon. For the 22.1 keV in Ar, 850 e^- are produced. Finally, the absolute gain can be obtained using

$$G = \frac{MCA_{peak}\,(mV)}{F_{PA}\,(mV/e-) \times F_{Ampli}} \times \frac{W\,(eV/e-)}{E\,(eV)}. \tag{3.1}$$

The results for each Micromegas are shown in 3.17. MM1 and MM2 have similar gains, obtaining a maximum of 6×10^2 before sparks in both detectors. Moreover, detector MM4 shows a gain 3 times higher, obtaining a maximum of 3×10^3. With respect to previous Micromegas studies [150], the values in any of these detectors are much lower than those measured before, between 10-20 times smaller. However, they are the first and unique microbulk detectors of these dimensions constructed up to now and some imperfections can due to it, as well as they can be improve after improving the manufacturation technique.

3.4.3 Energy resolution

The energy resolution is obtained from the Gaussian fit to the 22.1 keV gamma of ^{109}Cd. A typical spectrum for each Micromegas is shown in Figure 3.18. The peak at the lowest energy corresponds to the 8 keV peak from the copper fluorescence, coming from the field cage made by copper rings. The main one corresponds to the 22.1 keV X-Ray. Each spectrum in Figure 3.18 was obtained at the highest gain in the mesh. The mesh and drift voltage were (335 and 2950 V), (330 and 2400 V), (340 and 2500 V), for MM1, MM2 and MM4, respectively.

The results obtained for the energy resolution in % FWHM varying the amplification field are shown in Figure 3.19. The best result corresponds to an energy resolution of 14% FWHM at 22.1 keV when the amplification field was of the order of 68 kV/cm. The drift field was of 120 V/cm. The three distributions of points show the same behaviour (excepting the first point in the set from MM2). Therefore, it is expected that at the same mesh voltages all the detectors

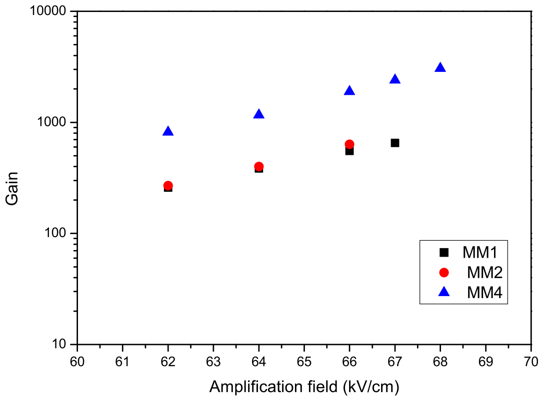

FIGURE 3.17: *Gain of the detectors as a function of the amplification fields in the Micromegas, in Ar-isobutane at 2% at 1 bar. The gain increases with respect to the amplification field polynomially, obtaining gains of the order of 500-1000 from one detector to another. The different set of points correspond to the different detectors studied: black square points to MM1, red circles to MM2 and blue triangles to MM4. The higher values are obtained just before the spark limit.*

could obtain similar values for the energy resolution. The differences observed in the amplitude for the 8 keV peak between spectrum are due to the position of the source.

3.4.4 Cosmic Rays

A run detecting cosmic rays was also obtained. The position of the Micromegas in the chamber is perpendicular to the ground, hence the vertical muons that cross the chamber leave a long track in the detector. Two examples are shown in Figure 3.20. The data were recorded at 1 bar in Ar-isobutane at 2%. The topological information is provided by the pixels signal.

The energy spectrum obtained is shown in Figure 3.21; it is the typical one obtained in surface. The peak corresponds to the vertical muons (incident angle $\theta = 0°$) that, in this gas and with the drift distance of 18 cm is of the order of 40 keV and the tail in the right corresponds with the muons that cross the chamber with θ different to zero. The slope is proportional to $cos\theta^2$. In Figure 3.21 can be seen the obtained spectra after rudimentary rejection of the cosmic rays. The peak corresponds to the 14 keV emission of ^{57}Co, source installed during these measurements.

3.5 Commissioning of the detectors and the electronics in NEXT-MM

Once the performance of the detectors has been tested in the small chamber, they are installed in NEXT-MM. Before measuring in pure Xe a commissioning of the Micromegas is done with the usual gas mixture of Argon-Isobutane at 2%. These tests were done in NEXT-MM and were used to prove, not only the detector performance, but also the electronic chain operation. First

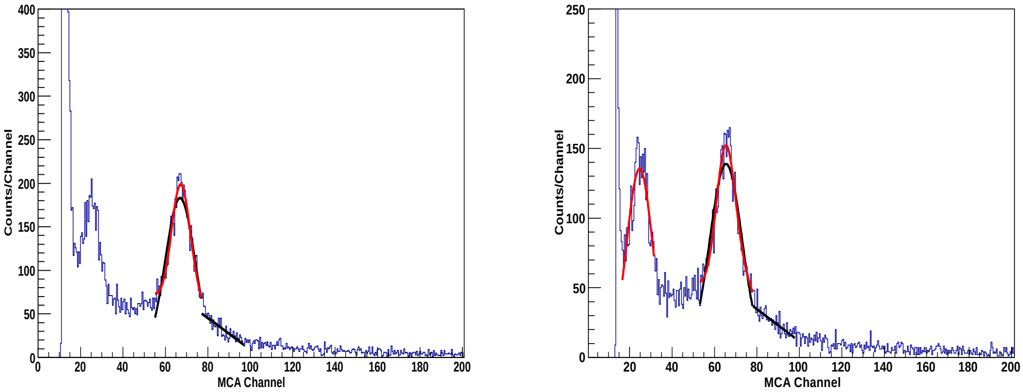

(a) MM1

(b) MM2

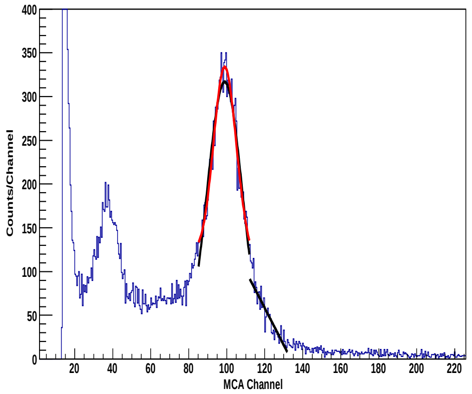

(c) MM4

Figure 3.18: ^{109}*Cd X-Ray spectrum, the 22.1 keV peak is observed and also the 8 keV fluorescence line from Cu. (a) Spectrum in MM1, at 335 V in the mesh and a drift voltage of 2950 V. (b) Spectrum in MM2, at 330 V in the mesh and a drift voltage of 2400 V. (c) Spectrum in MM4, at 340 V in the mesh and a drift voltage of 2500 V. In the three cases data was recorded in Ar-isobutane at 2% and in 1 bar of pressure.*

of all the bulk detector was installed and then the performance of the four microbulk detectors were also evaluated with an alpha source.

3.5.1 Bulk detector: First Results

The first set of data were obtained with the bulk detector in Ar-isobutane at 2%. The idea was to develop a fast run to test the operability of the TPC, hence a ^{222}Rn coming from a ^{226}Ra source was diffused in 1 bar of the premixed gas. The operational voltages for this run were 8000 V in the cathode (229 V cm^{-1} in the drift region) and a voltage in the mesh of 250 V, that induces an electric field of 50 kV cm^{-1} in the gap.

The signal from the mesh was measured and also used to trigger the pixel acquisition. In Figure 3.22 the spectrum is presented with the three expected alpha peaks (at 5.5, 6.0 and 7.7 MeV). From this signal, the rate evolution of the 5.5 MeV peak is monitored in Figure 3.23 and it is observed how this evolution fits with the ^{222}Rn half-life which value is 3.8 days.

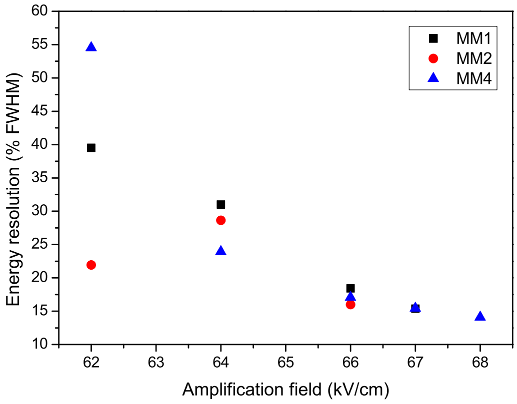

Figure 3.19: *Dependence of the energy resolution (% FWHM) with the amplification field for the three detectors studied. Value obtained with a two-step Gaussian fit to the 22.1 keV X-ray peak. The different set of points corresponds to the different detectors studied: black square points to MM1, red circles to MM2 and blue triangles to MM4.*

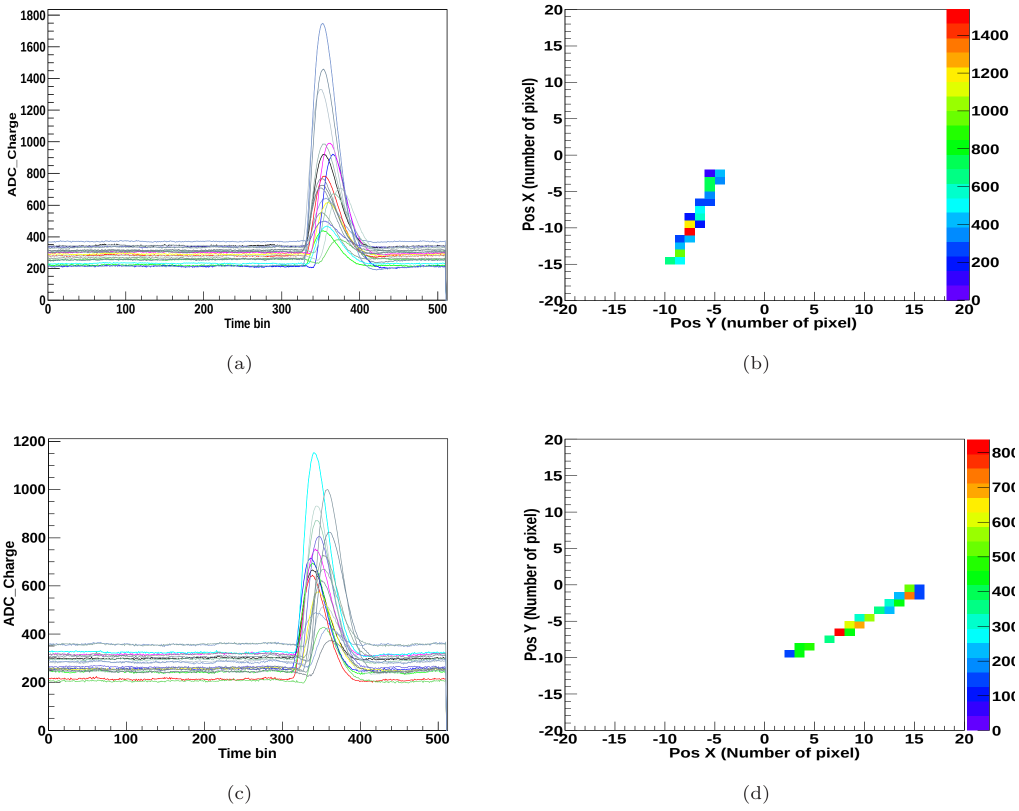

(a)

(b)

(c)

(d)

Figure 3.20: *Example of two vertical muons that cross all the detector. The Micromegas is placed perpendicular to the ground. The data was obtained in Ar-isobutane at 2% at 1 bar.*

3.5.2 Microbulk detector: First Results

First data with one of the microbulk detector were obtained also in Ar-iCH$_4$ at 2%. In this case an ^{241}Am source was installed at 8 cm from the detector and centred using a designed calibrator shown in Figure 3.24. Data was obtained only from pixels using the mesh pulse as trigger for

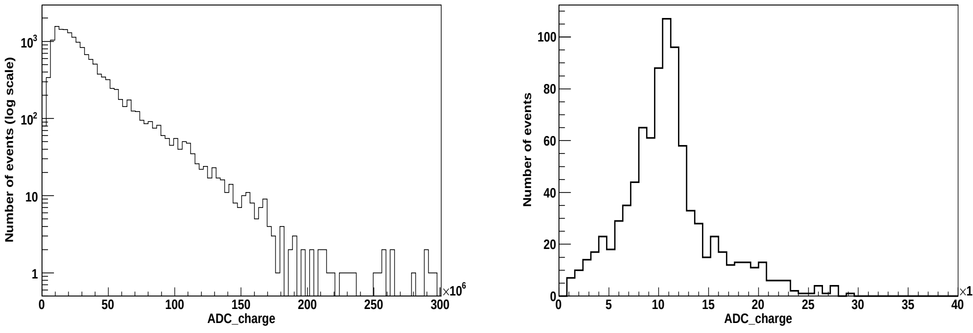

(a)

(b)

FIGURE 3.21: *Spectrum obtained in a run dominated by the background (mainly cosmic rays). An example of the tracks of the events are shown in Figure 3.20. In (b) is shown the structure of peaks that start to appear after rejecting the background (events that touch more than 10 pixels).*

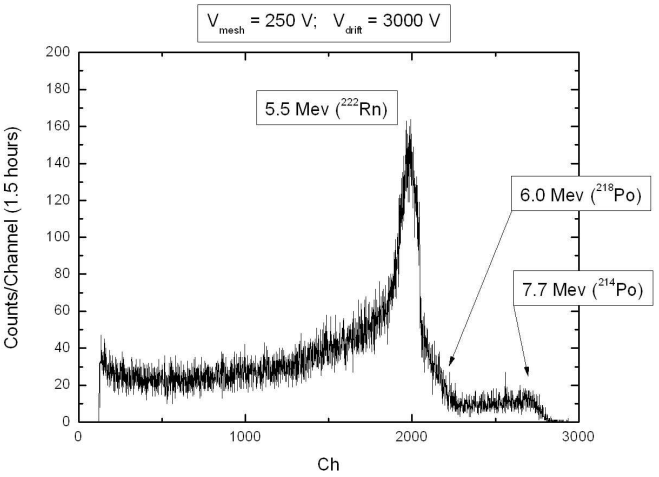

FIGURE 3.22: *Energy spectrum obtained reading the mesh, in arbitrary units, with a bulk detector installed in NEXT-MM. It was obtained in Ar-iCH$_4$ at* 2% *at 1 bar and with a* ^{222}*Rn source diffused in the gas. The three alphas from* ^{222}*Rn are observed at 5.5, 6.0 and 7.0 MeV.*

the acquisition. In Figure 3.25 the obtained spectrum reconstructing the signal in the pixels is displayed. The connectivity in the pixels was not more than 50% in this run, so the spectrum is plotted selecting an XY region were the connectivity was higher. Even in these bad conditions, and due to the fact that the expected track for the alpha of 5.5 MeV in Ar at 1 bar is of the order of 5 cm, a first result regarding energy resolution is obtained, of a $5.07 \pm 0.14\%$ FWHM. The objective of this test was to prove the pixel acquisition performance and to obtain the first tracks. In figures 3.26 and 3.27 the track in the peak and at higher energies are shown, respectively. The events at high energy are due to pile up events. As we can see the tracks are of the expected length (5 cm) mentioned before. This is also justified with the distribution of the number of pixels shown in Figure 3.28.

These first tests allow us to conclude the good performance of the Micromegas detectors as well as of the pixel acquisition system and the operability of NEXT-MM. The next step is the

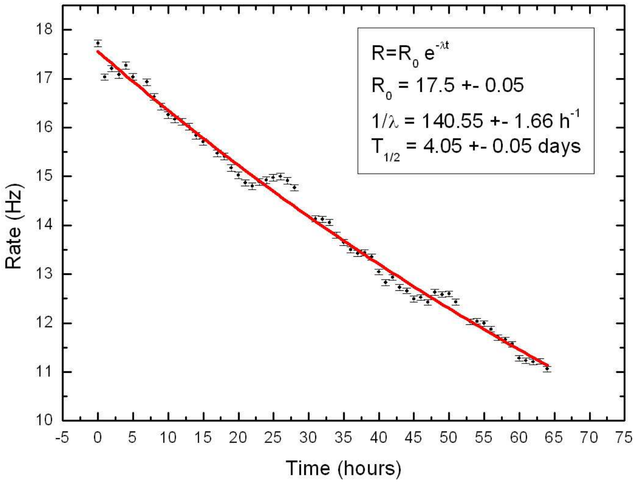

Figure 3.23: *Evolution of the rate of the peak corresponding to the 5.5 MeV alpha with time. If the data is fitted to an exponential function we obtain approximately the half-life of the ^{222}Rn (3.8235 d).*

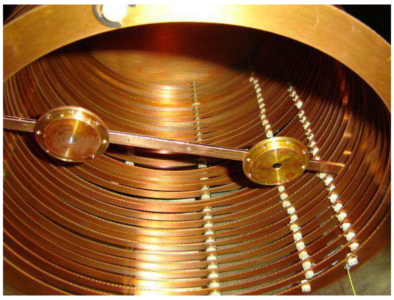

Figure 3.24: *Position of the ^{241}Am in a designed calibrator positioned at 8 cm from the detector.*

use of a Xe base gas in NEXT-MM. In the next chapter a detailed presentation of the analysis framework developed as well as a systematic study of the tracks obtained in Xe-TMA in different configurations will be presented. Moreover, results in energy resolution will be discussed.

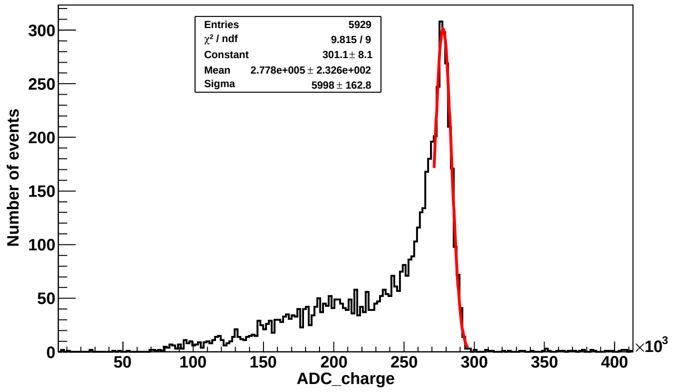

FIGURE 3.25: *Distribution of the charge recorded in pixels, in acquisition units, in a microbulk detector installed in NEXT-MM. It was obtained in Ar-iCH$_4$ at* 2% *at 1 bar and with an* ^{241}*Am source. The peak corresponds to the alpha emission of the source at 5.5 MeV. The distribution at the left is due probably to a bad recollection of the charge because the connectivity was low. The distribution at higher energies is due to pile-up.*

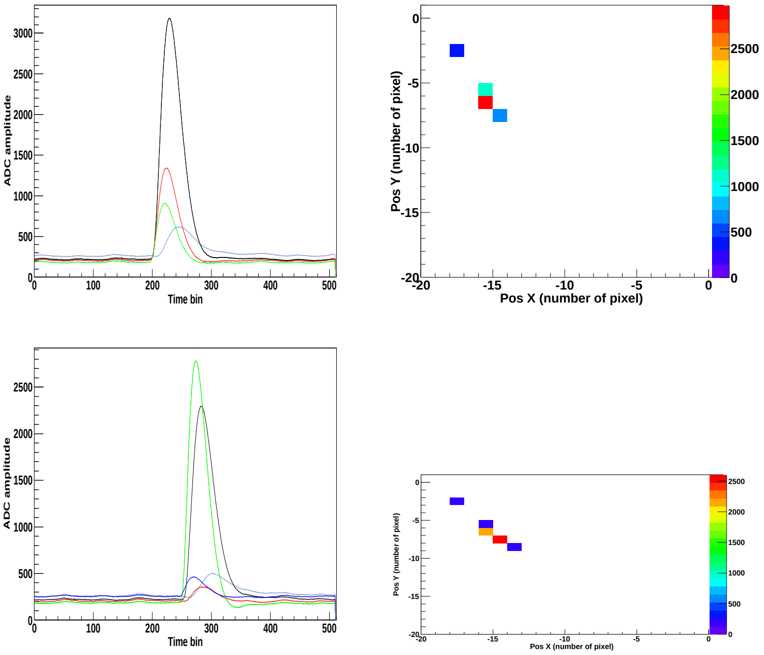

FIGURE 3.26: *Example of the tracks obtained looking at the events in the peak shown in 3.25. Left images: Registered pulses for each active pixel and right: XY projection for the activated pixels.*

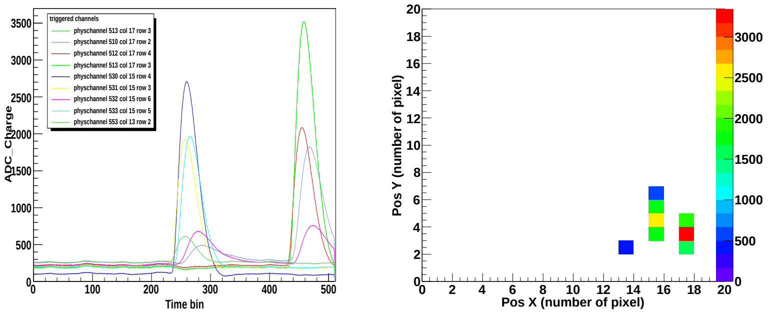

Figure 3.27: *Example of the tracks obtained looking at the events at higher energies than the peak showed in 3.25. There exists pile-up of two alphas of 5.5 MeV.*

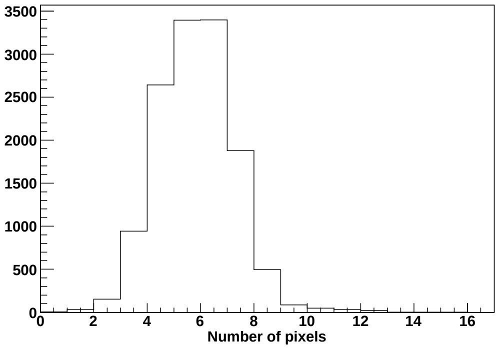

Figure 3.28: *Distribution of the number of pixels for the run with a microbulk detector installed in NEXT-MM. It was obtained in Ar-iCH$_4$ at 2% at 1 bar and with an ^{241}Am. The expected length of an alpha of 5.5 MeV in Ar at 1 bar is 4.5 cm in accordance with the obtained distribution peaked at 5 pixels (each one of* 0.8×0.8 *cm^2).*

Chapter 4

NEXT-MM: First data with Xe-TMA

Contents

4.1 Analysis code **88**

4.2 First tracks **89**

4.2.1 Energy resolution results 95

4.3 Tracking with more than one detector **96**

4.4 Trigger from an external source. **102**

4.4.1 Energy resolution 105

4.4.2 Drift velocity 117

4.4.3 Preliminary attachment results 117

4.5 Summary **119**

In the previous chapter, the NEXT1-MM prototype was described and the operational tests and the first results to commission the detectors were presented. Energy resolution is a crucial point in a neutrinoless double beta decay experiment. Nevertheless, is the background rejection power that can be improved with a good pattern recognition. In this chapter first results will be presented regarding the tracking of the detector, composed by four different microbulk, independently read. Data was taken in a Xe-TMA mixture. Xe-TMA has a low diffusion coefficient, as discussed, making the topological reconstruction clearer. In addition, previous tests [109] with this gas in a smaller prototype have shown promising results up to 10 bar; it is interesting to corroborate this behaviour at longer drift distances. Moreover, first results regarding energy resolution have been also obtained.

The structure of the chapter is as follows. In the first section a description of the analysis code is done. In the next sections, results with different setups and conditions are presented. First tracks and energy resolution studies are delivered. Next, first results about attachment and drift velocity are also obtained. Finally, some remarks for future work are discussed.

4.1 Analysis code

The code used to analyse the T2K acquisition files is composed by different methods and libraries based on C++ and ROOT called **T2K electronics library**. In the following the main elements are described. This code have been developed in [174], where a more detailed description is given and also it is shown its application to the CAST [121] detectors is presented. This code can be used with any pixelized detector, readout with the AFTER chip. It is based on the recording of pulses coming from different channels, as result of the detection of the interaction of a particle in the sensitive volume.

In Figure 4.1 a flux diagram of the different methods and classes is shown. The output file of the T2K DAQ is converted into a ROOT file. The amplitude pulses of each of the activated pixels in an event are stored in ROOT histograms. Also each pulse has asociated an electronic channel. A program called *acq2root* manages this conversion through the manager. To do this conversion different classes are used. *T2KReader* directly leads with the binary output files of the T2K DAQ, as the set-up distinguishes between the electronics configuration and the detectors architecture, the auxiliary class *T2KConfig* allows to manage this through a configuration file where the number of cards or channels are indicated. Also the type of readout is mentioned. The events are stored as a *T2KrawEvent*; it is a low level general holder class. It stores the information in a ROOT TObject. It reconstructs the pulses for each electronic channel in an histogram and keeps the event time. It also stores the electronic channel number and two coordinates to place the pulse in the 2D readout. An associated class, *ReadoutDecoding*, implements the relationship between the electronic channel and the physical position for a particular detector and cabling configuration. Different decoding maps are implemented as those for NEXT-MM (with the different cabling used), the one for the test chamber and also for CAST. New decodings can be implemented if necessary.At this low-level a 2D visualization of the events also exist and can be used as an off-line browser.

T2KTools is a set of functions to handle *T2KrawEvents*, using if necessary the readout configuration. Some of its functions allow to obtain the maximum amplitude of the pulses or are drawing functions. In general they are the basis for the analysis programs to be written.

Then, the events are converted into a *TRestPhysEvent*; it is a description of the event in terms of its energy and position. It is a pixelized event. The z coordinate is obtained converting the time information into length units using the drift velocity of the gas. To obtain the charge of the event an integration of all the channels that pass a threshold is done in a method called *ReconstructEventAsPhys* implemented in the class *Tt2kManager*. A calibration in energy must be done later correcting electronic effects. This class also has a 3D drawing method. Different variables are stored, like the number of pixels, for the analysis.

Once the events are reconstructed in a *TRestPhysEvent*, also in a ROOT Tree, different analysis programs can be written that access easily the event information. *SpectrumByFec* is a program to develop 1D selection criteria on the observables (number of pixels, energy and position) and can separate them in function of the Micromegas that is read (in this case we are reading up to 4 different FEC, one per Micromegas). *SelectTracks* allows to select events that fulfil different conditions and to visualize and save their 2D tracks.

The purpose of the *Tt2kManager* class is also to act as a bridge-class to RESTSoft package. This package will be explained in Chapter 5 and contains the main libraries to handle the simulation output from GEANT4 and implement the discrimination algorithms to do the analysis.

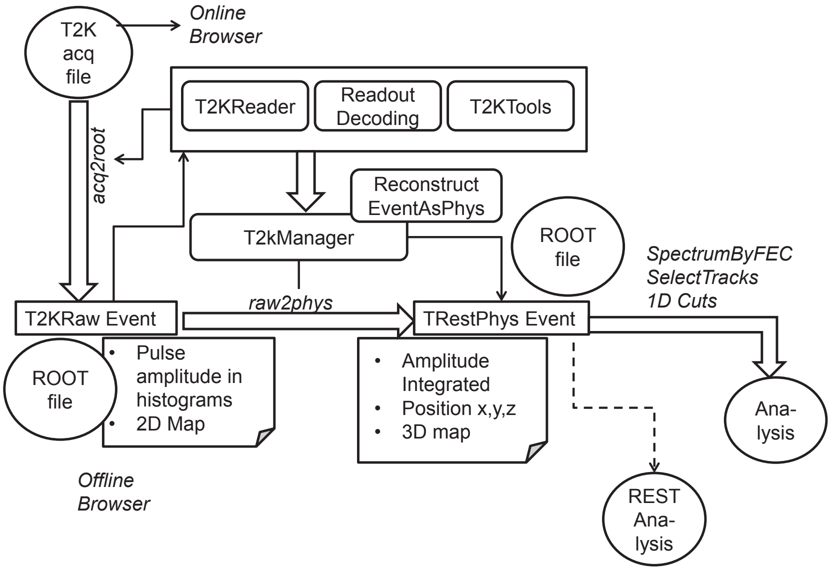

Figure 4.1: *Flux diagram of the methods and classes for the* T2K electronics library. *The acquisition file is converted into a ROOT file transforming each event in a* T2KRaw event *that consists in a collection of histograms, one per each pixel activated, that represents its pulse amplitude. It is done with the program* acq2root *and uses the libraries* T2KReader *and* Readout decoding *to associate a position xy to the electronic channel. It also uses the methods contained in the class* T2KTools. *In a second step the event is converted into a* TRestPhys Event *for which the charge is obtained integrating the amplitude of all the binning of the histograms over a threshold. At this stage also the 3D positions of the events are calculated. Finally, different analysis programs are used that allow to select events that fulfil several conditions.*

4.2 First tracks

The first studies were done at 1 bar of Xe-TMA (3.5%) with two calibration sources inside the chamber. One of the sources was a ^{241}Am source placed in the centre of the cathode. The other was a ^{57}Co placed in one lateral wall of the field cage, between two rings, at around 8 cm from the Micromegas plane. A sketch of the setup is shown in Figure 4.2. With two different sources, having emissions of multiple energies, high phenomenology in terms of different track-lenghts is expected. On the other hand, the placement of a source close to the detector minimizes the risk of detecting no events due to possible problems with the gas purity. Table 4.1 summarizes the expected emissions from the two different sources with the energy, intensity, origin and estimated range at 1 bar of Xe based on the CSDA [175] calculus for each one. The ^{241}Am source was placed shielding the alpha emission (that is used for trigger with a Silicon diode as will be discussed in detail in Section 4.3) and only the gammas and X-Rays will reach the drift region.

Origin	Particle	Energy (keV)	Intensity (%)	Range CSDA at 1 bar (cm)
^{241}**Am**	X-Ray	13.9	9.6	0.2
	X-Ray	16.8	2.5	0.2
	X-Ray	17.0	1.5	0.2
	X-Ray	17.7	5.7	0.3
	X-Ray	17.9	1.4	0.3
	X-Ray	20.8	1.4	0.4
	γ	26.4	2.4	0.6
	γ	59.5	35	2.0
^{57}**Co**	γ	14.5	10	0.2
	γ	122.1	85	8.0
	γ	136.5	10	8.0

Table 4.1: *Summary of the emissions from the two sources placed inside NEXT1-MM. The nature of the emission is shown, its energy and intensity as well as the expected CSDA range of the electrons in Xe-TMA at 1 bar.*

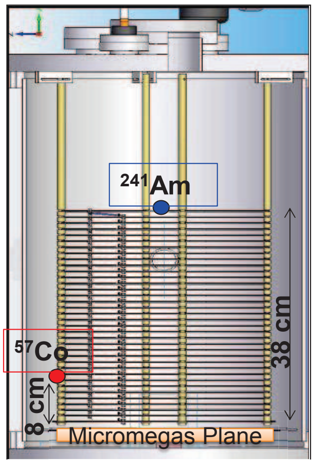

Figure 4.2: *Sketch of the first setup in which the calibration sources and their positions are shown.*

In addition, the escape peaks in Xe have to be taken into account. In Table 4.2 are summarized the Xe X-Rays energies. The incident particle can lose energy when exciting a Xe atom, losing the binding energy. Therefore, its final energy deposited will be less than the initial one. As shown in Table 4.2 the K_{alpha} shells are very close and are difficult to distinguish. Therefore, we can say that the two X-Ray can be detected with 4 keV of difference if the energy resolution of the detectors were good enough. As there are events with 60 and 122 keV coming from the sources, two escape peaks are expected: one at around 90 keV from the higher energy gammas of the ^{57}Co source and another at 30 keV of the 60 keV gamma from the ^{241}Am source or from the Xe characteristic X-Ray.

The data here commented corresponds to just one of the four sectors of the readout, MM2, that is the one closest to the ^{57}Co source. The mesh was at 275 V (55 kV cm^{-1} amplification field) and the drift at 5900 V (drift field of 155 V cm^{-1}). The signal from the mesh and from the pixels were recorded. The mesh signal was used to trigger the pixels acquisition. In Figure 4.3 is shown the recorded raw spectrum of the pixels after around 8 h of measurement. As mentioned, the charge has been obtained integrating the pulses that have an amplitude higher than a threshold

Shell	Energy (keV)
$K_{\alpha 1}$	29.4
$K_{\alpha 2}$	29.7
K_{β}	33.6
$L_{\alpha 1}$	4.1

TABLE 4.2: *Summary of the Xe characteristic X-ray energies.*

imposed through the configuration file and which is based on the pedestals. It is calculated in ADC charge per μs. Along this data-taking the time window was 80 μs sampled in 512 time bins. Up to now, the only selection applied is to reject those events that saturate the electronics.

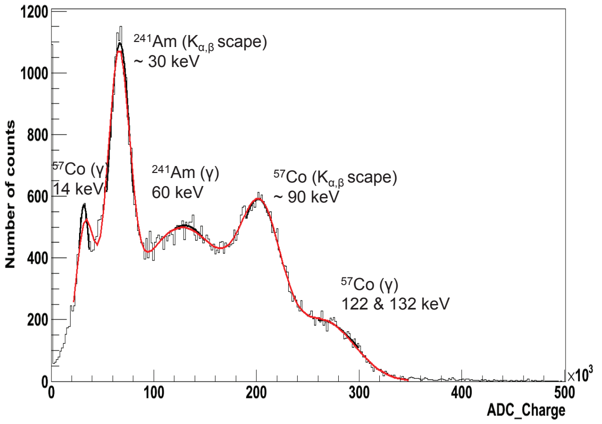

FIGURE 4.3: *Raw spectrum reading the pixels of the MM2 microbulk detector obtained with two calibration sources, ^{57}Co and ^{241}Am, placed in NEXT1-MM (see text for more details).*

Although no energy calibration is available for these data, the assignment of the energy of the peaks is straightforward because of their position, since they correspond to well separated known photon energies, and is given in Figure 4.3. However, we can consider another characteristic in order to increase our confidence: the length of their corresponding tracks. First of all is plotted the distribution xy of each peak, as is shown in Figure 4.4. It can be observed how the population in the 14 keV peak is closer to the position of the ^{57}Co source. The tracks coming from ^{241}Am and the more energetic ones are contained in the centre of the readout. This leads to think that selecting a smaller fiducial region, the peaks could be observed clearer because we are avoiding boundary effects that could produce that some charge was detected in another Micromegas or would fall outside the sensitive region. This is discussed in more detail in the next section. The range for each energy is shown in Table 4.1 and in Figures 4.5 and 4.6 different examples of tracks selecting events in each peak are shown. It can be seen how the length is in agreement with the expected CSDA range. It has to be reminded that the pixel size in these Micromegas is 0.8×0.8 cm^2.

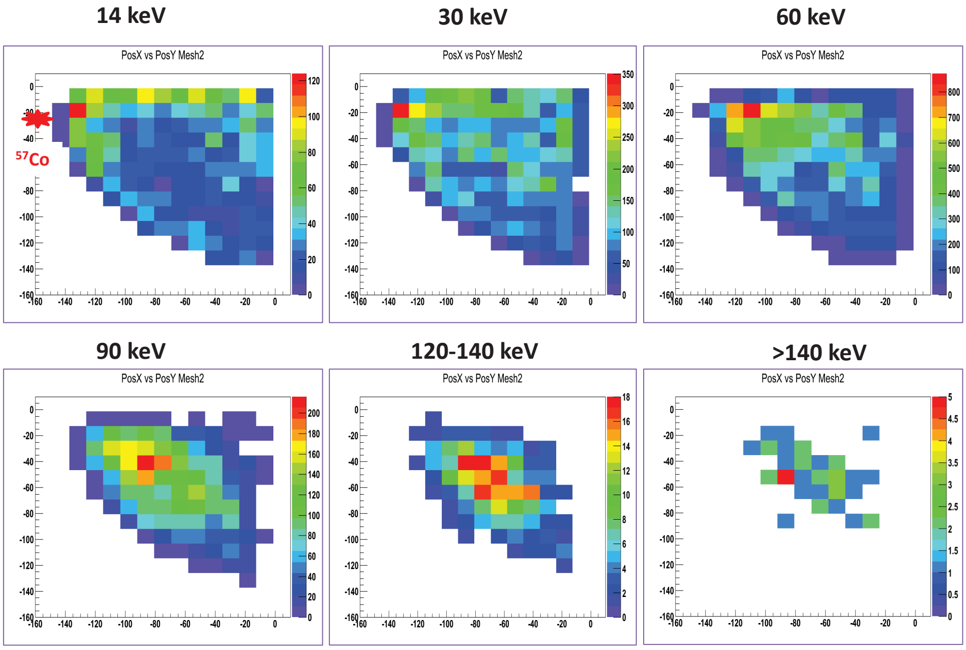

FIGURE 4.4: *xy distributions of the triggered pixels for each of the observed peaks and higher energy regions.*

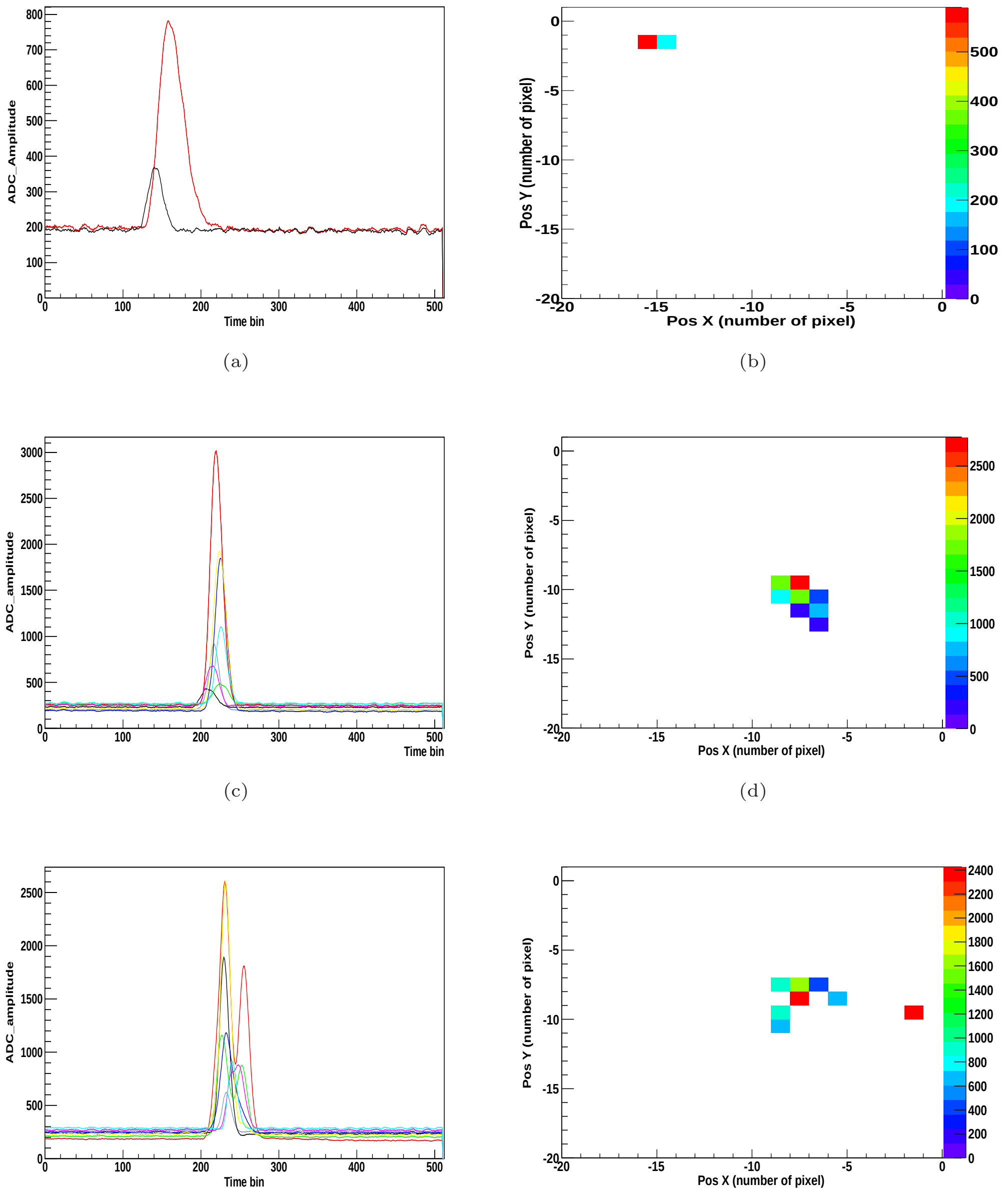

(a) (b)

(c) (d)

(e) (f)

Figure 4.5: *Example of events recorded in the pixel plane on the Micromegas MM2 for the* ^{57}*Co source. (a-b) 14 keV peak, (c-d) 90 keV peak and (e-f) 122 keV peak. Left images represent the registered amplitude for the active pixels and right plots are the xy projection of the events in the pixelized plane.*

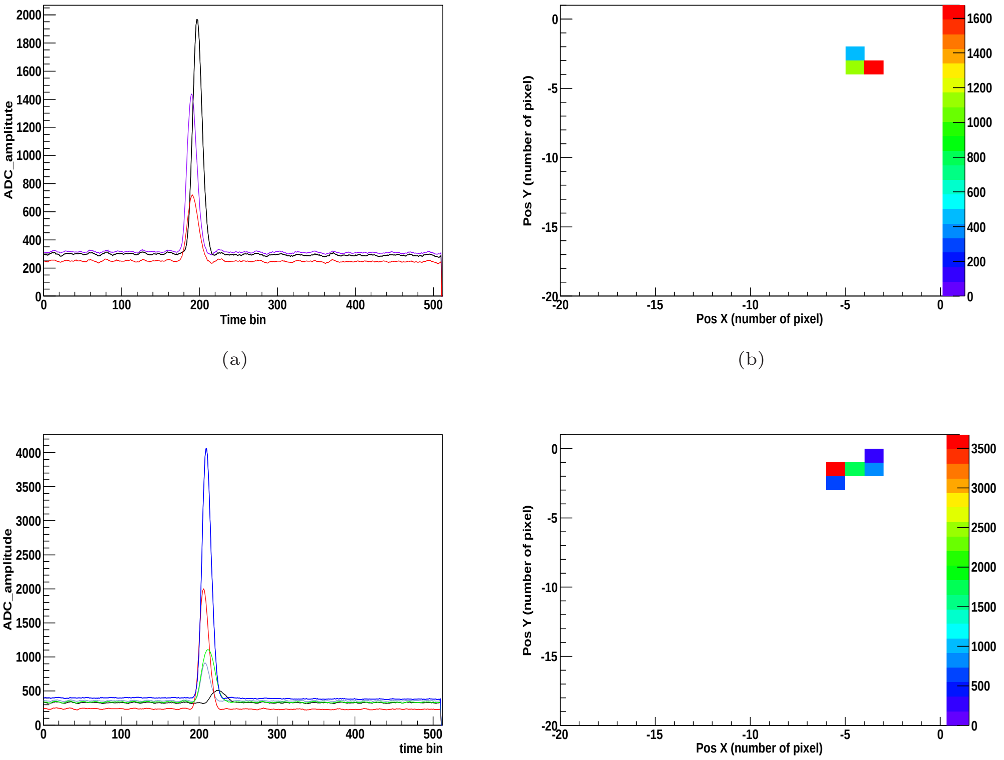

(a) (b)

(c) (d)

Figure 4.6: *Example of events recorded in the pixel plane on the Micromegas MM2 for the* ^{241}*Am source. (a-b) 30 keV peak and (c-d) 60 keV peak. Left images represent the registered amplitude for the active pixels and right plots are the xy projection of the events in the pixelized plane.*

4.2.1 Energy resolution results

After the assignment of the energies, the main peak, the Ag K_α line at 29 keV, corresponding to the Xe escape peak (K-shell) is used to obtain a first value of the FWHM by fitting it to a Gaussian. Based on data shown in Tables 4.1 and 4.2, two emissions of energy close to 29 keV are expected: the Xe escape peaks and the gamma of 26.4 keV from the ^{241}Am. These two peaks are fitted following a 2-step routine. First of all the range for the 30 keV peak is fitted to a Gaussian over a flat background. In the second step, two more Gaussian functions are added which correspond to the 29 keV and 26.4 keV. The input parameters have been obtained in the first step, taking into account the intensity for the 26.4 keV gamma with respect to the K_α.

The energy resolution is obtained from the 29 keV peak. In Figure 4.7 are shown the two Gaussians summed to do the total fit. The spectrum shown is the resulting one after selecting events with their mean position in an 2D region in the readout plane, in order to avoid boundary effects. Different xy regions in the centrer of the detector have been studied. In Table 4.3 are shown the results obtained considering all the detector or different regions that are represented in Figure 4.8. A better resolution (around 27% FWHM at 29 keV) has been obtained when only events whose mean positions are far from the boundary are selected. This effcet shows the homogeneity of the energy resolution in the active surface. If we focus on region 1, the obtained resolution extrapolates to 2.96% FWHM at 2458 keV, the transition energy of the ^{136}Xe $\beta\beta0\nu$ decay.

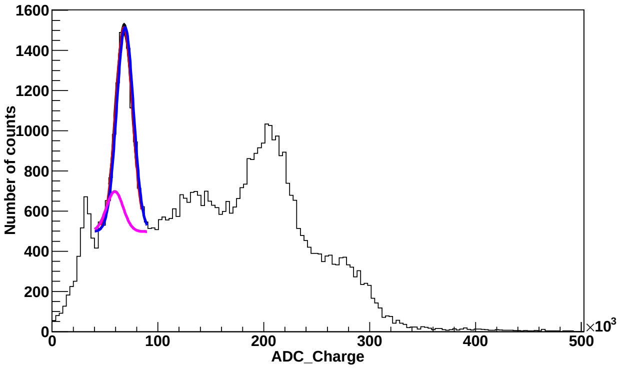

FIGURE 4.7: *Energy spectrum reading the pixels of MM2 microbulk obtained using two calibration sources, ^{57}Co and ^{241}Am, placed in NEXT1-MM after selecting an xy region (labelled as 1 in Figure 4.8). The ~ 30 keV peak is fitted to two Gaussian at the expected energies.*

xy selection	% of total events	Efficiency in the peak (%)	%FWHM at 29 keV	% FWHM at $Q_{\beta\beta}$
All plane	100		41.2	4.5
Region 1	70	58	27.3	2.9
Region 2	54	54	27.0	2.9
Region 3	40	53	27.9	3.0

TABLE 4.3: *Energy resolution obtained selecting events in different xy regions shown in Figure 4.8. Comparing the results considering all events or events in a region, the improvement in the energy resolution is around a factor 1.5. In the last column it is shown the expected energy resolution at the ^{136}Xe $Q_{\beta\beta}$ obtained extrapolating from the data at 29 keV.*

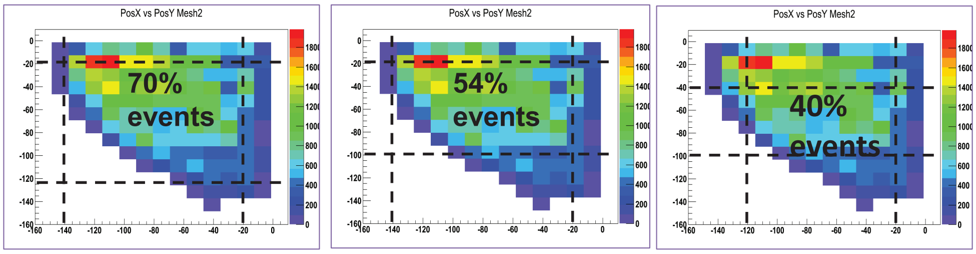

Region 1 Region 2 Region 3

Figure 4.8: *The xy plot obtained summing the energy of all the detected events and calculating the x and y position of the event as the mean position. It is shown the different selected xy regions to calculate the energy resolution. Region 1 is rejecting just around 1 cm in each direction. It contains the 70% of the events. Region 2 contains around the half of the events and in region 3 it is only kept the 40% of the events.*

4.3 Tracking with more than one detector

The next step was the acquisition with more than one microbulk. For this run the ^{57}Co source was taken out and only the gammas from the ^{241}Am source interact in the fiducial volume. Three detectors were taking data in this run: MM1, MM3 and MM4. MM2 shows a short-circuit with some element of the vessel and could not be used. The trigger of the T2K acquisition was an OR of the three mesh signals, or, in other words, any event detected in any sector gives the trigger. In Figure 4.9 can be seen the mean x and y position of all the detected events in the pixel plane (as it is the mean position, some of the values can fall out of the active region).

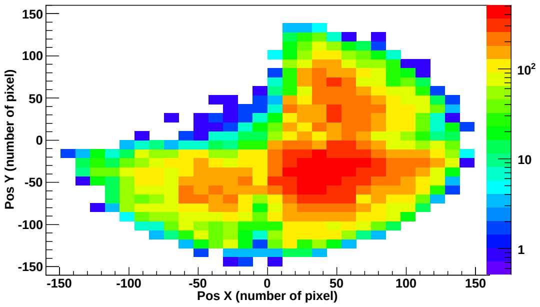

Figure 4.9: *Mean x and y positions of all the detected events in the pixel plane running with three Micromegas active.*

One of the main objectives of NEXT1-MM was to obtain fully contained electron tracks in the fiducial volume and detected in the Micromegas plane. In the previous section, different tracks detected in one sector have been shown. In this run, we are dominated by background and cosmic ray events and different particles can leave their energy in more than one detector. Some examples showing different topology are presented. In Figure 4.10 an alpha particle has been identified, with a charge of 7.95×10^7 ADC units per μs that corresponds to an energy around 200 keV. A saturation in the pixels is observed in the pulses. This can produce a loss in the proportionality between amplitude and charge for the event. In Figure 4.11 and in 4.12 two examples of electrons crossing more than one detector are shown, obtained in two different runs with the three detectors. The one in 4.11 has an energy around 180 keV and that of 4.12 of around 200 keV. As the detectors are parallel to the earth plane, most of the muons, that are practically vertical ($\theta \sim 0°$) or come in a very small angle, deposit their energy in no more than four or five pixels. However, some transversal muons can also be detected as shown in Figure 4.13. Events from the source are identified as the one in Figure 4.14 where two 30 keV tracks are observed, corresponding to the Xe excitation by a 60 keV gamma from the ^{241}Am and the detection of the remaining energy.

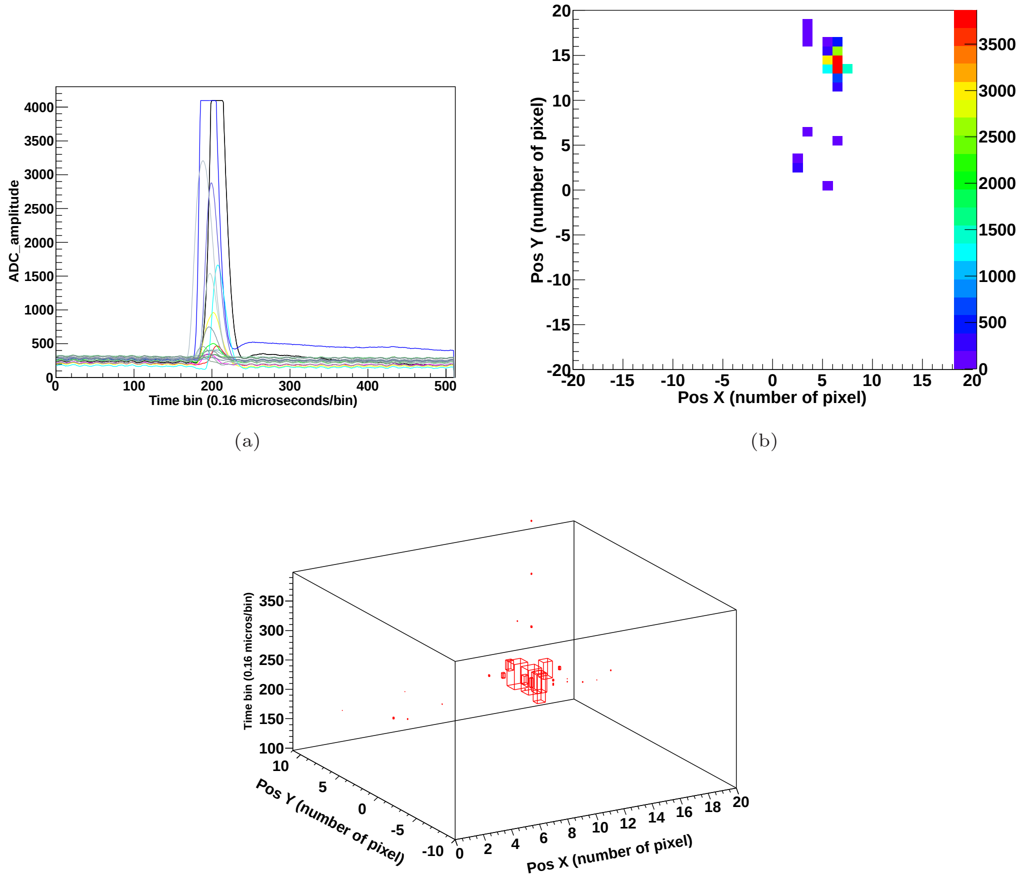

(a)

(b)

(c)

Figure 4.10: *Example of an alpha particle. (a) Pulses in the activated pixels, a saturation is observed. (b) xy projection of the track. (c) 3D reconstruction with a relative z position where can be seen the same deposited charge per pixel.*

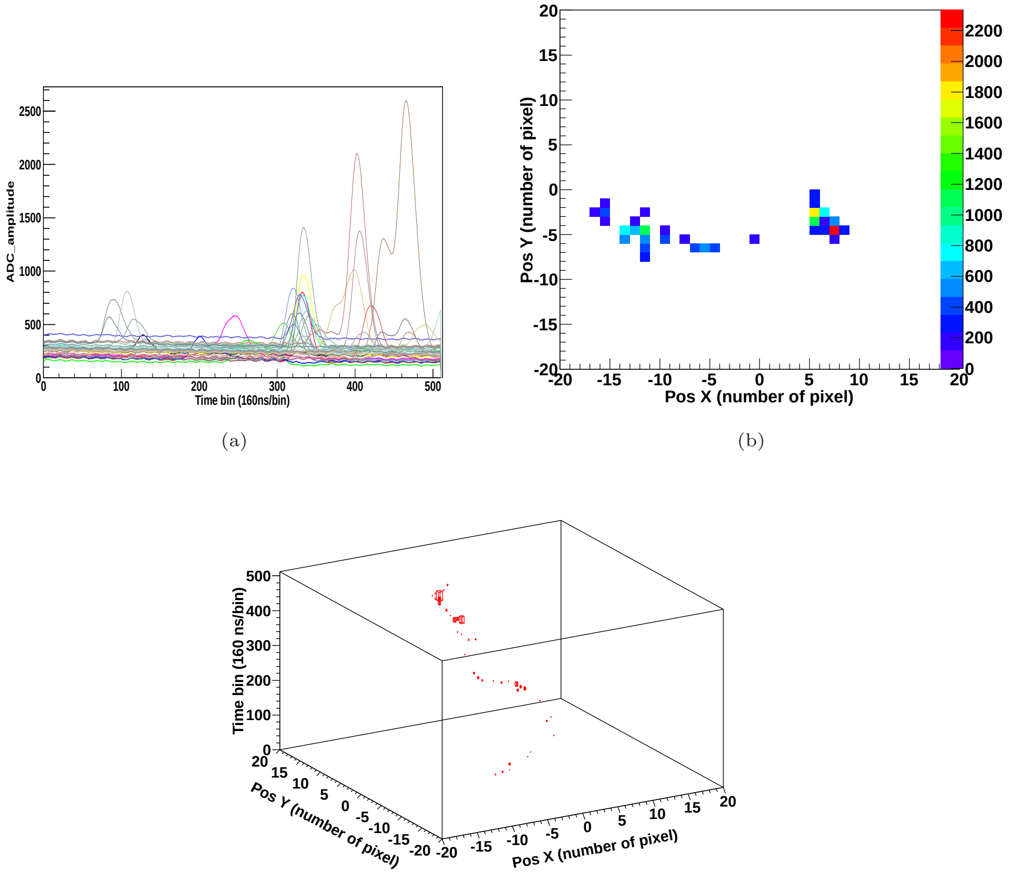

(a) (b)

(c)

Figure 4.11: *Example of an electron of around 180-200 keV crossing two detectors. (a) Pulses in the activated pixels. (b) xy projection of the track. (c) 3D reconstruction with a relative z position where a high deposition of charge at the end can be seen.*

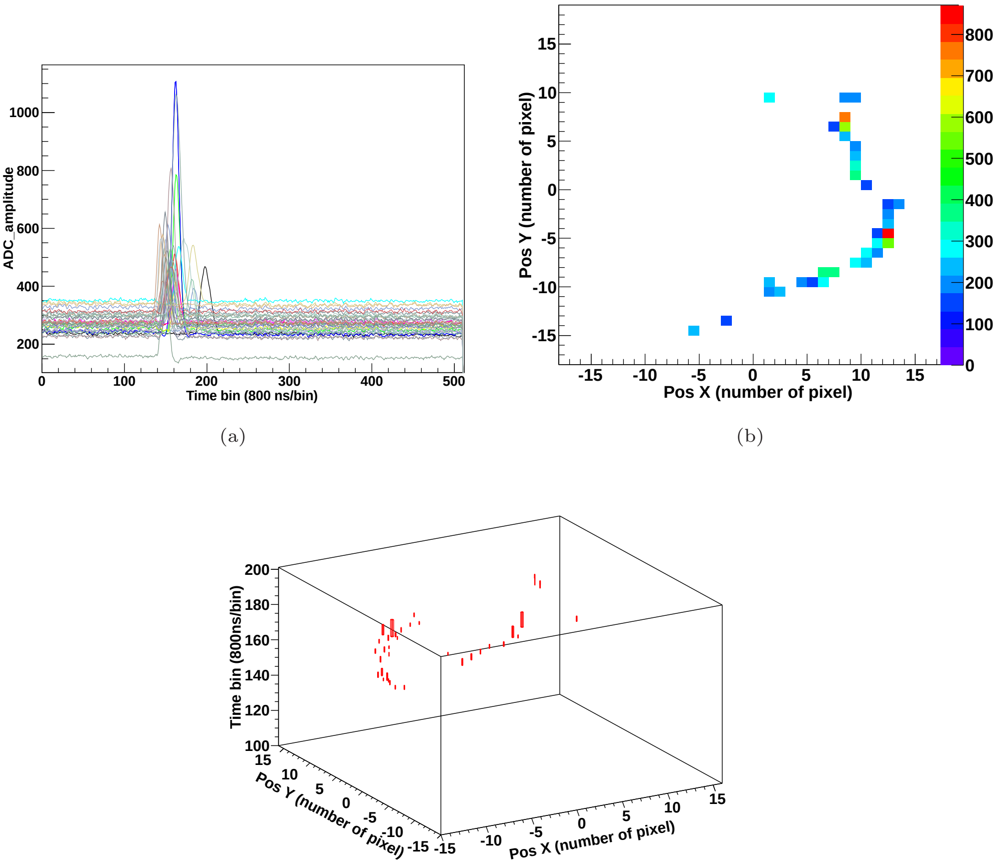

(a)

(b)

(c)

Figure 4.12: *Example of an electron of around 180-200 keV crossing the three active detectors. (a) Pulses in the activated pixels. (b) xy projection of the track. (c) 3D reconstruction with a relative z position where a high deposition of charge at the end can be seen.*

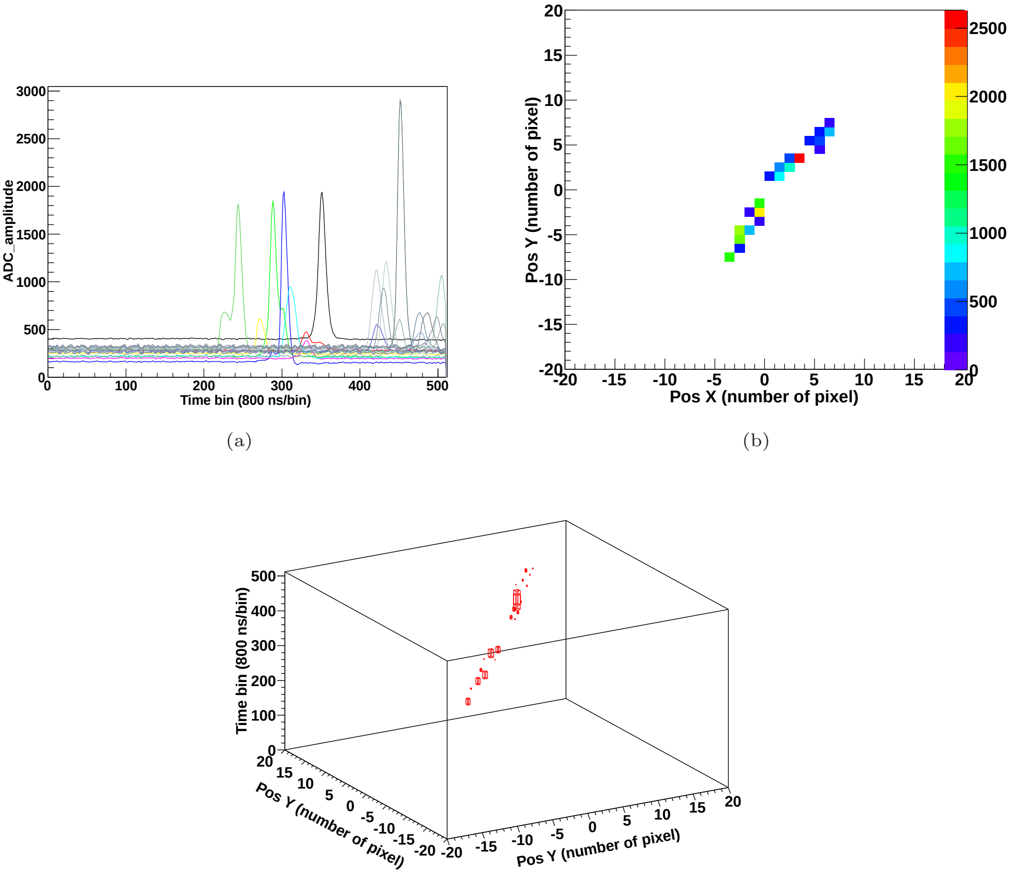

(a)

(b)

(c)

Figure 4.13: *Example of a muon crossing the three active detectors. (a) Pulses in the activated pixels. (b) xy projection of the track. (c) 3D reconstruction with a relative z position.*

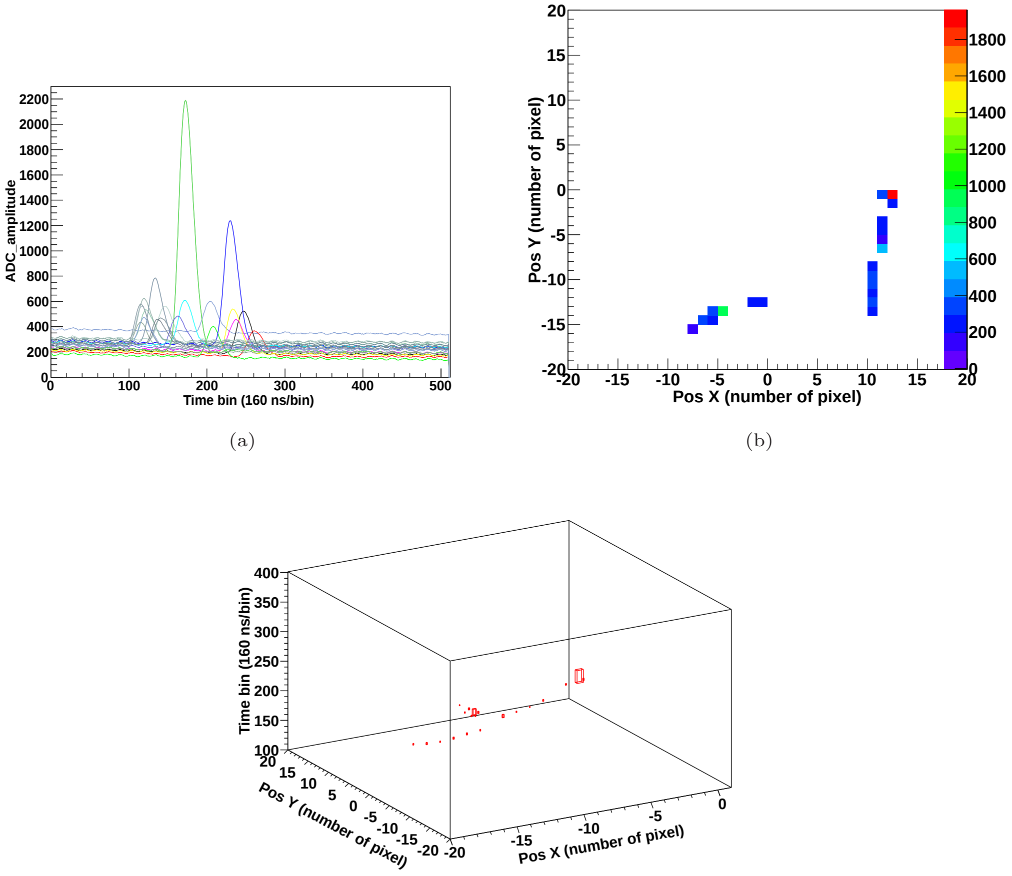

(a)

(b)

(c)

FIGURE 4.14: *Detection of two 30 keV events. (a) Pulses in the activated pixels. (b) xy projection of the track. (c) 3D reconstruction with a relative z position.*

4.4 Trigger from an external source.

A Silicon diode (Si) was installed in the cathode, as shown in Figure 4.15, in such a way so as information about the total z position of the event in the TPC can be extracted. The Si was enclosed in a Teflon tube to avoid sparks with the cathode at HV. It was also closed with a cylindrical piece of Teflon that can hold the ^{241}Am source. Then, the source was placed between the Si and the lower part of the Teflon. The Teflon tube was positioned in the cathode, in the central hole.

The ^{241}Am is an alpha emitter with an energy of 5.5 MeV. The source is deposited on a thin layer of aluminium. Then, the alpha emission escapes just from the source side pointing to the Si diode, while gammas and X-rays are distributed on both sides. Therefore, the Si detector is triggered with the alpha emissions. In 36% of the times this alpha emission is produced with a gamma of 60 keV. This emission can occur in all directions and, approximately, the half of the times will enter the drift region and therefore, may be detected in the Micromegas plane. A schematic view of the process can be seen in Figure 4.16. If the trigger is done with the signal from the Si, information about the origin of the events can be extracted from the data. In this run the ^{57}Co source was taken out because the rate of random coincidences was of the order of the expected coincidence with the Si making more difficult this study. Data were recorded making a coincidence between the Si and the mesh signal.

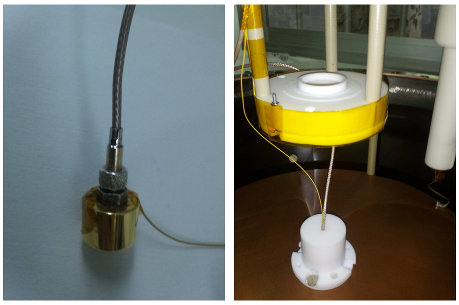

(a) (b)

Figure 4.15: *(a) Image of the Si diode installed in NEXT1-MM and used to trigger the T2K acquisition. (b) Placement of the Si in the cathode. It is covered by Teflon to avoid sparks with the metal surfaces. In the bottom part of the coverage is placed the radioactive source (^{241}Am).*

In order to acquire in coincidence with the Si, different electronic modules and delays are needed. The electronic chain used is sketched in Figure 4.17. First of all, the Si is powered at 50 V with an ORTEC 142C preamplifier by the bias line while the signal is read. Then it is passed to a Linear Scaling Amplifier (LA/SCA) and converted into a logical signal. In the case of the Micromegas they are fed with a CANBERRA 2004 preamplifier. The operational voltages for these tests were 270 V. Then, the signals are passed to a linear amplifier. The output is sent to a CAEN N844 Low Level Discriminator (LLD). In order to make an OR between the mesh signals, the CAEN N455 Quad Coincidence Logic Unit is used. Both, the logical Si signal from the LA, and the output of the OR from the Micromegas are fed to a Dual Timer model CAEN N93B. The Si signal pulse width is stretched by a time window equivalent to at least all the drift region. Using the end-marker of the pulse results in delaying the Si pulse. The Micromegas pulses are

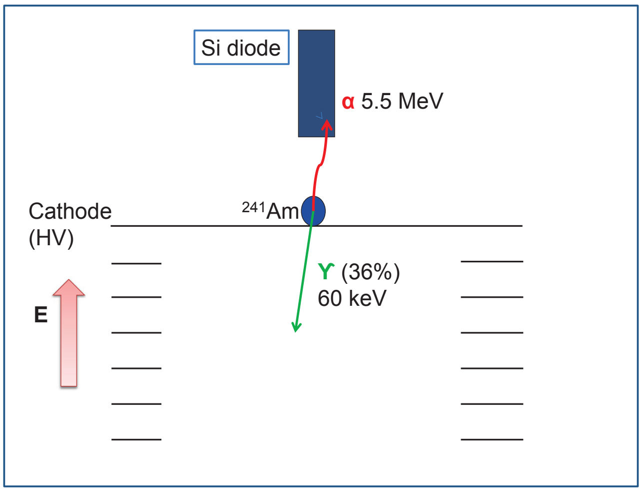

FIGURE 4.16: *Drawing of the setup with the Si diode. An* ^{241}*Am source is placed in the cathode. It emits an alpha particle of 5.5 MeV that can only escape to the upper part of the chamber where it is detected in the Si detector. This emission, the 36% of the times takes place with a gamma of 60 keV. As it can be emitted isotropically in all directions approximately half of the times it will enter the drift region and will be detected in the Micromegas plane.*

widened more than the Si to ensure that we are detecting all the relevant events. Finally, the end point from the Si and the Micromegas signal are passed again to the coincidence module and the AND output is used to trigger the pixels acquisition.

The data presented were recorded using two Micromegas: MM1 and MM4. They are covering half of the surface of the anode. Data were recorded in recirculation mode with a rate of 0.8 - 1 Hz. The working pressure was 1.03 bar in a Xe-TMA mixture at 3.5%. In Figure 4.18 (b) can be observed the xy projection of all the events detected in the pixel plane of the detectors. In Figure 4.18 (a) it is shown the charge spectrum obtained in each detector, integrating the charge for all the channels above an amplitude threshold. In order to generate the spectra for each detector, the events considered have all their active pixels in the same detector. Two peaks are expected in the spectrum: one at 60 keV from the gamma detection and another at around 30 keV from the escape peak in Xe, as commented in previous section. The number of detected events is approximately the same in both detectors while the gain is a factor 1.12 higher in MM4 than in MM1. From previous measurements a difference up to two was observed between the two detectors. The observed distribution has a higher 30 keV escape X-Ray than the 60 keV. This is corroborated from what is obtained in a simulation of the setup performed using GEANT4 in [176] with just one detector active. 75% of the times the events will come accompanied by a K-shell emmision [124] and the mean free path of the 30 keV energy is 20 cm. Therefore, some 30 keV events produced by the 60 keV that would fall in other detector would be measured increasing its probability with respect to the 60 keV. In Figure 4.19 (a) the obtained spectrum from the simulation can be seen.

In Figure 4.20 can be seen the time distribution in each Micromegas. The position of the trigger in the time window trigger was at 230 μs; as we are using it to trigger the acquisition, and it will detect the alpha while the gamma has to go across all the drift distance to be detected on the Micromegas plane, all the relevant information is pretrigger. In order to detect events in all

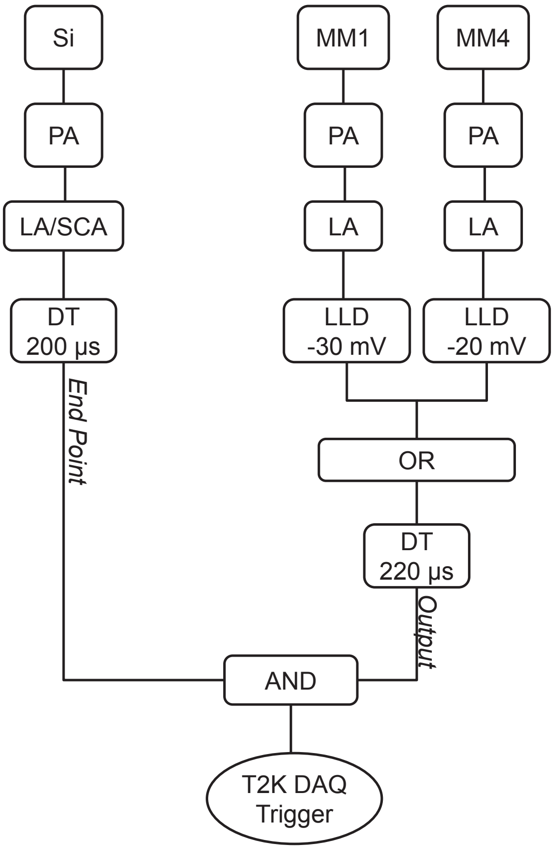

Figure 4.17: *Sketch of the electronic chain used to trigger the Micromegas detectors in coincidence with the Si diode. The Si diode detects an alpha. Its signal then is the input in a Dual Timer that enlarge it and gives the end-point of the window. It has to be enlarged at least by the drift distance to be able to see all the chamber. The mesh signals, after a PA, LA are fed to a Low Level Discriminator (LLD). The two of them have more or less the same S/N threshold that is imposed to be around -25 mV. Then, this logical signals are fed to a dual timer which output is an OR between the two mesh. Finally an AND between the output of the OR and the end-point of the* Si *is used to trigger the acquisition.*

the drift region the Si diode signal was delayed by 190 μs. This delay was obtained taking into account the expected drift velocity of Xe-TMA in a drift field of 150 $\mathrm{V\,cm^{-1}}$ from the Magboltz simulation shown in Figure 2.2. It is enlarged to be sure that events in all the drift region are detected. Therefore, the 0 position in the chamber (the Micromegas plane) has to be at 40 μs. The cathode could be assigned to the point in which the distribution falls down to the flat level again. This distribution has also be confirmed from the simulation of the setup as is shown in Figure 4.19 (b). It is not completely exponential, as expected for the mean free path of the particles. It fits to an exponential plus a constant line because there exist two contributions to take into account: on one hand the mean free path of the 60 keV gamma and the 30 keV that is around 20 cm, hence there is more probability that they interact in the upper part of the TPC, and on the other hand, the solid angle is much bigger close to the cathode because the source is not collimated.

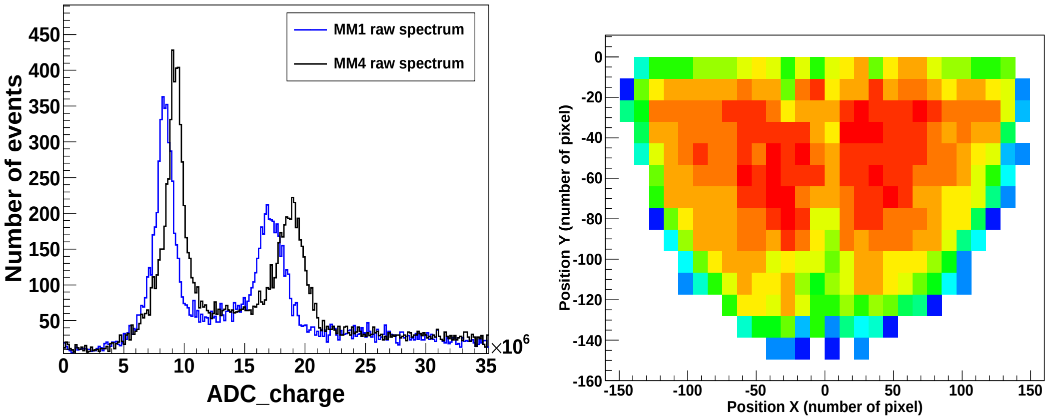

(a) (b)

FIGURE 4.18: *(a) Raw charge spectra obtained for the active detectors (MM1 in blue and MM4 in black) in 1 bar of Xe-TMA (3.5%). The 60 keV gamma peak from the* ^{241}*Am source can be seen and, also, the 30 keV from the scape peak of Xe. A difference in gain of* 1.2 *between the two detector exists. (b) xy projection of the total sum of charge of the active pixels.*

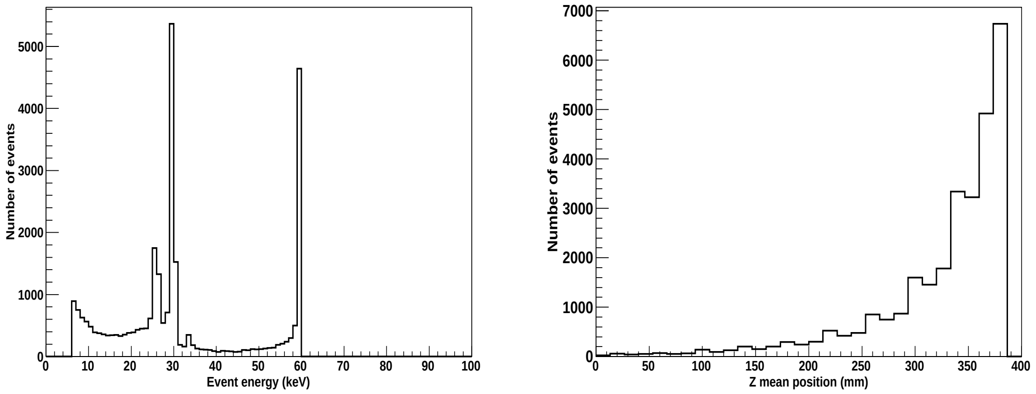

(a) (b)

FIGURE 4.19: *Results from a simulation performed with GEANT4 of the setup, extracted from [176]. In (a) is represented the energy spectrum showing that the 30 keV particles has a higher probability than the 60 keV gamma because just one detector is active. In (b) the z position distribution is plotted showing the same shape that the obtained with the data in Figure 4.20.*

4.4.1 Energy resolution

In Figure 4.18 (a) the background from cosmic muons, alphas and electrons from the natural isotopes can also be seen. Different selection criteria have been defined at this level to obtain a cleaner spectrum and therefore, a better energy resolution. They can also be useful to understand background. From the topological information of the events, differences between the events from the source and background are observed, as for example the number of triggered pixels. As seen in previous sections, events of 30 keV and 60 keV have a length of less than 10 pixels. The different selections defined are applied sequentially. The first one is to reject those events on which at least one pixel has an amplitude that saturates the electronics (as applied in Section 4.2). With this selection, not only noise events are rejected, but also alpha events (see Figure 4.10).

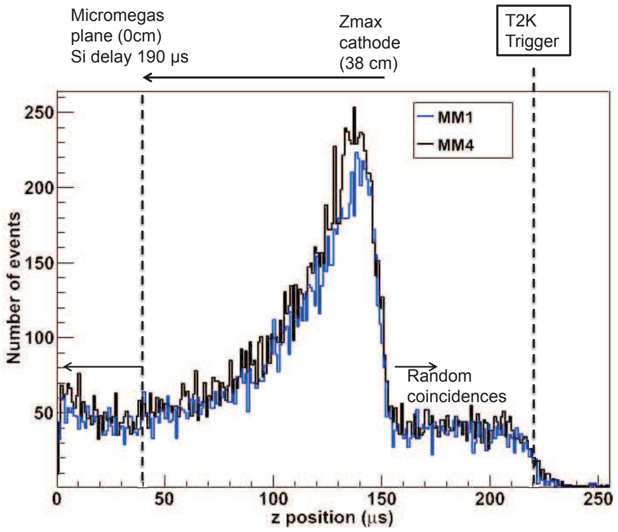

FIGURE 4.20: *z distribution in the two active detectors.*

Eventually some 30 keV events would also been rejected because they can deposit all the energy in just one pixel and saturate it, but the probability is around 1%. It does not happen with the 60 keV events since they spread on, at least 2 pixels.

Secondly, the observable Δz is defined as the difference between the maximum and minimum z position in an event. The expected length from the 60 keV gamma is of the order of 10 cm. If the event is completely vertical that would give the maximum Δz. On the other hand, vertical muons, that would be difficult to differentiate because they will leave all their energy in few pixels, will have a longer Δz, of the order of all the drift length. Also transversal muons and electrons will have a longer Δz than events coming from the source. In Figure 4.21(a) is shown the distribution of Δz for both detectors, MM1 and MM4, and the distribution of Δz versus the energy in Figure 4.21(b). For both Micromegas the same distribution is obtained. In 4.21(b) can be observed the distribution of the 30 keV and 60 keV. The events populating the region with a high charge and a low Δz could be alphas or electrons. At higher Δz there are electrons and muons. A selection for the events with a Δz smaller than 10 cm ($80 \mu s$) is done.

To consider only real coincidences and to avoid random ones, as we have a longer acquisition window, the net selection is to consider only events in the drift region. As explained previously the drift region goes from $z = 40\,\mu$s to $150\,\mu$s. However, there are still random coincidences from the background that populate mainly the 30 keV peak as can be seen in Figure 4.22 where it is shown the spectrum obtained when selecting events with a z between 0 and $30\,\mu$s (out of the Si diode window). The effect of the random coincidences is bigger at lower z's where the probability of interaction is smaller.

The next step is to perform a selection in the number of pixels. In Figure 4.23 is shown the distribution of the number of pixels selecting events in each peak. A selection of events with a pixel number between 1 and 12 is performed. As mentioned, vertical muons also touch few pixel but they are discriminated with the Δz variable. In Figure 4.22 (b) and (c) are shown the resulting energy spectrum and z distribution selecting events with more than 12 pixels, that justify this selection criteria.

The resulting spectra after each cut are shown in Figure 4.24 (a) for MM1 and (b) for MM4. In Tables 4.4 and 4.5 are shown the obtained efficiency and energy resolution fitting each peak over a flat background. The fit to obtain the energy resolution is made over a flat background, therefore, the energy resolution only changes slightly with them. The values obtained in MM1 extrapolates to an energy resolution of 2% FWHM at 2458 keV and less than 2% FWHM in MM4, proven, already an improvement with results shown in Section 4.2.1.

The last step is to define an xy region to avoid boundary effects. Different regions are studied as in Section 4.2. Mainly two of them are evaluated in this subsection, shown in Figure 4.25. For each detector the most activated region has been chosen. The x and y position of each event is calculated as the mean x and y position of all the pixels. In a first step the selection is done using that the mean position has to be in the selected region.

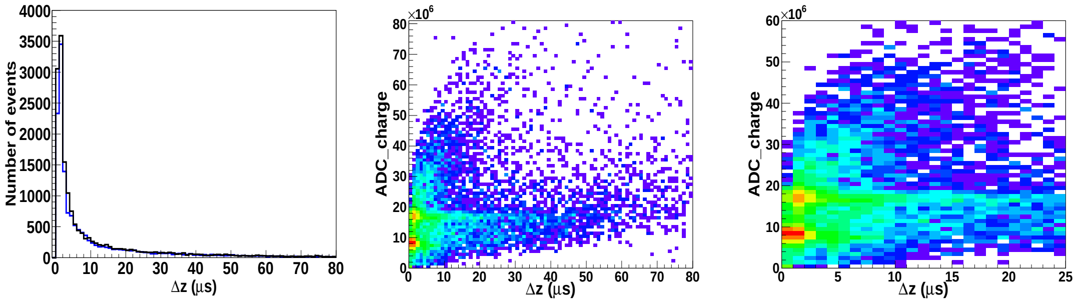

(a) (b) (c)

FIGURE 4.21: *(a) Distribution of the* Δz *variable defined as the difference between the maximum and minimum* z *position of the event for the two detectors: MM1 in black, MM4 in blue. (b)* Δz *versus energy for the MM1 (same distribution obtained for MM4). In (c) there is a zoom of (b) showing clearr two distributions corresponding to the two detected particles (*$\sim 30\,keV$ *and* $60\,keV$*).*

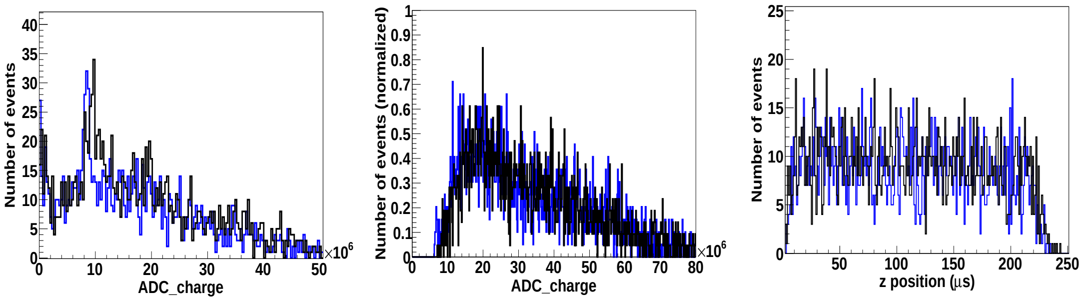

(a) (b) (c)

FIGURE 4.22: *(a) Charge spectrum obtained for both detectors in the region of random coincidences (*$z < 30\,\mu s$*). (b) Energy spectrum obtained selecting long events (with more than 12 pixels). It can be seen how the structure of peaks disappeared dominated by the cosmic background. In (c) the* z *distribution is flat when selecting events with more than 12 pixels. In the three plots the black-line corresponds to MM1 and the blue-line to MM4.*

The spectrum in Figure 4.26 is the resulting one after all the mentioned criteria for MM1 and in Figure 4.27 for the MM4 considering the more restrictive xy region. The fit is done in two

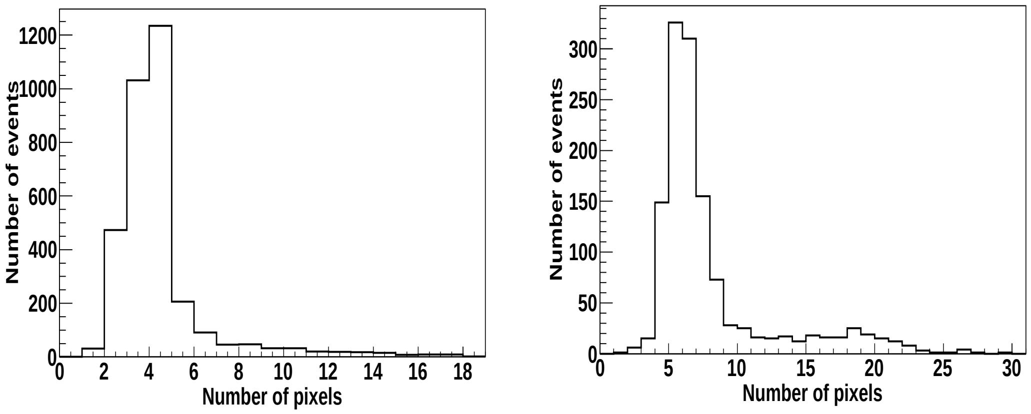

(a)

(b)

Figure 4.23: *Distribution of number of pixels for each peak: (a) selecting events in the 30 keV peak and (b) in the 60 keV peak. Events with less than 12 pixels were kept in the analysis.*

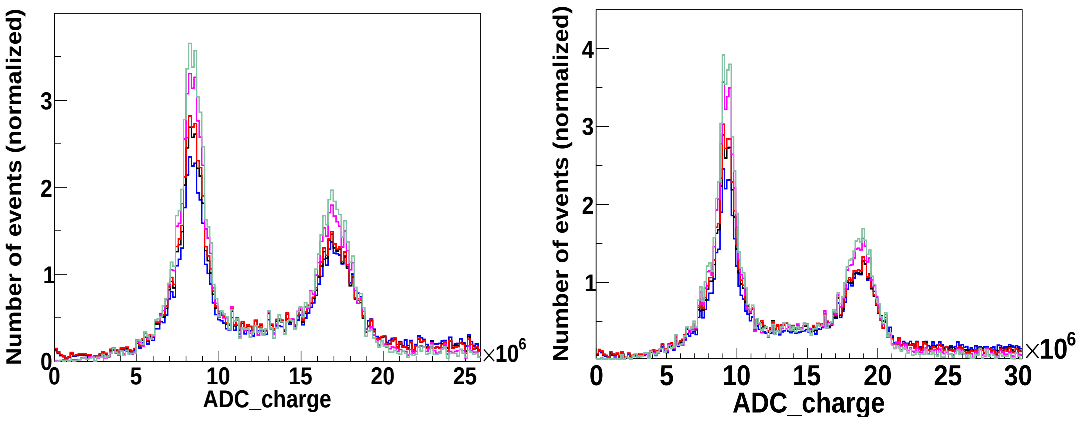

(a)

(b)

Figure 4.24: *Effect of the discrimination criteria on the charge spectrum for MM1 (a) and MM4 (b). The spectra are shown normalized and the criteria applied until now are the same for both Micromegas. They are: blue-line raw spectra, black-line: rejecting saturated pixels, red-line: applying $\delta z < 80\,\mu s$, magenta-line: selecting events in coincidence with the Si (Δz between 40-150 μs, and finally, selecting events with less than 12 pixels (soft green line).*

Selection	30 keV peak		60 keV peak	
	Surviving events (%)	%FWHM	Surviving events (%)	%FWHM
Raw spectrum		18.13 ± 0.62		13.16 ± 1.04
Rejecting pixel that saturate	100	18.13 ± 0.62	90	12.98 ± 1.03
$\Delta z < 80\,\mu$s	83	18.19 ± 0.62	86	13.12 ± 1.07
z selection (40-150 μs)	69	18.18 ± 0.63	76	13.79 ± 1.22
Number of pixels (1-12)	67	18.20 ± 0.63	73	13.79 ± 1.17

Table 4.4: *Efficiency and energy resolution obtained applying sequentially the different selections explained in the text for the MM1.*

steps: one first Gaussian in each peak to determine the peak position and to fix the range for the fit at $\pm 2.5\sigma$. The second Gaussian is defined over a flat background left as a free parameter, hence, it is different in each case. In the case of the MM1 (Figure 4.26) the scaling of the energy

Selection	30 keV peak		60 keV peak	
	Surviving events (%)	%FWHM	Surviving events (%)	%FWHM
Raw spectrum		13.51 ± 0.52		11.99 ± 1.42
Rejecting pixel that saturate	100	13.51 ± 0.52	84	11.75 ± 1.53
$\Delta z < 80\,\mu$s	99	13.56 ± 0.53	82	11.4 ± 1.44
z selection (40-150 μs)	86	13.44 ± 0.55	69	13.31 ± 2.57
Number of pixels (1-12)	75	13.44 ± 0.55	66	13.11 ± 2.39

TABLE 4.5: *Efficiency and energy resolution obtained applying sequentially the different selections explained in the text for the MM4.*

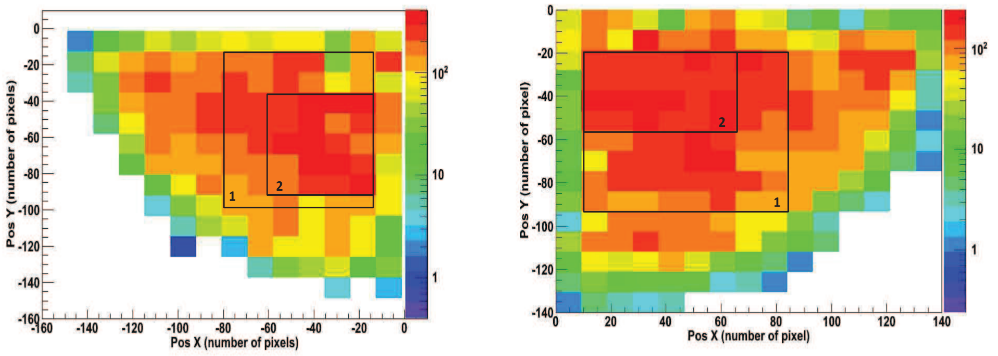

(a)

(b)

FIGURE 4.25: *Distribution of the charge of the pixels in both Micromegas under study (a) MM4 and (b) MM1. The different selected regions are shown in black rectangles, labelled as 1 and 2 as along the text.*

resolution is correct. In the case of the MM4 (Figure 4.27) it is not and the relative error is quite large, for the 60 keV peak. It might be because in this detector there were more dead pixels and the statistics was lower.

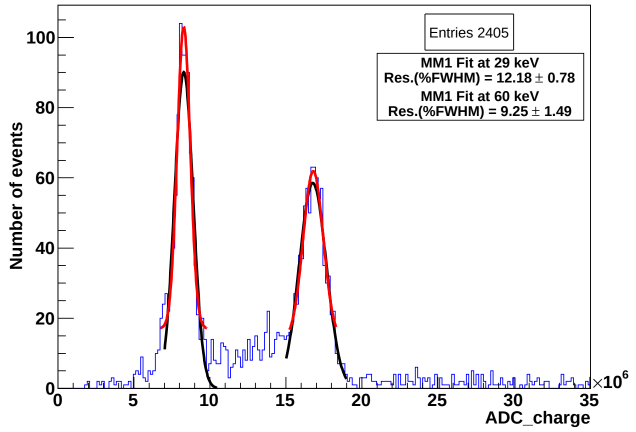

FIGURE 4.26: *Energy spectrum obtained in MM1 of the 16% final selected events in region 1 and that contains the 16% of the events. The fit is done at two stages over a flat background.*

In order to completely reduce the background events fully contained in a xy region were selected calculating the minimum and maximum x and y position of an event. The same two regions than

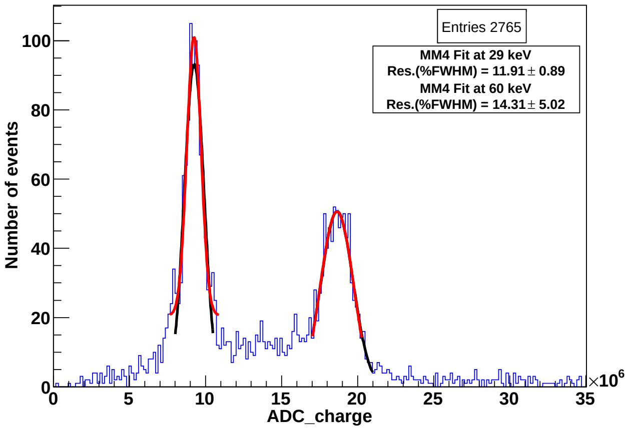

FIGURE 4.27: *Energy spectrum obtained in MM4 for the 13% of teh events passing all the selection criteria in region 1. The fit at 60 keV has a large error. The fit in each peak is done in tww steps over a flat background.*

before have been considered. The resulting spectra are shown in Figures 4.28 and 4.29 for MM1 and MM4 respectively and in the two regions considered. It must be noted that in the called 30 keV peak there is expected to have the contribution of three peaks: one centred at 29 keV from the scape peak of 29.7 and 29.4 keV from Xe and another at 26.4 keV from the 33.6 escape peak. Also at 26 keV is expected a gamma emission of the ^{241}Am with an intensity of 2.4%. In order to perform a two Gaussian fit it is interesting to know the relation between the two peaks. From the simulation shown in spectrum 4.19 we can conclude that in this geometry and with this gas at these conditions the ratio is around 0.3. The fit in the 30 keV region is done in two steps: first of all a Gaussian is defined in a wide range around the peak. With its mean position is defined the range of the second fit (between $\pm 2.5 - 3\sigma$). Secondly, a sum of two Gaussian is defined in this range, one with free parameters for the 29 keV and the second one (fit to the 26 keV) using the sigma of 29keV peak, a relative position of 0.89 (4 keV of difference) and we leave free the amplitude but controlling that the value is around the 0.3 ratio obtained from simulations. This sum of Gaussian is plotted in red (having a χ^2 value above 1). Finally, the separated Gaussian fits are in magenta and blue. The 60 keV has also been fitted in a similar way. As can bee seen in the smaller region for the MM4 this peak almost disappears. This could be because in region 1 around the 15% of the pixels are dead. This effect is more important in the 60 keV peak because the tracks are longer than the ones of 26-29 keV. Therefore, we will evaluate the energy resolution for the MM4 in the wider region 1. In Table 4.6 the results obtained for each Micromegas detector are shown.

An extrapolation to the expected energy resolution at $Q_{\beta\beta}$ can be done using both peaks (at 30 keV and 60 keV). The relation of the energy and the resolution is a quadratic one defined as

$$FWHM^2 = a * E + b, \tag{4.1}$$

where a and b are free parameters that depends on the detector and electronics. At high energy

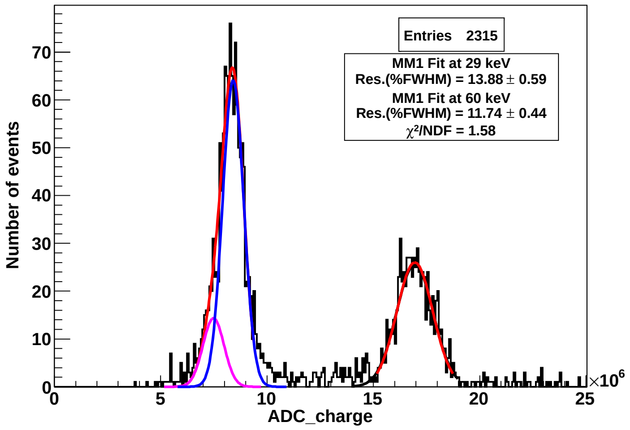

(a) Region 1

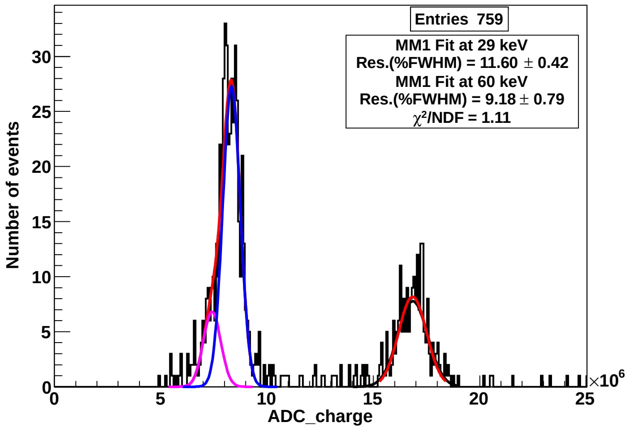

(b) Region 2

Figure 4.28: *Energy spectra obtained selecting events fully contained in a xy region defined by the mean positions of the events in MM1. (a) is the result in region 1 and (b) in region 2 (see Figure 4.25).*

Selection	30 keV peak		60 keV peak	
	Surviving events (%)	%FWHM	Surviving events (%)	%FWHM
MM1				
Region 1	26	13.88 ± 0.59	20	11.74 ± 0.44
Region 2	10	11.60 ± 0.42	6	9.18 ± 0.79
MM4				
Region 1	49	10.35 ± 0.60	31	12.65 ± 0.37
Region 2	13	9.46 ± 0.90	4	16.41 ± 2.58

Table 4.6: *Energy resolution obtained applying the different selections explained in the text for the MM1 in two xy regions.*

usually b could be approximated to 0 while at low energies the discrepancies from a linear behaviour crossing in the $(0, 0)$ are higher. The resulting fits are shown in Figure 4.30 for MM1 and MM4 in region 2 and MM4 in region 1 and 2. In Table 4.7 are summarized the obtained extrapolation to 2458 keV for both cases (line passing by $(0, 0)$ or not, perfect fit) and also calculating the a parameter directly from each peak (assuming that cross in $(0, 0)$). It is

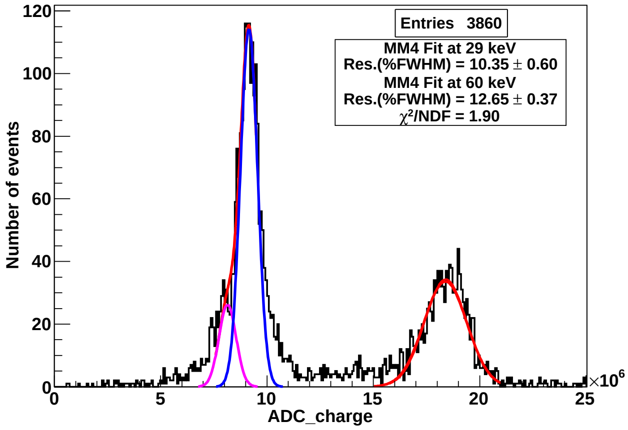

(a) Region 1

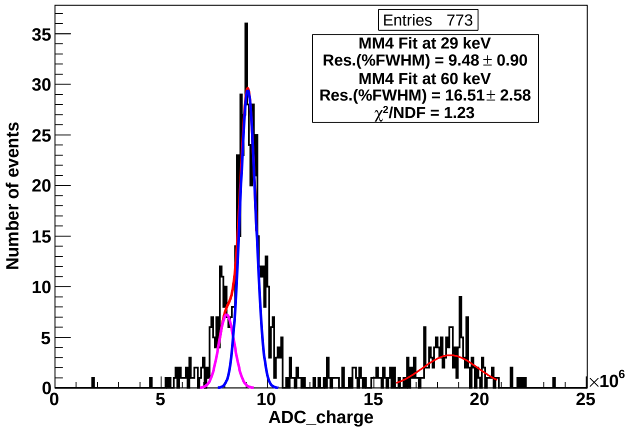

(b) Region 2

Figure 4.29: *Energy spectra obtained selecting events fully contained in a xy region defined by the mean positions of the events in MM4. (a) is the result in region 1 and (b) in region 2 (see Figure 4.25).*

interesting to note that the scaling of the energy resolution is better for the MM1. MM4 has a better scaling in region 1 where the number of active pixels is higher.

In conclusion, MM1 shows a better scaling of the energy resolution because, probably it has a better connectivity (less dead pixels) and in MM4 the 60 keV peak is not so well defined. From MM1 is obtained an energy resolution that extrapolates to a $1.4 \pm 0.4\,\%$ FWHM at $Q_{\beta\beta}$ considering both peaks. In the case of the MM4, as mentioned, the scaling is worst and the best value obtained is of $1.84 \pm 1.03\,\%$ FWHM with an error of 55%. In this case, if we extrapolate with just the 30 keV peak, better defined, an energy resolution of $1.05 \pm 0.46\,\%$ FWHM at $Q_{\beta\beta}$ is obtained. Therefore, in the optimistic case an energy resolution of 1.05% FWHM could be obtained, while, being more conservative, we can affirm than the 1.5% FWHM have been obtained. Results of the same order are obtained when selecting events completely in a *xy* region or when its mean position is contained in a *xy* region, with at least 1000 events in the peak over around 4000-5000 initial events in the peak.

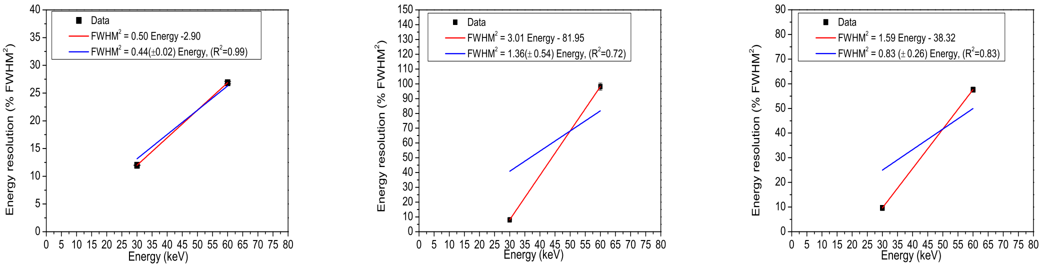

(a) (b) (c)

FIGURE 4.30: *Relation of the square root of the resolution (in FWHM) with respect to the energy. Results are fitted to two different lines crossing or not in (0,0). (a) and (b) are the results selecting events fully contained in the wider xy region (region 2) for the MM1 and MM4, respectively. In (c) is shown the result in region 1 for the MM4, altough in this region the resolution at the 29 kev peak is worse the scaling is better. With these results an extrapolation of the energy resolution to $Q_{\beta\beta}$ of Xe can be done and is summarized in Table 4.7.*

		Energy resolution (%FWHM) at $Q_{\beta\beta} = 2458$ keV
MM1	Linear Fit 1	1.57
	Linear Fit 2	1.40 ± 0.40
	From the 29 keV	1.28 ± 0.34
	From the 60 keV	1.43 ± 0.60
MM4, region 1	Linear Fit 1	2.53
	Linear Fit 2	1.84 ± 1.03
	From the 29 keV	1.14 ± 0.39
	From the 60 keV	1.98 ± 0.48
MM4, region 2	Linear Fit 1	3.48
	Linear Fit 2	2.35 ± 0.54
	From the 29 keV	1.53 ± 0.45
	From the 60 keV	1.83 ± 0.50

TABLE 4.7: *Energy resolution obtained at 2458 keV extrapolating from the results at 30 and 60 keV after applying all the different selections explained in the text and considering fully contained events in a xy region.*

Stability

The stability of the result is evaluated along a week of measurement. In this time the gas was in re-circulation mode and the measurements were done during between 8 and 12 hours per day. In Figure 4.31 the evolution of the peak position and the energy resolution for the 29 keV peak and the 60 keV peak in MM1 are shown, also in red the mean values are shown . In Figure 4.32 the same is shown for the MM4. The values were obtained after the application of all the criteria explained and applying the same analysis to fit the peaks. For MM1 it was considered region 2 and for MM4, since it is more stable, region 1. The spectra are shown in Figure 4.33 and 4.34 for MM1 and MM4 respectively.

A change in the gain is observed implying a change in the energy resolution. Therefore, in order to combine results these fluctuations have to be taken into account. However, the fluctuations in the gain are of the order of 2.5% maximum while for the energy resolution are less than 1%.

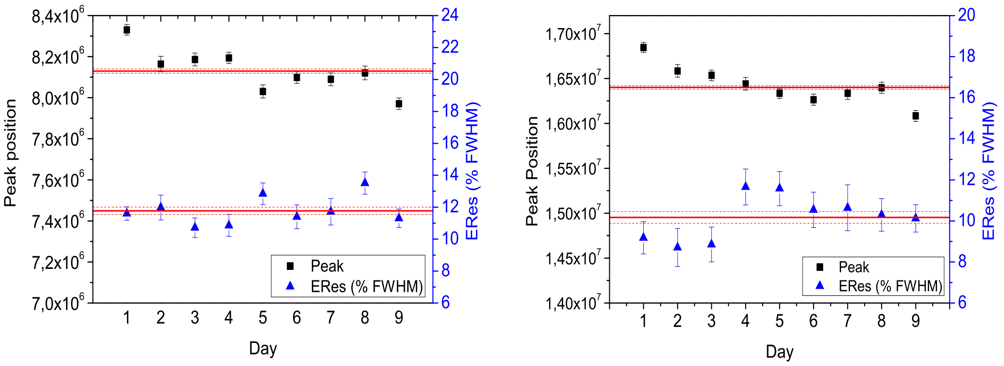

(a) (b)

FIGURE 4.31: *Time evolution of detector gain and energy resolution by studying the ^{241}Am gamma emissions of 29 keV (a) and 60 keV (b) in MM1. Changes are $< 2\%$ and due, probably, by variations in the HV source or in the gas purity.*

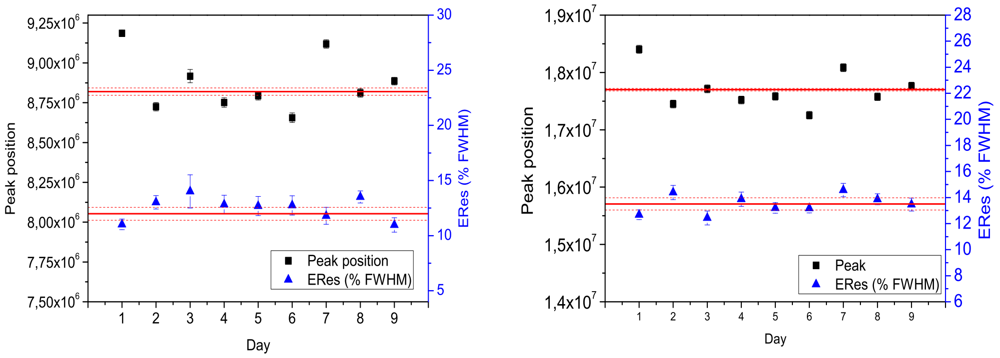

(a) (b)

FIGURE 4.32: *Time evolution of detector gain and energy resolution by studying the ^{241}Am gamma emissions of 29 keV (a) and 60 keV (b) in MM4. Changes are $< 2\%$ and due, probably, by variations in the HV source or in the gas purity.*

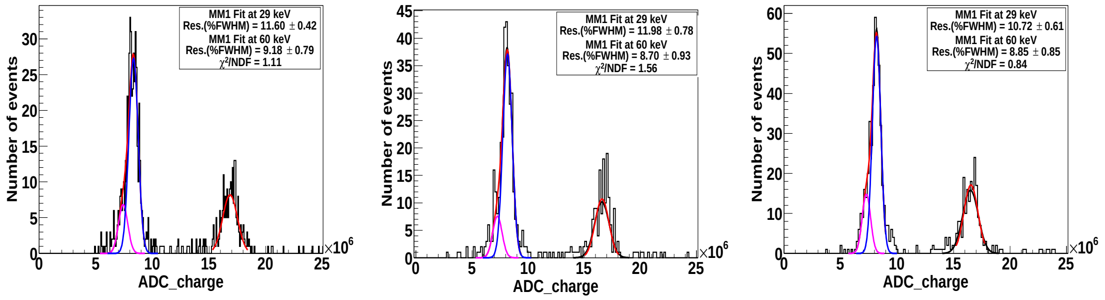

(a) Day 1 (b) Day 2 (c) Day 3

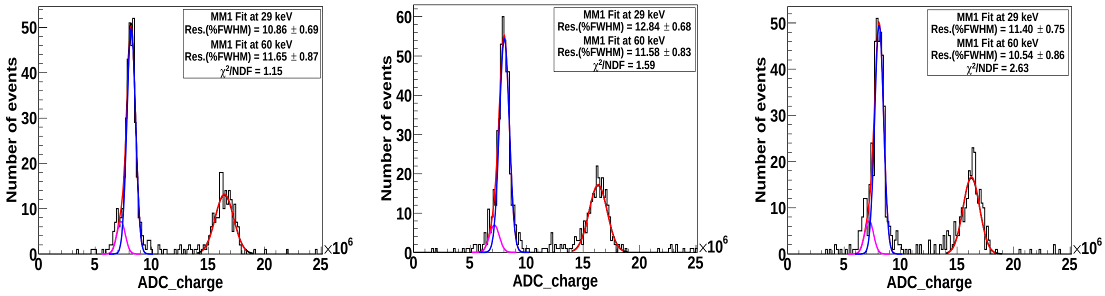

(d) Day 4 (e) Day 5 (f) Day 6

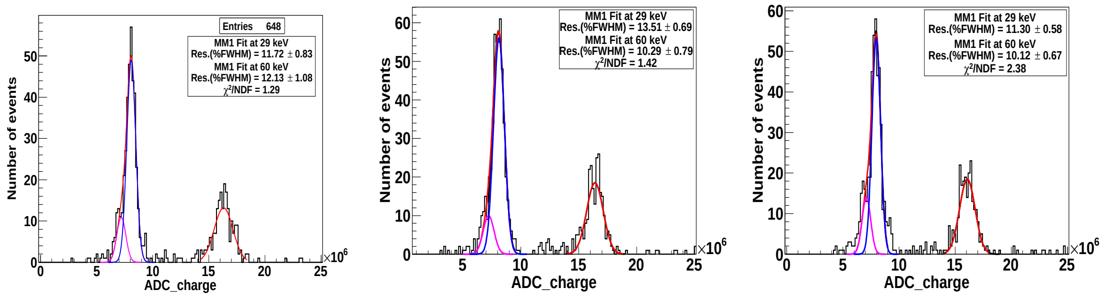

(g) Day 7 (h) Day 8 (i) Day 9

FIGURE 4.33: *Energy spectra obtained in MM1 selecting events fully contained in the 2D region labelled as 1. Results for 8 days of measurement. The spectrum recorded each day is fitted as explained in the text to two Gaussian at 26 and 29 keV and one at 60 keV. Energy resolution results are quite stable along time.*

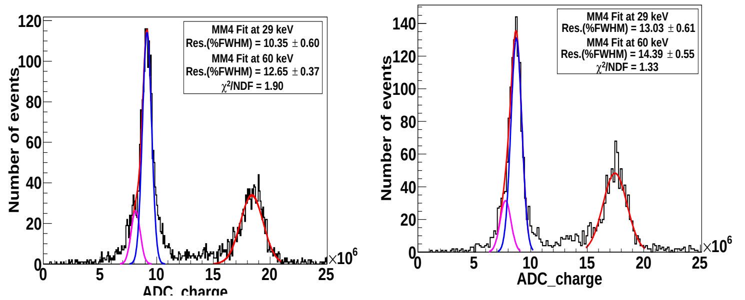

(a) Day 1 (b) Day 2 (c) Day 3

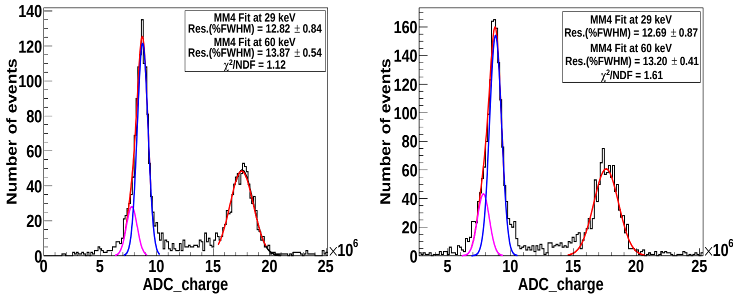

(d) Day 4 (e) Day 5 (f) Day 6

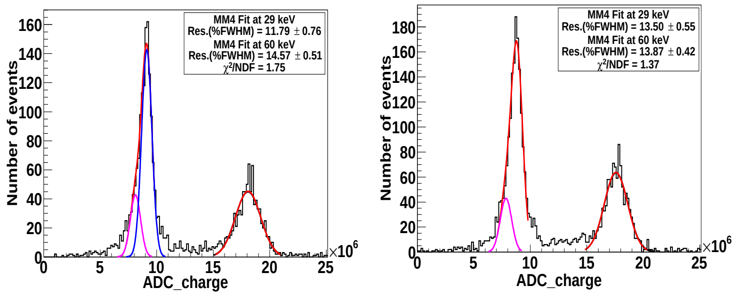

(g) Day 7 (h) Day 8 (i) Day 9

FIGURE 4.34: *Energy spectra obtained in MM4 selecting events fully contained in the 2D region labelled as 2. Results for 8 days of measurement. The spectrum recorded each day is fitted as explained in the text to two Gaussian at 26 and 29 keV and one at 60 keV. Energy resolution results are quite stable along time.*

4.4.2 Drift velocity

Xe-TMA is not a very common mixture but in the last years it has emerged because it can improve the gain and diffusion of the base gas [109]. Recently, the Magboltz program has implemented its cross-sections. In this section we will try to obtain a drift velocity from our measurements than can be compared with the results obtained with Magboltz. In Figure 4.20, as the trigger is done in coincidence with the detectors, it is possible to extract information of the drift time. Therefore, as the beginning of the chamber is at 40 μs and comparing with simulations, we have concluded that the cathode is where the distribution falls down to a flat value again, in this case at $\sim$150 μs, the drift time is 110 μs. Moreover, if only events in the 30 keV peak are selected, the resulted distribution in shown in Figure 4.35, it can be appreciated slightly the change at 40 μs. This drift distance corresponds to 38 cm when the Microbulk has been installed, therefore the velocity of the gas is around 0.35 cm μs^{-1}.

In Figure 2.2 are shown different results for the drift velocity in a Xe-TMA mixture with different proportions obtained with Magboltz. The data discussed here had a concentration of TMA around 3.5% and the drift field was 150 V cm^{-1} at 1 bar, therefore, from the Magboltz results, a value of 0.25 cm μs^{-1} is extrapolated for the velocity in this mixture, 0.1 cm μs^{-1} smaller than the obtained value. However some facts have to be mentioned. First, in a previous measurement done in a smaller TPC the same behaviour [177] was observed: a small increase of the velocity at this drift field with respect to the values from Magboltz. In addition, it has to be noted that previous measurement recirculating through the SAES filter show that it can modify slightly the concentration of TMA along time, either absorbing TMA or expelling it again. Therefore, as we did not measure the concentration of TMA routinely (because of technical problems) it could change at some point. Also, there could be uncertainties in the determination of the cathode plane because the end point of the z distribution is not so well define than in the simulations because, some effects are not implemented like the attachment or others related with the electronic chain (integration of the charge,...). However, they should not come a dominant effect. In addition to these effects, it has to be taken also into account that TMA cross-sections and diffusions have been recently implemented in Magboltz and with data only from simulations. Therefore, it could exist also some uncertainties.

4.4.3 Preliminary attachment results

The attachment, as explained in Chapter 2, produces a loss in the charge detected due to electronegative impurities present in the gas. This charge loss implies a decrease in the gain and in the proportionality of the charge detected to the energy of the particle, therefore it can worsen the resolution. The effect of the attachment has also a dependence with the z position being more important close to the cathode because the electron has to cross all the drift distance and the probability to be absorbed by some impurities is higher. If the z position is represented versus the charge, a slightly negative slope can be observed at higher z's as it is shown in Figure 4.36 (a) (b) for the Micromegas MM1 and MM4 respectively.

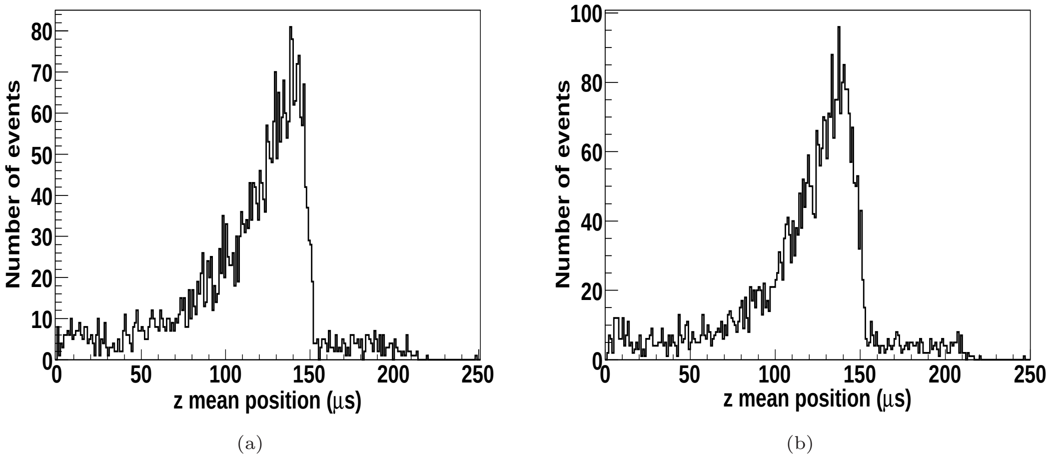

(a)

(b)

Figure 4.35: *z distribution of the events in the 30 keV peak in MM1 (a) and MM4 (b). In (a) the change in the distribution at* 40 *μs can be observed while in (b) it is less clear. In order to obtain the drift velocity the interval from* 40*to* 150 *μs was considered.*

In order to obtain an estimation of the attachment the electron mean-lifetime, τ_e, defined in 2.16 can be calculated. The expression 2.16 can be rewritten in terms of the amplitude or charge, A as

$$A = A_0 e^{-t/\tau_e}. \tag{4.2}$$

If τ_e is large enough with respect to t a Taylor expansion can be done, and fit the exponential to a line, with slope equal to A_0/τ.In order to estimate τ_e a region centred in the peak is chosen, as marked in Figure 4.36, and the mean charge is calculated in z slices of 10 μs each one. In Figure 4.37 is shown the distribution of the mean charge obtained in each slice for the 30 keV peak in the regions defined in Figure 4.36. We decide to do the study only in the 30 keV peak because the energy is deposited in just one cluster of pixels with a better defined z position. The z goes from 40 to 150 μs but in order to determine A_0 in the plot there is an x-axis translation of $x - 40\,\mu$s.

As can be seen in Figure 4.37 the mean charge distribution around the 30 keV region with respect to the mean z position shows two different behaviours: a plateau at low z and a slope with negative slope at higher z. At lower z, close to the Micromegas plane, we are dominated by random coincidences, as is shown in Figure 4.35. Also from this Figure we can see that the signal detected in coincidence with the Si starts to be a 10% dominant over the random coincidences at 100 μs. Therefore a fit is done for the last points obtaining a mean electron lifetime of 1.08 ± 0.12 ms in MM1 and 1.80 ± 0.25 ms in MM4. For the NEXT-MM drift distance of 38 cm an electron lifetime several times the drift time (of 110 μs) is desired, and with the current setup it is achieved. However, in the case of a bigger TPC that can handle 100 kg, the drift distance will increase up to 1.4 m, hence τ_e has to be several time 428 μs if operating with this Xe-TMA mixture, and even more for the future step with 1 ton of mass the drift distance will doubled. All this is supposing a knowledge of the t_0 of the event. The requirements are

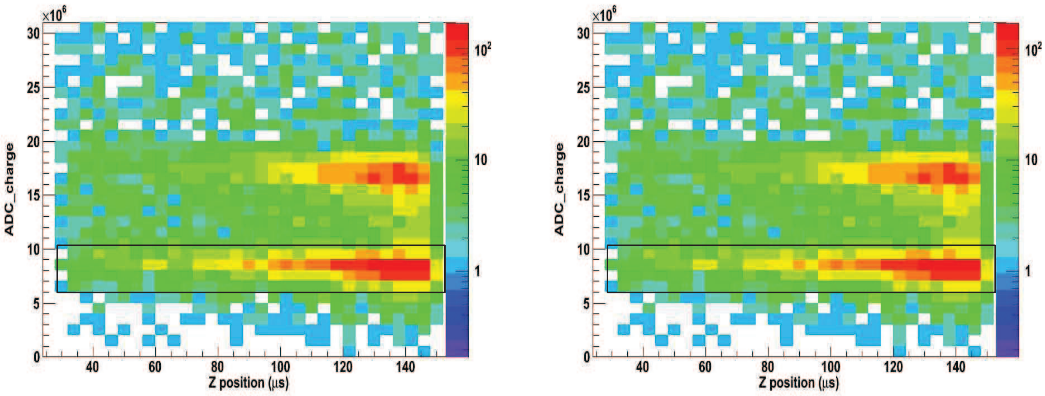

(a) (b)

FIGURE 4.36: *2D plot of the position z of the events versus their energy (in logarithmic scale) in MM1 (a) and MM4 (b). In the black rectangle is indicated the region used to calculate the attachment (see text for details).*

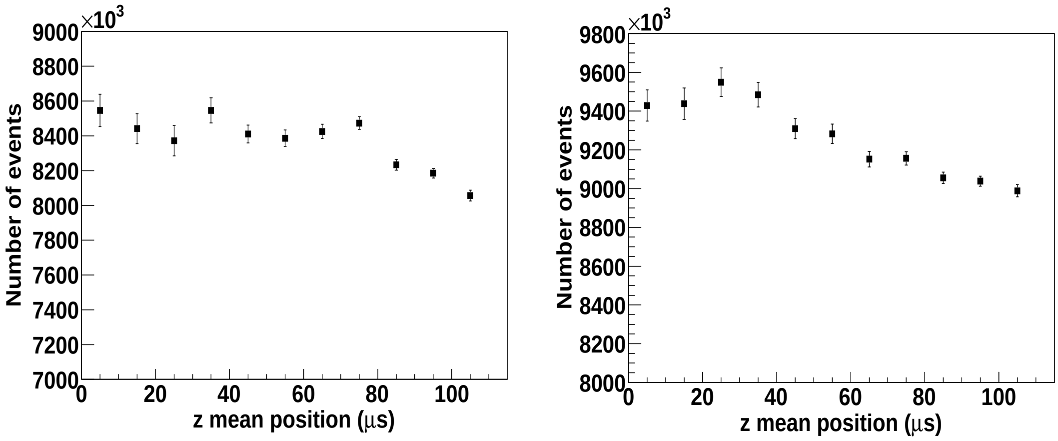

(a) (b)

FIGURE 4.37: *Mean charge distribution calculated in different z slices in the regions marked in Figure 4.36 for the 30 keV peak in the different Micromegas (a) Result for MM1 and (b) for MM4. In both cases, at lower z we are dominated by the effect of random coincidences and it is difficult to conclude something, However, from 60 μs, a decrease in the gain is observed that can be associated to attachment.*

more restrictivet if t_0 is not determined, demanding gain variations of the order of probably 1% along the drift distance.

4.5 Summary

The NEXT-MM prototype is routinely taking data. Here, first setups and results in Xe-TMA at 1 bar have been discussed. One of the objectives of the prototype has been fulfilled, as it was to prove the operation of the detectors in a long drift distance TPC. First results regarding attachment and purity of the gas show the capability to work with this setup. Moreover, another important point was the topological reconstruction of tracks. First tracks were obtained in a high-phenomenology setup (with two gammas calibration sources) identifying the expected length for each peak in one detector. The next step was to take data with more than one Micromegas active. First electron tracks and muons crossing different detectors have been shown. In addition, first energy resolution estimations are promising for a neutrinoless double beta decay experiment, extrapolating to around 1.5% FWHM at $Q_{\beta\beta}$ with a first analysis. In addition, it was the first time that microbulk Micromegas of these dimensions (sectors with a radius of 15 cm covering a surface with a diameter of 30 cm) have been fabricated and tested. First results of the state-of-the art of them show the high quality of these detectors and are very promising. The slight differences found between them can be reasonably improved with the progress of the manufacturing process. In conclusion, it have been proven the capability to perform calorimetry and tracking using the pixels plane.

The next steps are clearly focused in two directions. First, regarding the setup, the started-up of the RIM to improve the field lines from the drift field to the mesh, can make a clear improvement in recollection and, hence, in the energy resolution. Also, further steps are to go to higher pressures and to test the detectors in pure Xenon. Secondly, efforts have to be put to improve the analysis. One of these steps, is to reconstruct the events in different clusters or tracks and analyse them separately, in such a way as in the REST code does for the simulated event. We will discuss this code in detail in the next part of the work. Also important would be to correct the energy by the pixels gain, that can vary from one part to another (however, variations less than 1% are expected) and by the Micromegas gain.

Part III

Physics potential of a $\beta\beta0\nu$ experiment with Micromegas in a HP Xe TPC.

The use of a Xenon gaseous TPC as calorimeter for the neutrinoless double beta decay search of ^{136}Xe has only recently been considered competitive, after the new developments with MPGD. The Gothard's TPC [89] was pioneer on this approach showing the enhanced capabilities of background discrimination based on the topology of the events reconstructed in the TPC. This idea has been recently resuscitated by the NEXT (Neutrino Experiment with a Xenon TPC) collaboration [68].

The state-of-the-art Micromegas readouts has demonstrated its features for the $\beta\beta0\nu$ searches as its excellent energy resolution [108, 109] and their high radiopurity [156]. Micromegas detectors combined with a gaseous TPC can fulfil the requirements for an experiment in terms of background rejection and energy resolution. ^{136}Xe is considered a good $\beta\beta0\nu$ isotope regarding their nuclear structure, that it is easily enriched, and its high $Q_{\beta\beta}$.

In this part of the work it is studied the different expected backgrounds in a high pressure TPC for the ^{136}Xe $\beta\beta0\nu$ search. A full simulation has been done to generate the particles and their interactions inside the TPC. Also it has been simulated the physical processes that occurs in a TPC with a pixelized detector: ionization, diffusion (two different diffusion coefficients have been studied) and pixelization of the charge. Specially, the topological differences between background and signal events are studied and are used to develop discrimination algorithms that allow to decrease the background to the requires level. Finally, preliminary values of the background and sensitivity for a possible 100 kg HP Xe TPC experiment equipped with Micromegas have been obtained. These algorithms have been also used to evaluate the sensitivity for a 1 ton extension of the experiment.

Chapter 5

Background studies and discrimination algorithms

Contents

5.1 Simulation codes 126

5.1.1 Decay0 127

5.1.2 Geant4 127

5.1.3 Simulation of the Physical system and anylisis: RESTSoft 128

5.2 Simulated Events 131

5.2.1 Signal 131

5.2.2 Background 133

5.3 Simulated geometry 137

5.4 The topology of the events 138

5.4.1 Signal Events 138

5.4.2 Background 139

5.4.3 Deterioration of pattern recognition 142

5.5 Discrimination Algorithms 149

5.5.1 A figure of merit for background reduction 149

5.5.2 Energy 150

5.5.3 Track selection 150

5.5.4 Topology Selection 153

5.5.5 Fiducial rejection 160

5.5.6 Summary 160

5.6 Background Rejection 160

5.6.1 High diffusion gas: Pure Xenon 161

5.6.2 Low diffusion gas: Xenon-TMA. 162

5.6.3 Comparison between the two diffusions 163

5.6.4 Surviving events 165

5.7 Energy Resolution studies 168

5.8 Background level 173
5.9 Sensitivity for the neutrino effective mass 178

The sensitivity in a neutrinoless double beta decay experiment, depends on several factors like the background level, the detection efficiency of the expected events or the energy resolution of the detectors. All these factors are related to the intrinsic characteristics of the experimental setup. To evaluate them and, specially, to have a good knowledge of the background, it is important to develop precise Monte Carlo simulations that take into account the geometry of the setup as well as the generation of the charge in the gas. The understanding of the background can also help to develop discrimination algorithms to distinguish between background and signal events. A gas time projection chamber (TPC), combined with a pixelized Micromegas detector, offers a very high spatial resolution [148] which can help to identify events: for example, in the case of a muon it will be a long straight line crossing all the detector or an alpha event in a high pressure gas chamber will be a short track with a high concentration of charge as shown in previous chapter. The characterization of the signals and background expected in the experiment before the data-taking starts is an important point in order to know the expected background rate and to develop analysis tools.

In this chapter, a description of the simulation codes used to generate events and to study their interactions is presented as well as a discussion of the main backgrounds concerning an experiment searching for $\beta\beta0\nu$ in Xenon. The topology of the signal and background events is studied. Then the chapter continues with a description of the selection criteria applied, several of them based on the topology of the events. In the next section the algorithms developed are applied on the simulated backgrounds and signal events. Two different conditions of diffusion are considered and the rejection power and efficiency are computed in both cases. In addition, the nature of the surviving background events and rejected signal is studied. Moreover, different energy regions are considered and the rejection factor on them obtained. In the last section, the background level produced with the surviving events is calculated based on measured activities of materials and it is also obtained the expected sensitivity to the effective neutrino mass with these background levels, efficiency and different energy resolutions.

5.1 Simulation codes

A full Monte Carlo simulation has been performed to produce the events in a TPC filled with Xe gas at 10 bar. The interactions and processes that the events suffer in the gas, as well as the physical processes that occur in a TPC and the analysis of the events, are implemented in three logical blocks.

1. Generation of signal and background events in a gas
    - Diffusion studies with Magboltz and event generation with Decay0.
    - Simulation of the geometry and the interactions of the particles with Geant4.

2. Simulation of the physical system: diffusion of the ionization charge and simulation of the readout pixelization.
3. Analysis with a code based on C++ and implemented in ROOT: RESTSoft

In the following, the different steps of the simulation chain are described in detail.

5.1.1 Decay0

Decay0 [178] is a FORTRAN code developed in the 90's to generate double beta decay events (with and without neutrinos) and in general, radioactive isotopes which study can help in the search of a double beta decay. Decay0 is structured in two main parts:

- INIT searches and interprets the nuclear parameters and decays needed to carry out the simulations. The data are read mainly from the libraries *Evaluated Nuclear Structure Data File* (ENSDF) [179] and *Evaluated Atomic Data Library* (EADL) [180] in order to build up the nuclear and atomic decays diagrams.
- GENDEC, a Monte Carlo event generator. From it, an ASCII file is obtained containing all the information about the final state of the decay: energy, time of emission, direction and polarization of all the final particles produced in the decay (electrons and positrons from single and double β decays, alpha particles, ...). Each collection of particles is called an event.

5.1.2 Geant4

Geant4 (GEneration ANd Transport) [181, 182] is a program that allows users to simulate complex geometries and the transport and the interactions of the elementary particles through the different materials. It was initially conceived for high energy experiments but the latest versions, based on C++, have been developed in a much more multidisciplinary way allowing their application to medicine, biology, aeronautics and radioproteccion. This development also contains the simulation of low energy particles including the double beta decay range of energies.

The package Geant4 has a set of simulation tools that allow users to define a complete experimental setup: definition of the geometry and materials, transport and interaction of the particles through them, detector response, events management and visualization. The interaction radiation-matter can be studied through a wide range of libraries that describe the physical processes. About the particles, Geant4 offers a wide library based on the data published by the *Particle Data Group* [70] where the particles and their main characteristics are described. The modular architecture of the program allows to use just the needed tools in each case optimizing the simulation. The physical processes are described in [183]

For the presented work a specific Geant4 code with a specific geometry have been used and modified; the Geant4 version used was the 4.9.2.p02. As Geant4 is developed in C++, a class structure has been created by the user with the desired setup. In Table 5.1 the different classes of the package used are summarized. Some of them are mandatory and others are optional. In the table is also marked which classes of the developed code are implemented. In all Geant4 codes it is mandatory to have a *G4RunManager* that is the control class. It is responsible for all the initializing processes to build and run the simulation, for example, how the detector should be constructed or the particles and physical processes to be simulated. For the generation of the particles, using the *G4UserPrimaryGeneratorAction*, a specific routine was implemented to use Decay0 files as input events. In the Physics List a flag is introduced to be able to follow the different interactions. This information is very useful to study the secondary emissions as it will be discussed later in 5.4.3 and in Section 5.6.4. Finally a class called *Hits* records the information of the initial vertex, simulated particles and the hits, defined as any deposition of energy in the sensitive volume. The events are then saved in a binary file controlled by the *DataOut* class. A *Manager* reads a configuration file where the dimensions of the geometry, type of events and output paths are given. A diagram of the class structure of the specific code developed is in Figure 5.1.

Geant4 Class	Character	Methods	Functions	User Class implemented
G4VDetector Construction	Mandatory		Materials, geometry &sensitive volumes definition.	DetectorConstruction and PhysicsList
G4User PhysiscsList	Mandatory	ConstructParticles, ConstructProcess, AddTransportation, SetCuts	Particles def., physical process added and cuts values.	DetectorConstruction and PhysicsList
G4UserPrimary GeneratorAction	Mandatory	GeneratePrmaries	Position,direction type and energy of the primary particles.	Generator
G4User EventAction	Optional	BeginOfEventAction, EndOfEventAction AddTransportation, SetCuts	Initialize variables and tools of each simulated event.	EventAction
G4User SteppingAction	Optional	UserStepping Action	Epecific tools of each step of the simulation.	SteppingAction

Table 5.1: *Definition of the Geant4 classes that have to be defined by the user (optional or mandatory), including their methods and functions. It is also mentioned in which class of the specific code developed are inherited.*

5.1.3 Simulation of the Physical system and anylisis: RESTSoft

A TPC uses a readout detector which registers the ionization charges produced in the interaction of particles with the gas molecules, as explained in Chapter 2. The output of the Geant4 simulation is a binary file with a collection of energy deposits defined as hits. A software structure called **RESTSoft** (Rare Event Search TPC Software) has been used to reproduce the specific features of a TPC and to analyse the events. It was initially conceived for dark matter searches in 2005 and afterwards implemented for double beta searches [138]. For a previous application in double beta searches, [138] can be consulted. For an application on dark matter searches, [174] can be read. In this work, an implementation for the application to high diffusive gases,

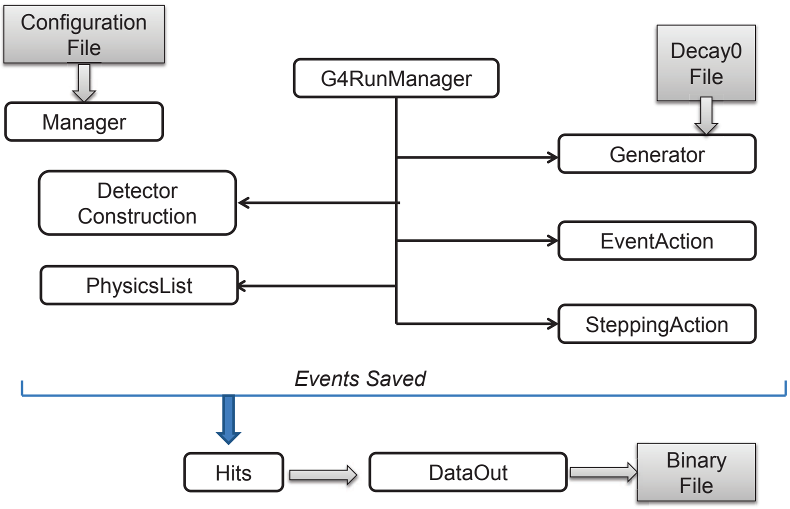

Figure 5.1: *Sketch of the Geant4 simulation code used. A configuration file is read with the geometry information and output paths. The program is implemented to read Decay0 files that are used as initial particles. After the generation of the interactions the events are saved as hits in a binary dataout file.*

as Xenon, has been carried out and the discrimination algorithms have been changed optimizing the efficiency to 40% while keeping a high rejection factor.

RESTSoft is a software structure based on C++ classes. It is implemented with ROOT [184] for recording data in an organized way and to produce plots. RESTSoft has a modular design to simulate each component of the TPC and to do the analysis of the final events. The general sketch of the simulation of a double beta event, with the different functions involved, is presented in Figure 5.2. Four methods are used:

- *ConversionPhys:* The output of the Geant4 simulation is read and each event converted to an object called TRestG4Event. Each event is recorded in a branch of a ROOT tree that contains the information of the initial particles and the list of hits. An object called TRestSetup is also created with the information of the geometry simulated with Geant4.
- *ConversionDaq:* method that converts the Geant4 output event to a pixelized event. The gas diffusion and the effect of the electronics is simulated in this step with three auxiliary methods: *TRestCharge(), TRestDrfit() and TRestPixelize().* These methods create the charge, simulate the gas diffusion and the pixelization depending on the real detector to be used (in this case a Micromegas detector). Each converted event is recorded into an object called *TRestDaqBB* and saved in a ROOT tree. Also at this level an EventBrowser has been developed using ROOT that allows to visualize the reconstructed event in 2D projections and also in its 3D view. Examples will be presented later. This can help to

validate the methods and to think of possible topological differences between signal and background

- *Analysis:* in this step the discrimination algorithms explained in 5.5 are applied. The method defines a list of variables called observables and the analysis over each event gives a value for each observable recorded in leaves of a branch. Those objects are in ROOT language subfolders which keep a relation, i.e., it is possible to get for each analysed event the values of all its observables.
- *PlotAnalysis:* to load an analysed file and to plot its observables in ROOT histograms or graphs. A condition can be imposed and then only the events that fulfil it will be selected and plotted.

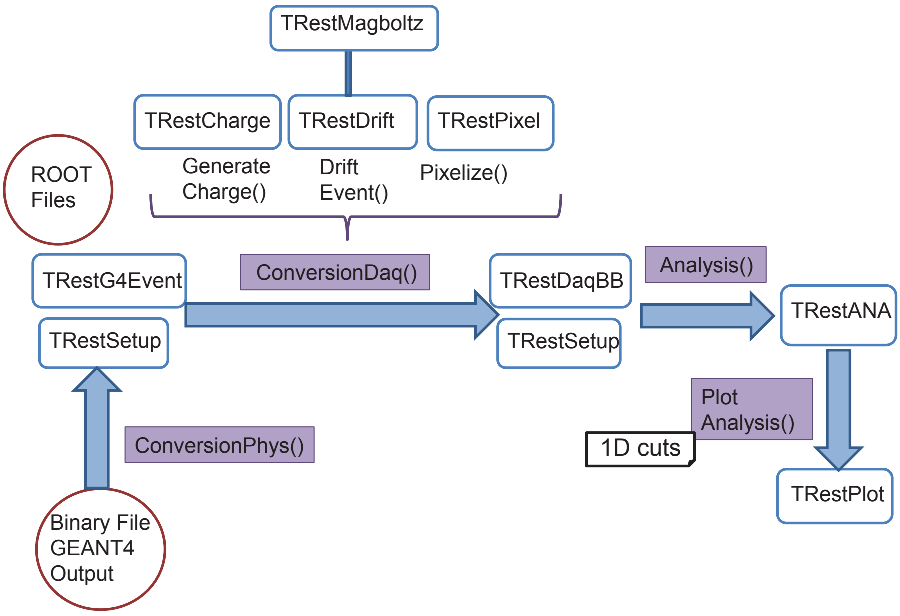

FIGURE 5.2: *Sketch of the simulation and analysis chain. First of all the Geant4 output is converted into a ROOT file. Afterwards, the charge generation, diffusion and effect of the readout pixelization is applied to the events. Finally, the analysis algorithms are applied with the possibility to perform different selections and plots.*

In order to generate the features of the TPC in the second step, first of all the charge created by an energy deposition is calculated. Based on the ionization process explained in Section 2.1, it is obtained using the W-value of the gas under consideration. Therefore, for an energy deposition E_{dep}, the charge deposited, is $Q_{dep} = E_{dep}/W_{gas}$. Charge fluctuations are not included in this step.

Once the charge of the interaction is calculated, the diffusion effect is simulated. As it was explained in 2.2.1, due to the transport theory of gases, the width of the electron cloud produced in the ionization of the medium increases along their drifting to the readout. To reproduce this effect, the position of each energy deposition is varied following a Gaussian distribution. First of all, the diffusion coefficients, σ_T and σ_L, are obtained with Magboltz. The values used were summarized in Table 2.1. Then, the diffusion after a distance z is calculated multiplying the square drifted distance by the corresponding coefficients, $\sigma_i(z) = \sigma_i \times \sqrt{z\,(cm)}$. With these new diffusion values, $\sigma_T(z)$ and $\sigma_L(z)$, the final position of the event is attained running in each direction by a random number obtained from a Gaussian distribution. The Gaussian is centred in 0 and with a width given by the diffusion coefficients obtained. The final position is

$$x = x_0 + \delta_t \times cos(\theta), \tag{5.1}$$

$$y = y_0 + \delta_t \times sin(\theta), \tag{5.2}$$

$$z = z_0 + \delta_l, \tag{5.3}$$

$$\tag{5.4}$$

where δ_t and δ_l are the two values generated by the Gaussian distribution and θ is an arbitrary angle between [0,2π]. (x_0, y_0, z_0) is the initial position of the event.

Finally, the granularity of the readout is introduced. Charges are grouped into pixels (boxes). The length of the box is defined by the user according to the readout device. In all the work presented here, it is of $1 \times 1\,\mathrm{cm}^2$.

Once the TPC and readout features are included in the interactions produced with the Geant4 code, the next step, the analysis, follows. It will be described in detail in Section 5.5 where the discrimination algorithms are presented.

5.2 Simulated Events

In order to develop discrimination algorithms and to design the experiment a simulation of the different events is needed to understand the detector performance. The simulated events can be divided into two categories: events simulating the expected signal, and background events.

5.2.1 Signal

The expected signal is the $\beta\beta0\nu$ decay of ^{136}Xe. If both electrons emitted in the process deposit all their kinetic energy in the fiducial volume, this signal will have an energy equivalent to the transition energy of the decay, which value is $Q_{\beta\beta}(^{136}\mathrm{Xe}) = 2458.7 \pm 0.6\,\mathrm{keV}$ [158].

To generate these events the program Decay0 has been used. As commented before, it can generate double beta decay events in their two modes, with or without emission of neutrinos. For the expected signal the electrons produced in the $\beta\beta0\nu$ mode will be considered. The mode $\beta\beta2\nu$ has been recently measured by [45] and [104], and it is treated as background in this work because for energy resolutions better than a 10% FWHM its contribution has been calculated to be below $10^{-4}\,\mathrm{c\,keV^{-1}\,kg^{-1}\,y^{-1}}$. Therefore, the expected signal generated by Decay0 is the nuclear transition

$$^{136}_{54}Xe \rightarrow ^{136}_{56} Ba + 2e^{-}. \tag{5.5}$$

In this kind of transitions, the electrons are emitted in the S and P states respectively, and with an angular momentum of $j = \frac{1}{2}$ [185]. The final state is the fundamental state so the transition energy is shared between the emitted electrons. For a comparison with the ^{76}Ge the reader is referred to [17]. The angular distribution have been evaluated in [138] and corresponds to the correct angular distribution shown in [186].

The distribution of events resulting from the analysis chain after the charge creation, diffusion and pixelization (explained in Section 5.1.3), and before the application of any event selection, is shown in Figure 5.3. At the left it is the distribution obtained where the expected peak at $Q_{\beta\beta}$ can be seen as well as the region at the left of the peak that corresponds to events that lose some energy due to Bremsstrahlung radiation. The escape peak of Xenon at ($Q_{\beta\beta} - 30\,\mathrm{keV}$) (shell energy) can also be seen. At the right it is observed the same spectrum after it was convoluted with a Gaussian with sigma corresponding to an energy resolution of 2% FWHM at $Q_{\beta\beta}$. This is the considered energy resolution along the analysis of the simulated events and it defines a Region of Interest (RoI) of 100 keV around $Q_{\beta\beta}$. However, the events are simulated without taking the resolution into account. This is higher than the energy resolution for most of the current experiments as mentioned in the first chapter, as well as the expected using Micromegas detectors; but a higher energy window allows a better understanding of the backgrounds. In Section 5.7 there will be a discussion of the effect over the efficiency and rejection power if the energy resolution is better.

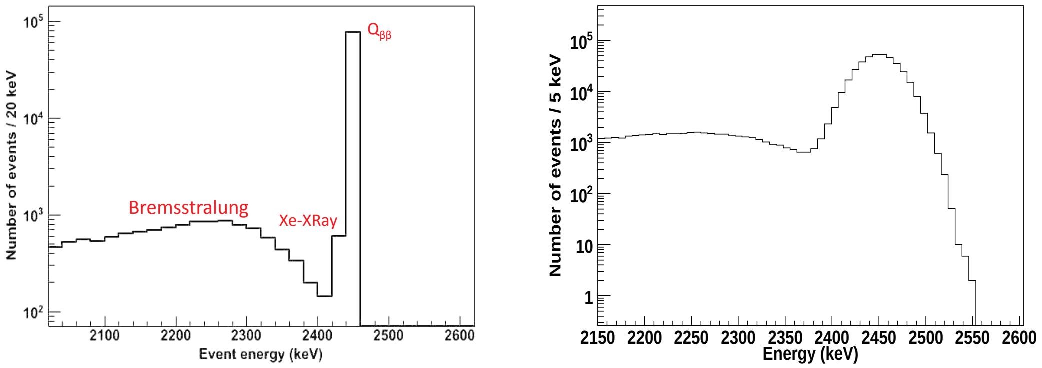

(a)

(b)

FIGURE 5.3: *(a) $\beta\beta0\nu$ spectrum simulated. The main peak is the $Q_{\beta\beta}$ signal at 2458 keV. Also visible are the escape peak of the Xe X-ray at $Q_{\beta\beta} - 30$ keV and the tale where some of the events have lost part of their energy due to Bremsstrahlung radiation. (b) Same spectrum after its convolution with a Gaussian function to take into account the energy resolution effects (an energy resolution of 2% FWHM have been applied). The escape peak is not distinguished now.*

5.2.2 Background

The other group of events to simulate is the background. In chapter 1, the main components that contribute to the background in a $\beta\beta0\nu$ experiment are described in general. Before starting any simulation, it is useful, first of all, to analyse which contributions can be neglected and which ones cannot, in order to optimize the simulation-time. A factor that can help to decide which isotopes are desired to be simulated is the energy window or region of interest (RoI) of the experiment. Anything well below the $Q_{\beta\beta}$ energy can be neglected. It is not the same for particles with higher energies because, through different processes, they can lose part of their energy and end up in the energy window. The RoI considered in the main parts of the work, as commented, is from 2400 to 2500 keV (that represents, roughly, an energy resolution of 2% FWHM at $Q_{\beta\beta}$).

Another natural selection is to divide the contributions for the background into internal and external. *Internal* embraces any contribution coming from the detector itself as it could be the construction materials, the electronics or the $\beta\beta$ emitter. *External* includes any contribution coming from the environment, as the walls of the laboratory or the radon in the air. The external component produced by gammas is reduced using passive shielding. For muons an active veto can be used. In the case of the internal contribution, there are not only gammas but also electrons and alpha particles depositing energy in the sensitive volume.

Internal contaminations

The materials for the detector setup and shielding contain impurities of radioactive elements. Natural radioactivity decay chains of ^{232}Th and ^{238}U and the isotopes of ^{40}K and ^{60}Co are the most important ones.

^{40}K emits a gamma of 1460 keV, and is only relevant for the $\beta\beta2\nu$ mode. ^{60}Co can appear by cosmogenic activation of the copper. It consists of a β emission of 318 keV and two gammas of 1173 and 1332 keV. Different physical processes can allow these three particles to deposit energy in the RoI but their contribution can be easily rejected through the analysis as shown in [138], due to the fact that they deposit their energy with a large spatial separation producing a multi-track event. In general, alpha decays are easily identified and rejected because they will leave all their energy in small tracks close to the walls.

^{232}Th Chain

In the natural decay chain of ^{232}Th the only emission that can deposit energy in the RoI is the ^{208}Tl produced by the ^{212}Bi decay. In Figure 5.4 its energy levels are shown; the 99% of the times it decays emitting a gamma with an energy of 2615 keV, higher than the $Q_{\beta\beta}$ value but that can deposit an energy in the RoI by several processes that will be discussed in detail later on.

^{238}U chain

The main isotope from this chain than concerns in the search of the ^{136}Xe $\beta\beta0\nu$ is the ^{214}Bi. In this case, several gamma emissions, summarized in Table 5.2, can deposit energy in the RoI. The levels with an intensity higher than a 1% are shown in Figure 5.5. Among them, there is a

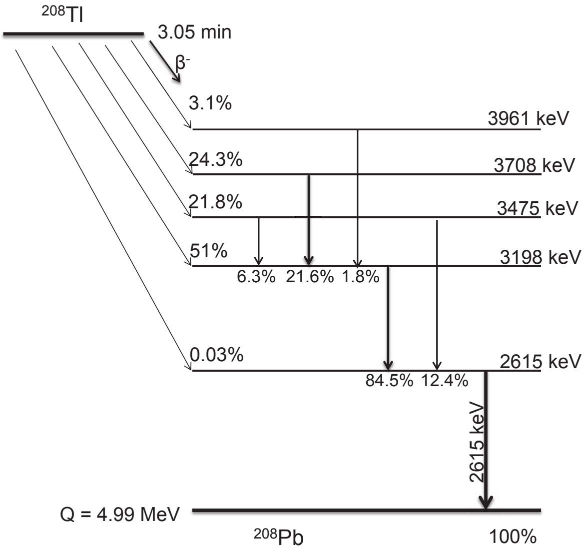

Figure 5.4: *Decay levels of the ^{208}Tl. The diagonal arrows are β decays and the vertical arrows are γ decays. The percentages indicate the decay probability.*

beta emission with a transition energy of 3272 keV and a gamma emission of 2447 keV combined with a beta emission of 824 keV. Also important is the ^{222}Rn since it decays 88% of the times into ^{214}Bi also.

Energy (keV)	Intensity(%)	Energy (keV)	Intensity(%)
2447.9	1.57	2921.9	0.01
2694.7	0.03	2978.9	0.01
2769.9	0.03	3053.9	0.02

Table 5.2: *Gamma emissions of the ^{214}Bi isotope with energies higher than 2.4 MeV.*

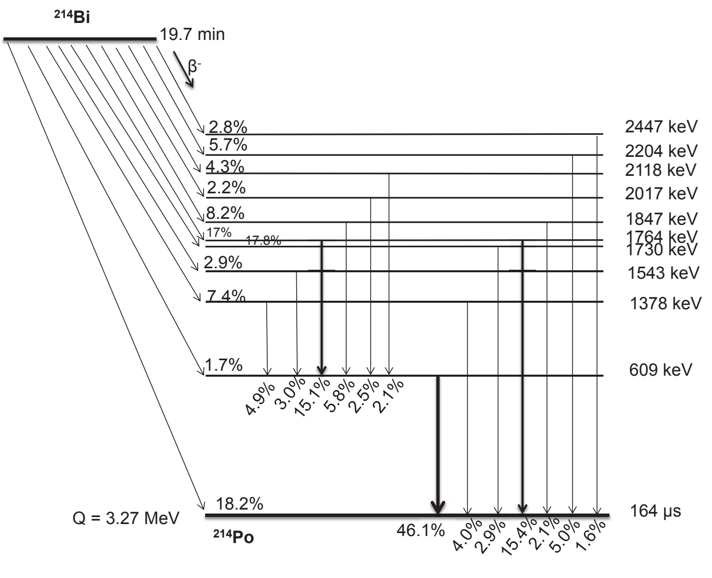

Figure 5.5: *Decay levels of the ^{214}Bi. The diagonal arrows are β decays and the vertical arrows are γ decays. The percentages indicate the decay probability.*

Double beta decay

The source of the $\beta\beta0\nu$ decay, the ^{136}Xe has also some contaminants from ^{232}Th and ^{238}U. These activity have been measured in the Gothard experiment being at the level of 5×10^{-12} g^{232}Th/g and 9×10^{-12} g^{238}U/g. Xenon can also be activated cosmogenically, ^{136}Xe(n,γ)^{137}Xe by neutron capture. ^{137}Xe has a beta emission the 67% of the times with an energy of 4173 keV and the 30% of times a beta plus gamma emission of 3173 keV and 455 keV respectively. The initial activity, A$_0$, is defined

$$A_0(kg^{-1}d^{-1}) = R\left(1 - e^{-\lambda t_{exp}}\right), \tag{5.6}$$

where R is the production rate, λ is decay constant and t_{exp} is the exposure time. As its decay half-life is very short (3.8) minutes, the initial activity is equivalent to the production rate. With this half-time its contribution is negligible.

For the $\beta\beta2\nu$ mode, its contribution to the $\beta\beta0\nu$ can be calculated with Equation 1.25. Taking into account the recent results presented in [45] and [104] for the $T^{2\nu}_{\frac{1}{2}}$ and the limits for the $T^{0\nu}_{\frac{1}{2}}$ the fraction of $\beta\beta2\nu$ in the RoI of the $\beta\beta0\nu$ mode is 2.2×10^{-9}. Hence it can be neglected with a 2% FWHM at $Q_{\beta\beta}$.

External contaminations

Among the possible external contaminations, the muons can be clearly reduced when working underground. Specifically, in the Underground Laboratory of Canfranc (LSC, 2450 m.w.e) the flux is reduced by 5 orders of magnitude as shown in Figure 5.6, where different underground laboratories are compared.

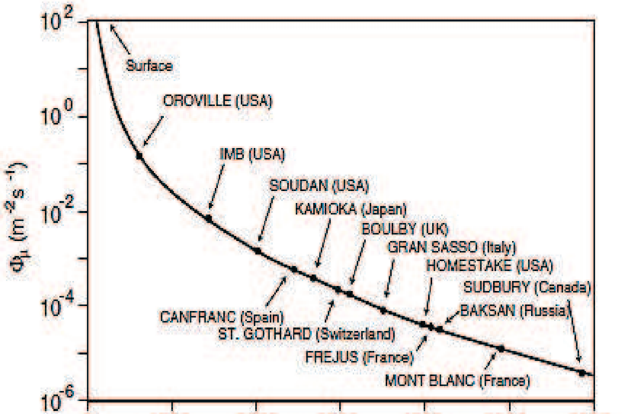

FIGURE 5.6: *Graphic where the flux of muons measured in different underground laboratories is shown. In the case of the Canfranc Underground Laboratory this flux is of the order of* $10^{-3}\,m^{-2}s^{-1}$.

The other main contribution comes from the natural radioactivity chains of contaminants present in the laboratory rocks. As they are generated outside the setup, only energetic gammas can reach the detector. Although their contribution maybe higher than the internal one, a passive shielding, usually made of lead or water, can reduce it to levels below those of the internal components. Studies about which thickness is needed in each case to have a background level of the order of few 10^{-4}c keV^{-1} kg^{-1} y^{-1}, have been performed. Simulation of gammas coming from the laboratory walls have been carried out. An external flux of $0.13\,\gamma/cm^2/s$ (from measurements in the LSC [187]) has been considered. Then a water shielding surrounding the detector was simulated, considering three different thicknesses: 30, 50 and 100 cm.Without shielding and using as input the $0.13\,\gamma/cm^2/s$ flux a background of 10 c keV^{-1} kg^{-1} y^{-1} is produced after the application of the rejection criteria that are explained later. In order to obtain a rejection factor of 10^6, as from internal contaminants (see Section 5.6), a 300 cm thickness of water is needed. Another option is to use radiopure lead. Taking into account that it has a density 12 times higher than water it can be calculated that, to obtain the same rejection factor, a thickness of lead of around 25 cm is needed. It is also important the Radon present in the air because it decays into ^{214}Bi. A way to reduce its contribution is to purge the volume between the shielding and the detector with Nitrogen.

Summary

After these discussions, the simulated events to be considered in this work are:

- $\beta\beta0\nu$ events: signal events generated with Decay0 and homogeneously emitted inside the fiducial volume of the Geant4 geometry previously defined.
- ^{208}Tl: the complete decay chain of this isotope using Decay0 file as input for the Geant4 geometry. It has been simulated for the different geometrical elements discussed in Section 5.3.
- ^{214}Bi: the complete decay chain of this isotope using Decay0 file as input for the Geant4 geometry. It has been simulated for the same geometrical elements as for ^{208}Tl.

The number of simulated events are summarized in Table 5.3. They have been analysed assuming two diffusions, high diffusion as in pure Xenon or Argon, and a low diffusion like in Argon-Isobutane or in a Xenon mixture with, for example, Trimethilamine (TMA). The number of simulated events in all cases is more than one million with the intention that for all the estimations and calculus done with them, statistical relative errors, smaller than the 1%, are obtained.

Events ($\times10^7$)	$\beta\beta0\nu$	Vessel		Field Cage		Readout		Cathode	
		^{208}Tl	^{214}Bi	^{208}Tl	^{214}Bi	^{208}Tl	^{214}Bi	^{208}Tl	^{214}Bi
Pure Xe	0.12	1.7	19.7	1.6	6.11	7.4	28.1	1.1	2.7
XeTMA	0.12	1.9	22.9	0.8	23.1	1.5	1.5	1.1	2.7

Table 5.3: *Number of simulated events from different parts of the internal setup to study the internal background. Signal events have been launched isotropically in the fiducial volume. Both, signal and background, have been studied for two diffusions: pure Xenon (high diffusion) and in a low diffusion Xenon mixture.*

5.3 Simulated geometry

The designed geometry and the materials have been selected according to several factors as the required background level or the requirement to work at high pressure (HP), that implies mechanical restrictions. Also the experience with the NEXT-MM prototype has helped to define different elements. The simulation has been performed to be easily scalable in case some of the dimensions need to be changed.

The vessel has been chosen to be made of Copper. Copper has shown to have a high degree of radiopurity [165] and it can hold high pressure (HP). The chosen thickness is 3 cm to increase the auto-shielding effect and to be able to work at 10 bar. The simulated end-caps have a spherical geometry to allow the work at high pressure. The dimensions of the vessel are: a length of 1.5 m and an inner diameter of 1.6 m. There is a distance between the vessel and the field cage of 5 cm in each side; this space is filled with the desired gas.

The field cage is based on the design used in NEXT-MM. It consists of a Teflon cover, to avoid the possible sparks, with Cu rings embedded on it. The length is the same as for the vessel and the inner diameter is 1.39 m. There are a total of 134 rings with a thickness of 1 mm and they are separated by 1 cm. A cathode is placed on top of the field cage, with the same outer radio and thickness as the rings. It is also made of Cu and has an 88% of transparency. At the bottom of the field cage is placed the readout. The sensitive volume, where the interactions are registered, is the volume defined between the field cage, the cathode and the readout, and is filled with Xenon gas at 10 bar. The volume is 2.24 m^3 that means 124 kg of Xe at 10 bar and at 20 °C. Two flanges and two endcaps at both sides of the vessel have been simulated to enclose it. A sketch of the design is shown in Figure 5.7. Images of the resulting geometry simulated with G4 and visualized with the software *vrml* are in Figure 5.8.

The background events are simulated from the volume of the lateral vessel and field cage and from the surface of the cathode and readout plane. Previous studies simulating from the end-caps and feedthroughs have shown that the contribution is much smaller because of the solid angle and distance than from these volumes or surfaces closer to the fiducial volume.

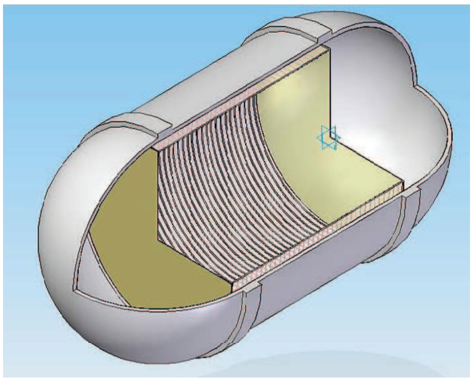

FIGURE 5.7: *Artistical view of the simulated vessel.*

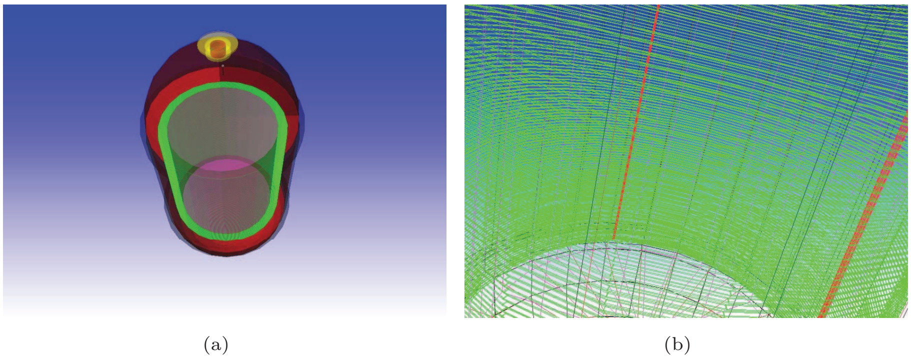
(a) (b)

FIGURE 5.8: *Images of the simulated geometry obtained using Geant4. (a) General view of the different parts: in red the vessel with its semi-spherical end-caps, in green the field cage and in magenta the fiducial volume. (b) Detail of the Cu rings simulated for the field cage. In this image the Teflon is not shown.*

5.4 The topology of the events

In a gaseous TPC detector the path that a particle follows along the medium (track) can be determined with a pixelized detector. This allows to do pattern recognition with a high accuracy and it gives the possibility to define some discrimination algorithms to reject background, a crucial point to be able to detect such a rare process as neutrinoless double beta decay (can be seen in Equation 1.31). Moreover, the topology of the events depends on the gas (diffussion coefficients) and on the working pressure. Higher pressures and diffusion may complicate track detail recognition.

As described before, an event is a set of energy depositions produced in the gas when a particle (signal or background) interacts with its molecules. Each one of the energy deposits, as mentioned in 5.1.3, is converted into charge, is drifted and spread according to diffusion parameters and, finally, pixelized. After these processes, the energy depositions produce a set of 3D pixels. Depending on the initial particles, initial positions and gas conditions (pressure and diffusion) this collection of pixels will have a characteristic topology. In this Section these features, that make them unique and that can help to differentiate between a $\beta\beta0\nu$ signal and background, will be commented. For simplicity, only the contaminants from the background events simulated that can generate a signal in the RoI will be discussed. Previous studies were carried out to better understand the phenomenology of the events and to fit with a higher accuracy the discrimination methods. These results are also presented, as for example, what is the effect of a charge threshold in the readout, or the effect of diffusion in pattern recognition.

5.4.1 Signal Events

A $\beta\beta0\nu$ event will have a very characteristic topology: a long track with two high accumulations of charge where the electrons emitted in the process are recombined with the gas. The length of the track depends on the operational pressure. A ^{136}Xe $\beta\beta0\nu$ event at 10 bar is expected to be up to 30 cm long. Extra short tracks produced by Bremsstrahlung radiation or other secondary processes can appear (it will be discussed in more detail in Section 5.4.3). An example of a typical $\beta\beta0\nu$ event obtained in pure Xe at 10 bar can be seen in Figure 5.9. In this example one electron has an energy of 1.7 MeV while the other has 0.8 MeV. The track length is of the order of 20 cm due to warping. Thanks to the software it is possible to obtain the 3D reconstruction of the event (5.9 (a)) and the projection of the track in the XY plane of the readout (as in 5.9 (b)). In the plots the different colours represent the deposited charge per pixel (in number of electrons), and the scale is shown on the right of the xy plot.

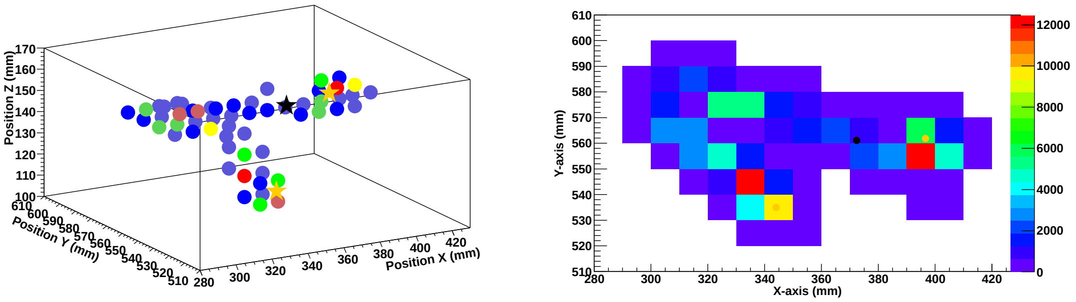

(a)

(b)

FIGURE 5.9: *An example of a neutrinoless double beta decay in* ^{136}*Xe obtained with the simulation. The work conditions are a pixel of a 1 cm*^{2} *and at 10 bar in pure Xe. The two blobs can be seen at both ends of the track. In this example the energy of the electrons was 1.7 MeV and 0.8 MeV, respectively, and all the energy of the event (2.45 MeV) was registered in the fiducial volume. In (a) the 3D view is shown and (b) is the projection of the track in the XY plane.*

Hence, a signal event will have three characteristics that can help us to discriminate between background and signal:

- Most of the signal events will have a single track. In the case of secondary emissions the final event have at least a long main track with most of the energy.
- The longest track ends in two high energy deposits, due to the Bragg absorption of the electrons, called *blobs*.
- The events are isotropically distributed in the fiducial volume.

5.4.2 Background

Background events are generated by contaminants in the materials or in the gas itself and may deposit energy in the RoI. It is important to study, not only the initial particles but also the physical processes that they suffer to understand the final topology of the events. As discussed in Section 5.2 the only isotopes that are simulated are ^{208}Tl and ^{214}Bi. Here the different physical processes and the expected topology of such events are presented.

^{208}Tl events: photon interactions

As discussed previously the main contribution from this isotope is its gamma of 2615 keV. The different photon interactions are:

1. Photoelectric absorption. The energy depositions are far from the RoI if the energy resolution is below a 5% FWHM at 2458 keV. But, in around the 15% of the cases, the photoelectric absorption comes with a secondary energetic electron radiation (by Bremsstrahlung process). This electron usually has an energy of the order of 100-200 keV. Two effects can arise:
    - The electron escapes from the fiducial volume and the final event will have an energy in the RoI. In principle it would be discriminated when looking for two blobs.
    - More than one Bremsstrahlung electrons of this energy occur. Then, one can leave the detector and another can produce a secondary fake blob at one end of the track that mimics a $\beta\beta0\nu$ track.
2. Compton Scattering inside the TPC. Electrons with an energy up to 2381 keV and photons from 233 keV to 2615 keV are generated. The three more dangerous cases are:
    - A photon that interacts again close to the main track. It can occur if a low energy gamma is emitted with an energetic electron that produces the main track. If the lower energy gamma interacts again inside the detection volume the event will have two tracks. To be in the RoI part of the energy has to leave the detector. In this case, it will happen in most of the case due to Bremsstrahlung radiation of the energetic electron. In principle, this case should be easily rejected except in the case where the interaction happens too close to the first electron track.
    - The emission of a lower energy electron plus an energetic gamma. In this case the electron can produce a secondary blob close to the main track being difficult to reject. If the gamma escapes from the fiducial volume, then the final event would be outside the RoI, or it can suffer a secondary Compton scattering where just part of the energy leaves the detector and, therefore, the event would be in the RoI. In this case the event will be a multi-track event with at least one larger second track far from the first one.
3. Compton interaction in materials outside. A lower energy photon enter the fiducial volume and deposits its energy by photoelectric effect. Small Bremsstrahlung emissions interacting close to the track may mimic blobs

In conclusion, for the ^{208}Tl most of the events will consist in several tracks. Events with one single long track depositing its energy in the RoI are a photoelectric absorption with a radiation lost or Compton or multi-Compton events. An example of each case can be seen in Figure 5.10. Figure 5.10 (a) and (b) represent a photoelectric event of 2615 keV, and in this case the event is a single-track but with just one blob at one end; (c) and (d) correspond to a multi-Compton event.

^{214}Bi events

Different gammas from the ^{214}Bi have an energy higher than 2.4 MeV as summarized in Table 5.2. As mentioned, the most important one is the gamma of 2447.8 keV. It can deposit all its energy by photoelectric absorption and would be completely contained in the RoI unless an energy resolution better than 0.5% FWHM at $Q_{\beta\beta}$ is reached. In principle they would be single track

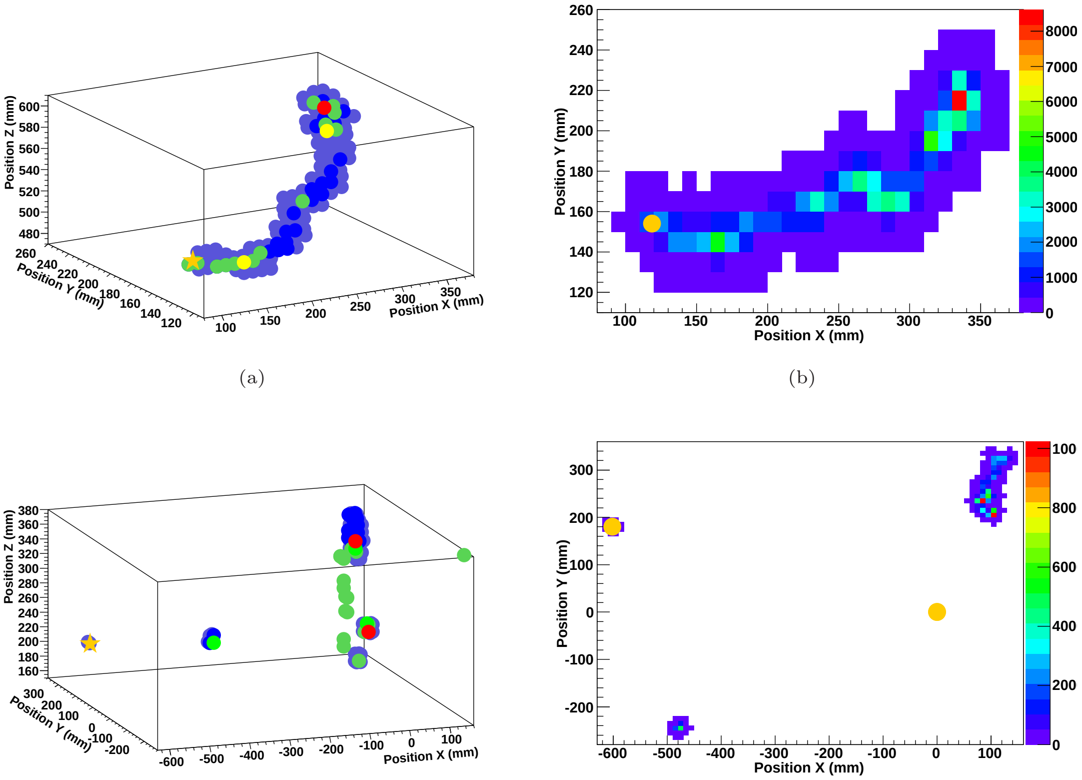

(a) (b)

(c) (d)

FIGURE 5.10: *^{208}Tl events registered in a pixelized detector in a TPC fill with Xe at 10 bar. (a) 3D reconstruction of the track that corresponds to an event that has deposited its energy due to photoelectric effect (energy of 2.615 keV) (b) xy projection of the event in the pixelized readout. In this case the event is a single-track but with just one blob at one end. (c) and (d) similar plots for a multi-Compton event.*

events with only one blob at one one of the two ends. However, if a secondary emission via Bremsstrahlung radiation deposits all its energy in the detection volume and has such a high energy as to produce a blob close to the main track, then, the track would be misidentified as a signal track, as in the case of the ^{208}Tl.

Other gammas with higher energies can deposit their energy in the RoI due to Compton scattering, as explained in the case of the ^{208}Tl, but their intensity is too low to be relevant. However, the full chain has been simulated.

Together with the gamma emission, in the ^{214}Bi decay, two beta emissions can be produced:

- Electrons with a continuous beta spectrum with its transition $Q_{\beta\beta}$ at 3272 keV. This case has an intensity of 18%. An electron can easily be confused with a signal event if a secondary blob appears. But the only ones that can reach the RoI are those emitted from the surfaces close to the fiducial volume and in these cases they will leave energy near the walls and can be rejected using a veto volume.
- The second electron beta spectrum has a maximum energy at 2663 keV and a gamma emission of 824 keV. Different processes can allow these two particles to leave energy in the

RoI but they can be easily rejected, either using a veto volume or rejecting events with more than one energetic track.

In conclusion, ^{214}Bi can produce multi-track events, as in ^{208}Tl, or single track with just one blob. This single track can come from the beta emission or from the gamma at 2457 keV. Examples obtained can be seen in Figure 5.11, (a) and (b) are for a gamma that deposits all its energy inside the chamber via a photoelectric effect and (c) and (d) represent the track produced by an electron coming from the walls that deposits an energy of 2300 keV. In both cases the event has just a single blob.

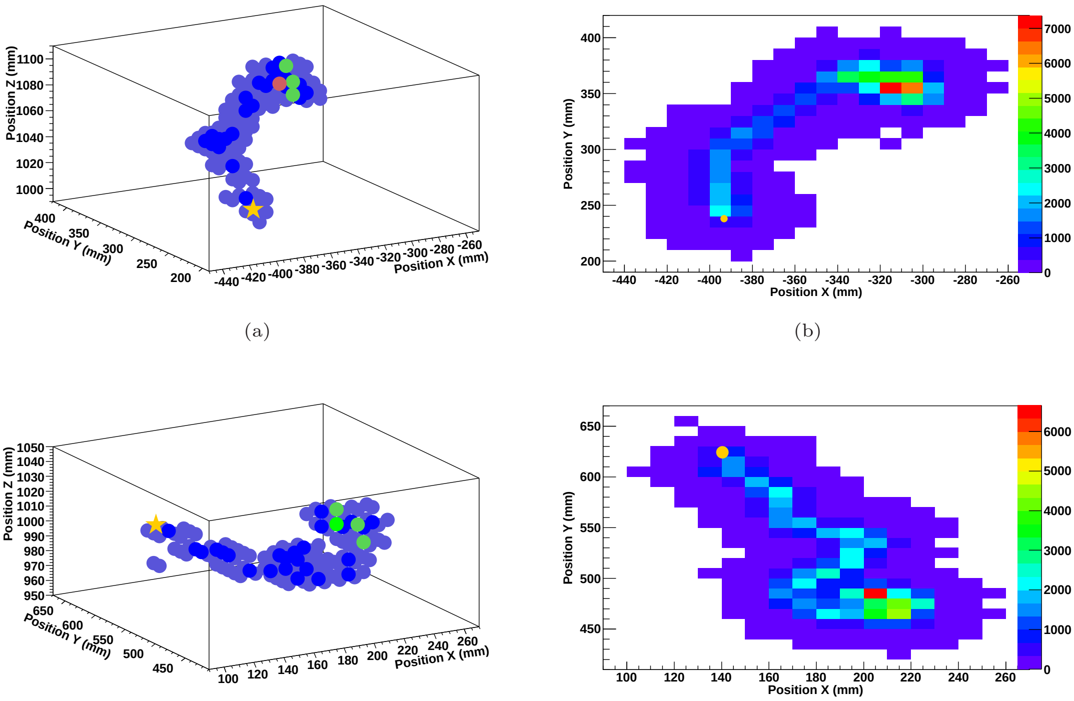

(a) (b)

(c) (d)

Figure 5.11: ^{214}*Bi events registered in a pixelized detector in a TPC filled with Xe at 10 bar. (a) 3D reconstruction of the track that corresponds to an event that deposits its energy by the photoelectric absorption of the 2447 keV gamma. (b) XY projection of the event in the pixelized readout. (c) and (d) similar plots for a beta emission coming from the walls. In both cases the events have just a single blob.*

5.4.3 Deterioration of pattern recognition

Effect of the energy threshold per pixel

All readouts have a lower threshold in the energy (charge) that can be detected. A study was performed to understand the effect that this threshold in the pixels has on the efficiency to detect electrons. Different charge thresholds were imposed in order to consider a pixel active or not. The range of the study is from 0 to 10 keV. The effect on signal events and background events was studied. In Figure 5.12 is shown the efficiency for signal events as a function of the pixel threshold. There exists a plateau for the pixel threshold, between 0 and 2 keV, where the number of detected signal events does not change.

These results are for a pixel size of $5 \times 5\,\mathrm{mm}^2$. Therefore, for this pixel size the threshold should be equal to or lower than 2.5 keV. Above this value the efficiency decreases considerably. There exists a dependency with the pixel size, so, extrapolating to a pixel of $10 \times 10\,\mathrm{mm}^2$, the upper threshold admitted for a good charge recollection would be 10 keV per pixel (4 times higher because the length is double in each direction, xy). In Micromegas readouts the charge threshold per pixel is usually of the order of 1 keV. This is the value used in the simulations.

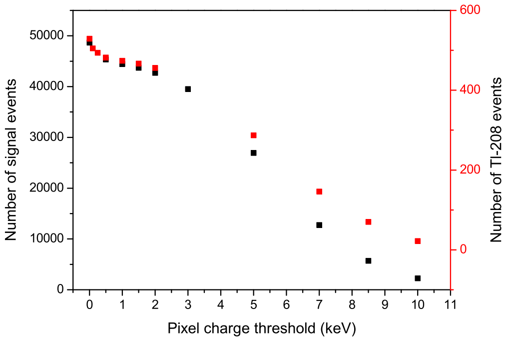

FIGURE 5.12: Effect of the pixel energy threshold on the charge recollection. For a pixel size of $5 \times 5\,\mathrm{mm}^2$, it exists a plateau from 0 to 2.5 keV. After it the charge collection efficiency starts to decrease polynomially.

Effect of diffusion on the spatial resolution

A very important point when working with gases in a fiducial volume with long drift distance is the effect of the diffusion in the transport of the charge as shown in Chapter 2 in Equation 2.7. This effect can worsen the spatial resolution due to the spread of the charge around the main track. It could also make two different deposits of energy appear joined in just one track. In Xenon the charged particles have higher diffusion than in other noble gases such as Argon.

Two diffusion coefficients have been studied in this work: high diffusion, with values of $\sigma_L = 300\,\mu\mathrm{m\,cm}^{1/2}$ and $\sigma_T = 1000\,\mu\mathrm{m\,cm}^{1/2}$ as representative for pure Xenon or pure Ar and a lower diffusion, with $\sigma_L = 100\,\mu\mathrm{m\,cm}^{1/2}$ and $\sigma_T = 100\,\mu\mathrm{m\,cm}^{1/2}$. These values can be obtained if we add some additive to pure Xenon like Trimetilamine (TMA) or CF4, obtaining a low diffusion Xe mixture. Studies to know the diffusion coefficients were carried out using Magboltz and to obtained the values used in this work. The diffusion coefficients change in function of the electric field strength and the pressure. The drift field was considered to be $1\,\mathrm{kV\,cm}^{-1}$ (to guarantee the optimum operation of the Micromegas) and the pressure 10 bar in all the cases. An example, of the same $\beta\beta0\nu$ event, with the two different diffusion coefficient is shown in Figure 5.13. The upper images are for an event in pure Xe and the 3D plot (left) and the projection of the track (right) in the pixelized readout can be seen. The pixel is $1 \times 1\,\mathrm{cm}^2$ and the different colours represent the deposited charge per pixel. The lower ones are the same plots obtained for the same event but for a lower diffusion coefficient. The points marked in black are the vertices of the events and the yellow's tag the point where the particles are reabsorbed, information obtained from the simulation.

In Section 2.2.1, the relation between the z coordinate (the direction of the electric field) and the effect of diffusion was studied. This effect is shown in Figures 5.14 and 5.15, where events produced at higher and lower z are depicted. In Figure 5.16 is plotted the distribution of the number of pixels (with a charge higher than 1 keV) in the main track versus the z position. In this image it can be observed how the number of pixels increases with the z position and how this effect is much bigger in a gas with a higher diffusion coefficient.

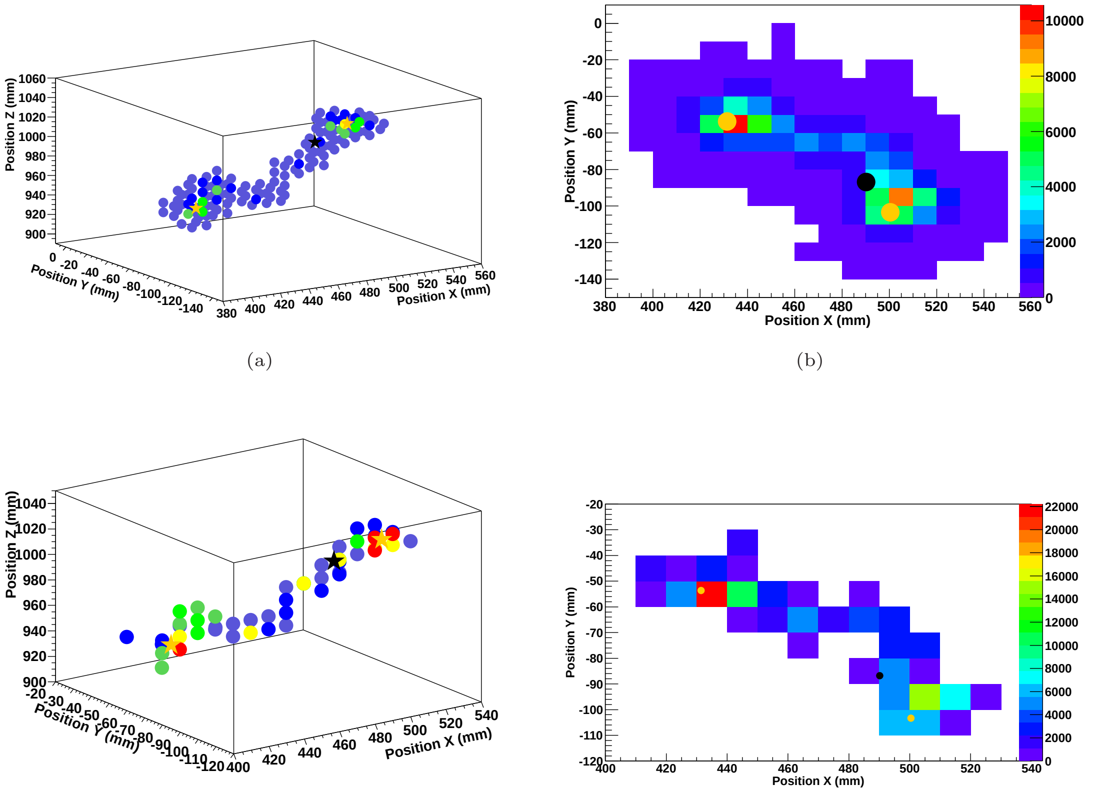

(a) (b)

(c) (d)

FIGURE 5.13: *Effect of the diffusion over the same* $\beta\beta0\nu$ *event. (a) and (b) are the 3D track and the XY projection of the track, respectively, considering a high diffusion coefficient as in pure Xe. (c) and (d) represent the same plots but for a low diffusion Xe-mixture. In both cases the working pressure is 10 bar and the pixel size of* $10 \times 10\,mm^2$*. The different colours represent the deposited charge per pixel as shown in the linear scale at the right.*

Straggling

Another effect that can make more difficult the reconstruction of the track is that at HP the deposition of the charge and its range can vary sharply. Therefore, the events can deposit the same energy not so homogeneously than at lower pressures. For this reason a higher straggling effect exists at these working conditions. This effect can be observed in Figure 5.17. It can produce tracks that are more twisted and circular making the identification of the two blobs more difficult.

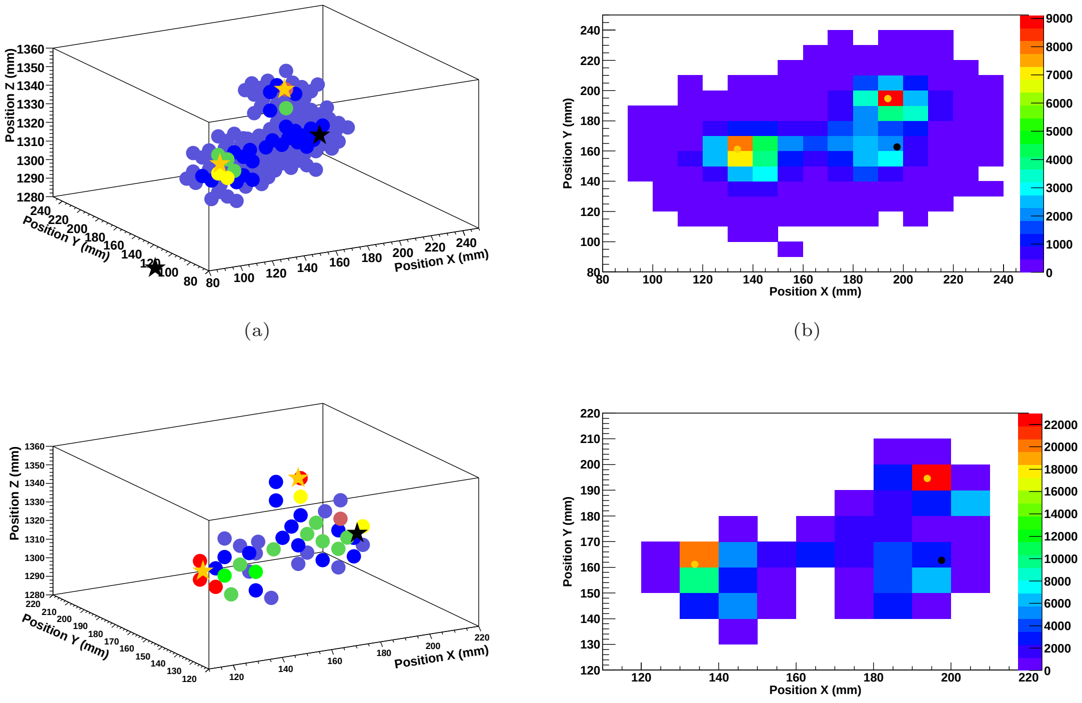

(a)

(b)

(c)

(d)

FIGURE 5.14: *A high z position $\beta\beta0\nu$ event is plotted in the two diffusions, showing a relation between the diffusion and the position z. The higher the z position, the bigger the effect of the diffusion. (a) and (b) are the 3D track and the XY projection of the track, respectively, considering a high diffusion. (c) and (d) represent the same plots but for a low diffusion gas. In both cases the working pressure is 10 bar and the pixel size of $10 \times 10\,mm^2$. The different colours represent the deposited charge per pixel.*

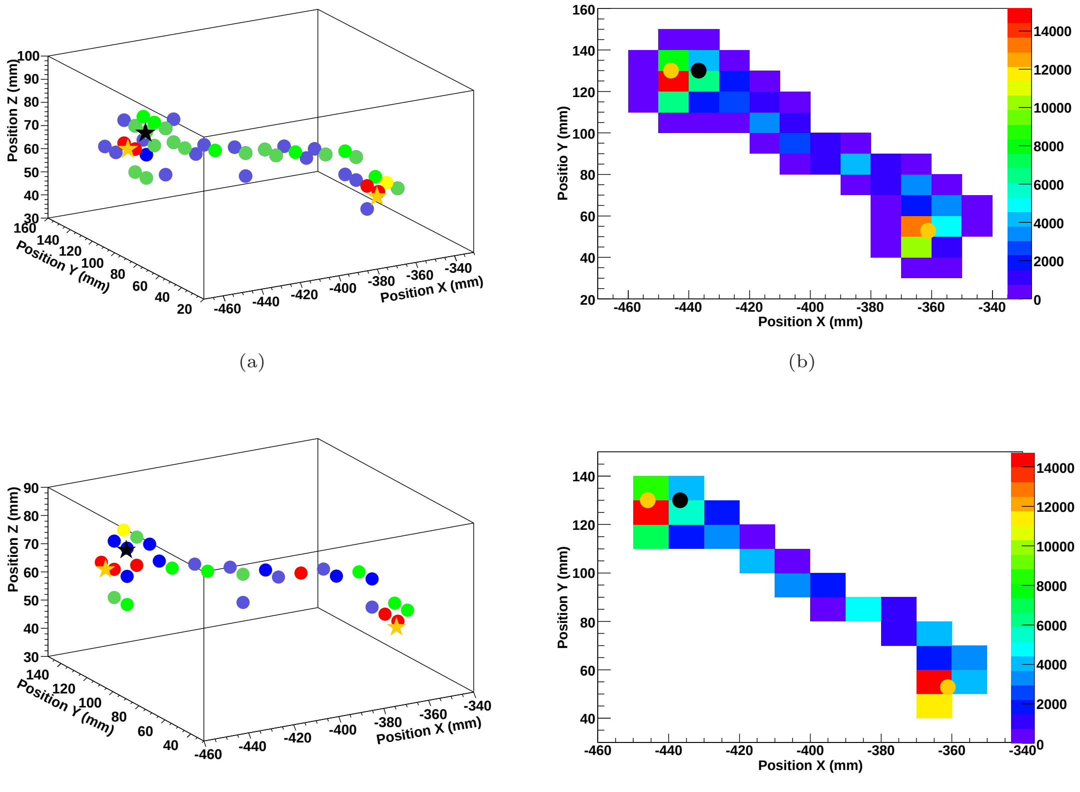

(a) (b)

(c) (d)

Figure 5.15: *A low z position $\beta\beta0\nu$ event is plotted at the two different diffusions studied to show that at lower z the diffusion has a small effect over the reconstruction of the track. (a) and (b) are the 3D track and the XY projection of the track, respectively, considering a high diffusion. (c) and (d) represent the same plots but for a low diffusion Xe mixture. In both cases the pixel size is* $10 \times 10\,mm^2$ *and the pressure 10 bar. The different colours represent the deposited charge per pixel.*

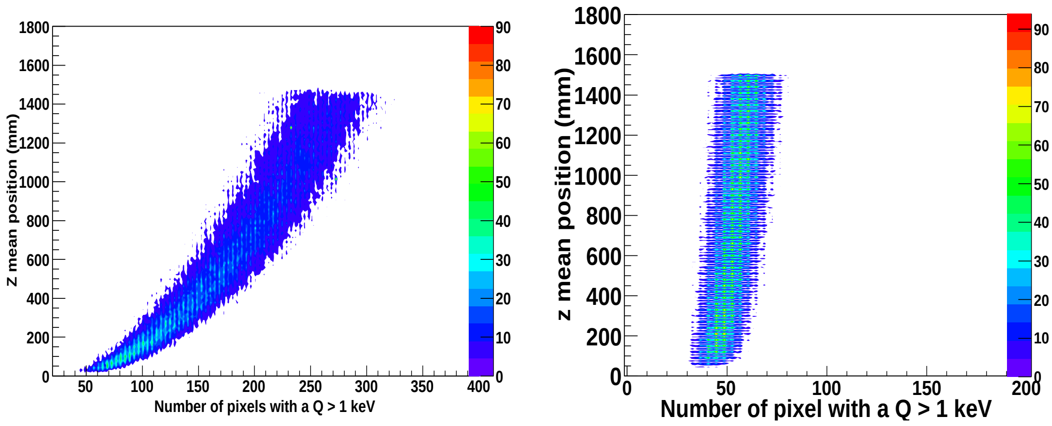

(a) (b)

Figure 5.16: *Number of pixels with a charge higher than 1 keV in the main track versus the z position of the event (calculated as the mean z position). (a) In a gas with a high diffusion coefficient. (b) In low diffusion Xe. In both cases the linear scale of colours represents the multiplicity. In a gas with a higher diffusion coefficient the spread of the charge along the z position is higher than in a low diffusion gas and the effect can make more complicated the reconstruction of the main track.*

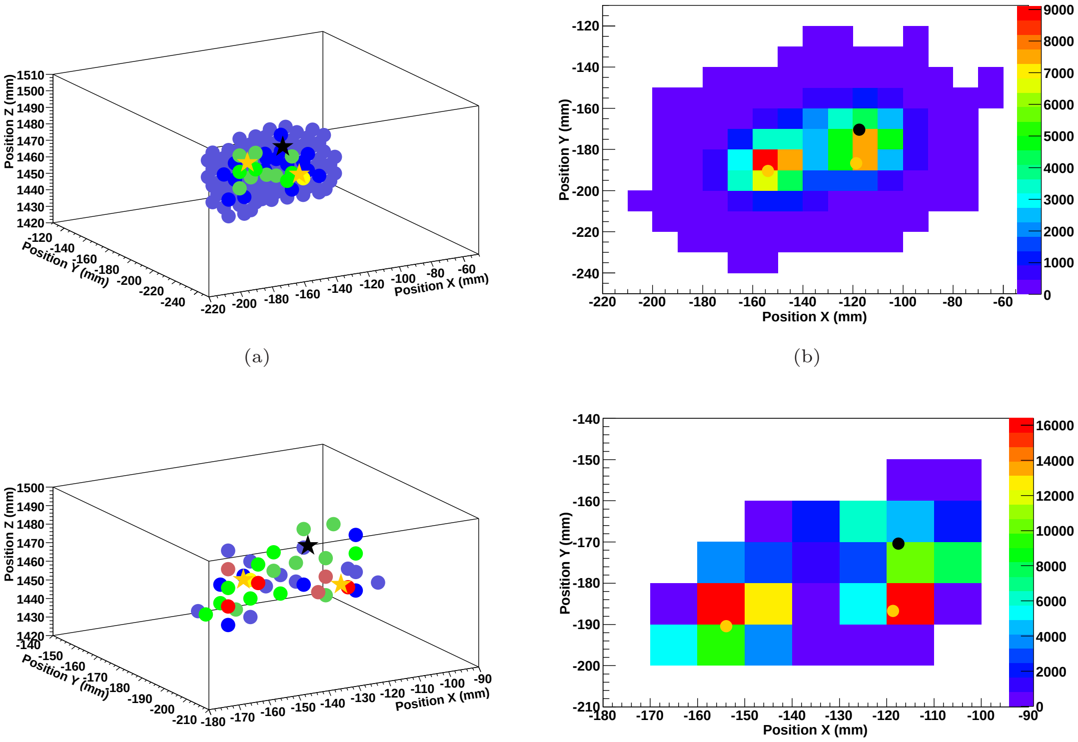

(a) (b)

(c) (d)

Figure 5.17: *Signal event at 10 bar in which a high straggling effect is observed; it may make more difficult the identification of the blobs. (a) 3D reconstruction of the event and (b) XY projection for a high diffusion gas. (c) and (d) represent the same plots for the same event in a Xe mixture with a lower diffusion coefficient. In all the cases the colour scale represents the charge deposited per pixel.*

Effect of secondary emissions

This section studies the effect of the possible secondary emissions of the simulated events. As commented before, these secondary emissions can make more complicated the discrimination, specially if the gas has a high diffusion coefficient. In order to study them and to better understand their phenomenology, different flags where introduced in the Geant4 code and included in the REST code to follow the secondary particles arising during the interactions. The relevant interactions and possible secondary emissions produced in these interactions are:

1. *Delta-ray:* electrons dragged from the internal shells of the Xe by the incident particles. The process is flagged if the energy is larger than a minimum one (50 keV).

2. *X-Ray:* emission of the X-Rays of the Xenon when exciting its atoms. They are emitted when desexcitation of the atoms occurs. For Xe, these energies are, as listed in Table 4.2, of: 4.2, 29.4, 29.7 and 33.6 keV. Hence, a selection in the energy is imposed choosing events with an energy between 29 and 34 keV in the kinetic energy deposited in the G4step (the simulation step in Geatn4). Bremsstrahlung with these energies will be misidentified and will also be considered as X-Ray. If the final event is completely detected in the fiducial volume it will consist in two deposits of energy, the main one with an energy of the $(Initial\ Energy) - (binding\ energy)$, and a secondary one with the energy of the X-Ray.

3. *Bremsstrahlung:* radiation emitted by the electrons when stopped by the nucleus. A gamma is emitted in the process. Two possibilities have been flagged:

   - Inside the target: the gamma of the corresponding energy is identified inside the target.
   - Outside the target: the code looks for the gamma of the corresponding energy in any of the outer volumes.

   A study simulating electrons of different energies was carried out to calculate the expected Bremsstrahlung radiation for the different energy electrons and to study its dependence with the initial energy of the electrons. Figure 5.18 represents the obtained percentage of events that have lost part of their energy through Bremsstrahlung radiation inside and outside the TPC.

4. *Compton events*: both, inside and outside the fiducial volume. In this case and in the previous one the code looks also for events in which the emission has an energy higher than 100 keV.

5. *Multi-Compton events:* events with more than a Compton emission. If all the energy is deposited in the fiducial volume then the event is a multi-track event.

With the help of these flags it is possible to study the events passing the discrimination algorithms and with this information improve them. A discussion of the surviving background events and rejected signal after the selection applied is done in Section 5.4.3.

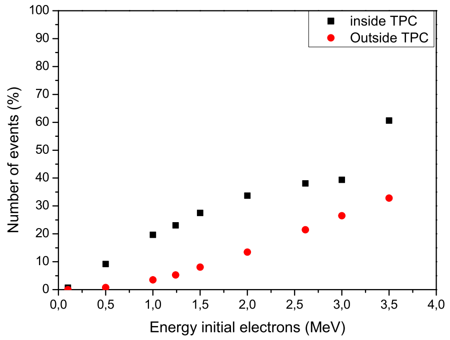

Figure 5.18: Percentage of expected Bremsstrahlung radiation inside (black squares) and outside (red circles) the chamber for different energies of the primary electrons simulated distributed isotropically in Geant4.

5.5 Discrimination Algorithms

The Gothard TPC Experiment [89] was pioneer in the introduction of new ideas for the topological discrimination of signal and background in a gaseous TPC, as for example, the distinctive charge at the end and the beginning of a double beta event. Moreover, they was able to prove the topological potential on background discrimination. However, the identification of blobs was made by eye. In this section the discrimination algorithms developed to analyse the simulated events are presented. The aim is to develop automatic selection criteria based on the differences expected between the signal and the background events to select only signal events. Some of the criteria applied are essential like the energy window selection and the fiducial rejection. Others are based on the topology of the events. The main goal is to decrease the background maximizing the efficiency of detection. These algorithms were initially defined in [138]. Here an evolution of them is presented in several ways: they have been implemented to work with gases with higher diffusion coefficients, new algorithms are applied trying to increase the efficiency while the rejection factor remains more or less constant and also the effects of the secondary emissions have been computed.

The topology the program looks for is a long main track that ends in two high energy deposits. As already mentioned, these energy depositions are called *blobs* and are due to the Bragg peak of the electrons emitted in a $\beta\beta0\nu$ process. On the other hand, the main problematic background are the electrons due to their similar track, but in this case they will end in just one blob (they are just one electron). Several algorithms are applied in order to differentiate between the two populations. The algorithms take into account the pixelization of the readout and the diffusion of the gas at a given pressure. This diffusion, as it has been commented, can complicate the discrimination.

5.5.1 A figure of merit for background reduction

The study of a selection of events to discriminate between background and signal is based on two parameters: the selection efficiency (ϵ) and the rejection factor (F), as the aim is to reduce the contaminants keeping the maximum efficiency. The efficiency is defined as the ratio of signal events after and before the application of a criterion; it quantifies the acceptance of signal events. The second variable, the rejection factor, is the ratio of background events before and after the application of the selection and quantifies the background discrimination power. An ideal selection criterion should have an efficiency near 100% and a very high rejection factor. As this is not normally the case, a figure of merit (f.o.m.) is usually defined. Based on the expected sensitivity in a $\beta\beta0\nu$ experiment expressed in Equation 1.31, it can be deduced that $T_{0\nu}^{1/2} \propto \epsilon \cdot \sqrt{\frac{1}{b}}$, b being the background level and, therefore, the f.o.m can be defined as

$$f.o.m. = \sqrt{F} \cdot \epsilon, \tag{5.7}$$

5.5.2 Energy

The first and most important criterion to identify a $\beta\beta0\nu$ event is to select an energy window around $Q_{\beta\beta}$. The selection of a RoI around the $Q_{\beta\beta}$ eliminates most of the background but it also affects the efficiency of the signal. An energy resolution of 2% FWHM $Q_{\beta\beta}$ is considered only to fix a wide RoI, of 100 keV. The better the energy resolution of the detector, more background events are eliminated. However, any event that deposits energy in the region may be mistaken for a signal event. Therefore, it is also needed to develop extra analysis to handle with this and to reduce it at maximum.A detailed study of the effect of a better energy resolution was also carried out and is discussed in last Sections of the chapter.

5.5.3 Track selection

The method explained below regroups the pixels of the events in, what is called, tracks. A track is defined as a collection of pixels connected by a relation of proximity. It follows the ideas of graph theory [188, 189]. The graph theory applied on track selection consists on identifying the pixels of the event with the vertex of a graph and their links with the segments of the graph. One event can have more than one track.

First, a charge threshold is imposed to consider a pixel to be in a track. This threshold depends on the pixel size and has been chosen to be reasonably compatible with the actual threshold levels in pixelized detectors (1 keV in our case). Once the pixels are defined the segments are then generated to join them. There has to exist a minimum distance to link the pixels, this distance is called *segment distance*, s_{dist}, and it has to be at least as long as the pixel size. In order to take into account the effect of the diffusion and to avoid possible track gaps, we can increase this distance or define a minimum charge around a pixel for it to be considered, $Q_{track\ pixel}$. The second criteria is what has been used in our method. This charge is calculated as the charge enclosed in a sphere of a certain radius, $r_{track\ pixel}$, centred in any pixel.

The algorithm to create the segments first calculates the distance between pixels for all of those that have higher charge than a given value around them. If it is equal to, or smaller than, s_{dist}, then, they are grouped in the same track. Finally, the set of pixels associated to a continuous graph form a *track*. Each event can have just one track or more than one if in their trajectory a Bremsstrahlung emission has taken place or if it is a multi-Compton event, for example. A schematic description of the method is shown in Figure 5.19.

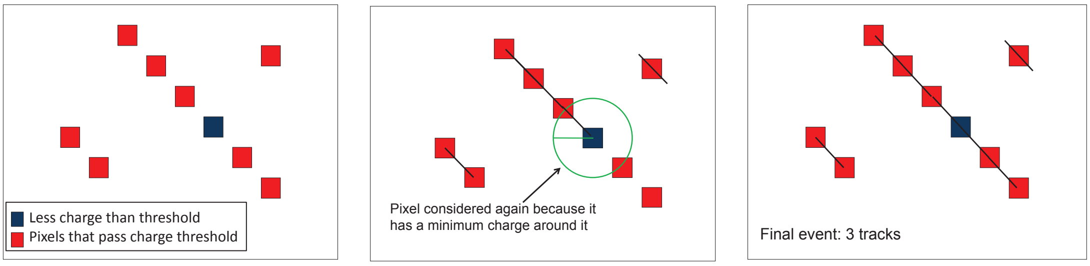

(a) (b) (c)

FIGURE 5.19: *Sketch of the tracks search method. (a) Pixels are considered if they have a minimum charge. (b) The distance between pixels is calculated, if this distance is smaller than the segment distance then they are linked. To avoid possible gaps and to take into account diffusion effects, the charge around a pixel is calculated defining a minimum radius around it. If the charge in the enclosed sphere is bigger than a given one, then the pixel is considered to be again in the same track. (c) Final events can have more than one track.*

"Short"tracks.

The possibility to select events not only with a long track but also with a small deposition of charge in a secondary track is studied. This secondary track has been chosen to have a charge less than or equal to 100 keV and are called *short tracks*. In Figure 5.20 the number of total tracks (a), short tracks (b) and long tracks (c) for signal and background events can be observed. For $\beta\beta0\nu$ events most of them have one or even two short tracks and if the method keeps events with up to one of the *short*-tracks, a 20% of efficiency is recovered.

However, two possibilities have been evaluated: to consider events with one short track or two. Obviously, the efficiency increases as well as the surviving events from background. To evaluate which criteria is more powerful, the f.o.m has been calculated for each case. Results are summarized in Table 5.4 where the final f.o.m for each background population after the track method is shown. It can be observed that for pure Xenon is clearly better to consider just one short-track for contamination coming from the lateral walls. For the other contributions there is no difference or it is small. In the case of a low diffusion Xe mixture, there is almost no difference between considering just one or two *short*-tracks. In conclusion, the method will select events with a long main track plus just a short one; that allows to recover a 20% of signal events with a very sligt loss in rejection power being the f.o.m. better in this scenario.

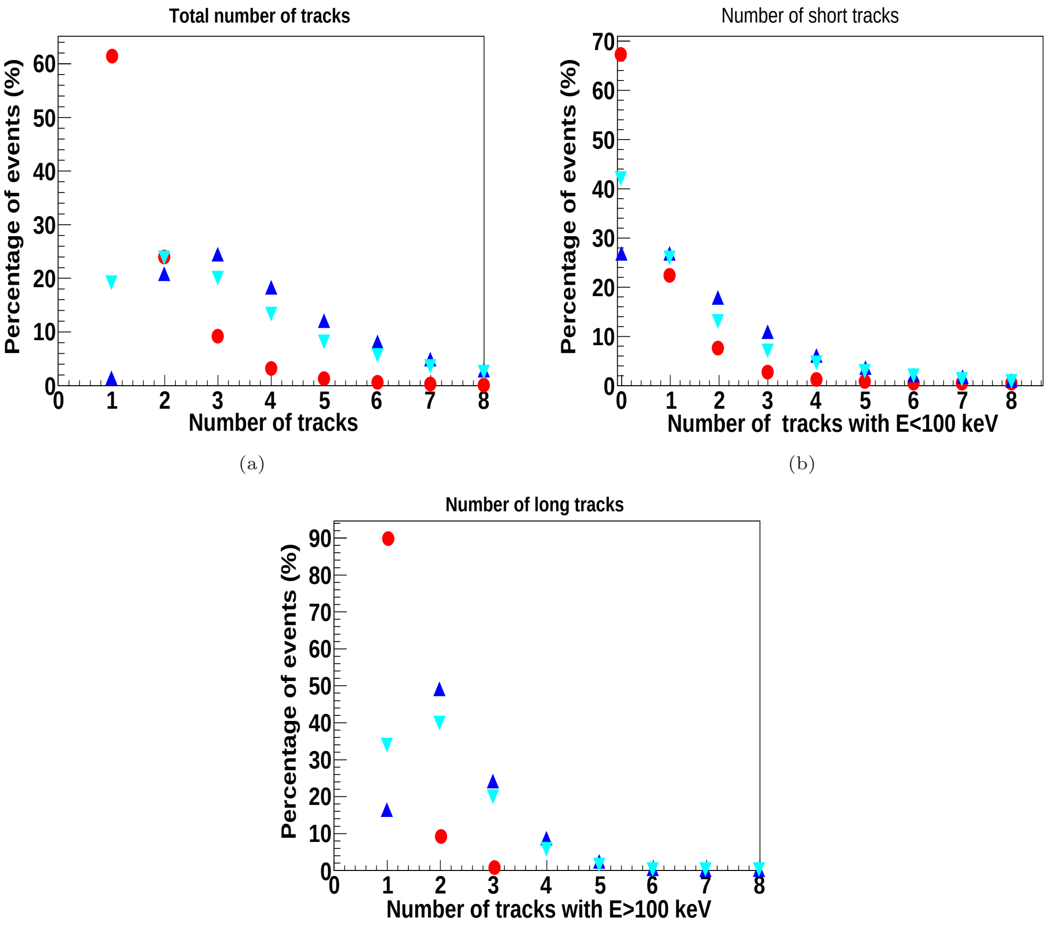

(a)

(b)

(c)

FIGURE 5.20: *Study of the number of tracks in signal and background events (a) Total number of tracks for signal and background events. (b) Number of short-tracks, defined as tracks with less than 100 keV, for signal and background events. (c) Number of long tracks, defined as tracks with more than 100 keV, for signal and background events. In the three cases red circles are for $\beta\beta0\nu$ events, blue triangles for ^{208}Tl and cyan inverted triangles for ^{214}Bi events.*

		Pure Xe		**Low diffusion Xe mixture**	
Origin		One *short track*	Two *short track*	One *short track*	Two *short track*
Vessel	^{208}Tl	3.0	2.3	2.8	2.7
	^{214}Bi	2.1	0.5	1.9	1.9
Drift	^{208}Tl	3.5	3.1	3.6	3.0
	^{214}Bi	1.2	1.2	1.2	1.2
Readout	^{208}Tl	4.3	3.6	4.9	4.0
	^{214}Bi	1.1	1.1	1.3	1.3
Cathode	^{208}Tl	4.0	3.4	3.5	3.0
	^{214}Bi	1.3	1.1	1.0	1.1

TABLE 5.4: *Factor of merit after the application of the track selection in the case of events whit one* long *track, and one or two* short *tracks. In all cases errors are of* ±0.1.

5.5.4 Topology Selection

Once the events are classified by the number of tracks, the second condition is applied: the signal has a long track ending in two high energy depositions. First of all it is defined what a blob is and the program selects the blob candidates in this track. A *blob* is a deposition of high energy in some pixels due to the Bragg peak of the electrons in the gas. In our method, it is defined as a maximum charge, Q_{blob} enclosed in a sphere centred in the more energetic pixel and with a given radius, r_{blob}, fixed by the user. r_{blob} depends on the pixel size and on the diffusion of the gas under study. In the Gothard's analysis these was done by eye [118]; a crucial point was to develop a blind method, as was introduced in [138]. In addition, the topological recognition in [89] was easier because they had an smaller pixel ($3.8 \times 3.8\,\mathrm{mm}^2$) and works at lower pressure (5 bar) in a less diffusive gas.

The possibility of topological recognition is the most important advantage of a gaseous detector versus a liquid one and it should be fully exploited. Different ideas were studied (length, curvature or compactness of the track, distance between first and end point, number of blobs, ...). An algorithm was developed in [138] in order to define the longest track-line joining, if possible, two blobs. The algorithm acts on the longest and more energetic track found from the previous method and works as follows:

1. N blob candidates are defined. Even if it is known that the signal has just two high energy depositions, more than two blob candidates are selected since it is needed to take into account extra blobs that could be due to delta-ray, X-Ray or low energy Bremsstrahlung. The best results for the method were obtained supposing $N = 6$ blob candidates.

2. Once the blob candidates are defined, the longest track (a continuous set of segments) between any pair of blob candidates is calculated, l_1.

3. Then the longest distance between any blob and any point of the track, l_2, is also calculated.

4. If l_2 is around 30% longer than l_1 (number chosen to increase the effectiveness of the method), then l_2 is chosen as the main track. Otherwise, l_1 is taken. The method looks for the longest track because in a $\beta\beta0\nu$ signal the two electron absorptions happen at the end of the ionization track and, therefore, the distance between them is maximum. With this comparison we try to avoid errors in the reconstruction of the longest track due to extra blobs in the middle, we will call it *track-line*. Schematically, the algorithm is represented in Figure 5.21.

5. Once the longest track-line is chosen, the method will locate the two blobs, one at each end of the track. Their charge is calculated in a sphere of a given radius R_{blob}, and they are tagged as *big* and *little* blob in function of their charge. The charge distribution for both blobs present a high degree of superposition for signal events, while there exist a separation in the case of background events (Figure 5.22 and Table 5.5).

Two examples of a $\beta\beta0\nu$ event with a precise track-line are shown in Figures 5.23 and 5.24. One of them corresponds to an event that can be easily identified as a $\beta\beta0\nu$ and that has been well

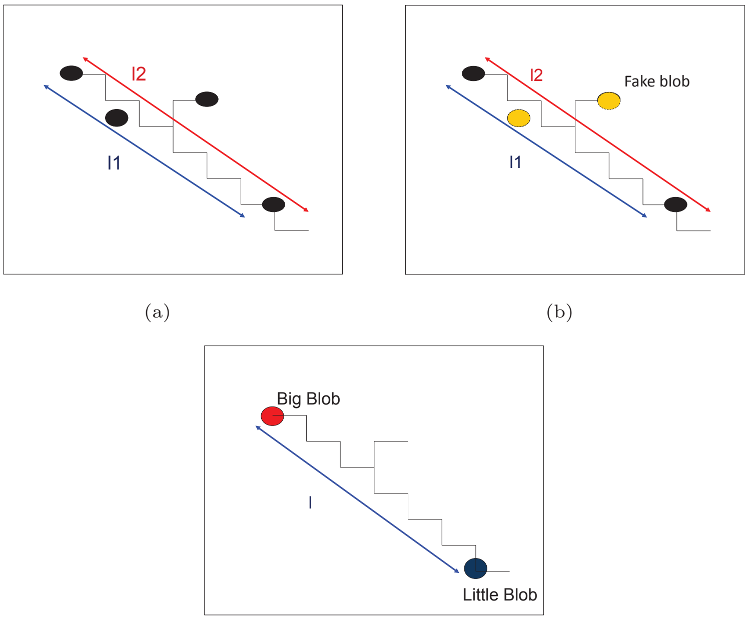

(a) (b)

(c)

FIGURE 5.21: *Sketch of the blob search method. (a) Once the longest track for the event is found, N blob candidates are defined. Those are pixels with a minimum charge around them. The radius to calculate it is 3 cm and the minimum charge required 132 keV. (b) The maximum distance between any pair of blobs is calculated: l_1. It is also calculated the maximum distance between a blob and any pixel, l_2. The ratio of the two distances is obtained, if l_2 is 30% longer than l_1, then l_2 is the main track, otherwise it is l_1. (c) A blob is defined at both ends of the chosen track. They are classified as little and big blob in function of their charge.*

	Big blob charge (keV)	*Little* Blob charge (keV)
Low diffusion Xe		
$\beta\beta0\nu$	914.8 ± 9.4	694.9 ± 6.1
^{208}Tl	840.4 ± 3.6	455.0 ± 3.0
^{214}Bi	836.2 ± 4.2	456.9 ± 3.0
Pure Xe		
$\beta\beta0\nu$	888.1 ± 1.4	681.6 ± 7.3
^{208}Tl	840.4 ± 4.0	556.6 ± 4.0
^{214}Bi	828.3 ± 5.7	556.2 ± 4.2

TABLE 5.5: *Charge of the two blobs found for the simulated background events and for the $\beta\beta0\nu$ events with the two diffusions under study, high and low diffussion Xenon. The method that the program uses is explained in detail in 5.5.4 and the charge of the blobs has been obtained as the mean value fitting the obtained distribution to a Gaussian.*

determined by the method, and the other one (also a $\beta\beta0\nu$ event), corresponds to a more difficult one that has also been well found by the algorithm. The real blob (marked from simulations) are in yellow while the track-line and the identified blobs are in red. However, the algorithm does not always work and another event that has not passed the method can be seen in Figure 5.25. Also, some background events can mimic a $\beta\beta0\nu$ event if they have a secondary emission along their trajectory. The success of this method can be evaluated, as in [138], calculating the distance between the real blobs (known from simulation) and the identified ones. The parameters of the method have been adjusted until an effectiveness of 70.5 % has been obtained, see Figure 5.26

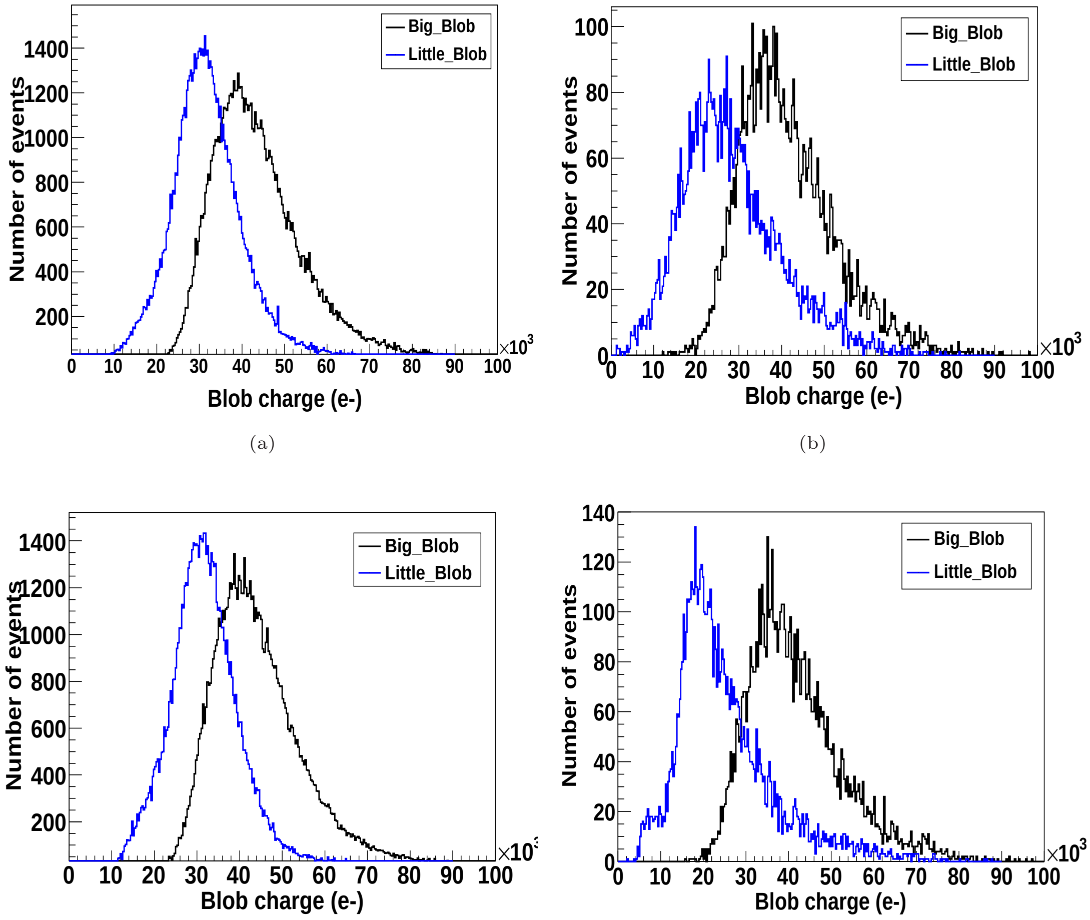

(a) (b)

(c) (d)

FIGURE 5.22: *Charge of the little and big blob obtained for different cases. (a) Signal events in pure Xe. (b) Background events from* ^{208}*Tl coming from the vessel in pure Xe. (c) signal events in a low diffusion Xe mixture and (d) background events from* ^{208}*Tl coming from the vessel in a low diffusion Xe mixture (graphs are normalized and the distributions are for the events that survives the track selection). It has to be noted that for each population of background the distributions are similar.*

(a). In this plot it can be seen that for the 70% of signal events the real and identified blob are closer than the pixel size.

Once the main track and the two blobs are selected (labelled as big and little blob) the selection criterion, called *topology*, is applied. First of all, a selection in the minimum charge for the little blob, $Q_{little\ blob}$ is applied, because in the case of background events it has a smaller value than in the case of signal events. This can be observed in Table 5.5 and in Figure 5.27 where the charge of the little blob for signal events and background events in Xe, (a), and in a low diffusion Xe mixture, (b), is plotted. The selected cut is around 20000 electrons in both gases, that translates into a minimum charge of 440 keV required for the little blob.

In more of the 95% of the signal events the two blobs have a similar charge and they are situated at both ends. Hence, the absolute value of the ratio of the charge of the two blobs is calculated. The condition that this ratio has to be less than or equal to 2 is then imposed. This is justified in the plot of Figure 5.28 where we can see this distribution for signal and background events

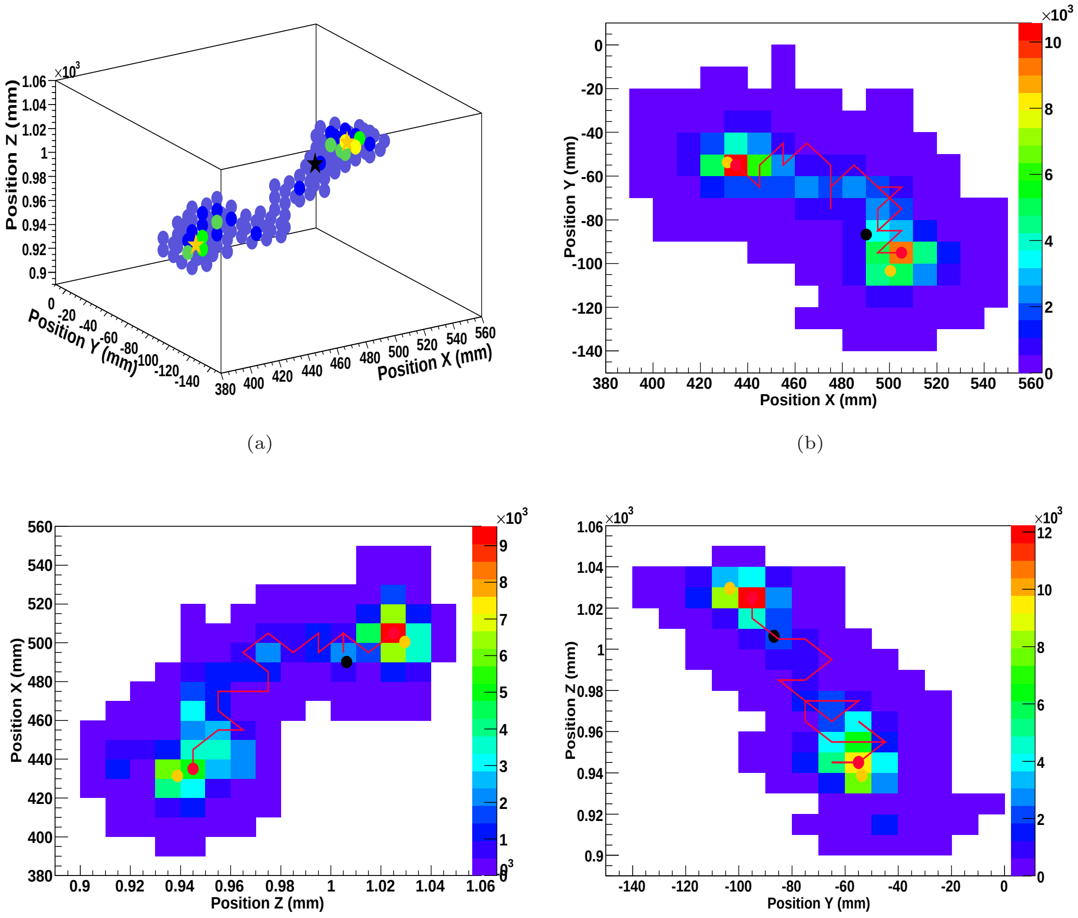

(a)

(b)

(c)

(d)

Figure 5.23: *Signal event in which the method has determined correctly the position of the blobs (red circles, in yellow are marked from the simulation) and the track-line (red line) in the 2D projections (b,c and d). This event is in pure Xe at 10 bar. The 3D view is also shown for completeness, but on it is not drawn the track-line.*

in pure Xe (a) and in low diffusion Xe (b). For the simulated signal events in the 71.1% of the cases the ratio fulfils the condition.

Coverage of the track

After these selection criteria the only events that are expected to survive are of the kind of a double beta decay: a long main track with two blobs at both ends. However, the method does not always work. In most of the cases when the track-line is not well selected, a blob occurs in the middle of the trajectory and the event has an energy smaller than the real one because the track-line is shorter than the real length, as can be seen in Figure 5.30. In order to try to recover these events, the charge around a given distance of the main track is calculated. It is like a *coverage* of the track with a given distance; then the charge inside it is calculated. The idea is to compare this charge with the charge of the longest found track-line. If the track-line were found correctly this ratio would be one. Therefore, we can apply an effective selection, based on that ratio. A figure of the distribution of this ratio can be seen in Figure 5.29 for high diffusion Xe (a) and for low diffusion Xe (b) where the obtained ratio for signal and background is compared.

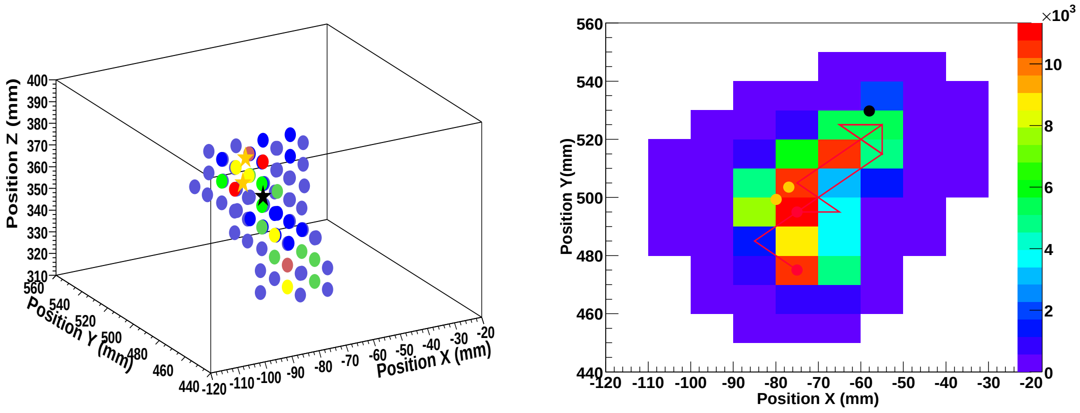

(a)

(b)

Figure 5.24: *Another example of a signal event in pure Xe at 10 bar in which the method has determined correctly the position of the blobs (red circles, in yellow are marked from the simulation) and the track-line (red line). In this case the event was more complicated because it has suffered a high straggling and the track is more like a sphere. The 3D track (a) as well as the XY projections (b) are shown.*

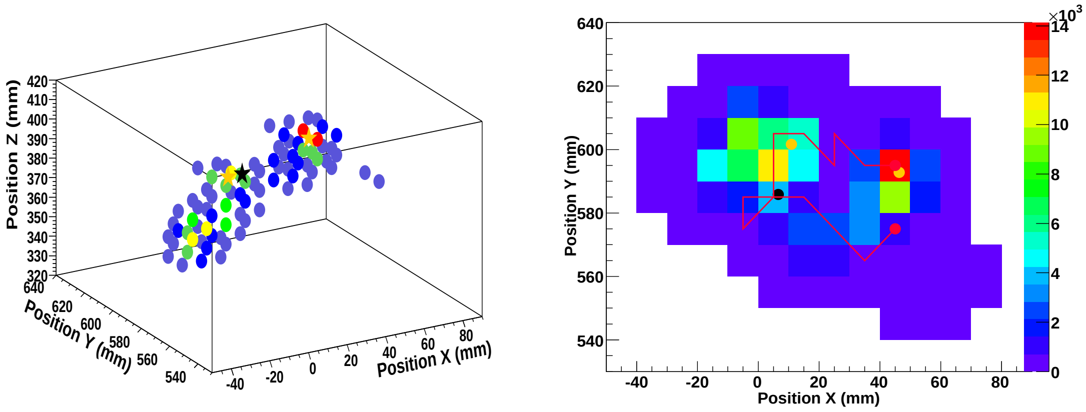

(a)

(b)

Figure 5.25: *Example of a signal event in pure Xe at 10 bar in which the method has not determined correctly the position of the blobs (red circles, in yellow are marked from the simulation) neither the track-line (red line). The 3D track (a) as well as the XY projections (b) are shown.*

In the case of high diffusion a cut in 0.95 is imposed while in the case of a low diffusion Xe mixture a more restrictive one, 0.98, can be selected due to the lower diffusion coefficient in this gas. With this selection, the rejection is improved while keeping a high efficiency. The distance to calculate this coverage has been determined to be 3 cm because in most cases where a fake blob was selected the real one was at around 3 cm.

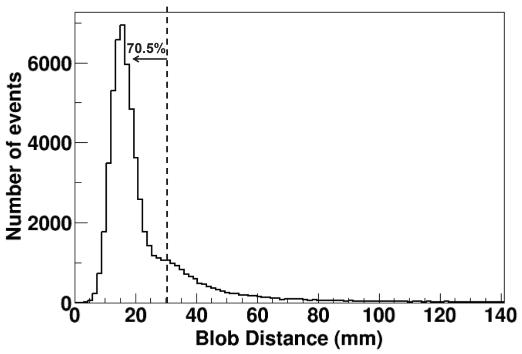

(a)

Figure 5.26: *Distribution of the distance between real (from simulations) and identified blobs calculated as described in the text. In the 70 % of the cases the distance is less than 30 mm.*

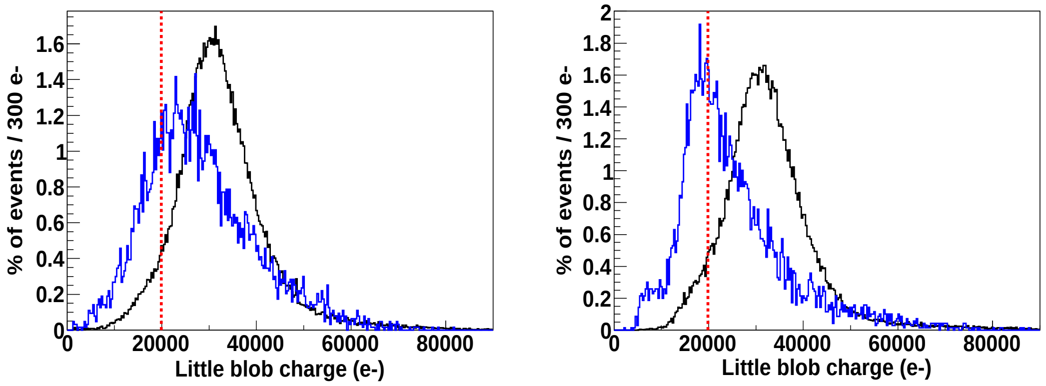

(a) High diffusion Xe

(b) Low diffusion Xe

Figure 5.27: *Distribution of the charge of the little blob for signal (black-line) and background (blue-line) events. (a) In pure Xenon. (b) In a low diffusion Xe mixture. In both cases the red line shows the applied selection that keeps events in which the charge of the little blob is higher than 440 keV.*

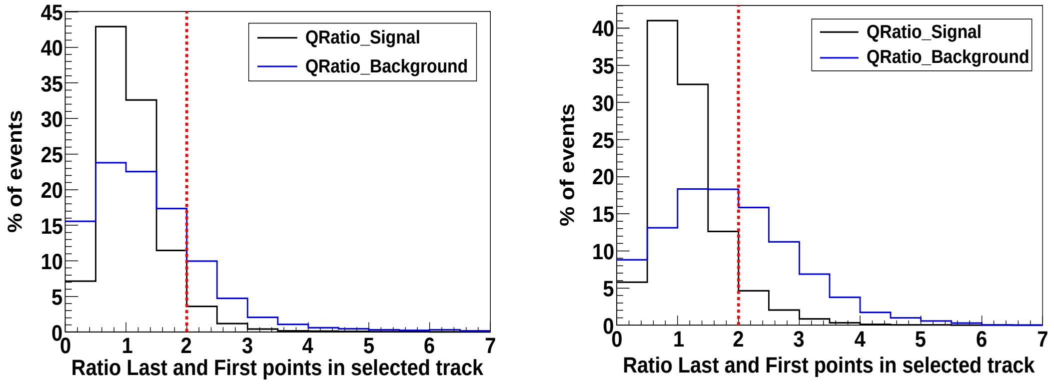

(a) High diffusion Xe

(b) Low diffusion Xe

Figure 5.28: *Charge ratio between the big and little blob found in the main track with the topological method. In black the distribution for signal events and in blue for background events. (a) In pure Xenon. (b) In a low diffusion Xe mixture. In both cases the red line shows the applied selection that keeps events in which the ratio is less than 2. A relative efficiency of 70% is obtained with this selection.*

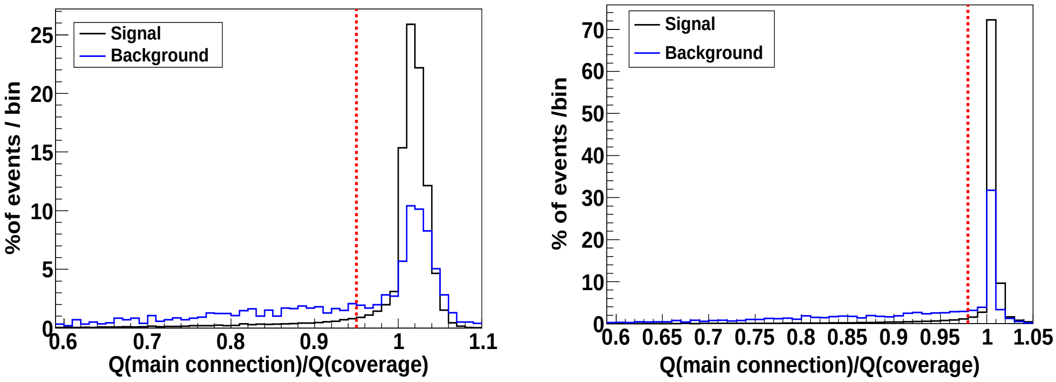

(a) High diffusion Xe

(b) Low diffusion Xe

FIGURE 5.29: *Distribution of the charge ratio between the charge in the longest main track and the charge in the found track-line. (a) In pure Xe (b) In a low diffusion Xe mixture. In both cases the red line shows the applied selection. Black-line corresponds to the signal and the blue-line represents the background produced by the* ^{208}*Tl from the walls.*

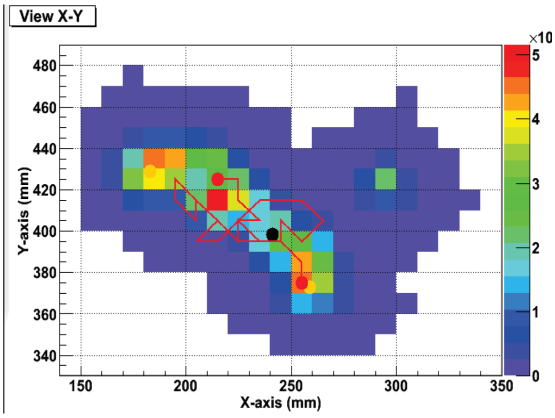

FIGURE 5.30: *An example of a neutrinoless double beta event where the track was not well obtained by the topological method. These events can be recovered applying a coverage to the main track and comparing the charge inside it with the charge in the longest track. The coverage distance is imposed to be 3 cm based on the results obtained. This can be seen in the figure and corresponds to the distance to the real blob (in the simulation is marked with a yellow point).*

5.5.5 Fiducial rejection

An active veto volume is defined next to the walls: an event depositing energy in this volume is rejected (mainly electrons). This selection will depend very much on the ability of the detectors (readout plane and t_0 detector) to determine the spatial position of the event. A veto distance of a pixel size, 10.0 mm, from the walls is imposed. The main effect is on the contaminations coming from the surfaces closer to the active volume and it has not a big effect on events coming from the volumes. In all the cases it is applied at the end of the selection sequence to quantify its real effect and to discuss the need or not to determine the start-of-event to improve the background rejection.

5.5.6 Summary

Different selection criteria have been explained. The methods depend on several parameters that are related to the gas that is considered, with the readout and with the working pressure. These parameters have been adjusted under different requirements. First of all, to have a reasonable high efficiency, of the order of 40% while reducing the background to a few c/y. Then, the characteristics of the readout have also to be taken into account, as its pixel size to define the *segment* distance. The diffusion of the gas is one of the most worrisome effects that have an influence on the topology of the event and then in the discrimination algorithms; for example, in the distance to define the *coverage*. The values of each selection for each gas are listed in Table 5.6. In the next section results of the application of this selections over the events at two different diffusions will be discussed.

			Track Selection One track+one short track		
		$Q_{short\ track}$	s_{dist}	$r_{track\ pixel}$	$Q_{track\ pixel}$
Pure Xe & Low diffusion Xe		100 keV	10 mm	10 mm	1 keV
			Topology Selection		
	Q_{blobs}	r_{blobs}	R_{blobs}	$Q_{little\ blob}$	*Coverage Ratio*
Pure Xe	> 130 keV	150 mm	30 mm	440 keV	0.95
Low diffusion Xe	> 130 keV	70 mm	30 mm	440 keV	0.98
			Fiducial Selection		
		Lateral	Bottom	Top	
Pure Xe & Low diffusion Xe		10 mm	10 mm	10 mm	

Table 5.6: *Summary of the parameters of the selection criteria explained along Section 5.5 for both diffusions considered: high diffusion in pure Xenon and low diffusion Xe. In the case of the track and fiducial selections they are the same for both gases.*

5.6 Background Rejection

After the explanation of the different selection criteria, in this section results of their effect on the simulated events are shown. As mentioned before, two different diffusion coefficients are studied. One corresponding to pure Xenon, a gas with a very high diffusion coefficient and another with lower values as corresponding to a mixture like Xe-TMA or other Xe-based mixtures. The reason to study this mixture is supported by very promising recent experimental results [109] improving the energy resolution with respect to pure Xe and by theoretical predictions that allow, possibly, the detection of the scintillation light in this gas [166]. Moreover, a gas with a low diffusion coefficient improves the pattern recognition as discussed.

The results are presented separately for each gas. The effect of each selection is quantified and explained, both over the background and the signal. The background reduction is quantified through the variable defined as *acceptance factor*. This is the coefficient between the final events after a selection over the initial ones. It can be interpreted as the number of events per detected event surviving each criterion. As it will be seen, they depend, not only on the isotope, but also on the origin of the contamination, whether it is superficial or not, or whether it is close to the sensitive volume or far away. In the next point of the section, a comparison of the total effect of them over the final surviving factors is done. In subSection 5.6.4 the nature of the surviving background events as well as the one of the rejected signal is discussed.

5.6.1 High diffusion gas: Pure Xenon

For signal and background cases, the effect of each cut is evaluated with respect to the events surviving the previous one to see the effect of each cut. The first criteria applied is the track selection. This is applied over the simulated events contained in an energy window from 2400 to 2500 keV. The *track selection* selects events with only one long track and up to one small track. By small track it is meant secondary emissions with a charge smaller than 100 keV, as explained in Section 5.5. Once this selection is done, the *topology selection* is applied. Finally, the fiducial rejection is done separately in the three directions: first in the laterals and then in the bottom and top (in the three cases 10 mm in each direction, the pixel size).

First of all, the effect over the signal efficiency is summarized in Table 5.7 (efficiency expressed in %). The $\beta\beta0\nu$ population suffers the biggest reduction after the track-selection cut because a secondary emission could have enough energy to deposit its charge far away from the main track. Then, the event is considered as a multi-track event and it is rejected. The application of the topological selection has an effect mainly because a fake blob can occur in the middle of the track due to straggling. Also, at high z, where it suffers a higher diffusion, making more difficult the blob identification. The fiducial selection has a higher effect in the laterals than in the top and bottom direction, where it is less than a 5%.

The effect of each criteria on the simulated backgrounds is presented in Table 5.8 as the percentage of surviving events. The track selection has a bigger effect on the ^{208}Tl population than over the ^{214}Bi. The number of events surviving is around $4-7\%$ for the ^{208}Tl and from 15% up to 50% for the ^{214}Bi. It corresponds with what we expect due to the fact that ^{208}Tl has a higher probability to interact Compton or multi-Compton producing events with more than one track. For the ^{214}Bi most of the background events in the energy window come from the photoelectric absorption of the 2447.9 keV gamma, as explained in Section 5.4. The big difference observed for the ^{214}Bi shows a dependence with the origin of the contamination, whether it comes from the parts far from the fiducial volume or closer to it (as it is the case of the readout or cathode contribution) due to the beta emission.

Once the single-track events are selected the *topological* criterion is applied. Its effect is the same for all contributions of background independently of origin and isotope. The surviving events after the application of this cut with respect to the previous one is of the order of 40%, except for the cathode where the effect of the diffusion is higher as they are produced at higher z position.

The fiducial rejection criterium has a different effect depending on the origin of the background, playing a more important role for surface contamination, as pointed out in Section 5.5.5. As shown in Table 5.8, the effect over the volume contamination far from the fiducial volume is of the order of 20% but it is higher over the surface contaminations closer to the fiducial volume. The main impact is over the ^{214}Bi surface contamination (mainly electrons) coming from the readout and cathode with a surviving factor of less than 1%. It also has an effect over the ^{208}Tl population due to the emission of a gamma plus an electron but it is smaller, having a surviving factor of around 20%.

		Track	Topology	Fiducial Rejection		
Origin				Lateral	Bottom	Top
Signal	$\beta\beta0\nu$	77.5 ± 0.4	85.4 ± 0.5	88.5 ± 0.5	99.1 ± 0.6	98.6 ± 0.6

Table 5.7: *Efficiency (in %) of the simulated $\beta\beta0\nu$ events after the successive application of the selection criteria. Track is applied over the events detected in the RoI and then, the number of surviving events for each selection is calculated with respect to the surviving events from the previous one to evaluate the effect of each one. The events are simulated in pure Xenon at 10 bar and considering a pixel size of 10×10 mm^2.*

		Track	Topology	Fiducial Rejection		
Origin				Lateral	Bottom	Top
Vessel	^{208}Tl	7.0 ± 0.3	41.9 ± 3.8	68.9 ± 8.1	100.0 ± 12.8	98.4 ± 12.6
	^{214}Bi	14.1 ± 0.5	43.1 ± 2.7	82.1 ± 6.4	99.7 ± 8.2	99.0 ± 8.1
Drift	^{208}Tl	4.8 ± 0.1	43.5 ± 2.0	33.9 ± 2.6	97.8 ± 9.3	97.7 ± 9.4
	^{214}Bi	41.9 ± 0.7	39.4 ± 1.0	12.7 ± 0.8	99.6 ± 8.8	98.1 ± 8.7
Readout	^{208}Tl	3.2 ± 0.1	40.7 ± 2.6	90.8 ± 7.1	16.8 ± 2.5	100.0 ± 19.4
	^{214}Bi	51.6 ± 0.5	36.6 ± 0.6	88.6 ± 1.7	0.40 ± 0.01	100.0 ± 32.4
Cathode	^{208}Tl	3.8 ± 0.1	56.9 ± 3.2	80.0 ± 5.3	100.0 ± 7.0	19.1 ± 2.4
	^{214}Bi	34.9 ± 0.4	65.7 ± 1.1	76.6 ± 1.5	100.0 ± 2.0	0.6 ± 0.1

Table 5.8: *Acceptance factor of the different sources of background simulated after the successive application of the selection criteria in the RoI in pure Xenon (high diffusion) at 10 bar and considering a pixel size of 10×10 mm^2. The percentage of events is calculated with respect to the previous one.*

5.6.2 Low diffusion gas: Xenon-TMA.

The diffusion of the gas has an effect on the spatial and the energy resolution of the detection. Up to now the results obtained in a gas with high diffusion coefficients, as it is pure Xenon,were discussed but the study has also been done over events drifted in a less diffusive gas, as for example, in a mixture of Xenon with trimethilamine (TMA). This mixture has been the object of many studies and proposed lately for TPCs [166]. Experimental studies and results about the gains and energy resolutions obtained in this Penning mixture have been recently published in [109].

The main motivation to study this mixture, is that, as it forms a Penning mixture with Xe, the gain and energy resolution in the gas improve. Moreover, the diffusion coefficient obtained is smaller than in pure Xe (3 times smaller for the longitudinal, and 10 times smaller for the transversal coefficient in a drift field of $1\mathrm{kV\,cm^{-1}}$). First results using this gas with Micromegas have proven an energy resolution of 7.3 (9.6) % FWHM at 1 (10) bar for the 22.1 keV gammas from ^{109}Cd [109]. The best value extrapolates to a 0.7 (0.9) % FWHM at $Q_{\beta\beta}$. These results and the mentioned lower diffusion make this gas a promising mixture to look for the $\beta\beta0\nu$ decay in a TPC in charge mode.

The effect of each selection criteria over the signal is summarized in Table 5.9. The use of a quencher to lower the diffusion allows a better determination of two separated tracks and high energy depositions. For this reason the obtained efficiency after the track and topology selection is slightly lower than in pure Xe. On the other hand, it is increased after the fiducial selection since less events (in the RoI) touch the walls because of the lower diffusion and, at the end, the same efficiency is obtained as in pure Xe.

For the background, results are summarized in Table 5.10. The discrimination algorithms depend on several parameters that have to be adjusted for each diffusion (for example charge around a pixel to consider it active or not). Once this is done the effect of the track selection is similar to the one obtained in pure Xe. However, after the topological selection an improvement of a factor 3 at least is obtained, having a surviving percentage of events with respect to the ones surviving the track selection of the order of 15% when the one obtained in pure Xe is around a 40%. This is mainly due to the fact that in a gas with a lower diffusion coefficient it is more difficult that a secondary emissions (as Bremsstrahlung radiation or X-Rays) could produce a secondary blob closer to the main track that could mimic a $\beta\beta0\nu$ event. In addition, the blob identification is better at lower diffusions and there are, also, less straggling effect and less twisted tracks. However, these values are smaller for ^{214}Bi contamination coming from the surface because the fiducial cut is not applied yet and some electrons, that touch the walls, have a secondary blob that could mimic the track with a signal event.

Finally, the fiducial selection is applied. In general, values are slightly worse for the lateral walls because at lower diffusion less events “touch”the walls but, in the case of a ^{214}Bi surface contamination, the reduction is two times better than in pure Xe.

5.6.3 Comparison between the two diffusions

Now that the effect of each criteria has been presented for each gas, the total surviving factor in each case is summarized. For signal and background events, the surviving factor is calculated in the RoI as well as the total surviving factor for each gas, after the application of all the discrimination algorithms.

Origin		Track	Topology	Fiducial Rejection		
				Lateral	Bottom	Top
Signal	$\beta\beta0\nu$	76.1 ± 0.4	78.9 ± 0.5	95.4 ± 0.6	99.4 ± 0.6	98.9 ± 0.6

Table 5.9: *Efficiency (in %) of the simulated $\beta\beta0\nu$ events after the successive application of the selection criteria. Track is applied over the events detected in the RoI and then, the number of surviving events showed for each selection, is calculated with respect the surviving events from the previous one. The events are simulated in a low diffusion Xe micture like Xenon-TMA at 10 bar and considering a pixel size of 10×10 mm^2.*

Origin		Track	Topology	Fiducial Rejection		
				Lateral	Bottom	Top
Vessel	^{208}Tl	7.1 ± 0.3	11.7 ± 1.6	83.1 ± 16.1	100.0 ± 20.2	98.0 ± 19.9
	^{214}Bi	16.0 ± 0.6	12.6 ± 1.2	93.4 ± 12.2	99.1 ± 13.2	100.0 ± 13.4
Drift	^{208}Tl	4.4 ± 0.2	14.7 ± 1.6	64.9 ± 10.7	100.0 ± 18.1	96.7 ± 17.7
	^{214}Bi	42.1 ± 0.4	10.6 ± 0.2	19.8 ± 1.1	99.3 ± 6.9	98.5 ± 6.9
Readout	^{208}Tl	2.4 ± 0.1	23.9 ± 2.2	92.8 ± 10.8	14.9 ± 3.5	100.0 ± 30.9
	^{214}Bi	37.2 ± 0.5	30.2 ± 0.8	89.8 ± 2.9	0.2 ± 0.1	100.0 ± 81.6
Cathode	^{208}Tl	4.8 ± 0.1	18.0 ± 1.4	93.6 ± 9.4	100.0 ± 10.2	24.1 ± 4.0
	^{214}Bi	57.4 ± 0.6	26.9 ± 0.5	83.6 ± 1.9	100.0 ± 2.4	0.3 ± 0.1

Table 5.10: *Percentage of the surviving events of the different sources of background simulated after the successive application of the selection criteria in the RoI in a low diffusion Xe mixture at 10 bar with a pixel size of 10×10 mm^2. The percentage of events showed is with respect the previous one.*

The efficiency is first discussed in Table 5.11. It is obtained a total efficiency of 40% for both diffusions, after the application of all the selections explained before. In the RoI the geometrical efficiency is already just a 70%. The 30% loss is due to incomplete charge collection by events near the walls depositing part of their energy out the gas volume or, mainly, to energetic bremsstrahlung emissions leaving it. Therefore the real effect of the algorithms is to reduce the signal in a 43% in total. As this loss is due to geometrical factors the same value is obtained for both gases. In Gothard's TPC (much smaller) this value was around 74% [89] in the RoI between 2 and 3 MeV. However, the total efficiency obtained there was 20%, a factor 2 worse than with this analysis.

Table 5.12 sums up the results for the different background simulated. For both diffusions, a total rejection of 6 orders of magnitude is obtained, being the total percentage of surviving events of the order of 10^{-6} for all the contributions. However, the total rejection is bigger in low diffusion Xe. In a gas with a lower diffusion a value at least 3 times better is obtained than in pure Xenon. The bigger effect is over the ^{214}Bi coming from the surfaces, being around 4 times better in the case of the readout. It is worse in the case of the cathode because the drift distance may introduce a diffusion effect.

In this work, a rejection factor obtained with the topology analysis is around 60% in pure Xe and close to 90% in a low diffusion Xe mixture. Comparing with Gothard, their topological method obtained a rejection factor of 91.4%. However, as mentioned, the pixel size was smaller and worked at lower pressure in a low diffusion Xe-mixture making the comparison difficult.

The pixel studied in this work was fixed at 10×10 mm^2, too wide for the low diffusion case. The factor three of difference is limited by the pixelization, therefore, it is a conservative limit.

Origin		Efficiency in the RoI (%)	Total Efficiency (%)	
			Pure Xe	Low diffusion Xe
Signal	$\beta\beta0\nu$	71.1 ± 0.2	40.71 ± 0.18	40.02 ± 0.18

Table 5.11: *Percentage of surviving events of the simulated $\beta\beta0\nu$ (efficiency) after the selection of a RoI of 2% at $Q_{\beta\beta}$. In the last columns is presented the total efficiency after the application of all the discrimination algorithms for both of the studied gases, pure Xe and low diffusion Xe mixture. They are simulated at 10 bar and considering a pixel size of 10×10 mm^2.*

Origin		Surviving factor (x 10^{-3})	Surviving factor (x 10^{-6})	
		RoI	Pure Xe	Low diffusion Xe
Vessel	^{208}Tl	0.38 ± 0.04	6.98 ± 0.64	2.54 ± 0.37
	^{214}Bi	0.031 ± 0.001	1.50 ± 0.09 0.49 ± 0.05	
Drift	^{208}Tl	1.98 ± 0.01	13.4 ± 0.10	7.23 ± 0.94
	^{214}Bi	0.203 ± 0.001	4.14 ± 0.26	1.74 ± 0.08
Readout	^{208}Tl	2.70 ± 0.01	5.37 ± 0.74	2.13 ± 0.46
	^{214}Bi	1.385 ± 0.001	0.87 ± 0.20	0.23 ± 0.13
Cathode	^{208}Tl	2.23 ± 0.01	7.39 ± 0.84	4.36 ± 0.64
	^{214}Bi	1.03 ± 0.001	1.09 ± 0.20	0.38 ± 0.12

Table 5.12: *Number of survived events of the different sources of background simulated after: first column, the selection of a RoI at 2% 2σ at $Q_{\beta\beta}$, and, in the last two columns, it is presented the total acceptance factor after the application of all the discrimination algorithms, for both gases, high purity Xe (high diffusion) and low diffusion Xe mixture. They are simulated in a 1 cm-length pixelized detector filled at 10 bar.*

5.6.4 Surviving events

After the application of all the discrimination algorithms it is very interesting to study the surviving background events. With the help of the flag that has been included in the Geant4 simulation, the nature of the interaction can be followed. It is also important to know which signal events have been rejected. With this information the selection criteria can be improved in the future. In Table 5.13 the percentage of surviving events that have had zero, one or two secondary emissions (Bremsstrahlung, Compton or X-Rays) is listed. For Bremsstrahlung and Compton interactions only those with an energy higher than 100 keV are selected. In this part of the work were studied events of ^{208}Tl and ^{214}Bi coming just from two different parts of the geometry: the vessel, far from the fiducial volume, and events coming from the readout, close to the fiducial volume. In both cases the results are similar. In most of the events there is an X-Ray emission with low energy (30 keV) but not a secondary emission due to Compton or Bremsstrahlung. But on those events in which one high energetic secondary emissions has occurred, as the method has selected events with just one track, they must have produced an extra blob attached to the main track. If the energy is inside the RoI these events would pass the discrimination criteria applied. In Figure 5.31 there is an example of one background event that fakes a signal event. In particular it is a 2447 keV gamma from ^{214}Bi that has produced a Compton of 322 keV that produces an additional blob. As it has an energy inside the RoI, this event will survive all the cuts.

Pure Xe										
Origin		Bremsstrahlung			Compton			X-Rays		
		0	1	2	0	1	2	0	1	2
Vessel	^{208}Tl	82.1%	18.6%	$< 4\%$	55.2%	29.8%	13.4%	28.4%	41.8%	37.3%
	^{214}Bi	95.1%	3.1%	$\ll 1\%$	69.0%	29.1%	$\ll 1\%$	18.0%	39.9%	36.3%
Readout	^{208}Tl	87.6%	11.1%	$< 1\%$	42.0%	40.7%	17.3%	32.1%	42.0%	24.7%
	^{214}Bi	97.8%	2%	$\ll 1\%$	62.3%	33.3%	$< 2\%$	17.8%	40.0%	44.0%
Low diffusion Xe										
Vessel	^{208}Tl	85.9%	11.7%	3.9%	62.5%	25.0%	9.4%	32.8%	34.4%	32.8%
	^{214}Bi	96.9%	11.1%	$\ll 1\%$	70.4%	29.6%	$\ll 1\%$	22.2%	44.4%	33.3%
Readout	^{208}Tl	86.9%	13.0%	$< 7\%$	21.7%	24.6%	49.3%	32.1%	42.0%	24.7%
	^{214}Bi	98.0%	$< 2\%$	–	72.0%	26.0%	$< 4\%$	10.0%	46.0%	48.0%

TABLE 5.13: *Percentage of surviving background events that has zero, one and two or more Bremsstrahlung, Compton and X-Rays emissions. These emissions can produce an extra blob and are one of the reasons that a background event survives all the discrimination algorithms if it has an energy inside the RoI.*

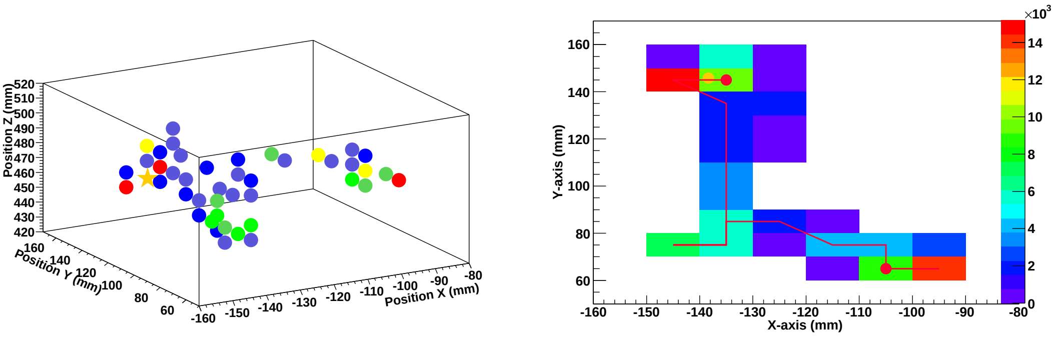

(a)

(b)

FIGURE 5.31: *^{214}Bi gamma emission with an energy of 2447 keV. Along its path it has produced a Compton interaction of $>$ 440 keV that in the case of low diffusion, produces a extra blob that allows this event to pass all the selection criteria due to its similarity with a signal event. It has an energy inside the RoI. (a) and (b) represents the 3D and XY projection of the event in pure Xe while (c) and (d) are for a low diffusion Xe mixture.*

The rejected signal events were also studied. In this case, from a Bremsstrahlung interaction, a Compton or a multi-Compton event can be produced. Therefore in this case it is important the number of multi-Compton events produced that makes the signal to be rejected by the selection of the track. In addition, if some Bremsstrahlung radiation escapes from the sensitive volume then the final event will have less charge than $Q_{\beta\beta}$ and will be rejected. The emission of X-rays, as they would produce a secondary emission of 30 keV is only important if more than one are produced at the same time, case in which the event will be rejected as a multi-track event. In Table 5.14 is summarized the percentage of rejected events with a secondary emission.

Visualizing the rejected signal events can help to classify them in several categories. Approximately 20% are rejected because they have one or two secondary emissions with an energy higher than 100 keV. Another 20% is excluded because the track is not well defined, either because a fake blob occurs in the middle (15%) or because some charge is out of the track found (5%). There is a 12% that has an energy smaller than $Q_{\beta\beta}$ because some energy was deposited outside by Bremsstrahlung radiation that escapes. Then, 5% of the times one electron has an energy smaller than 400 keV and around 8% of the times one of the two blobs has much small energy than the other. The rest is rejected with the fiducial cut or because of some errors in the code. Some examples of rejected signal can be seen in Figure 5.32 and 5.33.

There is a clear relation with the z position because at higher z the event suffers a higher diffusion and it is more difficult to identify. In Figure 5.34 is plotted the distribution of the z position after each selection criteria for the two diffusions considered. The dependence of the number of signal events rejected with the z position is more marked in a gas with a higher diffusion coefficient as Xe than at lower diffusion. Therefore, at higher z the reconstruction of the track is more difficult due to the effect of the diffusion and more signal events are rejected. In addition, it produces a bigger straggling effect as mentioned in 5.4.3.

	Bremsstrahlung In			Bremsstrahlung Out			Compton		
	0	1	2	0	1	2	0	1	2
$\beta\beta0\nu$ in pure Xe	75.0%	18.0%	$< 7\%$	84.0%	15.0%	$\ll 1\%$	99.0%	$< 1\%$	$\ll 1\%$
$\beta\beta0\nu$ in low diffusion Xe	74.3%	17.8%	$< 8\%$	83.3%	14.7%	$\ll 1\%$	98.1%	2.0%	$\ll 1\%$

TABLE 5.14: *Percentage of rejected signal events that has zero, one and two or more Bremsstrahlung deposited in and out of the chamber. The number of Compton emissions (they are produced by a Bremsstrahlung photon) are also summarized. These emissions can produce extra blobs in the middle of the track decreasing the total energy of the event in the selected track.*

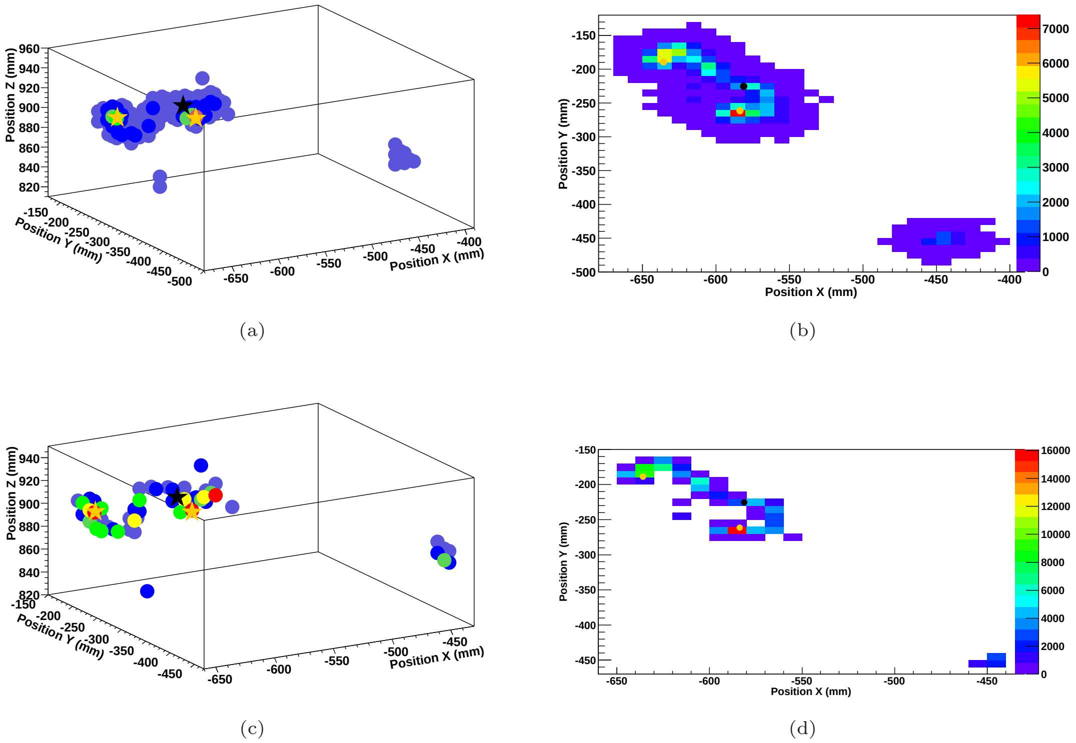

(a) (b)

(c) (d)

FIGURE 5.32: *A $\beta\beta0\nu$ event that produces two separated tracks due to the emission of Bremsstrahlung radiation that produces an extra deposition of energy of 227 keV far from the main track. This event will be rejected. (a) and (b) represent the 3D and XY projection of the event in pure Xe while (c) and (d) are in a low diffusion Xe mixture.*

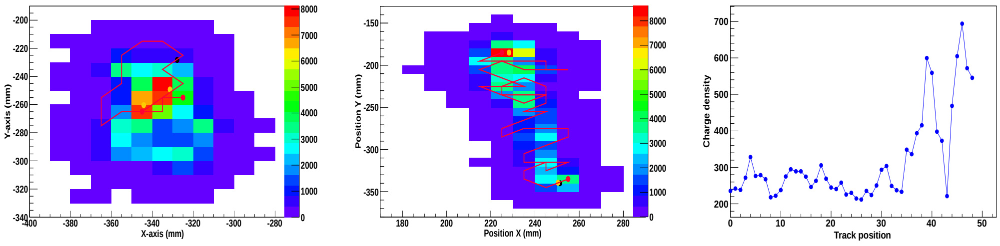

(a) (b) (c)

Figure 5.33: *Signal events that have been rejected. (a) In this case the track was not well identified. Even if the blobs were well identified (in yellow are the "real" ones from the simulation and in red the identified ones) some charge is out the main track. This event will be rejected because it has an energy smaller than 2458 keV. (b) An event where one of the two blobs has much less energy than the other and the algorithm identifies as just one blob. (c) Charge density along the track of the event shown in (b). It is clear that it looks as if it has just one blob.*

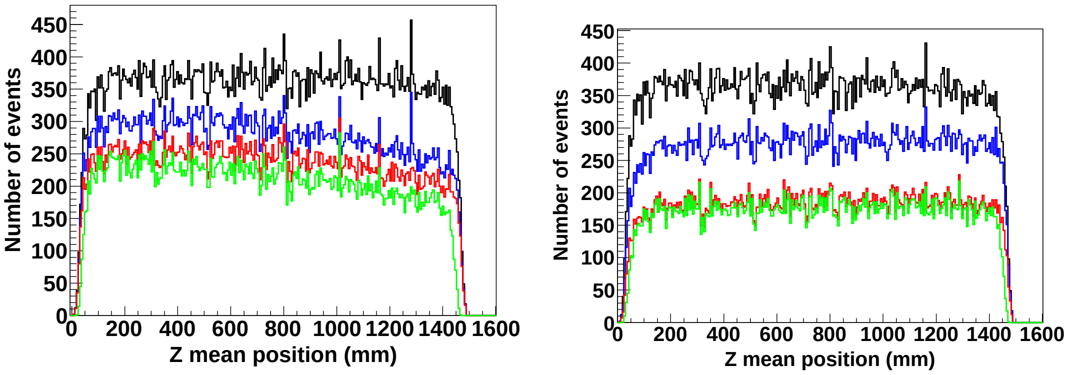

(a) Pure Xe

(b) Low diffusion Xe

Figure 5.34: *z position of the events (calculated as the mean position) after the application of each of the selection criteria. (a) In pure Xe. More events are rejected at higher z because of the effect of the diffusion that makes more difficult the reconstruction of the track. (b) In low diffusion Xe this effect is much lower. Black-line represents events in the RoI, the blue-line after the track selection, red-line after the topological selection and green-line after the fiducial veto.*

5.7 Energy Resolution studies

In the previous discussions, an energy resolution of 2% FWHM at $Q_{\beta\beta}$ has been considered to select events in a wide energy window (100 keV) to a better understanding of the backgrounds. In this section, results of the efficiency and background rejection, varying the RoI, are presented. Three regions are defined: from 2400 to 2500 keV (2% FWHM at $Q_{\beta\beta}$), from 2433 to 2483 keV (1% FWHM at $Q_{\beta\beta}$) and from 2446 to 2470 keV (0.5% FWHM at $Q_{\beta\beta}$).

First of all, the efficiency, in %, for each region in Table 5.15 is evaluated. There is no difference changing the RoI, effect also observed in the spectra in Figure 5.35. In this plot the energy spectrum for the $\beta\beta0\nu$ distribution has been convoluted with a Gaussian of the required energy resolution in each case. If the RoI is increased, the detector will start to be sensitive to the

Bremsstrahlung tale that we observe in the spectrum before cuts in Figure 5.3 and therefore the efficiency will increase, but also the background will increase.

Secondly, we study the effect in the rejection power. It is interesting to study exactly its effect and compute a factor of merit as before in order to quantify it. In Table 5.16 are listed the acceptance factors obtained for each population of background in the two considered cases of diffusion. They are computed in the different RoI and the final values are obtained after the application of the same discrimination criteria explained before.

Focusing the attention on the results obtained in the different RoI's, in the case of the ^{208}Tl isotope, its contribution is reduced linearly with the energy window. It is what we expect because the contribution from this isotope is more or less flat as because the three regions considered are far from the 2615 keV gamma, photoelectric peak and also from the Compton edge. The same effect is observed when studying the final surviving factors. On the contrary, the contribution of ^{214}Bi coming from the volumes in the RoI remains more or less constant if the energy resolution changes from a 2% to a 1% FWHM at $Q_{\beta\beta}$. It starts to change by 20%, on average, when changing to a 0.5% FWHM at $Q_{\beta\beta}$ window. That is attributed to the fact that the main contribution comes from the gamma at 2447.5 keV. Its energy range, if the same energy resolution as at $Q_{\beta\beta}$ is considered, is completely covered at 1% FWHM at $Q_{\beta\beta}$ but starts to decrease when the resolution is 0.5% FWHM. Moreover, for the ^{214}Bi the effect is highly dependent on the origin of the contamination. In the surfaces close to the fiducial volume (the readout or cathode), the dependence of the rejection factor is linear with the RoI, as for the ^{208}Tl. For surface contaminations the beta spectrum of ^{214}Bi dominates over the gammas. The beta emission from ^{214}Bi is absorbed by the material when simulating volumetric contaminations but not when considering superficial ones. Only after the fiducial cut, the gamma contribution dominates. Afterwards, the final factors remain more or less constant, also for the ^{214}Bi coming from surface since beta contribution has been eliminated by fiducial cuts.

To compare between each energy resolution the factor of merit has also been computed in each region and for each contribution and are summarized in Tables 5.17 and 5.18 (pure Xe and low diffusion Xe, respectively). The factor of merit is slightly better at an energy window of 0.5% FWHM but the differences are neglecteable in the case of ^{214}Bi. For the ^{208}Tl as the background decreases linearly a factor 2 of improvement is obtained between a 2% and a 0.5% FWHM at $Q_{\beta\beta}$. The better f.o.m. in the ^{208}Tl with respect to the one for ^{214}Bi could be beacause there is a higher probability to produce a multi-track event, and could increase the probability to produce an extra blob (from Tables 5.8, 5.10 and 5.13) making it easier to reject.

In conclusion, a better energy resolution helps to reduce the background of the detector. In the case of ^{208}Tl it decreases linearly with the energy window. In the case of ^{214}Bi, as the main contribution comes from the gamma of 2447 keV hardly changes. It is also interesting to mention that the efficiency does not change in one RoI or other, because we are far from the Bremsstrahlung tail in the three cases.

	2% FWHM at $Q_{\beta\beta}$	1% FWHM at $Q_{\beta\beta}$	0.5% FWHM at $Q_{\beta\beta}$
RoI	71.1	70.5	70.5
After selections			
Pure Xe	40.7	40.6	40.6
Low diffusion Xe	40.0	40.0	40.0

TABLE 5.15: *Efficiency of the simulated $\beta\beta0\nu$ events in the different energy windows. Efficiency in the region of interest in each case as well as after all the discrimination criteria applied in pure xenon and a mixture of Xe TMA (96/4). The statistical error in all the cases is* ±0.2.

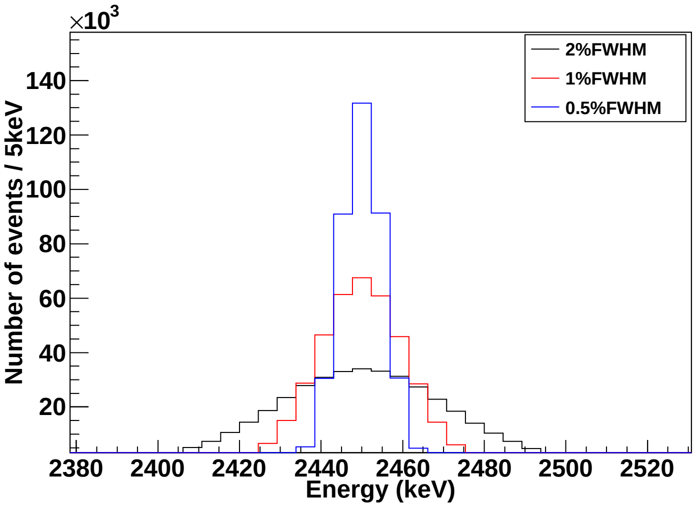

FIGURE 5.35: *$\beta\beta0\nu$ spectra for each energy resolution studied. The simulated spectra have been convoluted with a Gaussian of the corresponding energy resolution for each case. The binning for each one is 5 keV. If the range for each energy resolution is observed it is clear that we are not losing efficiency. The ranges are: from 2400 to 2500 keV (2% FWHM at $Q_{\beta\beta}$), from 2433.4 to 2482.6 keV (1% FWHM at $Q_{\beta\beta}$) and from 2445.7 to 2470.3 keV (0.5% FWHM at $Q_{\beta\beta}$).*

Origin			2%	1%	0.5%
Vessel	RoI(10^{-4})	^{208}Tl	3.76 ± 0.05	1.83 ± 0.03	0.89 ± 0.02
		^{214}Bi	0.30 ± 0.01	0.24 ± 0.01	0.24 ± 0.01
	Final Pure Xe(10^{-6})	^{208}Tl	6.98 ± 0.64	3.31 ± 0.44	1.40 ± 0.29
		^{214}Bi	1.50 ± 0.08	1.37 ± 0.08	1.26 ± 0.08
	Low diffusion Xe(10^{-6})	^{208}Tl	2.54 ± 0.36	1.01 ± 0.23	0.58 ± 0.18
		^{214}Bi	0.48 ± 0.04	0.43 ± 0.04	0.41 ± 0.04
Drift	RoI(10^{-4})	^{208}Tl	19.80 ± 0.11	9.78 ± 0.08	4.90 ± 0.05
		^{214}Bi	2.03 ± 0.02	1.38 ± 0.02	1.08 ± 0.01
	Final Pure Xe(10^{-6})	^{208}Tl	13.40 ± 0.92	7.23 ± 0.67	3.58 ± 0.48
		^{214}Bi	4.14 ± 0.26	3.73 ± 0.25	3.63 ± 0.24
	Low diffusion Xe(10^{-6})	^{208}Tl	7.23 ± 0.94	3.43 ± 0.65	1.47 ± 0.43
		^{214}Bi	1.74 ± 0.08	1.60 ± 0.03	1.53 ± 0.08
Readout	RoI(10^{-4})	^{208}Tl	27.00 ± 0.16	11.02 ± 0.12	5.60 ± 0.09
		^{214}Bi	13.80 ± 0.08	5.16 ± 0.05	2.23 ± 0.03
	Final Pure Xe(10^{-6})	^{208}Tl	5.37 ± 0.74	3.65 ± 0.70	1.62 ± 0.47
		^{214}Bi	0.87 ± 0.20	0.64 ± 0.15	0.64 ± 0.15
	Low diffusion Xe(10^{-6})	^{208}Tl	2.13 ± 0.46	0.58 ± 0.02	0.45 ± 0.17
		^{214}Bi	0.23 ± 0.13	0.21 ± 0.12	0.21 ± 0.12
Cathode	RoI(10^{-4})	^{208}Tl	22.30 ± 0.01	11.20 ± 0.10	5.66 ± 0.07
		^{214}Bi	10.30 ± 0.06	5.57 ± 0.05	2.97 ± 0.03
	Final Pure Xe(10^{-6})	^{208}Tl	7.39 ± 0.84	3.13 ± 0.54	1.71 ± 0.40
		^{214}Bi	1.09 ± 0.20	1.05 ± 0.20	1.02 ± 0.19
	Low diffusion Xe (10^{-6})	^{208}Tl	4.36 ± 0.64	1.80 ± 0.41	1.23 ± 0.34
		^{214}Bi	0.38 ± 0.12	0.30 ± 0.11	0.26 ± 0.09

Table 5.16: *Percentage of the surviving events of the different sources of background simulated changing the energy window. The results in the corresponding RoI are presented and also the values after the application of all the discriminations criteria under each diffusion considered. As it is indicated the numbers of the table are multiplied by* 10^{-4} *and* 10^{-6}*, respectively.*

Origin		2%	1%	0.5%
Vessel	^{208}Tl	154.1 ± 7.7	223.2 ± 15.8	344.0 ± 36.7
	^{214}Bi	332.7 ± 11.2	347.8 ± 12.2	362.2 ± 13.1
Drift	^{208}Tl	111.2 ± 4.3	151.1 ± 7.7	214.6 ± 15.2
	^{214}Bi	200.0 ± 7.2	210.4 ± 8.0	213.2 ± 8.11
Readout	^{208}Tl	175.7 ± 12.9	212.8 ± 21.4	319.1 ± 47.5
	^{214}Bi	436.3 ± 52.0	507.7 ± 62.1	507.7 ± 62.1
cathode	^{208}Tl	149.7 ± 9.2	229.8 ± 21.0	311.2 ± 38.0
	^{214}Bi	389.6 ± 37.8	395.8 ± 39.2	403.1 ± 40.6

Table 5.17: *Factor of merit calculated as in 5.7, with the corresponding energy resolution from Table 5.15 and its rejection factor (the inverse of the surviving factor) in pure Xe at 10 bar.*

Origin		2%	1%	0.5%
Vessel	^{208}Tl	251.1 ± 19.3	397.9 ± 47.5	523.0 ± 81.2
	^{214}Bi	572.2 ± 29.6	609.9 ± 33.6	622.7 ± 34.9
Drift	^{208}Tl	148.8 ± 10.4	215.4 ± 21.3	329.0 ± 49.0
	^{214}Bi	303.7 ± 9.0	315.7 ± 9.7	322.7 ± 10.1
Readout	^{208}Tl	274.4 ± 31.2	521.7 ± 89.3	591.6 ± 114.5
	^{214}Bi	834.3 ± 244.6	879.5 ± 257.9	879.5 ± 257.9
Cathode	^{208}Tl	191.7 ± 15.00	297.3 ± 35.5	359.5 ± 51.5
	^{214}Bi	652.2 ± 106.1	727.0 ± 131.8	777.2 ± 150.4

TABLE 5.18: *Factor of merit calculated as in 5.7, with the corresponding energy resolution from Table 5.15 and its rejection factor (the inverse of the surviving factor) in low diffusion Xe at 10 bar.*

5.8 Background level

Once the rejection potential has been obtained in different scenarios of energy resolution and diffusion, the expected background in c keV^{-1} kg^{-1} y^{-1} is calculated as

$$b = F \cdot Ac \cdot M_{material} \frac{1}{\Delta E \cdot M_{Xe}}, \tag{5.8}$$

where F is the rejection factor defined as percentage of surviving events after the application of the selections with respect to the initial ones; Ac is the effective activity of the material, that can be normalized by the mass of the emitter material, and is expressed in Bq/kg, or can be normalized by the surface, hence is expressed in Bq/cm^2 and M is the mass of this material (or the surface if the effective activity is superficial). ΔE is the energy resolution in keV and M_{Xe} the mass of the $\beta\beta$ emitter in kg, in this case Xenon (124 kg in the fiducial volume simulated). To obtain the background, expressed in c keV^{-1} kg^{-1} y^{-1} we have to pass from s^{-1} to y^{-1}. The background for each of the simulated elements has been calculated using the representative effective activities listed in Table 5.19 and obtained from different measurements (reference is shown in the first column). The vessel and cathode are made of Copper, the readout is a microbulk Micromegas and the field cage is made of copper and Teflon. A value taking into account the mass of each element present in the field cage and the activities in the Table 5.19 was obtained.

Material	Ref.	^{232}Th (mBq/kg)	^{238}U (mBq/kg)
Copper	[165]	4.1×10^{-3}	1.2×10^{-2}
Teflon	[190]	8.3×10^{-3}	4.1×10^{-3}
Kapton	[191]	< 1.1	< 27
	Ref.	^{232}Th (mBq/cm^2)	^{238}U (mBq/cm^2)
Micromegas	[156]	$< 4.6 \times 10^{-3}$	$< 1.1 \times 10^{-2}$

Table 5.19: *Activities from ^{232}Th and ^{238}U for the different materials considered in the simulation. In the second row there is the reference for the activities considered. They are expressed in (mBq/kg) or in (mBq/cm^2) if they are superficial. From the ^{238}U is obtained the contribution of ^{214}Bi and from the ^{232}Th the one of the ^{208}Tl (with a branching ratio of 36%).*

Apart from the elements simulated and discussed in Section 5.6, another main component are the end-caps, made of copper, that have also been simulated to determine a more realistic background scenario. All these elements, represent, at least, the 80% of the final mass. Other small elements, like the resistors in the field cage, wires to read the pixels, feed the detectors or the pieces or epoxy to do the electric connections, have not been considered and could introduce a high contamination if the elements are not chosen to be radiopure since they are placed close to the fiducial volume. Nevertheless, these elements will in principle, represent low mass, therefore first good approximation results can be obtained. It has to be noted that the background model not only depends on the mass but also on the isotopes. Here are only considered the contribution from the ^{208}Tl and ^{214}Bi because, as it has been discussed in Section 5.2, they are the main components that concern us, as the contribution from other sources like muons or alphas could be easily rejected.

In Table 5.20 are listed the background levels obtained for each contamination in the different regions of interest considered (that represents a 2%, 1% and 0.5% FWHM at $Q_{\beta\beta}$) and with the two diffusion coefficients simulated (pure Xe and low diffusion Xe mixture). As values are given in terms of counts/keV, the energy resolution considered just determines the region where the background is obtained. In order to evaluate the most important contribution, the background from each element and isotope are shown separately. The main contribution comes from the readout because it is the closest element to the fiducial volume and has a high surface of emission. In this case we have considered a microbulk Micromegas, the radiopurity of which was measured with a high purity Ge spectrometer (HPGe) in the Canfranc Underground Laboratory [156] obtaining upper bounds limited by the minimum detectable activity of the detector. In addition, these limits appear artificially high because the samples measured were of low mass. Therefore, as only an upper bound was obtained, the resulting background is also an upper bound and lower values seem possible to be reached. Further studies are planned to obtain more accurate measurements and to try to reduce this background with a careful selection of materials and treatment of the Micromegas during its manufacturing process, because the origin of the contamination seem to be localized, possibly, in the rest of epoxy and in the etching bath. In any case Micromegas detectors have shown to be one of the most radiopure detectors nowadays.

The second main element are the vessel and end-caps due to the high amount of mass that they represent (around 4 ton of copper). Two different scenarios are considered in order to obtain the total background. The sum of all items, independently if they are upper bound or not is called the "conservative scenario". In a more realistic one, is supposed that the Micromegas have a lower activity value and an estimation is done to obtain it. The microbulk Micromegas consists of two layers, each one with a Kapton-Copper-Kapton layer structure. The sample measured in [156] was one of this layers with a thickness of $50\,\mu$m of copper and 5 and $5\,\mu$m of Kapton. With the dimensions of the Micromegas and the activities of the elements from Table 5.19 the possible radiopurity of the Micromegas, in the case its contribution comes completely from the Cu and Kapton, was obtained. The Kapton considered is a Kapton film from DuPont and also the measure with a HPGe gives only upper bounds. With these calculations an activity of $6.20 \times 10^{-4}\,\mu$Bq/cm^2 in ^{208}Tl and $3.83 \times 10^{-2}\,\mu$Bq/cm^2 in ^{214}Bi is obtained for one layer of Cu-Kapton. The total background applying these values to the background coming from the readout is calculated in the so-called "realistic scenario".

Looking at the total result in the "conservative scenario"in a region at the 2% FWHM around 2458 keV (100 keV), a background level of $(9.47 \pm 1.45) \times 10^{-4}\,\mathrm{c\,keV^{-1}\,kg^{-1}\,y^{-1}}$ is obtained in pure Xe while a reduction of around 3 is observed in a low diffusion Xe mixture, having a level of $(3.34 \pm 0.95) \times 10^{-4}\,\mathrm{c\,keV^{-1}\,kg^{-1}\,y^{-1}}$. The same difference between one gas and another is obtained in the different energy windows considered. In the case of the "realistic scenario"the total background is improved by a factor between 3 and 4, being of $(2.53 \pm 0.18) \times 10^{-4}\,\mathrm{c\,keV^{-1}\,kg^{-1}\,y^{-1}}$ in the case of pure Xenon and $(1.06 \pm 0.11) \times 10^{-4}\,\mathrm{c\,keV^{-1}\,kg^{-1}\,y^{-1}}$ in a low diffusion Xenon. In both scenarios it is reached the background level of the new generation of experiments, of $\sim 10^{-4}\,\mathrm{c\,keV^{-1}\,kg^{-1}\,y^{-1}}$, needed to be sensitive to neutrino masses below 100 meV. In the other scenarios the value is of the same order of magnitude.

In addition, if the total value is compared in each of the energy windows (100 keV, 48 keV, 24 keV), the total background in c keV^{-1} kg^{-1} y^{-1} is worse the wider the energy window is. Studying separately the contribution from each isotope makes sense because the ^{208}Tl decreases linearly with the energy window, therefore, the total value in c keV^{-1} is the same, and the ^{214}Bi changes slightly because it is dominated by the 2447 keV gamma. However, as the energy resolution improves, the background is reduced in c kg^{-1} y^{-1} due to the reduction in the ^{208}Tl.

The total spectra for each isotope have been obtained summing the contribution of all the simulated elements. For the 2% RoI and in the "conservative scenario"are shown in Figures 5.36 for pure Xe, as an example to see the effect of each selection. In the Figure is shown the background in a wide energy window, but depending on the energy resolution the RoI will be different: 2400-2500 keV (2% FWHM), 2433-2483 keV (1% FWHM) and 2246-2470 keV (0.5% FWHM). Each spectrum is the combination for each isotope of all the simulated contributions (vessel, readout, cathode, field cage and two end-caps) that survive each selection criteria. It can be observed that the contribution for each isotope decreased by three orders of magnitude after the application of all the discrimination criteria. In the case of ^{208}Tl the application of the track selection makes clearer the photoelectric peak at 2615 keV and the Compton edge at 2382 keV. It can be observed that the topological selection has a bigger effect in the RoI. In the case of the ^{214}Bi we are dominated by the beta spectrum from the superficial contamination of the readout as we are considering all the contribution together. It is not until the fiducial veto is applied that the gamma peaks are not observed. The peak from the 2447 keV is completely contained in the RoI with the different energy resolutions considered In all cases the binning of the spectrum corresponds to 5 keV, a reasonable binning that can be given by any acquisition system.

In order to study the effect of the energy resolution in the total spectra, Figure 5.37 shows the final spectra after the application of all the selection criteria with the different energy resolutions considered. It has been obtained adding all the simulated contribution from ^{208}Tl and ^{214}Bi. In all the cases in black for the high diffusion case (pure Xe) and in red for a low diffusion Xe mixture. In Figure 5.38 are the same spectra considering the realistic background scenario.

		Background ($\times 10^{-4}$ c keV^{-1} kg^{-1} y^{-1})					
		2%		1%		0.5%	
Origin		Pure Xe	Low diffusion Xe	Pure Xe	Low diffusion Xe	Pure Xe	Low diffusion Xe
Vessel	^{208}Tl	0.54 ± 0.05	0.20 ± 0.03	0.52 ± 0.07	0.16 ± 0.04	0.44 ± 0.09	0.18 ± 0.05
	^{214}Bi	0.94 ± 0.05	0.31 ± 0.03	1.74 ± 0.11	0.55 ± 0.06	3.22 ± 0.20	1.05 ± 0.11
Drift	^{208}Tl	0.17 ± 0.01	0.09 ± 0.01	0.19 ± 0.02	0.09 ± 0.02	0.19 ± 0.03	0.08 ± 0.02
	^{214}Bi	0.13 ± 0.01	0.055 ± 0.003	0.24 ± 0.02	0.10 ± 0.005	0.47 ± 0.03	0.20 ± 0.01
Readout	^{208}Tl	$< 3.38 \pm 0.47$	$< 1.34 \pm 0.29$	$< 4.67 \pm 0.90$	$< 0.75 \pm 0.25$	$< 4.16 \pm 1.20$	$< 1.17 \pm 0.44$
	^{214}Bi	$< 3.58 \pm 0.82$	$< 0.95 \pm 0.55$	$< 5.35 \pm 1.26$	$< 1.72 \pm 0.99$	$< 10.70 \pm 2.52$	$< 3.44 \pm 1.99$
Cathode	^{208}Tl	0.0040 ± 0.0004	0.006 ± 0.0009	0.0033 ± 0.0006	0.0019 ± 0.0004	0.0036 ± 0.0008	0.0026 ± 0.0007
	^{214}Bi	0.0046 ± 0.0008	0.002 ± 0.0005	0.0089 ± 0.0001	0.0025 ± 0.0009	0.017 ± 0.003	0.004 ± 0.002
1 End Cap	^{208}Tl	0.11 ± 0.01	0.082 ± 0.010	0.08 ± 0.01	0.06 ± 0.01	0.08 ± 0.02	0.05 ± 0.02
	^{214}Bi	0.25 ± 0.01	0.115 ± 0.007	0.49 ± 0.02	0.25 ± 0.01	0.95 ± 0.04	0.44 ± 0.03
Total	^{208}Tl	4.31 ± 0.55	1.80 ± 0.35	5.54 ± 1.01	1.12 ± 0.33	4.95 ± 1.36	1.53 ± 0.55
	^{214}Bi	5.15 ± 0.91	1.54 ± 0.59	8.33 ± 1.43	2.82 ± 1.08	16.3 ± 2.85	5.57 ± 2.16
TOTAL	Conservative	9.47 ± 1.45	3.34 ± 0.95	13.87 ± 2.44	3.94 ± 1.41	21.28 ± 4.20	7.10 ± 2.71
TOTAL	Realistic	2.53 ± 0.18	1.06 ± 0.11	3.88 ± 0.29	1.49 ± 0.18	6.49 ± 0.50	2.52 ± 0.30

TABLE 5.20: *Background level obtained in c keV^{-1} kg^{-1} y^{-1} using the activities in Table 5.19 is shown for each element simulated, separating the contribution from ^{208}Tl and ^{214}Bi, in the different cases regarding energy resolution and diffusion that have been considered. In the last row the total contribution is listed for each isotopes and finally the total background expected summing them in the two discussed scenarios (note that the contribution from the end-caps have to be summed twice because there are two).*

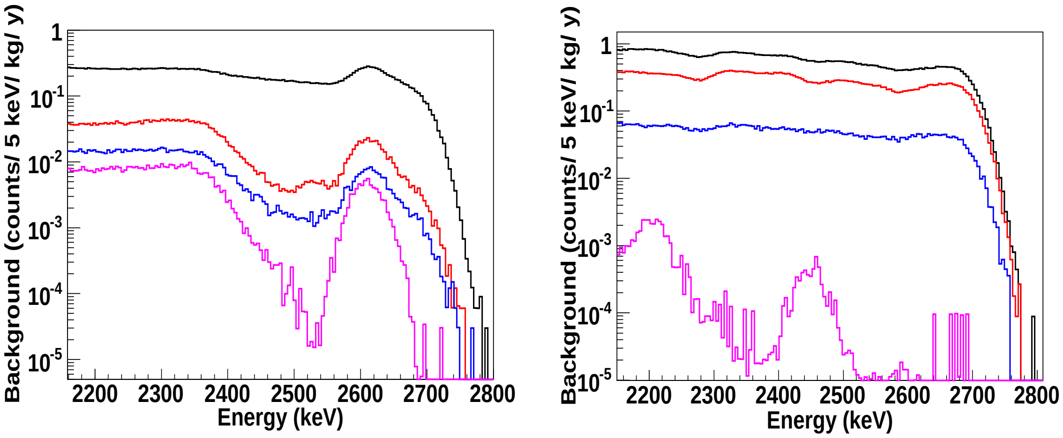

(a) (b)

FIGURE 5.36: *Background spectrum considering the "conservative scenario"after the application of the discrimination algorithms for* ^{208}*Tl and* ^{214}*Bi simulated in pure Xenon at 10 bar with a pixelization of* $10\times10\,\mathrm{mm}^2$*. (a) Contamination generated by* ^{208}*Tl in a wide energy window. (b) Contamination generated by* ^{214}*Bi in a wide energy window. In all cases: black-line indicates raw data, red-line events surviving the one-single track selection, blue-line after the topological selection, magenta-line after fiducial rejection and in green-line final contamination subtracting the main one coming from the readout. For all spectra the binning is 5 keV. Depending on the energy resolution the RoI wiil be different: 2400-2500 keV (2% FWHM), 2433-2483 keV (1% FWHM) and 2246-2470 keV (0.5% FWHM).*

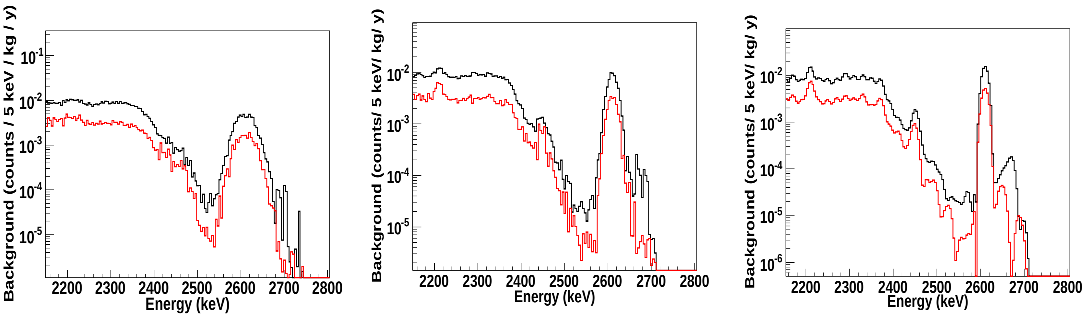

(a) (b) (c)

FIGURE 5.37: *Final background spectra in the "conservative scenario"combining all the contributions for* ^{208}*Tl and* ^{214}*Bi after the application of all the discrimination algorithms. (a) Applying an energy resolution of 2% FWHM at* $Q_{\beta\beta}$*. (b) With an energy resolution of 1% FWHM at* $Q_{\beta\beta}$*and (c) applying an energy resolution of 0.5% FWHM at* $Q_{\beta\beta}$*. In all the cases the black-line represents the final background in pure Xenon and the red-line in low diffusion Xe and with a bin size of 5 keV.*

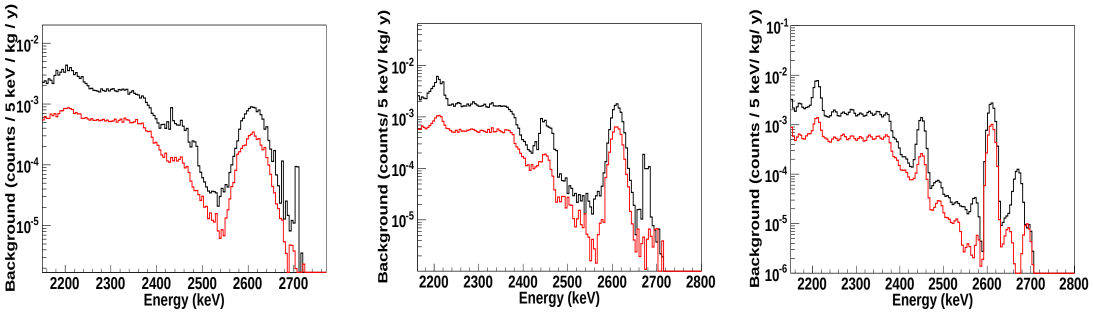

(a) (b) (c)

FIGURE 5.38: *Final background spectra in the "realistic scenario"combining all the contributions for ^{208}Tl and ^{214}Bi after the application of all the discrimination algorithms. In black the final background in pure Xenon and in red in low diffusion Xe. (a) Applying an energy resolution of 2% FWHM at $Q_{\beta\beta}$. (b) With an energy resolution of 1% FWHM at $Q_{\beta\beta}$ and (c) applying an energy resolution of 0.5% FWHM at $Q_{\beta\beta}$. In all the cases with a bin size of 5 keV.*

5.9 Sensitivity for the neutrino effective mass

With the background level and efficiency obtained after the application of the discrimination techniques, the physical potential of the results can be evaluated and an estimation of reachable limits to the effective neutrino mass can be derived. As it has been mentioned, the simulated elements represent approximately the 80% of the total mass of the experimental setup, therefore, a representative value can be obtained even if it is not a complete background model. The sensitivity for a possible $\beta\beta0\nu$ experiment is obtained using expression 1.29. The calculation is done using RooFit [192, 193] and RooStats [194–196] with a program developed in our group. The method is as follows: first of all 10^3 MonteCarlo of the background around $Q_{\beta\beta}$ are performed. The model consists in a peak simulating the signal, a peak simulating the ^{214}Bi contribution (with the input from previous results), a flat background from ^{208}Tl and the Compton edge from ^{208}Tl. The width of the peaks is the considered energy resolution. Secondly, the probability density function (pdf) for the model is defined as an extended pdf as the sum of the different functions. Then, the likelihood function is built with this pdf upon the counts using the signal and the backgrounds generated. The RooFit package that allows to define the Likelihood function also gives the expected signal, in this case, as the 95% C.L upper limit to the signal intensity. For the cases of very low background, it is obtained by the integration of the Bayesian posterior probability. A MonteCarlo is simulated for different exposures and in the different scenarios mentioned: with different input background and resolution. The different background levels have been obtained in previous section after the application of the discrimination algorithms considering a high diffusion or low diffusion Xe and they have been labelled as "conservative"or "realistic"scenarios. The total background and efficiency used as input for the MonteCarlo are summarized in Table 5.21, where the background level is given in c/y and the efficiency is in all the cases of a 40%. The Likelihood was performed in an energy window of 200 keV around $Q_{\beta\beta}$. From the limit to the signal obtained in c/y, the half-life time of the decay can be calculated using Equation 1.29. Then, from expression 1.22 a value for the effective neutrino mass can be calculated. In Table 5.22 are the values for the common parameters in expression 1.22 for any experiment with ^{136}Xe. The $G^{0\nu}$ and $M_{0\nu}$ values are obtained from a recent $\beta\beta$ decay review [43]. As $M_{0\nu}$ is not completely established by the theory, a range of values was considered that

Gas	Background scenario	Background (c/y)		Efficiency (% of events) (%)
		^{208}Tl	^{214}Bi	
Xe	Conservative	5.43	6.47	0.4
Xe	Realistic	1.23	2.04	0.4
LD Xe	Conservative	2.27	1.93	0.4
LD Xe	Realistic	0.61	0.76	0.4

TABLE 5.21: *Background and efficiency used as input for the MonteCarlo simulations launched to evaluate the physics potential in the background scenarios considered and supposing pure Xe and low diffusion Xe in a 124 kg HP TPC.*

Parameter	Value
f	1 (from simulations)
W	131.29 g
$G^{0\nu}$	4.0×10^{-14} y
$M_{0\nu}$	from 1.8 (ISM theory) to 4.1 (GCM theory)

TABLE 5.22: *Values for the common parameters for any experiment with ^{136}Xe used to obtain the sensitivity with Equation 1.22.*

cover all the possible values predicted by the nowadays theories. The other parameters depend on the experiment. To obtain the curves a mass of 124 kg (the mass defined in the sensitive volume in the simulation if working at 10 bar) and an exposure of 1240 kg× y was simulated. The results are shown in Figure 5.39 for the two scenarios in pure Xenon and considering the three energy resolutions. In Figure 5.40 are the same plots in a low diffusion Xe. In all the cases is marked the limit to be sensitive to an effective neutrino mass of 100 meV and 50 meV. In Table 5.23 are summarized the obtained neutrino mass for an exposure of 620 kg× y (equivalent to 5 y of measure) and 1240 kg× y (equivalent to 10 y of measurement).

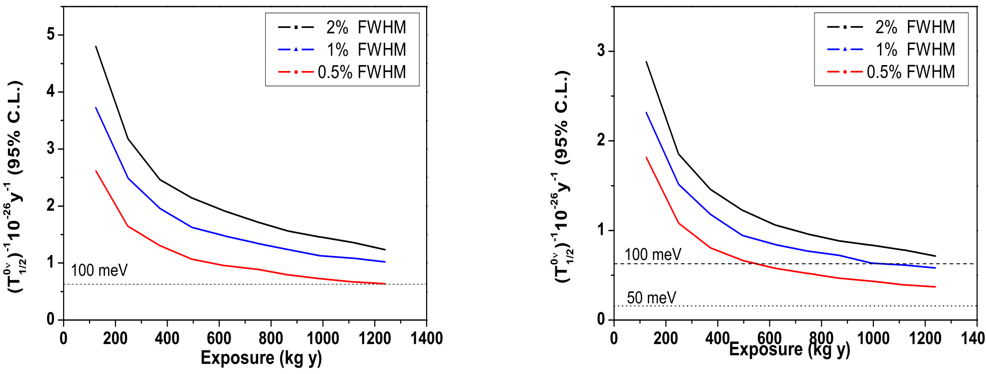

(a)

(b)

FIGURE 5.39: *Estimated half-life of the ^{136}Xe $\beta\beta0\nu$ in function of the exposure in a 124 kg HP TPC setup considering pure Xe for three different energy resolutions (2% FWHM: black-line, 1% FWHM: blue-line and 0.5% FWHM at $Q_{\beta\beta}$:red-line) (a) is evaluated in the "conservative"background scenario and (b) in the "realistic"one (see text for details of these scenarios).*

The Klapdor claim [74] can be evaluated if the experiment is sensitive to neutrino mass below 300 meV. To investigate the inverted hierarchy region of masses a sensitivity down to 50 meV is

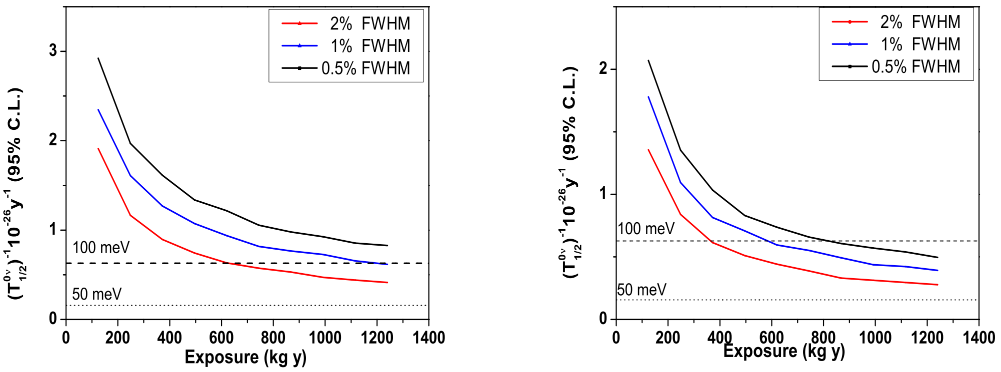

(a)

(b)

FIGURE 5.40: *Estimated half-life of the ^{136}Xe $\beta\beta0\nu$ in function of the exposure in a 124 kg HP TPC setup considering a low diffusion Xe mixture for three different energy resolutions (2% FWHM: black-line, 1% FWHM: blue-line and 0.5% FWHM at $Q_{\beta\beta}$:red-line) (a) is evaluated in the "conservative"background scenario and (b) in the "realistic"one (see text for details of these scenarios).*

Gas	Background scenario	E. Res (% FWHM)	$\langle m_\nu \rangle$ ($MT = 620\,\text{kg}\times\,\text{y}$) (meV)	$\langle m_\nu \rangle$ ($MT = 1240\,\text{kg}\times\,\text{y}$) (meV)
Xe	Conservative	2%	175 – 264	140 – 211
		1%	153 – 232	127 – 192
		0.5%	123 – 186	100 – 152
Xe	Realistic	2%	130 – 196	106 – 161
		1%	116 – 175	96 – 145
		0.5%	96 – 145	77 – 116
Low Diffusion Xe	Conservative	2%	139 – 210	115 – 173
		1%	122 – 184	99 – 150
		0.5%	100 – 151	81 – 122
Low diffusion Xe	Realistic	2%	108 – 164	89 – 134
		1%	97 – 147	79 – 119
		0.5%	84 – 127	66 – 100

TABLE 5.23: *Sensitivity for the neutrino mass after an exposure of 620 kg× y (equivalent to 5 y of measure) and 1240 kg× y (equivalent to 10 y of measure) in the different scenarios considered in a 100 kg HP TPC with ^{136}Xe.*

needed, as can be seen in Figure 1.5. To fully cover this region the mass range has to go from 50 to 20 meV. This is the region expected to be evaluated for the next generation of experiments (1 ton of mass) as discussed in chapter 1. To enter in the direct hierarchy region, with effective masses around 3 meV, much lower background levels and even an increase of target mass is required

From the Table 5.23 and Figure 5.39 can be concluded that, in pure Xenon, the Heidelberg-Moscow mentioned claim could be investigated in all the scenarios evaluated. In order to be sensitive to a $\langle m_\nu \rangle = 100$ meV ($T^{0\nu}_{1/2}{}^{-1}$ from 2.75×10^{-27}-6.28×10^{-27} y, depending on the nuclear matrix element used) an energy resolution of 0.5% FWHM at 2458 keV and 10 y of measurement are needed in the case of a "conservative"scenario of background, while in the "realistic"case

10 y would be needed if an energy resolution of 2% is considered but if it is improved down to 1% it could be explore in 6 y. It is interesting to evaluate the sensitivity up to an exposure of 1240 kg× y because it is when the sensitivity starts to have an asymptotic behaviour and the improvement along more time of data taking would not be enough to reach a better sensitivity. With this diffusion and mass seems difficult to reach the inverted hierarchy region of masses (a mass of 50 meV can be explore if ${T_{1/2}^{0\nu}}^{-1}$ is between 1.57×10^{-27}-$6.89 \times 10^{-28}\,\mathrm{y}^{-1}$).

In the case of low diffusion Xe, in the "conservative"scenario for the background a sensitivity for the effective neutrino mass of 100 meV can be reached after 10 y of measurement with an energy resolution of 1% while if it is improved to 0.5% it could be investigated in 5 y. In the " realistic "case the 100 meV can be reached with the three energy resolutions considered and would start to be close to the 50 meV limit for the inverted hierarchy region of mass if an energy resolution of 0.5% FWHM is obtained. Again the Klapdor claim can be confirmed or refuted in all the scenarios.

In conclusion, the Klapdor claim can be investigated in all the scenarios proposed and neutrino mass down to 100 meV can be reached in pure Xenon with a 1% FWHM in the "realistic"scenario. In the case of low diffusion gas it could be reached in a worse case of background. However, in order to enter in the inverted hierarchy region of masses it would be needed to go to higher masses of isotope or to improve the background, as occurs in the new generation of experiments that aims to have masses of 1 ton of isotope. In next chapter this possibility is evaluated.

Chapter 6

Perspectives for a 1 ton HPXeTPC

Contents

6.1 Signal **184**
6.2 Rejection Factor **185**
6.3 Expected sensitivity **186**

The next generation of experiments aims to reach enough sensitivity to explore the inverted region of masses ($\langle m \rangle_\nu$ between 20 and 50 meV). In order to improve the sensitivity for the neutrino masses the background level has to be smaller, the energy resolution better than a 1% FWHM and it is needed to have higher masses of isotope. From the previous discussions we have conclude that in the best scenario of energy resolution and background the sensitivity does not enter in the 50 meV region. As the radiopurity of the different elements seems difficult to improve and also, this would not be not enough to improve the sensitivity [15], the next step in most of the new generation of experiments is to scale to 1 ton of emitter isotope. In this chapter this option is evaluated for a HP Xe gaseous TPC applying the discrimination algorithms obtained in chapter 5.

The considered setup for the extension of the TPC keeps the proportion between volume and radius, $h = 2 \times r$. Therefore, in order to handle 1 ton of Xe at 10 bar, the radius has to be 1.43 m (double than before) and the height of the fiducial volume of 2.86 m. The study was done simulating the signal isotropically distributed in the active volume and background coming from two of the most dangerous elements as the field cage and readout (the closest elements to the fiducial volume) simulating ^{208}Tl and ^{214}Bi isotopes chains. The number of simulated events are summarized in Table 6.1. The treatment of the events is done as in the previous chapter. In the next sections results of the efficiency and the rejection power are obtained for both diffusions coefficients considered along this work: high diffusion as in pure Xe or a low diffusion Xe (LD Xe) mixture. Simulating these two contributions one can have a good idea of the expected improvements or drawbacks of this option.

Events ($\times 10^6$)	$\beta\beta0\nu$	Field Cage		Readout	
		^{208}Tl	^{214}Bi	^{208}Tl	^{214}Bi
Pure Xe	1.4	4.8	31.3	4.4	11.7
LD Xe	1.4	4.8	31.3	4.4	10.3

TABLE 6.1: *Number of simulated events to study the rejection factor in a 1 ton extension of the experiment. In this case only background from the field cage and from the readout have been simulated. The Xe signal is isotropically simulated in the sensitive volume. Two gases are studied pure Xe (high diffusion) and low diffusion XE mixture (LD Xe).*

6.1 Signal

One of the major advantages in a bigger volume is that signal events that lose some of their energy outside the chamber in smaller setups, will be recovered in this case, translating in an increase of the efficiency. Selecting events in an RoI of 100 keV around $Q_{\beta\beta}$, an efficiency of 80% is obtained, while in previous case, due to the geometrical factor, the efficiency was of 70% (see Table 5.11). However, the long drift distance will produce a drastic effect due to the diffusion in the case of pure Xenon when applying the discrimination algorithms, as can be observed in Figure 6.1 (a) where the distribution of the z position of the events is plotted after the application of each selection criteria. In a low diffusion Xe this effect is negligible as can be seen in Figure 6.1 (b). Therefore, to avoid bigger diffusion effects and to take advantage of the bigger confinement of the events, it seems very convenient to change the detection concept replacing the cathode by a central one with two detector planes at both sides of the TPC, changing from an asymmetric TPC to a symmetric TPC. Also beneficial will be to combine the Xe gas with some quencher, as TMA, to decrease the diffusion.

These two options have been evaluated applying the selection algorithms with a central cathode (symmetric TPC) and with an upper one as before (asymmetric TPC). The efficiency after the application of each one of the discrimination algorithms is summarized in Table 6.2 with respect to the previous one. It can be observed that, at the end, the total efficiency is around 40% for the asymmetric TPC, as previously, but it improves to a 50% in the symmetric approach, taking advantage of the bigger confinement of the events in the bigger volume. In the case of low diffusion Xe the cuts have not such a big dependence with the z position as is proven in 6.1 (b).

Studying the effect of each one of the different discrimination algorithms separately we can conclude that the efficiency decreases when applying the connection cut with respect to the previous case (Tables 5.7, 5.9 and 5.11) due to the extra confinement of events that increases the number of multi-track signal events. But this loss is recovered after the topological cut.

The symmetric TPC reduces the difficulty to give the high voltage in this large distance (2.86 m). Moreover, as discussed, it decreases the effect of the diffusion. The main drawback of this option is that the number of electronic channels to be read is duplicated, because now there are two readout planes, also a possible increase of the initial background level of the setup due to this duplication, although it does not seem a problem in this case considering the current level of radiopurity of the Micromegas detectors. If we want to determine also t_0 an option could be the deposition of CsI in the cathode to detect the scintillation light produced on it. To evaluate the rejection power of this TPC and in based on the results obtained for the efficiency, we will consider a central cathode.

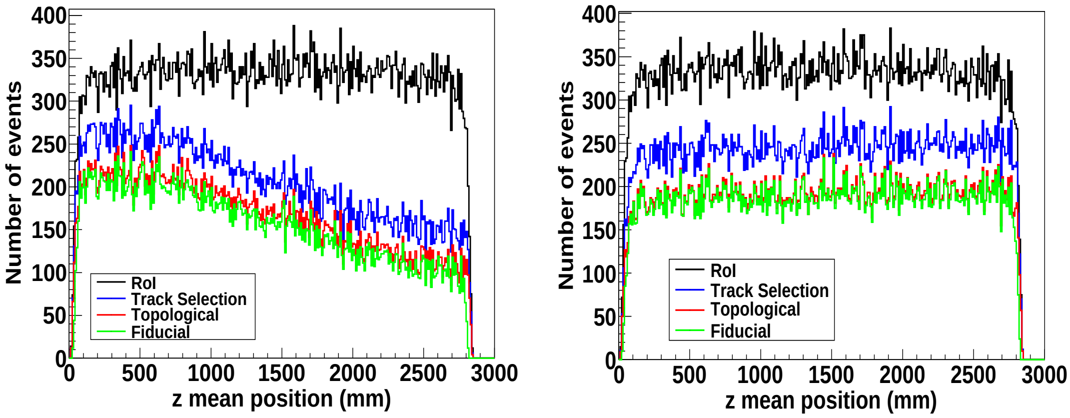

(a)

(b)

FIGURE 6.1: *z position of the events (calculated as the mean position) after the application of each of the selection criteria. (a) In pure Xe in an asymmetric TPC. The effect of the diffusion is much higher than in the 100 kg TPC because the drift distance has doubled (see Figure 5.34). (b) Same plot in a low diffusion Xe mixture, as the diffusion is much smaller , the number of finals events is independent of the distance.*

	Track	Topology	Fiducial Rejection			**Total**
$\beta\beta0\nu$			Lateral	Bottom	Top	
Pure Xe						
Asymmetric TPC	62.6 ± 0.3	81.3 ± 0.5	93.5 ± 0.6	99.5 ± 0.7	99.3 ± 0.7	38.1 ± 0.2
Symmetric TPC	75.6 ± 0.6	89.2 ± 0.7	93.0 ± 0.8	94.6 ± 0.8	99.1 ± 0.9	47.7 ± 0.3
LD Xe						
Asymmetric TPC	73.6 ± 0.4	78.6 ± 0.5	97.8 ± 0.6	99.7 ± 0.6	99.4 ± 0.6	45.4 ± 0.2
Symmetric TPC	73.4 ± 0.5	78.6 ± 0.7	97.9 ± 0.9	99.3 ± 0.9	99.9 ± 0.9	45.6 ± 0.3

TABLE 6.2: *Efficiency of the simulated $\beta\beta0\nu$ events in a 1 ton TPC after the successive application of the selection criteria. The events are simulated for in Xenon at 10 bar.*

6.2 Rejection Factor

The surviving number of background events after the application of the successive criteria is obtained. It has been considered a symmetric TPC with a central cathode. The number of background events (^{208}Tl and ^{214}Bi simulated from the field cage and readout) in the RoI also increases, around a factor 2.5, with respect to the 100 kg TPC. Therefore, the initial background is higher than in the 100 kg chamber. If the effect of each selection is studied separately (see Table 6.3), the track selection improves with respect to the value obtained in the smaller chamber for both diffusions considered by approximately a factor 1.5 (1.9) for the drift (readout) for the ^{208}Tl and by a 1.5 for ^{214}Bi from both elements. This is because more multi-track events are contained in the volume. The topological selection has the same effect, as expected, because it is independent of the geometry once the main track is selected, and, again it is around 3 times higher in the case of a low diffusion Xe mixture.

At the end, the total percentage of surviving events, summarized in Table 6.4, is higher than in the 100 kg chamber, a factor 1.6 for the ^{208}Tl population and around 2.5 for ^{214}Bi from the drift, and in the case of the readout a factor 1.5 for the ^{208}Tl population but around a factor 4 for ^{214}Bi. However, when normalizing the background in c keV^{-1} kg^{-1} y^{-1}, it has improved with respect to the one in the 100 kg TPC as can be observed in Table 6.5. To obtain the background level the activities in Table 5.19 have been used, so the level from the readout is an upper bound. We consider the conservative scenario to compute the values for Table 6.5. Comparing to the 100 kg case, background levels in units of c keV^{-1} kg^{-1} y^{-1} should be reduced by a factor 10. However, it has also to be taken into account that the mass of the field cage and surface of the detectors are larger and the rejection factors are lower. Hence, at the end, the improvement is of 2.7 (3.1) for ^{208}Tl in pure Xe (low diffusion Xe) and of 2.0 (2.4) for ^{214}Bi in pure Xe (low diffusion Xe).

Origin		Track	Topology	Fiducial Rejection		
				Lateral	Bottom	Top
Pure Xe						
Drift	^{208}Tl	3.4 ± 0.2	35.8 ± 4.8	57.1 ± 10.8	93.2 ± 20.2	99.9 ± 22.1
	^{214}Bi	26.4 ± 0.8	35.6 ± 1.8	23.4 ± 2.3	99.9 ± 12.5	99.9 ± 12.5
Readout	^{208}Tl	1.7 ± 0.1	31.1 ± 3.2	80.2 ± 10.7	19.8 ± 4.8	95.0 ± 30.4
	^{214}Bi	35.9 ± 0.5	31.3 ± 0.7	93.6 ± 2.6	0.6 ± 0.2	99.9 ± 35.4
Low Diffusion Xe						
Drift	^{208}Tl	3.2 ± 0.2	14.6 ± 2.8	63.3 ± 18.6	99.9 ± 32.2	99.9 ± 32.2
	^{214}Bi	26.4 ± 0.8	11.0 ± 0.9	26.0 ± 4.4	99.9 ± 21.0	99.9 ± 21.0
Readout	^{208}Tl	1.3 ± 0.1	21.0 ± 2.9	95.4 ± 16.9	19.4 ± 6.1	99.9 ± 40.8
	^{214}Bi	25.8 ± 0.4	34.1 ± 0.9	94.7 ± 3.2	0.6 ± 0.2	99.9 ± 44.7

TABLE 6.3: *Aceptance factor of the surviving events of the background simulated in a 1 Ton symmetric TPC at 10 bar after the successive application of the selection criteria in an RoI of 100 keV around $Q_{\beta\beta}$. The percentage of events shown is with respect the previous one and two diffusion coefficients were considered.*

Origin		1 ton TPC (10^{-6})		100 kg TPC (10^{-6})	
		Pure Xe	LD Xe	Pure Xe	LD Xe
Drift	^{208}Tl	26.1 ± 0.4	12.1 ± 2.7	13.4 ± 0.10	7.2 ± 0.9
	^{214}Bi	10.8 ± 0.1	3.7 ± 0.5	4.1 ± 0.3	1.7 ± 0.08
Readout	^{208}Tl	4.4 ± 0.1	2.8 ± 0.8	5.4 ± 0.7	2.1 ± 0.5
	^{214}Bi	1.35 ± 0.03	0.97 ± 0.03	0.9 ± 0.2	0.2 ± 0.1

TABLE 6.4: *Aceptance factor of the surviving events of the simulated background after the successive application of the selection criteria in the TPC at 10 bar with 1 ton of gas. Values are compared with the ones obtained in a 100 kg TPC.*

6.3 Expected sensitivity

The physics potential of the symmetric 1 ton TPC option was evaluated as in Section 5.9 launching a Montecarlo that simulates the background and with a Likelihood to obtain the minimum sensitivity to signal in c/y at 95% C.L. From the results shown in Table 6.5 an improvement in

Origin		1 ton TPC (10^{-4})		100 kg TPC (10^{-4})	
		Pure Xe	LD Xe	Pure Xe	LD Xe
Drift	^{208}Tl	0.06 ± 0.01	0.018 ± 0.002	0.17 ± 0.01	0.09 ± 0.01
	^{214}Bi	0.066 ± 0.006	0.03 ± 0.003	0.13 ± 0.08	0.06 ± 0.03
Readout	^{208}Tl	$< 1.22 \pm 0.24$	$< 0.20 \pm 0.07$	$< 3.38 \pm 0.47$	$< 1.34 \pm 0.29$
	^{214}Bi	$< 1.40 \pm 0.33$	$< 0.45 \pm 0.26$	$< 3.58 \pm 0.82$	$< 0.95 \pm 0.08$

TABLE 6.5: *Background in c keV^{-1} kg^{-1} y^{-1} of the simulated elements in a 1 ton symmetric TPC operating at 10 bar and under two different diffusions. Results are compared with the ones obtained in a 100 kg TPC (from Table 5.20). In these values a RoI of 2% FWHM around $Q_{\beta\beta}$ has been considered.*

Gas	Background scenario	Background (c/y) ^{208}Tl	^{214}Bi	Efficiency (% of events) (%)
Xe	Conservative	17.1	14.35	0.5
Xe	Realistic	5.29	3.11	0.5
LD Xe	Conservative	5.08	5.97	0.5
LD Xe	Realistic	1.99	1.53	0.5

TABLE 6.6: *Background and efficiency used as input for the MonteCarlo simulations launched to evaluate the physics potential of the 1 Ton HPTPC option. It is evaluated within the two background scenarios considered and supposing pure Xe and low diffusion Xe.*

the background in c keV^{-1} kg^{-1} y^{-1} of, on average, 3 with respect to the 100 kg scenario is expected. As before, two different scenarios of background were considered, the "conservative" and the "realistic" in which the contamination coming from the Micromegas is lower. The input background level and efficiency for the ^{214}Bi peak and ^{208}Tl background are listed in Table 6.6. To obtain the half-life of the decay Equation 1.29 and parameters listed in Table 5.22 were used. In Figures 6.2 and 6.3 are represented the half-life of the decay with respect to the exposure for the two background scenarios and in the two gases simulated (high and low diffusion Xe respectively). It was evaluated at three different energy resolutions: 2% FWHM, 1% FWHM and 0.5% FWHM at $Q_{\beta\beta}$. Also in Figures 6.2 and 6.3 are marked the limits of the inverted hierarchy region of masses (50-20 meV) considering the highest value predicted for the nuclear matrix elements.

From results in Figures 6.2 and 6.3 an upper limit for the effective neutrino mass can be obtained with the relation 1.22. Taking into account the uncertainties on the nuclear matrix elements, a range for the neutrino mass is obtained. It was calculated after an exposure of $MT = 5000\,\mathrm{kg} \times \mathrm{y}$ and $MT = 10000\,\mathrm{kg} \times \mathrm{y}$ and results are shown in Table 6.7. With these results it can be conclude that in the 1 ton option the upper bound of the inverted hierarchy region of masses can be reached in the two background scenarios considered and for the two diffusion coefficients applied. Specifically, for pure Xe (see Figure 6.2) in the best case of energy resolution, 0.5% FWHM at $Q_{\beta\beta}$, the inverted hierarchy region is reached after 4 y of measurement if considering the conservative background scenario and in 2 y in the realistic one. In the conservative scenario at 1% and 2% it is also reached after 10 y of measurement while in the realistic scenario they would completely enter in the inverted hierarchy region of masses after 4 and 6 y, respectively. The lower value that can be investigated corresponds to a neutrino mass of 30 meV. The 100 meV

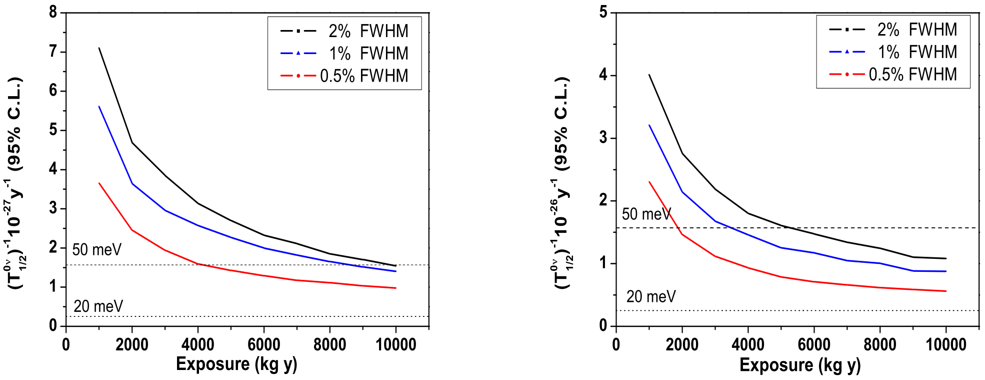

(a) (b)

FIGURE 6.2: *Estimated half-life of the* ^{136}*Xe* $\beta\beta0\nu$ *in function of the exposure in a 1 ton HP TPC setup considering pure Xenon for three different energy resolutions (2% FWHM: black-line, 1% FWHM: blue-line and 0.5% FWHM at* $Q_{\beta\beta}$*: red-line). In (a) it is calculated for the "conservative" background scenario and in (b) for the "realistic" one (see Section 5.9 for details of these scenarios).*

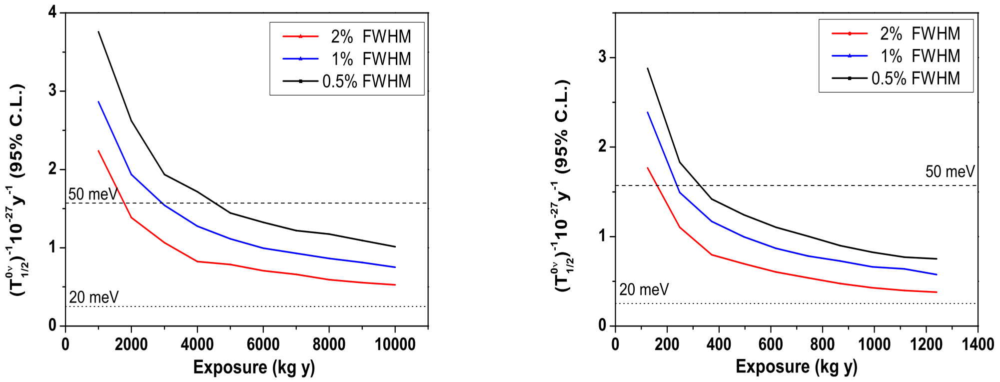

(a) (b)

FIGURE 6.3: *Estimated half-life of the* ^{136}*Xe* $\beta\beta0\nu$ *in function of the exposure in a 1 ton HP TPC setup considering a low diffusion Xe mixture for three different energy resolutions (2% FWHM: black-line, 1% FWHM: blue-line and 0.5% FWHM at* $Q_{\beta\beta}$*: red-line). (a) It is evaluated in the "conservative" background scenario and (b) in the "realistic" one (see text for details of these scenarios).*

region (${T^{0\nu}_{1/2}}^{-1}$ from 2.75×10^{-27}-6.28×10^{-27} y^{-1}) is fully covered after 1-2 y (2-5 y) of measure in the realistic (conservative) scenario.

In the case of a low diffusion Xenon mixture in the conservative scenario is already reached the upper limit of the inverted hierarchy region of masses (50 meV) after 4 y of exposure for the three energy resolutions considered. In the case of the best energy resolution the lower sensitivity that can be reached is 29 meV. In the realistic background scenario, almost all the inverted hierarchy region of masses can be explored with an energy resolution of 0.5% FWHM and at least up to 30 meV with a 1% FWHM energy resolution. With this gas the 100 meV region is fully covered after 1 y (1-2 y) of measure in the realistic (conservative) scenario.

Gas	Background scenario	E. Res (% FWHM)	$\langle m_\nu \rangle$ ($MT = 5000\,\mathrm{kg}\times\,\mathrm{y}$) (meV)	$\langle m_\nu \rangle$ ($MT = 10000\,\mathrm{kg}\times\,\mathrm{y}$) (meV)
Xe	Conservative	2%	$66 - 100$	$50 - 75$
		1%	$60 - 91$	$47 - 71$
		0.5%	$48 - 72$	$40 - 60$
Xe	Realistic	2%	$51 - 76$	$42 - 63$
		1%	$45 - 67$	$37 - 56$
		0.5%	$35 - 53$	$30 - 45$
Low Diffusion Xe	Conservative	2%	$48 - 72$	$40 - 61$
		1%	$42 - 64$	$35 - 52$
		0.5%	$35 - 53$	$29 - 44$
Low Diffusion Xe	Realistic	2%	$42 - 63$	$35 - 52$
		1%	$37 - 56$	$30 - 46$
		0.5%	$31 - 47$	$26 - 37$

TABLE 6.7: *Sensitivity for the neutrino effective mass after an exposure of 5000 kg× y (equivalent to 5 y of measure) and 10000 kg× y (equivalent to 10 y of measure) in the different scenarios considered in a 1 ton HP TPC with* ^{136}*Xe.*

In conclusion, the extension to a 1 ton of beta isotope emitter, as it has been evaluated in other experiments, allows to reach sensitivities to effective neutrino mass below 50 meV, covering part or all the inverted hierarchy region of masses in 5-10 y. However, this option implies a higher experimental challenge due to the possible technological difficulties and increases the cost of the experiment.

Chapter 7

Conclusions

The objective of this study has been to analyse the pattern recognition potential for background discrimination in a high pressure TPC equipped with Micromegas detectors looking for the ^{136}Xe $\beta\beta0\nu$ decay. In addition the commissioning of a medium size prototype equipped with Micromegas allow to do first recognition of tracks in long drift distances (38 cm) and to study the performance of this detectors on it.

$\beta\beta0\nu$ decay can give information on two fundamental questions about the neutrino nature, its mass scale and if they are Dirac or Majorana particles. As discussed in the first chapter, this process can only occur if neutrino and antineutrino are the same particle, i.e. if they are Majorana particles. In addition, a measurement of a $\beta\beta0\nu$ will give a value for the neutrino electronic effective mass, or at least an upper limit in the absence of a positive signal. Different $\beta\beta0\nu$ experiments, already finished, have constrained the neutrino mass down to 0.3-1.4 eV. The current generation of experiments, with a target mass of the order of 100 kg, aims at reach sensitivities to neutrino effective mass of the range of 50-100 meV, starting to explore the inverted hierarchy region. To fully explore this region, going down to sensitivities of few tens of meV, a target mass of 1 ton is needed. Apart from having a big amount of beta emitter, a very good energy resolution ($\sim$1% at $Q_{\beta\beta}$) and an ultra-low background ($\sim 10^{-4}$c keV^{-1} kg^{-1} y^{-1} for a $\langle m_\nu \rangle \sim 50$ meV) are also required. Among the proposals summarized in the first part of the work, those based in a gaseous TPC have the advantage to be able to reconstruct the track of the particle using pixelized detectors, as in the NEXT experiment. The NEXT experiment (Neutrino Experiment in Xenon with a TPC) [68] has the goal to measure the $\beta\beta0\nu$ decay of ^{136}Xe using a high pressure gaseous TPC with around 100 kg of Xe at 10 bar. The detection principle is based on the electroluminescent signal in Xenon that allows to obtain an energy resolution of the order of 1% FWHM at $Q_{\beta\beta}$ [159]. As part of the R&D program of the collaboration, the use of Micromegas detectors in charge mode is also being studied.

The Gothard's TPC [89] was a pioneer experiment using a Xe gas TPC equipped with multi-wires detectors that showed the background rejection potential of this approach based on topology discrimination [118]. However, the limitation on energy and spatial resolution was a drawback for this proposal not overcome until the origin of the Micropattern Gas Detectors (MPGD) in 1988 by A. Oed [119]. Since then, different technologies appeared, being one of the most promising the Micromegas detectors. They have proven the required $\beta\beta0\nu$ features in Xenon, as energy resolution and radiopurity, in different works [108, 109, 156]. Under the NEXT Experiment and the TREX project (TPC for Rare Event searches with Xenon) [117] a TPC prototype, NEXT-MM, has been constructed and commissioned. NEXT-MM is a medium size Micromegas TPC (30 cm diameter and 38 cm length) able to hold $\sim$1 kg of Xe at 10 bar, allowing to fully contain electron tracks. The description of the setup as well as first tracks and energy resolution results, at 1 bar of Xe-TMA, have been shown in chapter 3 and 4. This gas mixture, Xe-TMA, shows very promising results for the $\beta\beta0\nu$ search [109].

After constructing and commissioning NEXT-MM, the capability to carry out calorimetry and tracking using Micromegas detectors has been demonstrated. Different run conditions have been performed. First tracks in Xe-TMA have been obtained. Events depositing its charge up to 3 detectors have been presented, for which particle pattern recognition capabilities have been tested using a readout of a high-granular device (864 independent channels are read). In addition, first analysis routines have been discussed that allow the reconstruction of events and to perform event selection based on the observables of a pixelized event: positions, number of pixels and energy. With this first analysis the best energy resolution obtained was $11.60 \pm 0.42\%$ FWHM and 9.46 ± 0.90 at 29 keV for MM1 and MM4 respectively. These values are stable along time, with a maximum fluctuation of 2%. The obtained energy resolution extrapolates to 1.5% at $Q_{\beta\beta}$ of ^{136}Xe (2458 keV). Future work will consist in improving the analysis by equalizing the pixels gain or classifying the events by number of tracks (in a similar way as in the simulation analysis). The next step would be to obtain data at higher pressures and in pure Xe.

In the third part of the work, a complete simulation of a HP Xe gas TPC with a Micromegas readout has been carried out to study the efficiency and rejection factor in a possible future experiment equipped with these detectors. The simulations have been divided into three main blocks: the generation of the particles and interactions in the fiducial volume, the simulation of the physical processes in a TPC (charge creation, diffusion and pixelization), and event reconstruction and analysis. The events are generated by MonteCarlo simulation using DECAY0 and Geant4. The treatment of the events and analysis is done using with a C++ software structure, called RESTSoft that uses the ROOT package. Two different classes of events have been simulated: $\beta\beta0\nu$ signal events and background events. A first study on the possible internal backgrounds, that can be a problem in the region of interest of the ^{136}Xe $\beta\beta0\nu$ experiment, limit them to the study of ^{208}Tl and ^{214}Bi isotopes coming from the natural radioactive chains. In order to evaluate, not only the isotopes, but also the effect of the origin of the contamination on the background, these contributions have been simulated from different elements in the geometry: volume and surface contamination close to the active volume and further volume contamination coming from the vessel TPC. In addition, two diffusion coefficients have been considered simulating a high diffusion gas, as pure Xe, and a low diffusion Xe mixture as Xe-TMA. The diffusion affects the topological reconstruction of the tracks, as it has been shown.

Different discrimination algorithms, based on the graph theory, have been generated taking into account the topological characteristics observed in signal events with respect to those in background events. These characteristics, that make the signal unique, are: a long twisted track with around all the charge, two high energy deposits at both ends of the track due to the Bragg reabsorption of the emitted electrons, and an isotropically distribution in the fiducial volume, far from the walls. The algorithms work in three steps: first of all single track events are selected. Events with up to one secondary track with less than 100 keV are also considered, improving the efficiency a 20%. Then, events with two blobs at both ends are selected and the track between the blobs is found. Finally, a coverage around the track is defined to select events with more than 90% of the charge inside this coverage. After these selections a fiducial veto is also applied.

The parameters in the algorithms are based on physical assumptions and also they have been tuned to keep a high efficiency to the signal while keeping the background level as low as possible, which improves the sensitivity to a certain effective neutrino mass in the experiment. Quantitatively these criteria try to reduce the background to the order of 10^{-4}c keV^{-1} kg^{-1} y^{-1}. The detector efficiency is around 70%, while the total efficiency after the application of all the selection is 40% (a 22% of efficiency was estimated in the case of Gothard). This value is the same under the two diffusions.

The effect of the discrimination algorithms on the background events has also been evaluated obtaining a rejection factor of 6 orders of magnitude in the RoI. These values improve by, at least, a factor 3 in a low diffusion Xe gas. If the effect of each criteria over events in the RoI is evaluated, the one-track selection has a higher effect over ^{208}Tl events because there are more multi-track events, while the main contribution from ^{214}Bi is the photoelectric absorption of the 2447.8 keV gamma that produces a single track. The topological selection has the same effect over all the population; slight differences are due to the origin of the contamination. It is in this selection where a big difference exists between both gases because the low diffusion makes easier to determine the track of the event or to avoid secondary emissions that can produce an extra blob. The total effect of this selection is a reduction of 60% in pure Xe and near to a 90% in a low diffusion Xe mixture. Gothard obtained a net reduction with the topological selection done by eye of 91.4%. The analysis developed here has the advantage to be a blind analysis. It should also be reminded that Gothard works at low pressure (5 bar) and in a smaller TPC. Finally, the fiducial selection has an effect only on surface contamination close to the active volume, being more effective in the case of ^{214}Bi because of the beta spectrum. In addition, an improvement in the energy resolution reduce the background from ^{208}Tl linearly keeping a similar background from ^{214}Bi events until and energy resolution of 0.5% FWHM is imposed. The efficiency remains constant.

A detailed study of the accepted background events shows that most of them are single track events, but in around 30% of the cases a secondary emission with an energy higher than 100 keV (Bremstralung or Compton) has probably produced a fake blob and the event is misidentified with a $\beta\beta0\nu$ signal event. In addition, 20% of the rejected signal has a secondary emission with an energy higher than 100 keV and therefore are discriminated. Another 20% is excluded because the track is not well identified. Moreover, the events at higher z position suffer a bigger diffusion and it is more difficult to identify the track.

In the different cases studied, with three different energy resolutions and considering two different diffusion coefficients, the expected background in a high pressure Xe TPC has been evaluated from each element simulated after applying the discrimination algorithms. The main contribution to the background level comes from the readout because it is one of the closest elements to the sensitive volume and with a higher surface, and the vessel because of its high mass. However, the measured activity for the Micromegas is an upper bound and improvements are expected with a more sensitive measurement. Therefore, two different background scenarios have been considered: "conservative"and "realistic". In a RoI of 100 keV around $Q_{\beta\beta}$ the total background adding each contribution is of $(9,47 \pm 1,45) \times 10^{-4}\,\mathrm{c\,keV^{-1}\,kg^{-1}\,y^{-1}}$ in pure Xe while in a Xe mixture with a lower diffusion, this value goes down to the $(3,34 \pm 0,95) \times 10^{-4}\,\mathrm{c\,keV^{-1}\,kg^{-1}\,y^{-1}}$, because the topological recognition is easier at low diffusion. In the "realistic"scenario, the total background improves between a factor 3-4, obtaining $(2,53 \pm 0,18) \times 10^{-4}\,\mathrm{c\,keV^{-1}\,kg^{-1}\,y^{-1}}$ in pure Xe and $(1,06 \pm 0,11) \times 10^{-4}\,\mathrm{c\,keV^{-1}\,kg^{-1}\,y^{-1}}$ in a low diffusion Xe. However, as the energy resolution improves, the total background in the RoI increases mainly because the ^{214}Bi contribution remains constant until an energy better than 0.5% is reached.

From these results of the background level, the sensitivity for the effective neutrino mass of the experiment can be evaluated. In all the scenarios the Klapdor's claim [74] could be investigated. In the case of the conservative scenario, the lowest level obtained supposing the best energy resolution (0.5% FWHM) and after an exposure of 1240 kg×y, is of 100 meV. This value could be also explored in the case of a 1% FWHM in a low diffusion Xe (value that can be reached as demonstrated from results obtained experimentally). If the resolution improves to 0.5% FWHM, then, for a low diffusion Xe mixture the obtained value was of 81 meV. In the case of the "realistic"background escenario, the best value obtained would be of 77 meV in pure Xe and 66 meV for a low diffusion mixture. In all the cases the 100 meV is reached. However, with these inputs the inverted hierarchy region of masses, with an upper limit of 50 meV, would not be reached.

Finally, the option to scale to a 1 ton of isotope is also evaluated. In this case, if working in a high diffusion gas as Xe, the best option seems to define a symmetric TPC with a central cathode and two detector planes at both sides of the chamber. With these dimensions the total background level decreases in around a factor 3. With this background level the upper limit of the inverted hierarchy region of masses could be reached in all the considered scenarios of background, resolution and diffusion. In the best case of a resolution of 0.5% in the realistic scenario operating with a low diffusion Xe mixture the lowest value that could be investigated is 26 meV, covering almost all the inverted hierarchy region of masess. However, this option implies a major experimental challenge as well as it increases the costs of the experiment.

In conclusion, the work presented here shows promising results for a possible neutrinoless double beta decay experiment with a HP gaseous Xe TPC equipped with Micromegas. First tracks in a Xe-TMA mixture at 1 bar have been obtained in a medium size prototype with a drift distance of 38 cm and that can fully contain electron tracks showing the pattern recognition capabilities of this detector. Moreover, the acquisition with Micromegas (a high granularity device) is possible and an analysis framework that pixelize the events have been developed. However, this analysis is in its first steps and must be improved. In addition, a complete simulation has been carried out to better understand the backgrounds in a TPC with 100 kg of Xe. The effect of the diffusion and the secondary emissions in pattern recognition have been evaluated allowing to improve the discrimination algorithms proposed in [138]. An efficiency of 40% after the application of all the algorithms is obtained while the rejection factor is of 6 orders of magnitude. With this potential and using activities of measured materials as input [165], a background of the order of 10^{-4}c keV^{-1} kg^{-1} y^{-1} seems to be possible.

Resumen de la memoria y conclusiones

El objetivo del trabajo aquí presentado es estudiar la capacidad de reducir el fondo radioactivo en un experimento de búsqueda de la desintegración doble beta en ^{136}Xe en un cámara de proyección temporal (TPC) operando con gas a alta presión, basándose en el reconocimiento topológico de los sucesos registrados con detectores Micromegas. Además se ha construido y puesto en marcha una TPC prototipo, con capacidad de trabaja con un 1 kg de Xe a 10 bar. En ella se ha demostrado la operatibilidad de la tecnología Micromegas para el reconocimiento de sucesos en una mezcla Xe-TMA operando a 1 bar.

Los experimentos de oscilaciones indican que los neutrinos tienen masa, y que, en particular, el más ligero tiene una masa alrededor de 50 meV. Sin embargo, de estas mediciones sólo se pueden extraer resultados de diferencias cuadráticas de las masas. Además de la incertidumbre en su masa, todavía no se conoce la naturaleza del neutrino si es Dirac o Majorana, las simetrías subyacentes o la exacta representación de la mezcla leptónica. La desintegración doble beta sin neutrinos, $\beta\beta0\nu$, puede darnos información de ambas cuestiones ya que sólo es posible si el neutrino es igual que su antipartícula (Majorana).

$\beta\beta0\nu$ es un proceso nuclear de segundo orden de los denominados raros, que ocurre entre dos núcleos pares entre los cuales sea energéticamente prohibida la desintegración beta. Este proceso implica un cambio en la carga Z de dos unidades. Puede ocurrir en dos formas con la emisión de neutrinos ($\beta\beta2\nu$) o sin ella ($\beta\beta0\nu$)

$$(A, Z) \rightarrow (A, Z + 2) \, + \, 2e^- \, + \, 2\nu_e,$$

$$(A, Z) \rightarrow (A, Z + 2) \, + \, 2e^-.$$

El proceso con la emisión de neutrinos es un proceso permitido por el Modelo Estándard de partículas y que ha sido observado en diversos isótopos, recientemente también en el isótopo de Xenón ^{136}Xe [45, 104]. Sin embargo, el modo $\beta\beta0\nu$ implica física más allá del Modelo Estándard puesto que viola la conservación del número leptónico y es posible sólo si $\nu = \bar{\nu}$.

Experimentalmente, ambos procesos son distinguibles porque en el modo $\beta\beta0\nu$ toda la energía de transición (definida como $Q_{\beta\beta}$) se comparte entre los dos electrones, produciendo que todos los sucesos tengan la misma energía, y se espera un pico cuya anchura dependerá de la resolución energética del detector. En el caso de emisión con neutrinos el espectro final es un continuo de energía entre 0 y $Q_{\beta\beta}$ con un máximo en, aproximadamente, $Q_{\beta\beta}/3$. Ambas distribuciones de energía se pueden ver en la Figura 1. Si la resolución del detector no es lo suficientemente buena la cola de la distribución del modo con neutrinos puede entrar en la región de interés (RoI) del modo sin neutrinos.

El modo $\beta\beta2\nu$ tiene vidas medias entre $10^{18} - 10^{21}$ años dependiendo del istopo, mientras que en el decaimiento $\beta\beta0\nu$ se espera que sean más largas, del orden de 10^{25} años. La vida media del proceso $\beta\beta0\nu$ viene dada por la expresión

$$|T^{0\nu}_{1/2}(0^+ \to 0^+)|^{-1} = G_{0\nu}(Q_{\beta\beta}, Z) \left| M^{0\nu}_{GT} - \frac{g_v^2}{g_A^2} M^{0\nu}_F \right|^2 \frac{\langle m_\nu \rangle^2}{m_e^2},$$

donde $G^{0\nu}$ es la integral de fase que puede calcularse con precisión y $M^{0\nu}_{GT}$ and $M^{0\nu}_F$ representan la parte nuclear de la amplitud, normalmente escrita como $M^{0\nu} = M^{0\nu}_{GT} - \frac{g_v^2}{g_A^2} M^{0\nu}_F$. $\langle m_\nu \rangle$ es la masa efectiva del neutrino

$$| \langle m_\nu \rangle |^2 = \left| \sum_{i=1}^{3} U_{ie}^2 e^{\alpha_i} m_i \right|,$$

donde $\alpha_i/2$ son las fases de Majorana y U_{ie} los elementos de la matriz de mezcla. Si la desintegración doble beta es observada, además de establecer la naturaleza de neutrino, se podrán utilizar los datos de los experimentos de oscilaciones para establecer un rango de los valores absolutos de las masas de las tres familias de neutrinos (jerarquía normal, inversa o degenerada). En el caso de no observación se puede interpretar en términos de límites de la masa efectiva.

Diferentes experimentos pasados pusieron un límite en la masa efectiva del neutrino entre $0.3 - 1.4$ eV. La generación actual de experimentos, con una masa de isótopo emisor de unos 100 kg, pretende llegar a sensibilidades del orden de 50-100 meV, comenzándose a explorar la región invertida de masa. Para explorar completamente esta región, yendo a sensibilidades de unos pocos meV, es necesaria 1 tonlada de masa de isótopo emisor. Aparte de tener una gran masa de isótopo, para explorar estas regiones de masa se requiere una muy buena resolución en energía ($\sim$1% FWHM at $Q_{\beta\beta}$) y niveles muy bajos de fondo en la regin de energa donde se espera observar la seal($\sim 10^{-4}$c keV^{-1} kg^{-1} y^{-1} para una $\langle m_\nu \rangle \sim 50$ meV). Por lo tanto, la búsqueda de la desintegración doble beta supone un gran reto experimental. Entre las propuestas actuales, aquellas basadas en una TPC gaseosa tienen la ventaja de obtener la reconstrucción espacial de la traza dejada por la partícula usando detectores pixelizados, como es el caso de NEXT [68]. El experimento NEXT (Neutrino Experiment with a Xe TPC) tiene como objetivo la detección del modo $\beta\beta0\nu$ en ^{136}Xe usando una TPC gaseosa a alta presión (10-15 bar) que puede contener hasta 100 kg de Xe. El principio de detección está basado en la señal de electroluminiscencia medida con fotomultiplicadores situados en el plano contrario al de lectura, que puede dar una muy buena resolución energía como ha sido demostrado en los prototipos de la colaboración

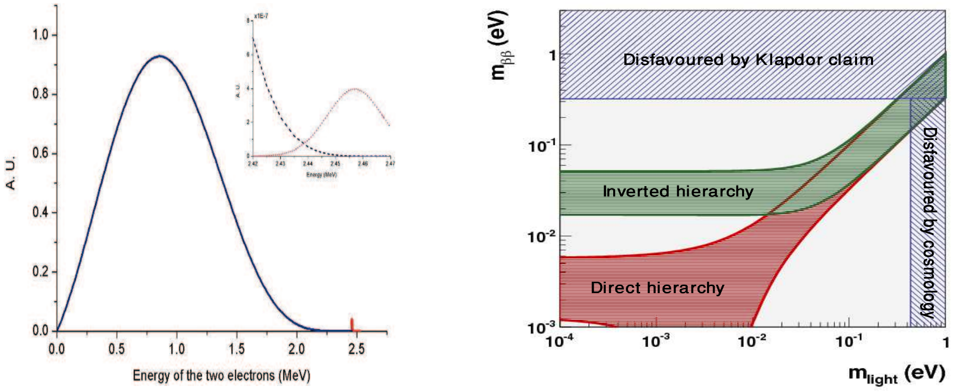

(a) (b)

FIGURA 1: *(a) Distribución de energía de los dos modos de la desintegración doble beta: con o sin emisión de neutrinos. Podemos ver como la resolución en energía juega un papel fundamental a la hora de discernir entre ambas señales. (b) Relación de la masa efectiva del neutrino que se mediría en los experimentos de desintegración $\beta\beta0\nu$ en función del neutrino más ligero. Las diferentes regiones de jerarquía de masas están indicadas así como el resultado positivo reclamado por parte de la colaboración Heidelberg-Moscow [74] y los límites obtenidos por las mediciones cosmológicas.*

[159, 160]. La reconstrucción de la traza se hará en un plano de fotomultiplicadores de Silicio. Como parte de la I+D de la colaboración se ha estudiado también el uso de detectores Micromegas que detecten la carga del evento, y sirvan como detectores calorimétricos y puedan reconstruir la traza del evento en el mismo detector.

El experimento de Gothard [89] fue pionero en el uso de Xe gas en una TPC equipada con un plano de hilos para la recogida de la carga que demostró el potencial de rechazo de fondo basado en la topología de los eventos [118]. Sin embargo, la limitada resolución energetica y espacial hicieron que la idea se abandonase hasta la invención de los detectores gaseosos "Micropattern" en 1988 por A. Oed. Desde entonces diferentes tecnologías han aparecido siendo de especial relevancia los detectores Micromegas (Micro-MEsh GAseous Structure) para la búsqueda de sucesos raros como la desintegracioón $\beta\beta0\nu$ o la materia oscura debido a su buena resolución en energía, resolución espacial y sus niveles de radiopureza probados en diferentes trabajos [108, 109, 156]. Bajo la colaboración NEXT y el proyecto TREX [117] (TPC para la búsqueda de sucesos raros), un prototipo equipado con detectores Micromegas se ha diseñado y construido en el grupo de la Universidad de Zaragoza: NEXT-MM. El prototipo NEXT-MM es una TPC cilindrica, de medio tamaño (30 cm de diámetro y 38 cm de deriva) que puede contener hasta 1 kg de Xe a 10 bar en su volumen fiducial, y así contener completamente trazas de electrones.

En la Figura 2 se puede ver una imagen de la TPC cerrada (a) y otra abierta con la estructura de la deriva (b). Esta está formada por 35 anillos de cobre espaciados 1 cm entre ellos y conectados mediante resistencias de 10 MΩ para igualar el campo a lo largo de la deriva; el cátodo es de cobre y conecta con el primer anillo de la deriva. Pruebas en Argón han demostrado que se puede alimentar hasta con 35 kV. La alta tensión se le da a través de un pasa cables especialmente diseñado para aguantar dichos voltajes. La deriva esta rodeada por una pantalla de Cirlex para evitar chispas con las zonas del detector conectadas a tierra, especialmente las paredes del detector. La vasija de la TPC es de acero de 3 cm de espesor con diferentes entradas para los cables de señal, dar el voltaje a los detectores y circular el gas. En ella se han probado diversas opciones teniendo cuidado en elegir aquellas con un bajo nivel de outgassing y a poder ser radiopuras.

Los detectores Micromegas consisten en una región de conversión entre el cátodo y el detector, donde se produce la ionización del gas y el transporte del electrón generado hasta el detector con campos eléctricos del orden de $10^{2-3}\,\mathrm{V\,cm^{-1}}$. La Micromegas como tal esta formada por dos planos paralelos: una microrejilla metálica (*mesh*) y un ánodo, separadas una distancia por lo general de entre 50-100 μm. Los electrones generados en la ionización atraviesan la rejilla y son amplificados en la región intermedia donde un campo eléctrico del orden de $10^4\,\mathrm{V\,cm^{-1}}$ se aplica. Cuatro detectores microbulk Micromegas [151] se han instalado en NEXT-MM para cubrir toda la superficie activa del detector, como podemos ver en la Figura 2 (c). Esta es la mayor superficie activa hasta el momento cubierta con esta tecnología. Todos los detectores son iguales, con un espaciado entre la mesh y el ánodo de 50 μm donde tiene lugar la avalancha de electrones. Los agujeros de la mesh tienen un diámetro de 35 μm y la distancia entre ellos es de 100 μm. El anódo esta pixelizado con un tamaño de 0.8×0.8 cm^2 cada uno, habiendo un total de 1252 pixels activos que son independientemente leídos. Al ser pixelizado se puede reconstruir en el ánodo el camino o traza dejada por la partícula en el gas, además de medir su energía tanto a partir de los pulsos eléctricos medidos tanto en la mesh como en el ánodo.

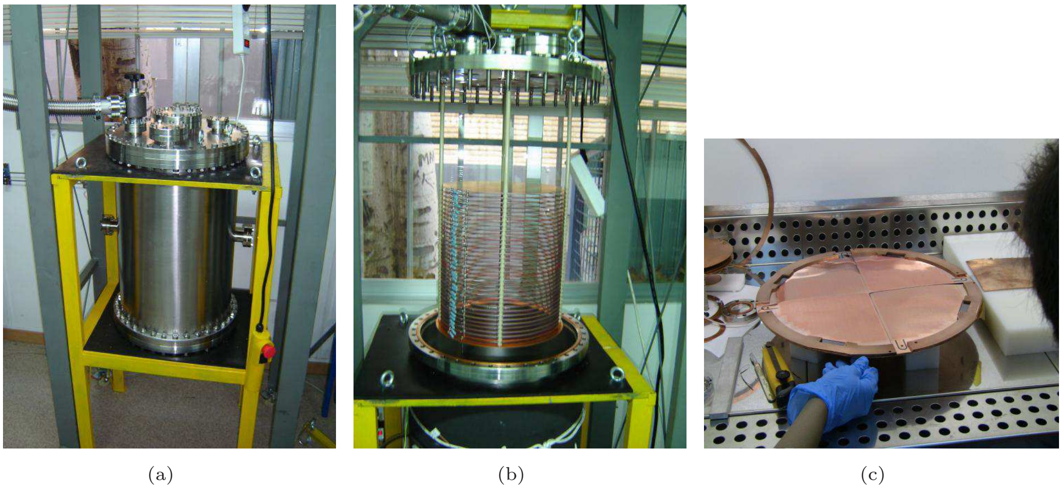
(a) (b) (c)

FIGURA 2: *Vista del prototipo NEXT-MM cerrado (a). En (b) se puede ver abierto y con la deriva. (c) Detectores microbulk Micromegas intalados en NEXT-MM.*

Tras su puesta en marcha y las primeras pruebas de funcionamiento, se han tomado datos en una mezcla de Xenon-trimetilamina (TMA) a 1 bar de presión. Esta mezcla ha demostrado ser especialmente interesante para un experimento $\beta\beta$ [109, 166] ya que forma un mezcla Pening con el Xe aumentando la ganacia y mejorando la resolución en energía. Los primeros datos han demostrado la capacidad de realizar calorimetría y reconocimiento de la señal (*tracking*) con ellas. En la Figura 3 podemos ver un ejemplo de traza registrada que atraviesa los tres detectores activos. En (d) podemos ver los tres planos activos.

Además se han desarrollado programas de ánalisis que permiten la reconstrucción del evento, como hemos visto, y permiten seleccionar eventos en función de los observables de un suceso

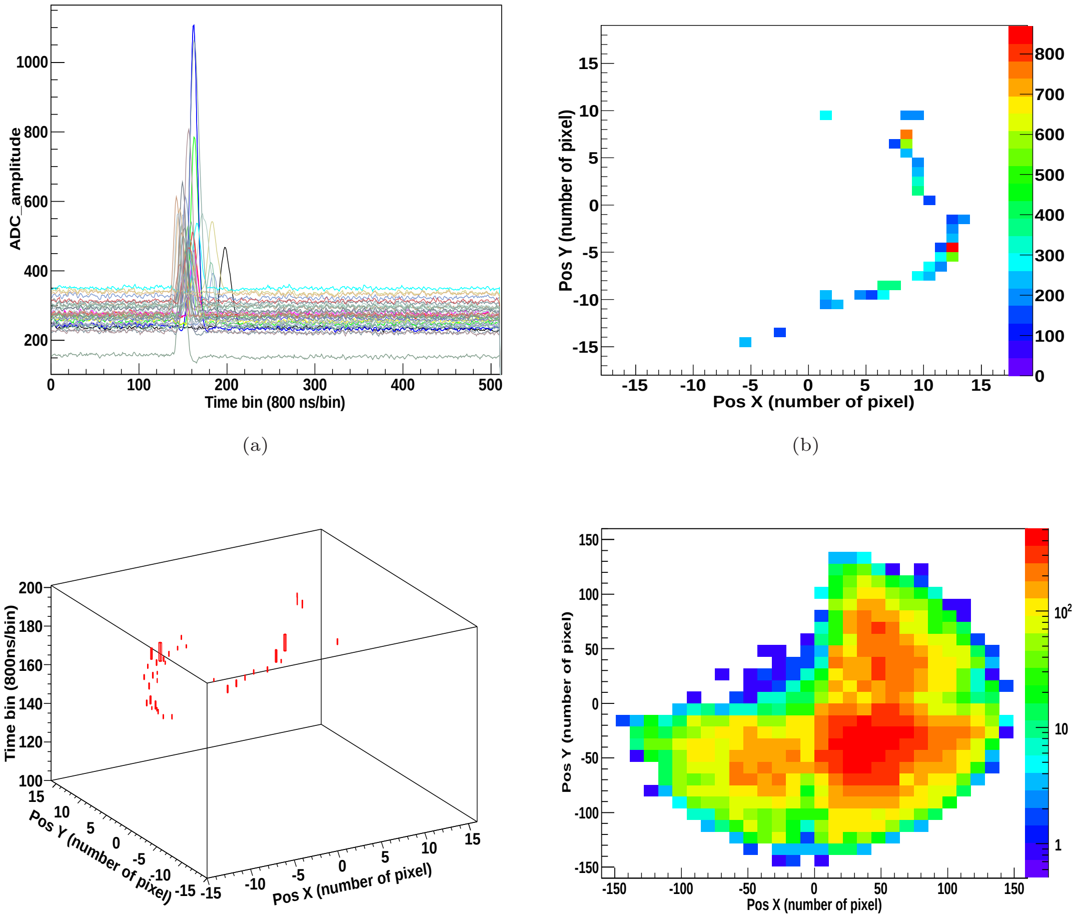

(a) (b) (c) (d)

FIGURA 3: *(a),(b) y (c) muestran distintias vista de un electrón de aproximadamente 180-200 keV atravesando los tres detectores activos. (a) Los pulsos registrados en los detectores activos. (b) Proyección xy projection de la traza. (c) Reconstrucción 3D con una posición z relativa. En (d) podemos ver la suma promedio de la carga en las posisicones x e y para los tres detectores activos.*

pixelizado como son su energía, posición y número de sucesos. De esta manera se pueden rechazar, casi por completo, los sucesos de fondo en una toma de datos con fuente de calibración. Para estos estudios se han tomado datos con dos detectores activos y con una fuente de ^{241}Am con su emisión alfa bloqueada. Dos picos de energías de $\sim$ 30 keV y 60 keV se esperan debido a la emisión gamma de la fuente (60 keV), el pico de escape del Xenón (29 keV) y el rayo-X del ^{241}Am de 26 keV. En este primer análisis resoluciones del orden de 11% FWHM para energías de 29 keV y de 9% para gammas de 60 keV se han obtenido. En la Figura 4 podemos ver los mejores resultados obtenidos para ambos detectores seleccionando eventos completamente contenidos en una región del detector. Esta resolución extrapola a un 1.5% FWHM al $Q_{\beta\beta}$ del Xenón (2458 keV). Si consideramos toda la superficie activa la resolución extrapola a un 2% FWHM. Los pasos futuros para mejorar el análisis son corregir las fluctuaciones de ganancia del detector observadas a lo largo del tiempo (aunque son del orden del 2%) así como mejorar el análisis en cuanto a la reconstrucción de trazas haciendo un estudio de depósitos de energía espacialmente separados. En cuanto al dispositivo experimental, ahora en fase estable de toma de datos, los siguientes pasos son tomar datos a mayor presión y en Xe.

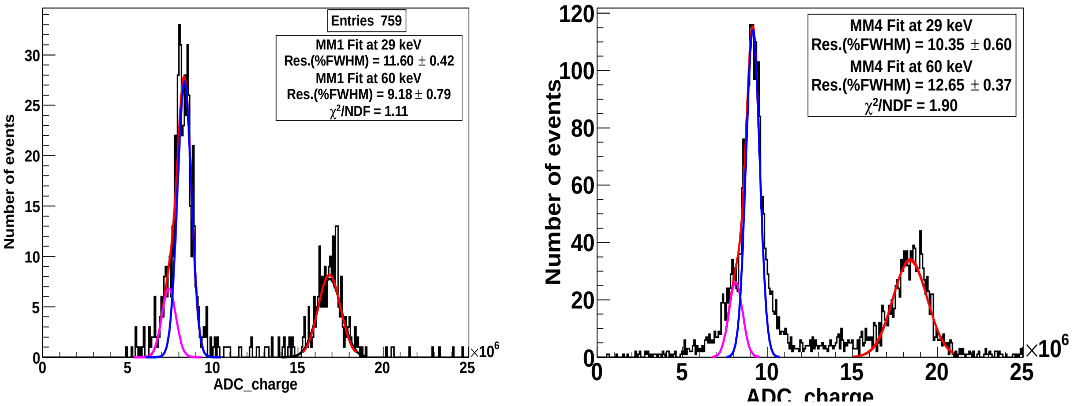

(a) Region 1

(b) Region 2

FIGURA 4: *Espectro de energía seleccinoando sucesos completamente contenidos en una región del detector de unos 16* cm^2*. En (a) resultados para una de las Micromegas (MM1) y (b) para otro detector (MM4). El espectro se ha obtenido integrando la carga registrada en el plano de pixels aquellos que hubieran superado un umbral. Ambos detectores fueron leídos simúltanemanete a 1 bar de Xe-TMA (3.5%). La MM4 puede tener un peor comportamineto porque tenía como el 15% de pixels desconectados en la región elegida. Dichos resultados extrapolan aproximadamente a un 1.5-2% FWHM a* $Q_{\beta\beta}$*.*

Para evaluar el poder de rechazo, la eficiencia y la sensibilidad esperada en un futuro detector TPC a alta presión con 100 kg de Xe para la búsqueda de su desintegración doble beta se ha llevado a cabo una simulación completa de una TPC con gas equipada con detectores pixelizados. La principal ventaja de una TPC gaseosa, como hemos comentado, es la posibilidad de realizar reconstrucción de la traza. Un suceso doble beta puede ser identificado como una trayectoria continua y tortuosa con mayores depósitos de carga en los extremos (*blobs*), debido a la mayor pérdida de energía a bajas energías para los electrones, y permitiendo depósitos aislados de carga (≥100 keV) por emisiones radiativas de los electrones. Un detector gaseoso con una lectura pixelizada , como la TPC propuesta, permite medir estas trazas, y distinguir el suceso doble beta de varios posibles fondos como partículas alfa, muones provenientes de los rayos cósmicos, electrones únicos (provenientes de la interacción fotoeléctrica o Compton de fotones energéticos, o desintegración beta), y sucesos de varios electrones debidos a dispersión Compton múltiple u otras interacciones múltiples de fotones (interacciones fotoeléctrica o Compton más radiación del electrón y posterior interacción del fotón emitido).

La simulación se ha dividido en tres bloques. En el pimer paso se generan las partículas e interacciones que tienen lugar en la TPC. Para ello se ha simulado la geometría de la vasija con Geant4. Se ha simulado una TPC de 0.73 m de radio y 1.45 m de altura. En ella hay una deriva formada por anillos de cobre embebidos en una panatalla de Teflón que definen un volumen fiducial de 124 kg de Xe a 10 bar dónde se registran las interacciones. Los sucesos se simulan usando Decay0. El resultado de la simulación con Geant4 son *hits* o depósitos de carga. El segundo paso es implementar los procesos físicos que tienen lugar en una TPC: creación de la carga, difusión y pixelización. Esto se hace con una estructura de librerias en C++ e implementadas con el paquete ROOT, desarrolladas en el grupo y llamada RESTSoft. Una vez generados los pixels el último paso es la reconstrucción de las trazas y el reconocimiento de blobs.

Dos clases de sucesos se han simulado: $\beta\beta0\nu$ señal y fondo. Un primer estudio de los fondos que puedesn ser problemáticos en un experimento $\beta\beta0\nu$ del ^{136}Xe limita su estudio a los isótopos ^{208}Tl y ^{214}Bi, provenientes de las cadenas radioactivas del ^{232}Th y ^{238}U respectivamente. Dicha contaminación puede estar presente en todos los elementos del detector y su entorno. Para el estudio se han simulado desde diversos puntos de la geometría y como contaminación superficial o volumétrica. Dichos elementos son: las paredes y tapas de la TPC, de cobre de 3 cm de grosor, la deriva (de cobre y teflón), el cátodo de cobre y el detector. La señal se ha simulado isotrópicamente en el volumen fiducial. Además se han implementado dos difusiones distintas, correspondientes a dos coeficientes de difusión: altos como puede ser el caso del Xe puro, o bajos como puede tener una mezcla de Xe con algún quencher como TMA o CF$_4$. El efecto de la difusión en la topología de la traza, y por lo tanto, en los algoritmos de discriminación, es muy importante.

Diferentes algoritmos de discriminación, basados en la teoría de grafos, se han implementado teniendo en cuenta las características topológicas de los sucesos de señal frente a los de fondo. Estas características, que hacen única la señal son: una traza principal larga que contiene la mayoría de la carga del suceso, dos députos de energía grandes en los extremos de la traza producidos por la reabsorción Bragg de los dos electrones emitidos en el proceso en el gas, y una distribución isotrópica en el volumen fiducial. Normalmente, los sucesos de fondo, producidos por un único electrón, tienen un único *blob*, o puede ser un evento de más de una traza si ha tenido lugar un multi-Compton o una radiación Bremsstrahlung. Además la radiación beta se producirá superficialmente y la mayoría de los eventos tocará las paredes. Sin embargo, algunos procesos pueden provocar la existencia de *blobs* extra pegados a la traza principal que pueden hacer que el suceso de fondo se asemeje a un $\beta\beta0\nu$ si el suceso depósita su carge dentro de la ventana de energía considerada. En las Figuras 5 y 6 podemos ver dos ejemplos de sucesos simulados: uno de señal y otro de fondo, correspondiéndose a una gamma de 2547 keV del ^{214}Bi (la más peligrosa de las radiaciones debido a su energía tan cercana al $Q_{\beta\beta}$), respectivamente.

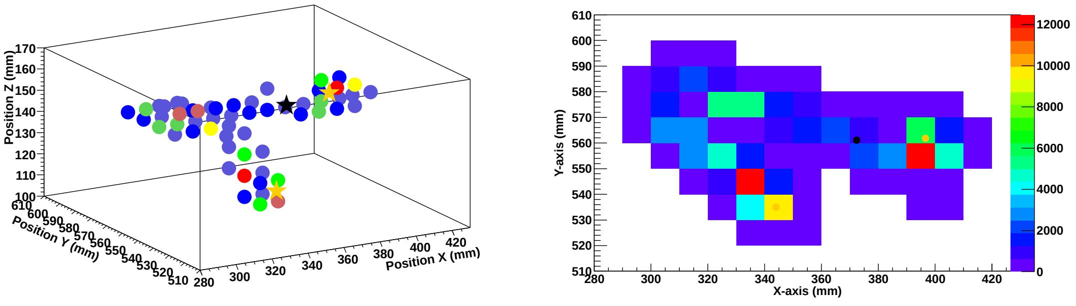

(a) (b)

FIGURA 5: *Ejemplo de un suceso doble beta sin neutrinos en* ^{136}*Xe obtenido con la simulación. Las condiciones simuladas fueron un pixel de 1* cm^2 *y 10 bar en un gas con alta difusión como puede ser Xe puro. Dos* blobs *pueden verse en ambos finales de la traza. En este caso uno de los electrones tiene una energía de 1.7 MeV mientras que el otro tiene 0.8 MeV, y toda la energía del suceso (2.45 MeV) ha sido registrada en el volumen sensible. En (a) podemos ver la reconstruccón 3D del suceso mientras que en (b) vemos su proyección en el plano XY pixelizado.*

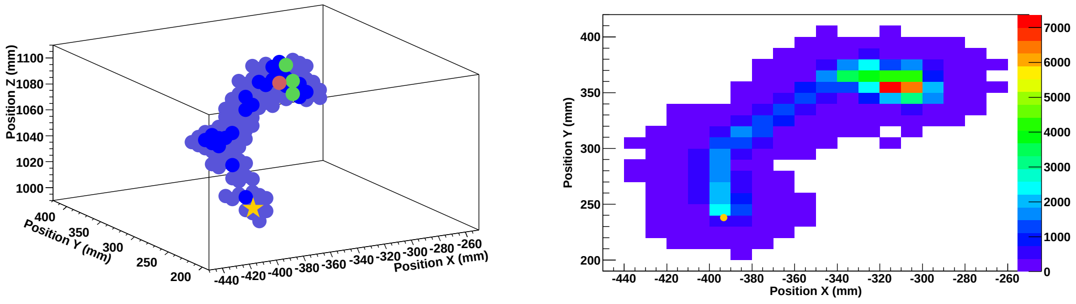

(a) (b)

FIGURA 6: *Evento de* ^{214}*Bi registrado en el plano pixelizado. El suceso se ha simulado en una TPC pixeizada con Xe puro (alta difusión) a 10 bar. (a) Reconstrucción 3D de un evento que ha depositado su energía al interaccionar su emisón gamma de 2447 keV por efecto fotoeléctrico. (b) Proyección en el plano XY pixelizado del suceso.*

Los algoritmos desarrollados trabajan en tres pasos: primero se seleccionan sucesos con una única traza larga. Sucesos con hasta un depósito extra de energía de 100 keV son también seleccionados. Esto mejora la eficiencia en la detección de la señal en un 20%. Posteriormente, se busca la línea de traza más larga que una todos los pixels y que tenga dos *blobs* en los extremos del suceso. Finalmente, se define un recubrimiento en torno a la línea de traza encontrada y se exige que los eventos seleccionados tengan más del 90% de la carga dentro de este volumen. Después de estas selecciones basadas en la topología se aplica un veto fiducial eliminando sucesos que depositen parte de su energía a menos de 1 cm de las paredes, cátodo y plano de lectura. Los parámetros usados en los algoritmos se basan en asumpciones físicas y se han ajustado para tener una gran eficiencia a la vez se aumentaba el factor de rechazo, mejorando la sensibilidad del experimento. Cuantitativamente se busca un nivel de fondo de aproximadamente 10^{-4}c keV^{-1} kg^{-1} y^{-1}. Los resultados se han evaluado en una amplia RoI (100 keV). Dicha ventana de energía corresponde a una resolución del 2% FWHM a $Q_{\beta\beta}$, mayor de la esperada a raíz de los resultados experimentales pero que nos permite un mejor entendimineto de los fondos.

La eficiencia del detector en la RoI es del 70%, mientras que tras la aplicación de criterios de selección antes mencionados, la eficiencia total es del 40%. El mismo valor se obtiene considerando un gas con alta o baja difusión.

El efecto de los algoritmos sobre los sucesos de fondo también ha sido evaluado, obteniéndose un factor de rechazo de 6 órdenes de magnitud en la RoI. Estos valores mejoran en al menos un factor 3, si suponemos una mezcla Xe con baja difusión. Si el efecto de cada criterio se evalúa por separado, la selección de eventos con una única traza es más potente en el caso del ^{208}Tl por que produce más Compton y multi-Compton, mientras que la contribución principal del ^{214}Bi es la absorción fotoeléctrica de la gamma de 2447.8 keV. La selección topológica tiene el mismo efecto en ambas contribuciones, como era de esperar ya que actúa sobre la traza principal; se observan peque˜as diferencias debidas al origen geométrico de la contaminación. Es en esta selección de eventos donde hay una mayor discrepancia al considerar una difusión u otra, porque el efecto de la difusión, que produce una extensión de la carga en todas las direcciones, empeora el reconocimiento de la traza. Por lo tanto, a baja difusión es más fácil la reconstrucción de la traza y más sencilla la separación de depósitos extra de carga de la principal. El efecto total de esta selcción es una reducción del 60% en alta difusión y cercana al 90% para baja difusión. La reducción obtenida por Gothard realizando un análisis visual de las trazas era del 95%. Hay que recordar que la TPC era más pequeña y trabajaban a 5 bar. El análisis utilizado en nuetro caso se trata de un análisis ciego. Finalmente, el veto fiducial tiene un efecto sólo sobre la contaminación superficial, siendo más relevante su rechazo para el caso de ^{214}Bi debido a su espectro beta. Si se varía la resolución en energía, la contaminación de ^{208}Tl reduce linealmente con la ventana mientras que la reducción del ^{214}Bi es prácticamente la misma. La eficiencia permanece constante.

Estudiando los eventos que sobreviven los algoritmos de discriminacón, en el 30% de los casos se ha producido una emisión secundaria de más de 100 keV (Bremsstrahlung o Compton), la cual ha producido un blob extra que hace que se identifique el suceso con un suceso de señal $\beta\beta0\nu$. Por otra parte, se ha visto que en los eventos producidos ms cerca del cátodo, al sufrir una mayor difusión, es más difícil identificar bien la línea de traza.

Con los factores de rechazo calculados podemos obtener el nivel de fondo esperado en términos de $\mathrm{c\,keV^{-1}\,kg^{-1}\,y^{-1}}$. Para ello se han utilizado actividades de materiales medidos como input [155, 165]. Se han estudiado dos diferentes escenarios de fondo, uno conservador, y uno realista en el que se espera que los detectores Micromegas tengan un mejor nivel de fondo, ya que midiéndolas mediante espectroscópia con un Ge, se ha obtenido una cota [156]. Además se han considerado las dos difusiones mencionadas. En el escenario conservador, en una región 2% FWHM en torno a $Q_{\beta\beta}$ se ha obtenido un nivel de fondo de $(9,47\pm1,45)\times10^{-4}\,\mathrm{c\,keV^{-1}\,kg^{-1}\,y^{-1}}$ en alta difusión, mientras que en una mezcla de Xe a baja difusión este valor es de $(3,34\pm0,95)\times10^{-4}\,\mathrm{c\,keV^{-1}\,kg^{-1}\,y^{-1}}$. En el caso de fondo más realista el fondo total mejora un factor entre 3 y 4, siendo de $(2,53\pm0,18)\ \times10^{-4}\,\mathrm{c\,keV^{-1}\,kg^{-1}\,y^{-1}}$ en alta difusión y bajando hasta $(1,06\pm0,11)\times10^{-4}\,\mathrm{c\,keV^{-1}\,kg^{-1}\,y^{-1}}$ en una mezcla de baja difusión. Este fondo es el objetivo de los experimentos de última generación para ser sensibles a masas del neutrino de 100 meV. Podemos ver el efecto de los algoritmos de discriminación sobre el nivel de fondo en la Figura 7 donde se muestra la contribución del ^{208}Tl y del ^{214}Bi por separado suponiendo una resolución del 2% FWHM y en Xe puro (alta difusión). Los espectros finales para cada difusión y ventana de energía se pueden ver en las Figuras 8 y 9.

A partir de estos resultados se puede obtener la sensibilidad a la masa efcetiva del neutrino. En todos los escenarios se puede investigar el resultado publicado por parte de la colaboración Heidelberg-Moscow [74]. En el caso de fondo conservador en Xe puro, la mayor sensibilidad alcanzada es de 100 meV con una resolución del 0.5% FWHM y tras una exposición de 1240 kg×año (equivalente a 10 años de medida). En el caso de una mezcla con baja difusión se alcanzarían 81 meV. En el caso de un escenario más realista se bajaría hasta 77 meV en Xe puro y 66 meV en baja difusión. En todos los casos se alcanzaría el valor de 100 meV. Sin embargo, la región de jerarquía invertida, cuyo límite superior esta en torno a 50 meV no sería alcanzada.

Finalmente, se ha evaluado la posibilidad de escalar el detector a 1 tonelada de isótopo emisor ^{136}Xe. En este caso se encuentra una mejora de aproximadamente 3 en el nivel de fondo obtenido ya que tenemos 10 veces más masa. Con este nivel de fondo la sensibilidad esperada alcanza los 50 meV tras 10 años de medida en el peor de los casos (escenario conservativo al 2% FWHM de resolución y alta difusión). En el mejor de los casos el límite obtenido es de 26 meV (escenario

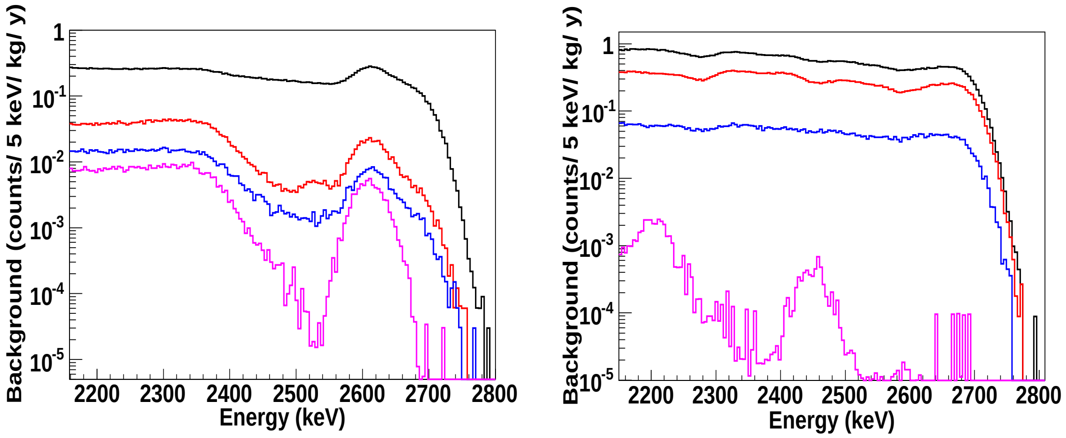

(a) (b)

Figura 7: *Espectro de fondo obtenido en el escenario "conservativo"tras la aplicación de los algoritmos de discriminación para ^{208}Tl (a) y ^{214}Bi (b) en Xe puro a 10 bar y un pixelizado de 10×10 mm^2. En todos los casos: la línea negra corresponde al espectro inicial, en rojo tras la aplicación de seleccionar eventos de una única traza, en azul tras la selcción basada en la topología y finalmente, en magenta, tras el veto fiducial. En todos los casos el bineado es de 5 keV.*

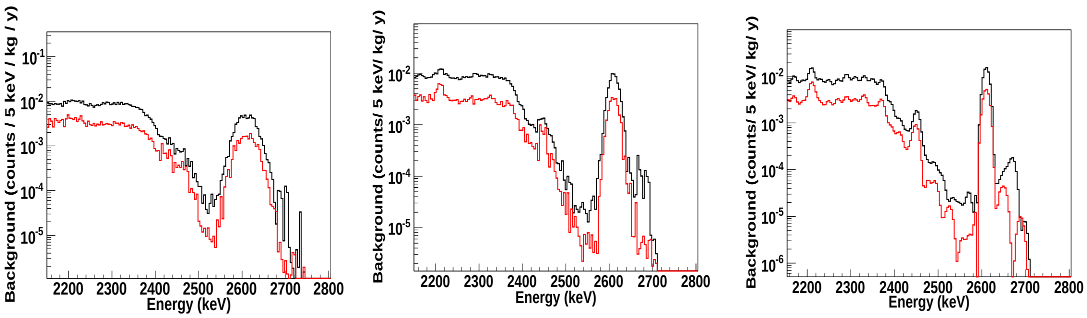

(a) (b) (c)

Figura 8: *Espectros finales obtenidos en el escenario de fondo inicial "conservative"combinando todas las contribuciones simuladas de ^{208}Tl y ^{214}Bi. Se han sumado tras aplicar todos los cortes. (a) Convolucioanndo el espectro con una resolución del 2% FWHM a $Q_{\beta\beta}$. (b) Con una resolución del 1% FWHM a $Q_{\beta\beta}$ y (c) del 0.5% FWHM a $Q_{\beta\beta}$. E los tres casos la línea negra representa el caso de alta difusión y la roja de baja difusión.*

realista en una mezcla de Xe de baja difusión y al 0.5% de resolucón). Por lo tanto esta opción permitiria investigar, casi por completo, la región de jerarquía de masas invertida. Sin embargo, tecnológicamente supone un reto aún mayor además de incrementar los costes.

En conclusión, se han presentado resultados prometedores para un experimento de búsqueda de la desintegración doble beta en ^{136}Xe usando una TPC gaseosa de alta presión equipada con Micromegas. Estos detectores han demostrado una muy buena capacidad de reconstrucción de trazas en un prototipo de tamaño medio con una distancia de deriva de 38 cm a 1 bar de Xe-TMA. Además de obtenerse resoluciones del 1,5% a $Q_{\beta\beta}$. Los siguientes pasos incluyen aumentar la presión y mejorar el análsis. Así mismo, se ha llevado a cabo una simulación completa de una TPC que pueda albergar 100 kg de Xe a 10 bar para estudiar el poder de rechazo de esta opción. Diferentes algoritmos de discriminación se han aplicado, basados en las diferencias topológicas observadas entre sucesos de fondo y señal, obteniendose un factor de

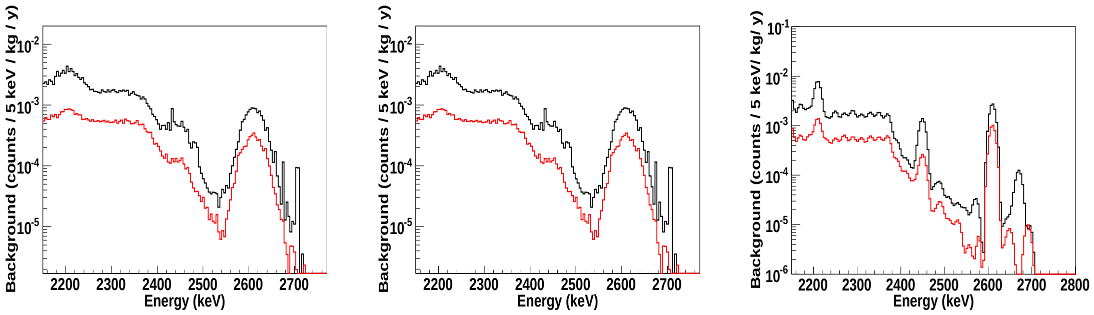

(a) (b) (c)

FIGURA 9: *Espectros finales obtenidos en el escenario de fondo inicial "realista"combinando todas las contribuciones simuladas de* ^{208}*Tl y* ^{214}*Bi. Se han sumado tras aplicar todos los cortes. (a) Convolucioanndo el espectro con una resolución del 2% FWHM a* $Q_{\beta\beta}$*. (b) Con una resolución del 1% FWHM a* $Q_{\beta\beta}$ *y (c) del 0.5% FWHM a* $Q_{\beta\beta}$*. E los tres casos la línea negra representa el caso de alta difusión y la roja de baja difusión.*

rechazo de 6 ordenes de magnitud. Este factor mejora en una mezcla de Xe con baja difusión. El nivel de fondo obtenido es de $(2,53 \pm 0,18) \times 10^{-4}\,\mathrm{c\,keV^{-1}\,kg^{-1}\,y^{-1}}$ en alta difusión y $(1,06 \pm 0,11) \times 10^{-4}\,\mathrm{c\,keV^{-1}\,kg^{-1}\,y^{-1}}$ en baja difusión. Estos resultados permitirían explorar regiones de masa del neutrino hasta 100 meV.

Bibliography

[1] W. Pauli, 1930. URL `http://cds.cern.ch/record/83282/files/meitner_0393.pdf`.

[2] E. Fermi. Tentativo di una teoria dei raggi β. *Nuovo Cim. 2*, 2, 1934.

[3] F. Reines et al. Evidence for high-energy cosmic ray neutrino interactions. *Phys.Rev.Lett.*, 15:429–433, 1965.

[4] G. Danby et al. Observation of High-Energy Neutrino Reactions and the Existence of Two Kinds of Neutrinos. *Phys.Rev.Lett.*, 9:36–44, 1962.

[5] K. Kodama et al. Observation of tau neutrino interactions. *Physics Letters B*, 504:218 – 224, 2001.

[6] Y. Fukuda et al. Atmospheric muon-neutrino / electron-neutrino ratio in the multiGeV energy range. *Phys.Lett.*, B335:237–245, 1994.

[7] Q. R. Ahmed et al. Measurement of the rate of $\nu_e + d \to p + p$+e$^-$ interactions produced by ^{8}B solar neutrinos at the sudbury neutrino observatory. *Physics Review Letters*, 87: 071301, 2001.

[8] B. Pontecorvo. Neutrino Experiments and the Problem of Conservation of Leptonic Charge. *Soviet Journal of Experimental and Theoretical Physics*, 26:984, 1968.

[9] M. Nakagawa Z. Maki and S. Sakata. Remarks on the unified model of elementary particles. *Progress on Theoretical Physics*, 28:870, 1962.

[10] R. Becker-Szendy et al. Electron- and muon-neutrino content of the atmospheric flux. *Physics Review D*, 46:3720, 1992.

[11] Y. Fukuda et al. Evidence for oscillation of atmospheric neutrinos. *Phys. Rev. Lett.*, 81: 1562–1567, 1998.

[12] S. Fukuda et al. Solar ^{8}B and hep neutrino measurements from 1258 days of Super-Kamiokande data. *Phys. Rev. Lett.*, 86:5651–5655, 2001.

[13] K. Eguchi et al. First results from KamLAND: Evidence for reactor anti-neutrino disappearance. *Phys.Rev.Lett.*, 90:021802, 2003.

[14] E. Majorana. Teoria simmetrica dell electrone e del positrone. *Nuovo Cimento*, 14:171, 1937.

[15] F.T. Avignone III et al. Double beta decay, Majorana neutrinos and neutrino mass. *Rev. Mod. Phys.*, 80:481, 2008.

[16] S. M. Bilenky. Neutrinoless Double Beta-Decay. *Lect. Notes Phys*, 817:139–158, 2010.

[17] Héctor Gómez. *Estudio de la sensibilidad de un experimento de desintegración doble beta con detectores de Ge de nueva generación.* PhD thesis, Universidad de Zaragoza, Zaragoza, Spain, May 2009.

[18] Y. Ashie et al. Evidence for an oscillatory signature in atmospheric neutrino oscillations. *Phys. Rev. Lett.*, 93:101801, 2004.

[19] Q. R. Ahmed et al. Direct evidence for neutrino flavour transformation from neutral-current interactions in the Sudbury Neutrino Observatory. *Physics Review Letters*, 89: 011301, 2002.

[20] Q. R. Ahmed et al. Measurement of day and night neutrino energy spectra at SNO and constraints on neutrino mixing parameters. *Physics Review Letters*, 89:011302, 2002.

[21] S.N. Ahmed et al. Measurement of the total active ^{8}B solar neutrino flux at the Sudbury Neutrino Observatory with enhanced neutral current sensitivity. *Phys. Rev. Lett.*, 92: 181301, 2004.

[22] B. Aharmim et al. Independent measurement of the total active ^{8}B solar neutrino flux using an array of ^3He proportional counters at the Sudbury Neutrino Observatory. *Phys. Rev. Lett.*, 101:111301, 2008.

[23] M. Apollonio et al. Limits on neutrino oscillations from the CHOOZ experiment. *Phys. Lett. B*, 466:415–430, 1999.

[24] M.H. Alm et al. Indications of neutrino oscillation in a 250 km long-baseline experiment. *Phys. Rev. Lett.*, 90:041801, 2003.

[25] E. Aliu et al. Evidence for muon neutrino oscillation in an accelerator-based experiment. *Phys. Rev. Lett.*, 94:081802, 2005.

[26] M.H. Alm et al. Measurement of neutrino oscillation by the K2K experiment. *Phys. Rev. D*, 74:072003, 2006.

[27] P. Admason et al. Measurement of neutrino oscillations with the MINOS detectors in the NuMI beam. *Phys. Rev. Lett.*, 101:131802, 2008.

[28] C. Arpesella et al. Direct measurement of the ^{7}B solar neutrino flux with 192 days of BOREXINO data. *Phys. Rev. Lett.*, 101:091302, 2008.

[29] F.P. An et al. Observation of electron-antineutrino disappearance at daya bay. *Phys. Rev. Lett.*, 108:171803, 2012.

[30] J. K. Ahn et al. Observation of reactor electron antineutrinos disappearance in the RENO experiment. *Phys. Rev. Lett.*, 108:191802, 2012.

[31] Y. Abe et al. Indication of reactor $\bar{\nu_e}$ disappearance in the double CHOOZ experiment. *Phys. Rev. Lett.*, 108:131801, 2012.

[32] K. Abe et al. Indication of electron neutrino appearance from an accelerator-produced off-axis muon neutrino beam. *Phys. Rev. Lett.*, 107:041801, 2011.

[33] P. et al. Adamson. Improved search for muon-neutrino to electron-neutrino oscillations in MINOS. *Phys. Rev. Lett.*, 107:181802, 2011.

[34] Ken Long. Neutrino production moves to an industrial scale. http://cerncourier.com/cws/article/cern/49351, 2012.

[35] Peter Minkowski. $\mu \to e\gamma$ at a rate of one out of 10^9 muon decays? *Physics Letters B*, 67 (4):421 – 428, 1977.

[36] W. Buchmuller, R.D. Peccei, and T. Yanagida. Leptogenesis as the origin of matter. *Ann.Rev.Nucl.Part.Sci.*, 55:311–355, 2005.

[37] Ch. Kraus et al. Final results from phase II of the Mainz neutrino mass search in tritium beta decay. *Eur.Phys.J.*, C40:447–468, 2005.

[38] V. N. Aseev et al. Upper limit on the electron antineutrino mass from the troitsk experiment. *Phys. Rev. D*, 84:112003, 2011.

[39] The KATRIN Collaboration. LOI KATRIN: A next generation tritium beta decay experiment with sub-ev sensitivity for the electron neutrino mass. arXiv.org:0109033v1.

[40] A. Nucciotti et al. The MARE project. *Journal of Low Temperature Physics*, 151:597–602, 2008.

[41] K.N. Abazajian et. al. Cosmological and astrophysical neutrino mass measurements. *Astroparticle Physics*, 35(4):177 – 184, 2011.

[42] F.T. Avignone III et al. Next generation double-beta decay experiments: metrics for their evaluation. *New J. Phys.*, 7(6), 2005.

[43] A. Giuliani, A. Poves. Neutrinoless double-beta decay. *Advances in High Energy Physics*, 2012:38, 2012.

[44] A.S. Barabash. Precise half-life values for two-neutrino double-beta decay. *Phys. Rev. C*, 81:035501, 2010.

[45] N. et. al Ackerman. Observation of two-neutrino double-beta decay in ^{136}Xe with the exo-200 detector. *Phys. Rev. Lett.*, 107:212501, Nov 2011.

[46] M. Goeppert-Mayer. Double-beta desintegration. *Phys. Rev.*, 48:512, 1935.

[47] W.H. Furry. On transition probabilities in double-beta desintegration. *Phys.Rev.*, 56:1184, 1939.

[48] S. R. Elliott, A. A. Hahn, and M. K. Moe. Direct evidence for two-neutrino double-beta decay in ^{82}Se. *Phys. Rev. Lett.*, 59:2020–2023, 1987.

[49] S.R. Elliot, J. Engel. Double beta decay. *J. Phys. G*, 30:R183, 2004.

[50] A.S. Barabash. Double beta decay experiments: beginning of a new era. *arXiv.org*, arXiv: 1209.4241, 2012.

[51] F. Simkovic J. D. Vergados, H. Ejiri. Theory of neutrinoless double-beta decay. *Reports on Progress in Physics*, 75:106301, 2012.

[52] J. J. Gómez-Cadenas, J. Martín-Albo, and F. Monrabal. Next, high-pressure xenon gas experiments for ultimate sensitivity to majorana neutrinos. *Journal of Instrumentation*, 7:C11007, 2012.

[53] M. Kortelainen and J. Suhonen. Improved short-range correlations and the $0\nu\beta\beta$ nuclear matrix elements of 76Ge and 82Se. *Physical Review C*, 75, 2007.

[54] M. Kortelainen and J. Suhonen. Nuclear matrix elements of neutrinoless double beta decay with improved short-range correlations. *Physical Review C*, 76, 2007.

[55] F. Simkovic V. A. Rodin, A. Faessler and P. Vogel. Assessment of uncertainties in QRPA $0\nu\beta\beta$-decay nuclear matrix elements. *Nuclear Physics A*, 793:213, 2007.

[56] A. Poves E. Caurier, G. Martnez-Pinedo and A. P. Zuker. The shell model as unified view of the nuclear structure. *Reviews of Modern Physics*, 77:425, 2005.

[57] Gerald A. Miller and James E. Spencer. A Survey of Pion Charge-Exchange Reactions with Nuclei. *Annals Phys.*, 100:562, 1976.

[58] M. Kortelainen, O. Civitarese, J. Suhonen, and J. Toivanen. Short-range correlations and neutrinoless double beta decay. *Phys.Lett.*, B647:128–132, 2007.

[59] H. Feldmeier, T. Neff, R. Roth, and J. Schnack. A Unitary correlation operator method. *Nucl.Phys.*, A632:61–95, 1998.

[60] J. Barea and F. Iachello. Neutrinoless double-beta decay in the microscopic interacting boson model. *Physical Review C*, 79:044301, 2009.

[61] T. R. Rodríguez and G. Martínez-Pinedo. Energy density functional study of nuclear matrix elements for neutrinoless $\beta\beta$ decay. *Physical Review Letters*, 105:252503, 2010.

[62] J. Schechter and J. W. F. Valle. Neutrinoless double-β decay in su(2)×u(1) theories. *Phys. Rev. D*, 25:2951–2954, Jun 1982.

[63] W. Rodejohann. Neutrino-less double beta decay and particle physics. *International Journal of Modern Physics E*, 20(09):1833–1930, 2011.

[64] T. Kirsten. Geochemical double beta decay experiments. AIP. *Conf. Proc.*, 66:396–410, 1983.

[65] O.K. Manuel. Geochemical measurements of double beta decay. *J. Phys. G:* N*ucl. Part. Phys.*, 17:221–229, 1991.

[66] W.C. Haxton et al. Radiochemical tests of double beta decay. *Phys. Rev. C*, 28:467–470, 1983.

[67] B. Majorovits. The GERDA neutrinoless-double-beta decay experiment. *Proceedings of Science (idm2008)*, page 069, 2008.

[68] F. Granena et al. NEXT, a HPGXe TPC for neutrinoless double beta decay searches. *arXiv.org*, arXiv:0907.4054, 2009.

[69] A. Chapon and The SuperNEMO collaboration. Supernemo status. *AIP Conf. Proc.*, 1417: 18, 2011.

[70] C. Amsler et al. Review of Particle Physics. *Phys. Lett. B*, 667:1–1340, 2008.

[71] G. F. Knoll. *Radiation Detection and Measurement.* John Wiley and Sons, Inc., third edition, 2000.

[72] A. Dolgolenko et al. M. Danilov, R. DeVoe. Detection of very small neutrino masses in double-beta decay using laser tagging. *Physics Letters Section B*, 480:12–18, 2000.

[73] I. Abt et al. Pulse shapes from electron and photon induced events in segmented high-purity germanium detectors. *Eur. Phys. J. C*, 52:19–27, 2007.

[74] H.V. Klapdor Kleingrothaus et al. Evidence for neutrinoless double beta decay. *Mod. Phys. Lett. A*, 16:2409–2420, 2001.

[75] A. Morales. Review on double beta decay experiments and comparison with theory. *Nucl. Phys. B (Proc. Suppl.)*, 77:335–345, 1999.

[76] C.E. Aalseth et al. Neutrinoless double beta decay of ^{76}Ge: first results from the International Germanium EXperiment (IGEX) with six isotopically enriches detectors. *Phys. Rev. C*, 59:2108, 1999.

[77] M. Gunther et al. Heidelberg-Moscow $\beta\beta$ experiment with ^{76}Ge: full setup with five detectors. *Phys. Rev. D*, 55:54, 1997.

[78] C.E. Aalseth et al. Comment on evidence for neutrinoless double beta decay. *Mod. Phys. A*, 17:1475, 2002.

[79] Y.G. Zdesenko et al. Has neutrinoless double beta decay of ^{76}Ge been really observed? *Phys. Lett. B*, 546:206, 2002.

[80] A.M. Bakalyarov et al. Results of the experiment on investigation of Germanium-76 double beta decay. experimental data of Heidelberg-Moscow collaboration November 1995 - August 2001. *Phys. Part. Nucl. Lett.*, 2:77–81, 2005.

[81] H. V. Klapdor-Kleingrothaus and I. V. Krivosheina. The evidence for the observation of $0\nu\beta\beta$ decay: the identification of $0\nu\beta\beta$ events from the full spectra. *Modern Physics Letters A*, 21:15471566, 2006.

[82] H.V. Klapdor Kleingrothaus et al. Search for neutrinoless double beta decay with enriched ^{76}Ge in Gran Sasso. *Phys. Lett. B*, 586:198, 2004.

[83] E. Fiorini and T. O. Niinikoski. Low temperature calorimetry for rare decays. *Nuclear Instruments and Methods in Physics Research A*, 224:83, 1984.

[84] Ettore Fiorini. Neutrino physics with cryogenic detectors. *Progress in Particle and Nuclear Physics*, 64:241 – 248, 2010.

[85] A. Alessandrello et al. New experimental results on double beta decay of ^{130}Te. *Phys. Lett. B*, 486:13, 2000.

[86] A. Alessandrello et al. A New search for neutrinoless beta beta decay with a thermal detector. *Phys.Lett.*, B335:519–525, 1994.

[87] E. Andreotti et al. 130Te Neutrinoless Double-Beta Decay with CUORICINO. *Astropart.Phys.*, 34:822831, 2011.

[88] Alexander Barabash and the Nemo Collaboration. Nemo 3 double beta decay experiment: Latest results. *Journal of Physics: Conference Series*, 173(1):012008, 2009.

[89] R. Luscher et al. Search for beta beta decay in Xe-136: New results from the Gotthard experiment. *Phys.Lett. B*, 434:407–414, 1998.

[90] J.C. Vuilleumier et al. Search for neutrinoless double beta decay in ^{136}xe with a time projection chamber. *Phys. Rev. D*, 48:1009, 1993.

[91] I. Abt et al. GERDA Letter of Intent, A new ^{76}Ge Double Beta Decay Experiment at LNGS. http://arxiv.org/abs/hep-ex/0404039, 2004.

[92] Barnabé et al. Performance of bare high-purity germanium detectors in liquid argon for the GERDA experiment. *IEEE Nuclear Science Symposium*, 68, 2008.

[93] The GERDA Collaboration. Measurement of the half-life of the two-neutrino double beta decay og ^{76}Ge with the GERDA experiment. *submitted to J. Phys. G: Nucl. Part. Phys*, arXiv:1212.3201, December 2012.

[94] The Majorana Collaboration. White Paper on the Majorana Zero- Neutrino Double-Beta Decay Experiment. http://arxiv.org/abs/nucl-ex/0311013, 2003.

[95] S. Elliot et al. The Majorana project. *J. Phys.: Conf. Ser.*, 39:341–343, 2006.

[96] P. Finnerty et al. The MAJORANA DEMONSTRATOR: Progress towards showing the feasibility of a tonne-scale 76Ge neutrinoless double-beta decay experiment. *To be published in IOP Conference Series*, arXiv:1210.2678, 2012.

[97] E. Aguayo et al (The MAJORANA Collaboration). The majorana experiment. *AIP Conf. Proc.*, 1417:95, 2011.

[98] C. Arnaboldi et al. Physics potential and prospects of the CUORICINO and CUORE experiments. *Astropart. Phys.*, 20:91–110, 2003.

[99] A.S. Barabash. NEMO-3 and SuperNEMO double beta decay experiments. *J. of* P*hys:* C*onf. Ser.*, 39:347–349, 2006.

[100] H. Gómez. Bipo: A dedicated radiopurity detector for the supernemo experiment. *Nuclear Instruments and Methods in Physics Research Section A: Accelerators, Spectrometers, Detectors and Associated Equipment*, 2012. doi: 10.1016/j.nima.2012.12.063.

[101] J. Hartnell (for the SNO+ collaboration). Neutrinoless Double Beta Decay with SNO+. *J. Phys. Conf. Ser.*, 375:042015, 2012.

[102] C. Kraus and S. J. M. Peeters. The rich neutrino programme of the SNO+ experiment. *Progress in Particle and Nuclear Physics*, 64:273277, 2010.

[103] Gando A. et al. *Phys. Rev. C*, 86:021601R, 2012.

[104] A. et al Gando. Measurement of the double-β decay half-life of ^{136}Xe with the KamLAND-Zen experiment. *Phys. Rev. C*, 85:045504, 2012.

[105] A. Gando for the KamLAND-Zen Collaboration. First results from the KamLAND-Zen Double Beta Decay with 136Xe experiment. volume 90, page 021802, 2012.

[106] P. S. Barbeau et al. M. Auger, D. J. Auty. Search for neutrinoless double-beta decay in 136Xe with EXO-200. *Physical Review Letters*, 109, 2012.

[107] A. Piepke and the EXO collaboration. Double beta decay: EXO-200 and beyond, 2012. Fundamental Symmetries and Neutrinos Meeting, Chicago, IL.

[108] S. Cebrián et al. Micromegas readouts for double beta decay searches. *Journal of Cosmology and Astroparticle Physics*, 2010:010, 2010.

[109] S. Cebrián et. al. Micromegas-tpc operation at high pressure in xenon-trimethylamine mixtures. *Journal of Instrumentation*, 8(01):P01012, 2013.

[110] H. Ejiri et al. Moon for neutrino-less double beta decays. *Eur. Phys. Journal*, 162:239, 2008.

[111] H. Ejiri et al. Multilayer scintillator responses for mo observatory of neutrino experiment studied using a prototype detector moon-1. *J. Phys. Soc. Jpn*, 76:114201, 2007.

[112] T. Kishimoto and the CANDLES Collaboration. Study of double beta decay of 48ca with candles. *Journal of Physics: Conference Series*, 120:052053, 2008.

[113] I. Dafinei et al. LUCIFER: an experimental breakthrough in the search for neutrinoless double beta decay, 2010.

[114] K. Zuber et al. COBRA double beta decay searches using cdte detectors. *Physics Letters B*, 519:1 – 7, 2001.

[115] S. K. Kim et al. Amore: Search for neutrinoless double beta decay with camoo4 crystals advanced molybdenum based rare process experiment. Presented at the MEDEX, Prague Czech Republic, 2011. URL `http://medex11.utef.cvut.cz/talks/Kim.pdf`.

[116] S.J. Lee et al. The development of a cryogenic detector with camoo4 crystals for neutrinoless double beta decay search. *Astroparticle Physics*, 34(9):732 – 737, 2011.

[117] I.G. Irastorza et al. Status of r&d on micromegas for rare event searches: the T-REX project. *EAS Pub. Series*, 53:147, 2012.

[118] H. T. Wong et al. Event identification with a time projection chamber in a double beta decay experiment on ^{136}xe. *Nucl. Instrum. Meth. A*, 329:163, 1993.

[119] A. Oed, P. Convert, M. Berneron, H. Junk, C. Budtz-JArgensen, M.M. Madsen, P. Jonasson, and H.W. Schnopper. A new position sensitive proportional counter with microstrip anode for neutron detection. *Nuclear Instruments and Methods in Physics Research Section A: Accelerators, Spectrometers, Detectors and Associated Equipment*, 284(1):223 – 226, 1989.

[120] J. P. Robert Y. Giomataris, P. Rebourgeard and G. Charpak. MICROMEGAS: A high granularity position-sensitive gaseous detector for high particle-flux environments. *Nucl. Instrum. Meth. A*, 376:29, 1996.

[121] K. Zioutas, C.E. Aalseth, D. Abriola, F.T. Avignone III, R.L. Brodzinski, et al. A Decommissioned LHC model magnet as an axion telescope. *Nucl.Instrum.Meth.*, A425:480–489, 1999.

[122] K. Zioutas et al. First results from the CERN Axion Solar Telescope (CAST). *Phys.Rev.Lett.*, 94:121301, 2005.

[123] S. Andriamonje et al. An Improved limit on the axion-photon coupling from the CAST experiment. *JCAP*, 0704:010, 2007.

[124] A. I. Bolozdynya T. Doke E. Aprile, A. E. Bolotnikov. *Noble Gas Detectors*. WILEY-VCH, 2006.

[125] W. R. Leo. *Techniques for Nuclear and Particle Physics Experiments: A How-To Approach*. Springer-Verlag, second rev. edition, 1994.

[126] W. Blum and L. Rolandi. *Particle Detection with Drift Chambers*. Springer-Verlag, 1993.

[127] S. N. Ahmed. *Physics and Engineering of Radiation Detection*. Academic Press, 2007.

[128] A. Peisser and F. Sauli. Drift and diffusion of electrons in gases: A compilation. *CERN, Experimental Physics Division*, 84-08, 1984.

[129] Magboltz - transport of electrons in gas mixtures, 2012. URL `http://consult.cern.ch/writeup/magboltz`.

[130] Robert E. Robson. *Introductory transport theory for charged particles in gases*. World Scientific, 2006.

[131] Eido Shibamura. Energy resolution in liquid ar or xe ionization chamber doped with photo-ionizing molecules. *Nuclear Instruments and Methods in Physics Research Section A: Accelerators, Spectrometers, Detectors and Associated Equipment*, 327(1):124–127, 3/20 1993.

[132] A. E. Bolotnikov et al. Properties of compressed xe gas as the detector medium for high-pressure xe spectrometers. In *Nuclear Science Symposium and Medical Imaging Conference, 1994., 1994 IEEE Conference Record*, volume 1, pages 74–78, 1994.

[133] S.A. Korff. *Electrons and Nuclear Counters*. Van Nostrand, 1946.

[134] M. E. Rose and S. A. Korff. An investigation of the properties of proportional counters. *I, Phys. Rev.*, 59:850, 1941.

[135] E. Nasser. *Fundamentals of Gaseous Ionization and Plasma Electronics.* Wiley-Interscience, 1971.

[136] Simon Ramo. Currents induced by electron motion. *Proceedings of the IRE*, 27(9):584–585, 1939.

[137] U. Fano. Ionization yield of radiations. ii. the fluctuations of the number of ions. *Phys. Rev.*, 72:26–29, 1947.

[138] Francisco J. Iguaz. *Development of a Time Projection Chamber prototype with Micromegas technology for the search of the Double Beta Decay of* ^{136}Xe. PhD thesis, Universidad de Zaragoza, Zaragoza, Spain, February 2010.

[139] J. Byrne. Statistics of electron avalanches in the proportional counter. *Nuclear Instruments and Methods*, 74(2):291–296, 10/15 1969.

[140] G. D. Alkhazov. Statistics of electron avalanches and ultimate resolution of proportional counters. *Nuclear Instruments and Methods*, 89(0):155–165, 12/1 1970.

[141] P. N. B. Neves, C. A. N. Conde, and L. M. N. Tavora. Drift field limitations to the energy resolution in time projection chambers for 136xe neutrino-less double beta decay search. *Nuclear Instruments and Methods in Physics Research Section A: Accelerators, Spectrometers, Detectors and Associated Equipment*, 641(1):87–91, 6/11 2011.

[142] E. Rutherford H. Geiger. An electrical method of counting the number of alpha-particles from radio-active substances. *Proc. Royal Soc. A*, 81:141, 1908.

[143] W. Muller H. Geiger. Electron counting tube for measurement of weakest radioactivities. *Die Naturwissenschaften*, 16:31, 1928.

[144] G. Charpak et al. The use of multiwire proportional counters to select and localize charged particles. *Nuclear Instruments and Methods*, 62(3):262 – 268, 1968.

[145] K. Kleinknecht. *Detectors for particle ratidation.* Cambridge University Press, 2nd edition edition, 21998.

[146] D. R. Nygren and J. N. Marx. The time projection chamber. *Physics Todays*, 31, 1978.

[147] I. Giomataris P. Colas and V. Lepeltier. Ion backflow in the micromegas TPC for the future linear collider. *Nucl. Instrum. Meth. A*, 535:226, 2004.

[148] Y. Giomataris. Development and prospects of the new gaseous detector micromegas. *Nucl. Instrum. Meth. A*, 419:239, 1998.

[149] B. Peyaud et al. KABES: a novel beam spectrometer for na48. *Nucl. Instrum. Meth. A*, 535:247, 2004.

[150] F.J. et al. Iguaz. Characterization of microbulk detectors in argon- and neon-based mixtures. *JINST*, 7:P04007, 2012.

[151] T. Papaevangelou et al. Development and performance of microbulk micromegas detectors. *Journal of Instrumentation*, 5(02):P02001, 2010.

[152] J. Derré et al. Spatial resolution in micromegas detector. *Nucl. Instrum. Meth. A*, 459: 523, 2001.

[153] A. Delbart et al. New developments of micromegas detector. *Nucl. Instrum. Meth. A*, 461: 84, 2001.

[154] I. Giomataris". Micromegas in a bulk. *Nucl. Instrum. Meth. A*, 560:405408, 2006.

[155] ILIAS database on radiopurity of materials. `http://radiopurity.in2p3.fr`, 2008.

[156] S. Cebrián et al. Radiopurity of micromegas readout planes. *Astroparticle Physics*, 34(6): 354–359, 1 2011.

[157] Laboratorio subterraneo de canfranc. URL `http://www.lsc-canfranc.es/en/`.

[158] P. M. McCowan and R. C. Barber. Q value for the double-β decay of ^{136}Xe. *Phys. Rev. C*, 82:024603, Aug 2010.

[159] V. Álvarez et al.NEXT Collaboration. Initial results of next-demo, a large-scale prototype of the next-100 experiment. *Journal of Instrumentation*, 8:P04002, 2013.

[160] V. Alvarez et al. (NEXT Collaboration). Near-Intrinsic Energy Resolution for 30 to 662 keV Gamma Rays in a High Pessure Xenon Electroluminescent TPC. *Nuclear Inst. and Methods in Physics Research A*, 114:101, 2013.

[161] V. Alvarez et al. (NEXT Collaboration). The NEXT-100 experiment for neutrinoless double beta decay searches (Conceptual Design Report). *ArXiv.org*, arXiv:1106.3630, 2011.

[162] V. Álvarez et al. Next-100 technical design report (tdr). executive summary. *Journal of Instrumentation*, 7(06), 2012.

[163] V. Àlvarez et al. NEXT Collaboration. SiPMs coated with TPB: coating protocol and characterization for next. *Journal of Instrumentation*, 7(02):P02010, 2012.

[164] V. Álvarez et al.NEXT Collaboration. Design and characterization of the SiPM tracking system of NEXT-DEMO, a demonstrator prototype of the NEXT-100 experiment. *ArXiv.org*, arXiv:1206.6199, 2012.

[165] V. Alvarez et al. Radiopurity control in the next-100 double beta decay experiment: procedures and initial measurements. *Journal of Instrumentation*, 8(01):T01002, 2013.

[166] Can the intrinsic energy resolution in xenon be surpassed? *J. Phys.: Conf. Ser.*, 309: 012006, 2011.

[167] C. A. B. Oliveira et al. Energy resolution studies for next. *Journal of Instrumentation*, 6 (05):P05007, 2011. URL `http://stacks.iop.org/1748-0221/6/i=05/a=P05007`.

[168] E.D.C Freitas et al. Secondary scintillation yield in high-pressure xenon gas for neutrinoless double beta decay search. *Physics Letters B*, 684(45):205 – 210, 2010.

[169] L. M. P. Fernandes et al. Primary and secondary scintillation measurements in a xenon gas proportional scintillation counter. *Journal of Instrumentation*, 5(09):P09006, 2010. URL `http://stacks.iop.org/1748-0221/5/i=09/a=P09006`.

[170] T. Dafni et al. Energy resolution of alpha particles in a microbulk micromegas detector at high pressure argon and xenon mixtures. *Nuclear Instruments and Methods in Physics Research Section A: Accelerators, Spectrometers, Detectors and Associated Equipment*, 608 (2):259 – 266, 2009.

[171] P. Baron et al. AFTER, the front end ASIC of the T2K Time Projection Chambers. 2009.

[172] P. Baron et al. After, an asic for the readout of the large t2k time projection chambers. In *Nuclear Science Symposium Conference Record, 2007. NSS '07. IEEE*, volume 3, pages 1865–1872, 26 2007-Nov. 3.

[173] G. Auday et at. Experimental study of the effective secondary emission coefficient for rare gases and copper electrodes. *Journal of Applied Physics*, 83:5917, 1998.

[174] Alfredo Tomás. *Study on Time Projection Chambers with Micromegas for Rare Event Searches*. PhD thesis, Universidad de Zaragoza, Zaragoza, Spain, 2013.

[175] M.J. Berger et al. Stopping-power and range tables for electrons, 2008. URL `http://physics.nist.gov/PhysRefData/Star/Text/contents.htmlh`.

[176] Elisa Ruiz Choliz. Caracterización del prototipo next-mm del experimento next para la búsqueda de la desintegración doble beta sin neutrinos del isótopo xe136. Master's thesis, Universidad de Zaragoza, 2013.

[177] Herrera D. C. Micromegas-TPC operation at high pressure in Xenon-trimethylamine mixtures. volume arXiv, page submit/0680872, 2013.

[178] O.A. Pokratenko et al. Event generator DECAY4 for simulating double-beta processes and decays of radioactive nuclei. *Phys. At. Nucl.*, 63:1282–1287, 2000.

[179] J.K. Tuli. The Evaluated Nuclear Structure Data File: a manual for preparation of data sets. Technical Report BNL-NCS-51655-01/02-Rev, Brookhaven National Laboratory, 2001.

[180] S.T. Perkins et al. Tables and graphs of atomic subshell and relaxation data derived from the LLNL Evaluated Atomic Data Library (EADL), z=1-100. Technical Report UCRL-50400 Vol.30, Lawrence Livermore National Laboratory, 1997.

[181] S. Agostinelli et al. GEANT4-a simulation toolkit. *Nucl. Instr. and Meth. A*, 506:250–303, 2003.

[182] J. Allison et al. GEANT4 developments and applications. *IEEE Transactions on Nuclear Science*, 53:270–278, 2006.

[183] GEANT4 Collaboration. Physics reference manual. http://geant4.cern.ch, 2005.

[184] R. Brun et al. ROOT webpage. http://root.cern.ch/drupal/, 2008.

[185] M. Doi et al. Approximations for double-beta-decay formulas. *Phys. Rev. C*, 37:2104–2120, 1988.

[186] I. V. Titkova H. V. Klapdor-Kleingrothaus, I. V. Krivosheina. Particle and nuclear physics parameters-how do they affect the tracks of double beta events in a germanium detector, and their separation from gamma events. *Physics Letters B*, 632:623, 2006.

[187] World Scientific Procc. of the 6th International Workshop on The Identification of Dark Matter, editor. *Characterization of the Canfranc Underground Laboratory: Status and future plans*, 2006.

[188] Bollóbas B. *Modern Graph Theory*. Springer-Verlag, 1998.

[189] Gondran M. and Minoux M. *Graphs and Algorithms*. John Wiley, 1984.

[190] E. Aprile et al. Material screening and selection for xenon100. *Astroparticle Physics*, 35 (2):43–49, 2011.

[191] D. Budjáš et al. Gamma-ray spectrometry of ultra low levels of radioactivity within the material screening program for the GERDA experiment. *Applied Radiation and Isotopes*, 67:755 – 758, 2009.

[192] W. Verkerke and D. Kirkby. The RooFit toolkit for data modeling. *ArXiv.org*, arXiv: 0306116, 2003.

[193] W. Verkerke and D. Kirkby. The roofit toolkit for data modeling homepage. URL `http://roofit.sourceforge.net/`.

[194] L. Moneta, K. Cranmer, G. Schott, and W. Verkerke. The RooStats project. In *Proceedings of the 13th International Workshop on Advanced Computing and Analysis Techniques in Physics Research. February 22-27, 2010, Jaipur, India. url="http://pos.sissa.it/cgi-bin/reader/conf.cgi?confid=93"¿http://pos.sissa.it/cgi-bin/reader/conf.cgi?confid=93¡/A¿, p.57*, volume arXiv, page 1009.1003, 2010.

[195] The roostats homepage. URL `https://twiki.cern.ch/twiki/bin/view/RooStats/WebHome`.

[196] G. Schott and for the RooStats Team. RooStats for Searches. *ArXiv.org*, arXiv:1203.1547, 2012.